

BAND STRUCTURE ENGINEERING
FOR ULTRACOLD QUANTUM GASES
IN OPTICAL LATTICES

DISSERTATION
ZUR ERLANGUNG DES DOKTORGRADES
DES DEPARTMENTS PHYSIK
DER UNIVERSITÄT HAMBURG

VORGELEGT VON
MALTE WEINBERG
AUS HAMBURG

HAMBURG
2014

Gutachter der Dissertation: Prof. Dr. Klaus Sengstock
Prof. Dr. Andreas Hemmerich

Gutachter der Disputation: Prof. Dr. Klaus Sengstock
Prof. Dr. Henning Moritz

Datum der Disputation: 12. Dezember 2014

Vorsitzende des Prüfungsausschusses: Prof. Dr. Daniela Pfannkuche

Vorsitzende des Promotionsausschusses: Prof. Dr. Daniela Pfannkuche

Dekan der Fakultät für Mathematik,
Informatik und Naturwissenschaften: Prof. Dr. Heinrich Graener

Abstract

The energy band structure fundamentally influences the physical properties of a periodic system. It may give rise to highly exotic phenomena in yet uncharted physical regimes. Ultracold quantum gases in optical lattices provide an ideal playground for the investigation of a large variety of such intriguing effects. Experiments presented here address several issues that require the systematic manipulation of energy band structures in optical lattices with diverse geometries. These artificial crystals of light, generated by interfering laser beams, allow for an unprecedented degree of control over a wide range of parameters.

A major part of this thesis employs time-periodic driving to engineer tunneling matrix elements and, thus, the dispersion relation for bosonic quantum gases in optical lattices. Resonances emerging in the excitation spectrum due to the particularly strong forcing can be attributed to multi-photon transitions that are investigated systematically. By changing the sign of the tunneling, antiferromagnetic spin-spin interactions can be emulated. In a triangular lattice this leads to geometrical frustration with a doubly degenerate ground state as the simultaneous minimization of competing interactions is inhibited. Moreover, complex-valued tunneling matrix elements can be generated with a suitable breaking of time-reversal symmetry in the driving scheme. The associated Peierls phases mimic the presence of an electromagnetic vector gauge potential acting on charged particles. First proof-of-principle experiments reveal an excellent agreement with theoretical calculations. In the weakly interacting superfluid regime, these artificial gauge fields give rise to an Ising-XY model with tunable staggered magnetic fluxes and a complex interplay between discrete and continuous symmetries. A thermal phase transition from an ordered ferromagnetic- to an unordered paramagnetic state could be observed. In the opposite hard-core boson limit of strong interactions the same system maps onto a quantum spin-1/2 XY model. Owing to the quantum nature of the pseudospins, geometrical frustration leads to a highly degenerate ground state which can result in exotic valence bond spin-liquid phases. First signatures of an order-by-disorder effect emerge in this regime.

A complementary approach to the manipulation of the band structure is investigated in a honeycomb potential. By rotating the quantization field of the system, the state-dependent energy offset between the twofold atomic basis of the hexagonal Bravais lattice can be adjusted. This purposeful breaking of inversion symmetry enables the continuous opening of an energy gap at the Dirac points of the honeycomb band structure. In addition, a striking influence of the band gap onto the lifetimes for atoms in the first excited energy band is observed.

In the last part of the thesis, both experimental manipulation techniques are discussed with respect to future applications for ultracold quantum gases in non-cubic optical lattices.

Zusammenfassung

Die physikalischen Eigenschaften eines periodischen Potentials werden wesentlich von seiner Bandstruktur beschrieben. Durch direkte Manipulation der Bandstruktur können sich experimentell bislang nicht realisierte, hochgradig exotische Phänomene ergeben. Modellsysteme ultrakalter Quantengase in optischen Gittern ermöglichen die Erschließung dieser Regime aufgrund unübertroffener Möglichkeiten zur Kontrolle und Manipulation über weite physikalische Parameterbereiche. Experimente im Rahmen dieser Arbeit beruhen auf der gezielten Veränderung der Bandstruktur verschiedener optischer Gitter, künstlicher Kristalle aus Licht, die durch interferierende Laserstrahlen erzeugt werden.

Zeitperiodisches Treiben optischer Gitter ermöglicht das Einstellen effektiver Tunnelmatrixelemente und damit die kohärente Manipulation der entsprechenden Dispersionsrelation. Die hohe Intensität dieser experimentellen Methode führt zum Auftreten von charakteristischen Mehrphotonenübergängen die im Rahmen dieser Arbeit systematisch untersucht werden. Eine Vorzeichenänderung der Tunnelmatrixelemente ermöglicht die Modellierung antiferromagnetischer Wechselwirkungen und geometrischer Frustration in einem Dreiecksgitter, da die gleichzeitige Minimierung aller Wechselwirkungen hier unmöglich ist. Darüber hinaus können durch das gezielte Brechen der Zeitumkehrsymmetrie des periodischen Treibens auch komplexwertige Tunnelmatrixelemente erzeugt werden. Die zugehörigen Peierlsphasen imitieren den Effekt eines elektromagnetischen Eichpotentials auf geladene Teilchen. Im schwach wechselwirkenden Regime ergibt sich daraus ein Ising-XY Modell mit alternierenden, voll einstellbaren magnetischen Flüssen und einem komplexen Zusammenspiel kontinuierlicher und diskreter Symmetrien. In diesem System konnte ein thermischer Phasenübergang von einem ferromagnetischen zu einem paramagnetischen Zustand nachgewiesen werden. Im gegenteiligen Grenzfall starker Wechselwirkung ergibt sich ein Quanten Spin- $1/2$ XY Modell. Geometrische Frustration führt hier zu einem hochgradig entarteten Grundzustand aus dem sich eine exotische Quanten-Spin-Flüssigkeitsphase ergeben kann. Erste Signaturen eines "Ordnung durch Unordnung"-Effekts wurden beobachtet.

Ein komplementärer Ansatz zur Manipulation der Bandstruktur basiert auf einer Rotation der Quantisierungsachse in einem hexagonalen Gitter. Hiermit kann ein zustandsabhängiger Energieversatz zwischen der zweiatomigen Basis des Bravaisgitters eingestellt werden. Diese Brechung der Inversionssymmetrie ermöglicht das kontinuierliche Öffnen einer Energielücke an den Dirac Punkten der Bandstruktur. Die Lebensdauer von Atomen im ersten angeregten Band wird entscheidend von dieser Energielücke beeinflusst.

Im letzten Teil der Arbeit werden beide Manipulationstechniken im Hinblick auf zukünftige Experimente mit ultrakalten Quantengasen in nicht-kubischen optischen Gittern diskutiert.

Publications

The following articles have been published within the scope of this thesis.

Publikationen

Im Rahmen dieser Arbeit sind die folgenden Veröffentlichungen entstanden.

- [1] J. Struck, C. Ölschläger, M. Weinberg, P. Hauke, J. Simonet, A. Eckardt, M. Lewenstein, K. Sengstock, and P. Windpassinger:
“Tunable Gauge Potential for Neutral and Spinless Particles in Driven Optical Lattices”
Phys. Rev. Lett. **108**, 225304 (2012)
- [2] P. Hauke, O. Tieleman, A. Celi, C. Ölschläger, J. Simonet, J. Struck, M. Weinberg, P. Windpassinger, K. Sengstock, M. Lewenstein, and A. Eckardt:
“Non-Abelian Gauge Fields and Topological Insulators in Shaken Optical Lattices”
Phys. Rev. Lett. **109**, 145301 (2012)
- [3] J. Struck, M. Weinberg, C. Ölschläger, P. Windpassinger, J. Simonet, K. Sengstock, R. Höppner, P. Hauke, A. Eckardt, M. Lewenstein, and L. Mathey:
“Engineering Ising-XY spin-models in a triangular lattice using tunable artificial gauge fields”
Nature Physics **9**, 738–743 (2013)
- [4] J. Simonet, J. Struck, M. Weinberg, C. Ölschläger, P. Hauke, A. Eckardt, M. Lewenstein, K. Sengstock, and P. Windpassinger:
“Tunable gauge potential for spinless particles in driven lattices”
EPJ Web of Conferences **57**, 01004 (2013)
- [5] D.-S. Lühmann, O. Jürgensen, M. Weinberg, J. Simonet, P. Soltan-Panahi, and K. Sengstock:
“Quantum phases in tunable state-dependent hexagonal optical lattices”
Phys. Rev. A **90**, 013614 (2014)

Contents

1	Introduction	1
2	Ultracold bosons in optical potentials	9
2.1	Experimental preparation of Bose-Einstein condensates	10
2.2	Atom-photon interaction: dipole potentials	11
2.2.1	Dressed state approach	11
2.2.2	Polarization modes	12
2.2.3	Effective magnetic field	13
2.2.4	Optical dipole traps	14
2.3	Periodic optical potentials	16
2.3.1	Non-interacting particles in lattice potentials	16
2.3.2	Bose-Hubbard model	17
2.4	Realization of optical lattices with hexagonal symmetry	20
2.4.1	Three-beam lattice setup	21
2.4.2	Triangular lattice	25
2.4.3	State-dependent honeycomb lattice	26
2.4.4	Polarization lattice	27
2.5	Revealing the momentum distribution by time-of-flight measurement . . .	29
2.6	Conclusion & outlook	32
3	Bose-Einstein condensates in strongly driven lattices	33
3.1	Tunneling renormalization by periodic driving	34
3.1.1	Semiclassical 1D-model	34
3.1.2	Effective description of driven systems	35
3.1.3	Application to driven lattices	38
3.2	Experimental realization of periodically driven lattices	40
3.2.1	Monochromatic driving of a one-dimensional lattice	41
3.2.2	Driving of the triangular lattice	45
3.3	Investigating strong-field excitations	48
3.3.1	Strong driving of the one-dimensional lattice	49
3.3.2	Excitation spectra of the triangular lattice	55
3.3.3	Periodic driving in the 3D-lattice	57
3.4	Conclusion & outlook	60

4	Engineering artificial gauge fields	61
4.1	Realization of tunable Peierls phases	62
4.1.1	Peierls substitution in the tight-binding model	62
4.1.2	Symmetry constraints of the forcing	64
4.1.3	Complex-valued tunneling in the one-dimensional lattice	64
4.2	Tunable gauge-invariant fluxes on the triangular lattice	68
4.2.1	Time-asymmetric elliptical forcing	69
4.2.2	Tuning of staggered fluxes	72
4.3	Emulation of the Ising-XY model	73
4.3.1	Mapping to the classical XY model	73
4.3.2	Symmetries of the Ising-XY spin model	74
4.3.3	Thermally driven phase transition	77
4.3.4	Statistical data analysis of symmetry breaking	80
4.3.5	Analysis of long-range phase coherence - $U(1)$ symmetry	84
4.4	Model-free statistical data analysis	85
4.4.1	Principal component analysis	86
4.4.2	Independent component analysis	90
4.5	Conclusion & outlook	91
5	Frustrated quantum antiferromagnetism in a triangular lattice	93
5.1	Quantum XY model	94
5.1.1	Inverse Holstein-Primakoff mapping	94
5.1.2	Frustration and ground-state degeneracy	96
5.1.3	Quantum phases on the frustrated triangular lattice	97
5.2	Characterization of the Mott-insulating phase	98
5.2.1	Superfluid to Mott insulator transition	98
5.2.2	Lifetime of the Mott-insulating state	101
5.2.3	Detecting on-site excitations	101
5.3	Realization of the antiferromagnetic Mott insulator by lattice driving . . .	104
5.3.1	Limitations of the parameter space	105
5.3.2	Superfluid to Mott insulator transition in the driven lattice	108
5.4	Quantum noise correlation analysis of the Mott-insulating state	109
5.4.1	Hanbury Brown-Twiss interferometry	110
5.4.2	Noise correlation observable in time-of-flight images	111
5.4.3	Experimental implementation of the noise correlation analysis . . .	112
5.4.4	Noise correlations in the antiferromagnetic Mott insulator	115
5.5	Order-by-disorder signature of the frustrated antiferromagnet	117
5.6	Conclusion & outlook	119

6	Probing Dirac points in the state-dependent honeycomb lattice	121
6.1	State-dependent honeycomb lattice	123
6.2	Inversion symmetry breaking by rotating the quantization axis	125
6.2.1	Effective magnetic quantum number	126
6.2.2	Opening of Dirac points	126
6.2.3	Experimental realization of the rotation	129
6.3	Band-selective microwave spectroscopy	129
6.3.1	Theoretical description	130
6.3.2	Experimental procedure	131
6.3.3	Spin-changing collisions	133
6.3.4	Microwave spectra in the tunable honeycomb lattice	134
6.3.5	Interaction effects	136
6.4	Probing inter-band dynamics	139
6.4.1	Excitation mechanism	140
6.4.2	Time-resolved band decay	142
6.4.3	Decay mechanisms	145
6.5	Conclusion & outlook	146
7	Towards the realization of exotic quantum phases	149
7.1	Periodic inertial forcing in the honeycomb lattice	150
7.1.1	Tight-binding description	150
7.1.2	Tuning of next-nearest-neighbor tunneling	153
7.1.3	Topologically non-trivial bands	155
7.1.4	Zig-zag lattice arrays	156
7.2	Homogeneous gauge fields in a stirred polarization lattice	157
7.3	From three- to six-beam lattices	160
7.3.1	Kagome lattice	161
7.3.2	Dice lattice	161
7.4	Conclusion & outlook	163
	Appendix A Data analysis and representation	165
A.1	Comparison of contrast methods	165
A.2	Color-coded data visualization	167
A.3	Defringing algorithms	168
A.4	Automated notch-filtering of correlation data	168
	Appendix B Correlation analysis of symmetry breaking	171
	Appendix C Single-shot symmetry breaking images	175

Appendix D Experimental imperfections	179
D.1 Measured three-beam lattice geometry	179
D.2 Residual oscillations in the crossed dipole trap	181
Appendix E Physical constants and rubidium line data	183
List of Figures	185
Bibliography	189

1 Introduction

This chapter provides a broader context of research and discusses specific issues that are addressed in this work. In addition, a short outline of the thesis is presented.

The Hilbert space of a quantum system grows exponentially with its size. This circumstance is owed to the possibility of superposition and renders the task of simulating large quantum many-body systems with classical computers practically impossible. In his keynote lecture on *Simulating physics with computers* in 1981 [6] Richard Feynman phrased that “[...] nature isn’t classical, dammit, and if you want to make a simulation of nature, you’d better make it quantum mechanical, and by golly it’s a wonderful problem, because it doesn’t look so easy.”

Indeed, as of today, the originally envisioned universal quantum Turing machine [7, 8] is still far from being realized. Nonetheless, Feynman’s seminal insight is widely regarded as the inspiration of quantum simulation in general. Since then, tremendous advances of creating, manipulating and detecting isolated quantum systems have been achieved. These newly developed experimental tools provide an unprecedented degree of control over quantum many-body systems and allow for a different approach to quantum simulation: In contrast to quantum information processing in terms of discrete quantum logic operations, the *analog* simulation of complex quantum systems relies on the direct modeling of a specific Hamiltonian which mimics certain aspects of the behavior of other systems [9].

Interest in such tailoring of quantum model systems, coined *quantum engineering*, has risen rapidly in recent years as quantum effects play an increasingly important role in modern technology. So far, many complementary proposals and realizations for quantum simulation of a wide range of physical problems have been conceived. Such model systems include quantum dots [10–13], trapped ions [14–19], cavity arrays [20–22], linear optics [23], superconducting circuits [24, 25] and nuclear spins [26, 27].

An essential and challenging aspect in the study of interacting quantum many-body systems is the understanding of solid state materials. Due to the complex interplay between interaction effects and the underlying crystal symmetry, many intriguing phenomena of solid state physics still remain to be explained. A particularly well suited ansatz for the modeling of such spatially periodic systems is provided by neutral ultracold quantum gases that are confined in optical lattices [28, 29]. These *artificial crystals of light* [30, 31], generated by the interference pattern of laser beams, enable the probing of quantum many-body physics in periodic potentials in a clean and controllable environment over a wide range of accessible parameters.

The fast-paced theoretical and experimental developments in the field of quantum degenerate gases were sparked by the groundbreaking achievement of Bose-Einstein condensation [32–34]. It marks the beginning of a new era to quantum optics, atomic and molecular physics. Since then, spectacular progress has been made in this novel interdisciplinary field of research. First fundamental studies on such macroscopic wave functions focussed on collective excitations [35, 36], coherence properties [37], atom lasing [38] and the formation of quantized vortices [39]. An important step towards the full control over the physical parameters is given by the ability to precisely adjust both the sign and the strength of interactions by means of Feshbach resonances [40, 41]. Together with the generation of quantum degenerate Fermi gases [42–44] it enabled the investigation of the crossover from a BEC (Bose-Einstein condensate) to the BCS (Bardeen-Cooper-Schrieffer) phase [45–51].

Early studies of atoms confined in optical lattices had already been performed for thermal ensembles [30, 31, 52, 53]. The regime of many-body physics, however, could not be explored until the realization of quantum degenerate gases. The seminal proposal [54, 55] and subsequent observation [56] of a quantum phase transition from a superfluid to a Mott-insulating state opened this young field of research to the strongly correlated regime. Further experiments include the observation of density-density correlations [57, 58], Fermi surfaces [59] and the fermionic Mott insulator [60, 61]. Increasingly sophisticated preparation schemes and control mechanisms have since further expanded the possibilities for quantum engineering with optical lattices. A paradigm example of this advancement is the development of quantum gas microscopes that allow for the precise detection and probing of lattice systems with single-site resolution [62–65]. An important aspect of this rapid technological progress in the field of degenerate quantum gases in optical lattices is the ability to tailor highly specified quantum many-body systems *beyond* the known solid state materials. Such intriguing experiments include the observation of condensation at nonzero quasimomenta in excited energy bands [66] and unconventional superfluidity [67–69], the detection of an Anderson-Higgs-type amplitude mode [70, 71] and the realization of negative absolute temperatures [72], only to name a few.

The symmetry of any kind of periodic potential has a profound influence on its properties. While first experiments with ultracold quantum gases dealt with simple cubic lattices [73], a variety of different lattice systems have been realized so far, ranging from triangular [74] and honeycomb [75, 76] geometries to chequerboard [66] and kagome lattices [77]. A characteristic feature of periodic potentials in general is the emergence of an energy band structure for allowed quasimomentum states that is closely connected to the geometry of the lattice. A leitmotif of the experiments on ultracold atomic ensembles in optical lattices performed within the scope of this thesis is the targeted manipulation of the energy band structure. Hereby, different geometries and physical phenomena are explored. The main topics of which are detailed in the following.

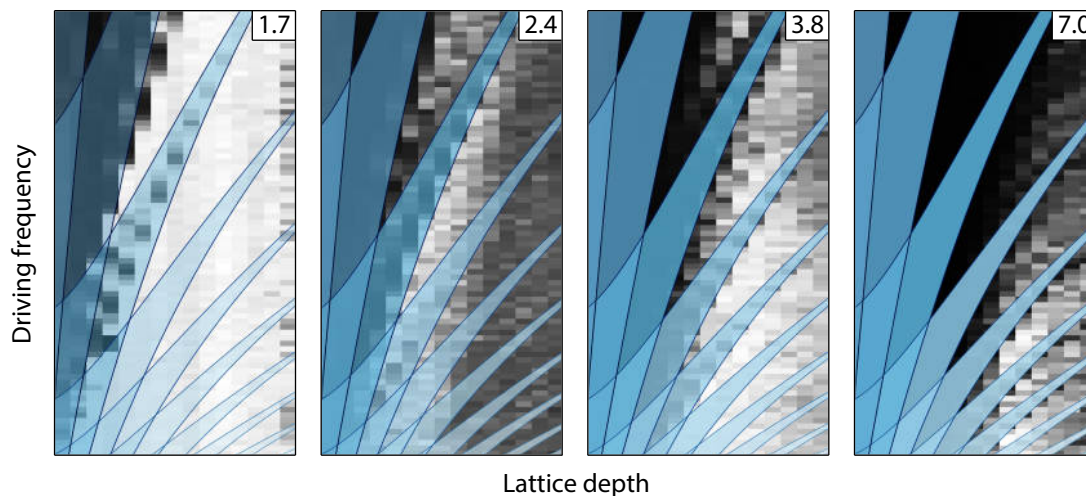


Figure 1.1: With increasing strength of the periodic lattice driving for the four data sets, indicated by the dimensionless forcing parameter in the upper right corners, more and more resonance features appear in the excitation spectrum. All of these excitations can be attributed to *ab initio* calculations of multi-photon transitions between the two lowest energy bands of the optical lattice (blue areas).

Periodically driven lattices

Pioneering experiments on periodically driven lattice systems have been performed within the scope of this thesis. Time periodic modulation in general is an important concept for the manipulation of ultracold atoms in optical lattices. Thereby, either the amplitude or the phase of the lattice potential can be altered. Amplitude modulation of the lattice depth is an established technique for the investigation of excitation spectra [78–80] and pump probe experiments [81, 82]. Further applications include the realization of an orbital excitation blockade and algorithmic cooling [83], photon assisted tunneling [84] and probing of correlations [85]. In contrast, phase modulation of lattice laser beams is well suited for inducing spatial translations of the interference pattern. Here, we utilize phase modulation for the creation of inertial time-periodic forces acting on the atomic ensemble in the co-moving reference frame. In a time-averaged effective picture these oscillating forces lead to a renormalization of tunneling matrix elements in both amplitude and sign [86–92].

Tunneling suppression by periodic driving has been successfully demonstrated for thermal atoms [93], Bose-Einstein condensates [94] and the superfluid to Mott insulator transition [95]. Beyond that, the tunability of tunneling matrix elements enables the coherent manipulation of the time-averaged energy band structure. The application of this technique to a triangular lattice allowed for the striking emulation of frustrated classical magnetism and a variety of Néel ordered phases [96].

An intriguing aspect of such time-periodic driving is the particularly strong forcing of the quantum many-body system [97]. While this circumstance can result in detrimental heating processes, it also opens the possibility to study the effects of strong-field physics

in a quantum many-body model system. We explore the coherent manipulation of the dispersion relation further and investigate the regime of strong forcing systematically with respect to the emergence of multi-photon transitions (see Fig. 1.1).

Artificial gauge fields

The striking influence of gauge fields in quantum physics is impressively demonstrated by the celebrated Aharonov–Bohm effect [98–100]. Here, a wave function is affected by an electromagnetic field in regions that are well separated from the particles trajectory due to the interaction with the electromagnetic vector gauge potential. This purely quantum-mechanical effect has no Newtonian analogy. It tackles fundamental issues of quantum physics such as the principles of locality and action. As of today, gauge fields represent an integral constituent to physics in general.

The close ties to electromagnetism motivate the emulation of strong gauge fields with quantum simulators, promising access to exotic condensed matter phenomena that are predicted for extremely large field strengths such as the integer and fractional quantum Hall effects [101–104] or the self-similar recursive energy spectrum of the so-called Hofstadter butterfly [105, 106].

Due to the lack of electric charge, ultracold atomic ensembles respond differently to electromagnetic fields as, e.g., a gas of electrons. Nonetheless, neutral atoms may be utilized for the mimicking of such effects. An intuitive approach for the simulation of gauge fields is the application of rotation based on the similarity between the fictitious Coriolis force and the Lorentz force [107–113]. However, a fundamental limitation of this technique is caused by centrifugal forces that cannot be compensated easily for high rotation frequencies. A different method for the generation of artificial gauge fields relies on the coupling of internal atomic states by Raman transitions. Such schemes were successfully applied to a variety of bulk [114–116] and optical lattice systems [117–122].

Within the scope of this thesis, we have developed a new and highly versatile approach to the creation of gauge fields: The influence of a vector gauge potential on a charged particle in a lattice potential is described within the framework of the Peierls substitution. In analogy to the Aharonov-Bohm effect discussed above, a wave function acquires a directional complex phase for each tunneling process between lattice sites. We have engineered complex-valued tunneling matrix elements and, thus, emulated the presence of a gauge field by expanding the previously described periodic driving scheme. The advantages of this technique are its independence from any internal atomic structure as well as the tunability of the simulated vector potential. The magnetic flux corresponding to the simulated gauge field is given by the summation of Peierls phases around a lattice plaquette. By applying the driving scheme to a triangular optical lattice, a system of fully tunable staggered synthetic magnetic fields with strengths on the order of a flux quantum have been realized. An investigation of intrinsic discrete and continuous symmetries gives rise to an Ising-like phase transition from an ordered to an unordered state with a magnetization behavior similar to ferro- and paramagnetism.

Frustrated quantum magnetism

The simultaneous minimization of all interaction energies in ordered many-body systems can be inhibited due to constraints imposed by the underlying geometry. Such *geometrical frustration* [123] gives rise to a multitude of intriguing phenomena in condensed matter physics. A paradigm example is quantum antiferromagnetism on a triangular lattice [124]. Here, the sign of the exchange coupling favors an antiparallel alignment of quantum mechanical spins [125, 126]. The inability to fulfill this condition, illustrated for a single triangular plaquette in Fig. 1.2, leads to a huge ground state degeneracy which may prevent ordering even at zero temperature. A possible ground state of such disordered systems emerges for the entanglement of pairs of spins into valence bond states which preserve the lattice symmetries [127]. These so-called valence bond spin liquids are expected to play a crucial role for high- T_c superconductivity [128–130] and may be utilized for topological quantum computation [131].

Frustrated quantum magnetism is inherently difficult to observe in solid state materials. First signatures of quantum spin liquid phases have been detected in geometrically frustrated triangular [132–136] and kagome-ordered materials [137, 138] using spectroscopic methods. Nonetheless, an emulation of quantum magnetism with ultracold atoms in optical lattices promises deep insights into such highly nontrivial states of matter. For example, a fermionic Mott insulator can mimic quantum magnetism in terms of pseudo spins comprised of two different internal states. However, this approach requires temperatures below the weak superexchange spin coupling. While these ultra-low temperatures are still far out of reach even for degenerate quantum gases, short-range quantum magnetism could recently be simulated by utilizing a redistribution of entropy [139].

In experiments presented within this thesis, we pursue a fundamentally different technique for the emulation of quantum magnetism in optical lattices by mapping the site occupation in the strongly correlated regime. Here, an antiferromagnetic exchange interaction can be introduced by engineering the tunneling matrix element between adjacent lattice sites with the aforementioned periodic driving scheme [140]. In a similar context, a phase transition of antiferromagnetic one-dimensional quantum pseudo spin chains has been studied with ultracold atoms [141]. As of today, the striking influence of geometric frustration and the formation of disordered quantum phases, however, remains an uncharted territory. Experimental results hint towards the feasibility of our approach and pave the way towards further systematic studies of artificial quantum magnetism. Beyond that, first promising signatures of a related order-by-disorder effect could be observed.

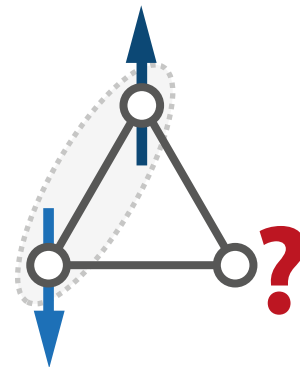


Figure 1.2: Frustrated quantum antiferromagnetism on a triangular lattice plaquette. While a pair of spins may align antiparallel, the third spin cannot be antiparallel to both of them.

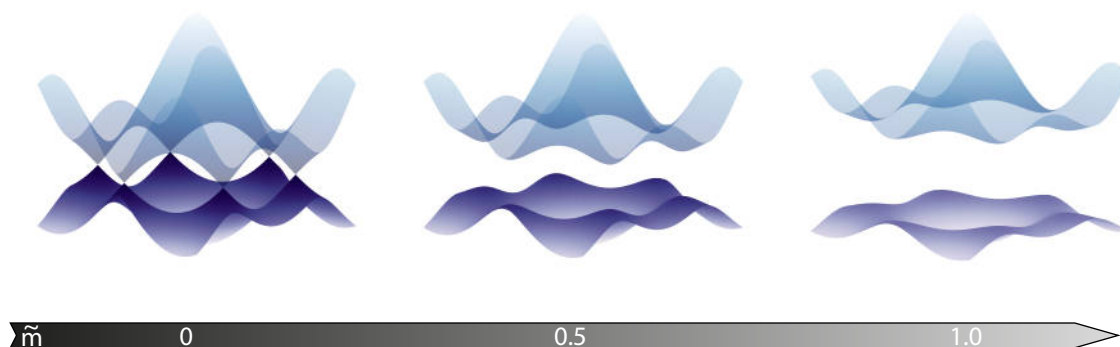


Figure 1.3: Tuning of Dirac points in the state-dependent honeycomb lattice. By adjusting the effective magnetic quantum number \tilde{m} the inversion symmetry of the lattice can be broken such that a band gap at the vertices of the first Brillouin zone opens up.

Tuning of Dirac points

Close-packing of equal spheres is a fundamental concept of geometry with a multitude of diverse manifestations in nature. In solid state physics, in particular the two-dimensional honeycomb lattice has attracted an enormous amount of attention in recent years as it is the basis for graphene [142]. This monolayer of carbon, an indefinitely large aromatic molecule, exhibits a variety of remarkable properties that are based on its two-dimensionality and the peculiar honeycomb symmetry [143–145]. Owing to the twofold atomic basis of the lattice structure, the two lowest energy bands touch at the vertices of the Brillouin zone. These so-called Dirac points represent a topological singularity that gives rise to massless relativistic quasiparticles [146].

The versatile possibilities for the manipulation of potential landscapes for ultracold atoms in optical lattices enable the *in situ* investigation of such peculiar systems [75]. So far, further observations include Klein tunneling [147], zitterbewegung [148], the merging of Dirac points [76] and the mapping of the Berry phase in momentum space [149]. Only recently, Haldane’s model [150] could be emulated by a combination of inversion- and time-reversal symmetry breaking in a *brick* lattice [151].

Within the scope of this thesis we have implemented a novel technique for the manipulation of a state-dependent honeycomb potential and its exceptional band structure. An effective quantum number \tilde{m} is created due to the projection of the state-dependent vectorial light shift onto the quantization axis of the quantum many-body system. By rotating the quantization field we tune the effective quantum number and, thus, the energy offset between the twofold atomic basis. As illustrated in Fig. 1.3, the control over the inversion symmetry allows the continuous opening of energy gaps at the Dirac points. Benchmark experiments verify the applicability of the tuning scheme and probe the spatial ordering of atoms. Further studies include the observation of decay mechanisms from excited energy bands with respect to the presence of Dirac points. The addressed physical mechanisms behind such decay processes still pose an open question.

In conclusion, the research presented in this thesis addresses several unresolved issues concerning quantum simulation of solid state systems including quantum magnetism, spontaneous symmetry breaking, quantum phase transitions, topological band structures and decay mechanisms. The application of novel manipulation techniques paves the way for further investigations in this dynamic field of research.

Structure of the thesis

The second chapter provides an introduction to the experimental setup and basic concepts concerning the optical lattice setup at hand. The main results of this work regarding experiments in a variety of different lattice systems are presented in the chapters 3 to 6. Chapter 7 gives a short outlook towards future experiments. Additional results and considerations are presented in the appendices. A brief outline of the contents of each chapter is provided in the following. For the readers convenience, these abstracts are repeated at the beginning of the respective chapters.

Chapter 2 – Ultracold Bosons in optical potentials

This chapter briefly introduces the experimental setup for the creation of Bose-Einstein condensates and reviews the concepts of periodic optical potentials. Properties of the implemented running-wave three-beam setup that generates an optical lattices with hexagonal geometry are discussed. Several fundamentally different realizations of the three-beam setup, namely the state-independent triangular lattice, the state-dependent honeycomb lattice and the purely state-dependent polarization lattice are presented together with a short survey of other possible configurations. Furthermore, the detection scheme used in all experiments throughout this thesis, relying on time-of-flight resonant absorption imaging, is established.

Chapter 3 – Bose-Einstein condensates in strongly driven lattices

In this chapter we develop the concept of far off-resonant time-periodic driving of optical lattices. We explain how this technique allows for the experimentally feasible engineering of tunneling matrix elements and, thus, of the dispersion relation in a time-averaged effective picture. Benchmark experiments for the verification of driving schemes are presented and discussed by means of the observed momentum distribution. Beyond that, we investigate the strong driving regime with respect to the occurrence of multi-photon transitions for different lattice dimensionality. We find an excellent agreement with *ab initio* calculations of the transition energies and discuss implications to further experiments.

Chapter 4 – Engineering artificial gauge fields

Here, we experimentally realize complex-valued tunneling matrix elements in optical lattices by a time-asymmetric far off-resonant driving technique that allows for the emulation

of artificial gauge fields. The feasibility of this approach is verified with excellent agreement to *ab initio* calculations in a proof-of-principle experiment on a one-dimensional lattice. We extend the concept to the triangular lattice, creating fully tunable gauge invariant staggered fluxes. This system represents the geometrically frustrated Ising-XY model that constitutes a generic spin model involving two coupled symmetries. Their associated order parameters are derived and analyzed with respect to the staggered flux strength and the temperature of the atomic ensemble.

Chapter 5 – Frustrated quantum antiferromagnetism in a triangular lattice

In this chapter we investigate the possibility of emulating frustrated quantum antiferromagnetism on the triangular optical lattice. In the hard-core boson limit of strong repulsive interactions the mapping of classical XY spins continuously approaches a quantum spin-1/2 XY model. On-site interactions are increased by an additional perpendicular optical lattice. We discuss limitations of the accessible parameter space for the harmonic lattice driving in the strongly correlated regime and probe the transition from a weakly interacting superfluid to a Mott-insulating state in both the static and the driven system. An analysis of quantum noise correlations reveals the feasibility of our approach. First hints towards an order-by-disorder effect in the frustrated system are observed.

Chapter 6 – Probing Dirac points in the state-dependent honeycomb lattice

Here, we present a novel method of controlling the geometry of a state-dependent honeycomb lattice: The energy offset between the two sublattices of the honeycomb structure can be tuned by rotating the atomic quantization axis. This enables us to continuously tune between a homogeneous graphene-like honeycomb lattice and a triangular lattice and to open an energy gap at the characteristic Dirac points. We probe the symmetry of the lattice with microwave spectroscopy techniques and investigate the behavior of atoms excited to the second energy band. We find a striking influence of the energy gap at the Dirac cones onto the lifetimes of atoms in the excited band.

Chapter 7 – Towards the realization of exotic quantum phases by lattice driving

This chapter provides an outlook on further possibilities for the engineering of quantum gas systems in the three-beam lattice. The previously introduced concepts of periodic lattice driving and the rotation of the quantization field are applied to state-dependent lattice systems. In addition, an expansion of the three-beam lattice setup is discussed that gives rise to peculiar lattice geometries.

2 Ultracold bosons in optical potentials

This chapter briefly introduces the experimental setup for the creation of Bose-Einstein condensates and reviews the concepts of periodic optical potentials. Properties of the implemented running-wave three-beam setup that generates an optical lattices with hexagonal geometry are discussed. Several fundamentally different realizations of the three-beam setup, namely the state-independent triangular lattice, the state-dependent honeycomb lattice and the purely state-dependent polarization lattice are presented together with a short survey of other possible configurations. Furthermore, the detection scheme used in all experiments throughout this thesis, relying on time-of-flight resonant absorption imaging, is established.

Ultracold quantum gases in optical lattices offer the unique possibility to study many-body physics in a clean and well controllable environment and a widely adjustable parameter space. Since first proof of principle studies [30, 31, 52, 53], optical lattices have evolved into a powerful tool for quantum simulation of condensed matter systems and novel quantum regimes [28, 29, 152]. These periodic potential landscapes are generated by interfering laser beams and consist of up to many thousands of microtraps. Atoms are confined to such lattice sites by the electric dipole force resulting from the oscillating electric light field acting on an induced atomic dipole moment.

In this chapter we describe the experimental setup used throughout this thesis with special emphasis on the running-wave three-beam optical lattice system. Atom-photon interactions leading to conservative optical dipole potentials for neutral atoms are introduced with regard to polarization modes and an effective magnetic field picture. We shortly discuss the description of non-interacting as well as interacting particles in periodic potentials, leading to the formulation of the well-known Bose-Hubbard model. Fundamental properties of optical lattice potentials with hexagonal symmetry are developed. We present three distinct realizations of such lattice structures arising from the three-beam lattice setup. Finally, we describe detection schemes relying on time-of-flight absorption imaging.

Parts of this chapter concerning the properties of the hexagonal optical lattice have been published in [74],[75] and [5] and are presented in the theses of C. Becker [153], P. Soltan-Panahi [154] and J. Struck [155]. Experimental data presented in section 2.5 has been acquired and processed by the author.

2.1 Experimental preparation of Bose-Einstein condensates

Degenerate quantum gases of an increasing number of atomic species are routinely created by confining a large, pre-cooled ensemble of atoms in magnetic or optical traps and performing evaporative cooling until quantum degeneracy is reached. All experiments described throughout this thesis start with a Bose-Einstein condensate of ^{87}Rb atoms in an optical dipole trap. This section briefly describes the experimental apparatus and procedure to reach the regime of quantum degeneracy and produce stable and pure Bose-Einstein condensates with an additional spin degree of freedom.

The apparatus on which all experiments presented in this thesis were performed was initially conceptualized and built by M. Erhard [156] and H. Schmaljohan [157]. It was extended further within the scope of the PhD theses of J. Kronjäger [158], C. Becker [153], P. Soltan-Panahi [154] and J. Struck [155].

At the heart of the experiment lies the vacuum setup. As widely used in apparatuses designed to create degenerate quantum gases it consists of a combination of two glass chambers that are linked by a differential pumping stage. This segmentation serves the purpose of being both able to capture large atomic ensembles while maintaining a vacuum background pressure as small as possible in the presence of the extremely fragile ultracold atomic ensemble. Here, the vacuum chambers are aligned vertically, whereby the upper vacuum chamber serves as an atomic reservoir. A constant background pressure of rubidium atoms at approximately 10^{-9} mbar is maintained by electrically heating a dispenser that is mounted inside the chamber. At the center of the chamber, a two-dimensional magneto-optical trap (MOT) captures and pre-cools a fraction of the background atoms along a thin vertical line directly above the differential pumping stage. The captured atoms are continuously transferred to the second glass cell below the narrow pumping stage by pushing them with a nearly resonant laser beam. Due to the absence of rubidium background gas this lower glass cell, the so-called science chamber, maintains a vacuum pressure around 10^{-11} mbar which is sufficient to rule out significant loss-mechanisms related to collisions of the BEC with hot background atoms. Here, the atoms are captured and cooled in a conventional, three dimensional MOT.

An experimental cycle for the creation of Bose-Einstein condensates always starts with the loading of the MOT in the science chamber, which typically takes between 10 and 15 seconds collecting up to 10^{10} atoms. During this time, the power of both the cooling light of the MOT and the pushing laser beam is lowered in three steps in order to minimize heating due to radiation pressure of re-emitted photons. Subsequently, the atomic ensemble is subjected to a short period of Sysiphus-cooling in an optical molasses [159–161]. All atoms are then optically pumped from the $F = 2$ hyperfine manifold into the $F = 1$ ground state manifold of ^{87}Rb . From here, atoms in the low-field seeking hyperfine state $|F = 1, m_F = -1\rangle$ are loaded into a magnetic trap [162]. By compressing the magnetic trap and performing radio frequency induced forced evaporation for 12 to 20 seconds the

atomic ensemble is brought close to the critical temperature of Bose-Einstein condensation but still remains a thermal gas. Nonetheless, with a sufficiently large phase space density the atoms are now effectively loaded into a red-detuned crossed dipole trap. Here, the final step of evaporative cooling is performed by exponentially lowering the dipole trap power in approximately six seconds until a pure BEC with no discernable thermal fraction is produced. Typically, the whole experimental cycle takes around 40 to 50 seconds leading to an overall atom number of 5×10^5 to 3×10^4 , depending on the loading time of the MOT and the dipole trap configuration. Experiments presented in this thesis have been performed in two different dipole trap setups, that will be described in the following section.

2.2 Atom-photon interaction: dipole potentials

Conservative potential landscapes for neutral atoms can be designed by utilizing electric dipole interactions with laser light fields. Even though ground state atoms such as ^{87}Rb do not possess a permanent electric dipole moment, the presence of an oscillating electric field of a laser leads to an induced electric dipole moment. On the other hand, the interaction of the induced dipole moment with the electric field results in an energy shift of the atomic states in accordance with the Stark effect (often referred to as the AC Stark shift).

2.2.1 Dressed state approach

Multi-level atomic systems interacting with a light field are well described in a fully quantized manner by the dressed-state approach [163, 164]. Here, the energy shift of a *dressed-state*, the new eigenstate of the coupled quantized systems of atom and light field, is given by perturbation theory. To first order, the energy shift of an i -th state

$$\Delta E_i = \sum_{j \neq i} \frac{|\langle j | \hat{\mathcal{H}}_{\text{AP}} | i \rangle|^2}{E_i - E_j}, \quad (2.1)$$

where $\hat{\mathcal{H}}_{\text{AP}} = -\hat{\mathbf{d}} \cdot \hat{\mathbf{E}}$ is the atom-photon interaction Hamiltonian, $\hat{\mathbf{E}}$ the electric field operator and $\hat{\mathbf{d}} = -e\hat{\mathbf{r}}$ the dipole operator [154, 165]. A detailed review on the topic of such light-matter interaction regarding optical traps is given by Ref. [166]. In the case of ^{87}Rb the generation of strong dipole potentials can be achieved by coupling the $5^2S_{1/2}$ ground state to the $5^2P_{1/2}$ and $5^2P_{3/2}$ states. The two transition lines are commonly referred to as the D_1 and D_2 lines at 780.24 nm and 795.98 nm respectively [167]. The Wigner-Eckart theorem allows for the calculation of the numerator in Eq. (2.1). For the optical detuning of the light field being comparable or larger than the hyperfine splitting of the excited states this leads to an expression of the dipole potential for the atomic hyperfine state $|F, m_F\rangle$ of

$$V_{\text{dip}}(\mathbf{r}) = -\frac{\pi c^2}{2} I(\mathbf{r}) \left(\mathcal{D}_1 + 2\mathcal{D}_2 - g_F m_F \mathcal{P}(\mathbf{r}) [\mathcal{D}_1 - \mathcal{D}_2] \right) \quad (2.2)$$

with the speed of light in vacuum c and the Landé g -factor $g_F = \mp 1/2$ of the atomic ground state $F = 1, 2$ respectively. The electric field operator $\hat{\mathbf{E}}$ in Eq. (2.1) has been replaced by a spatially varying light field $\mathbf{E}(\mathbf{r})$ of intensity $I(\mathbf{r})$ and frequency ω_L . We have used the abbreviation

$$\mathcal{D}_{1,2} = \frac{\Gamma_{D_{1,2}}}{\omega_{D_{1,2}}^3} \left(\frac{1}{\omega_{D_{1,2}} - \omega_L} + \frac{1}{\omega_{D_{1,2}} + \omega_L} \right) \quad (2.3)$$

for the contributions of the D_1 and D_2 lines with transition frequencies $\omega_{D_{1,2}}$ and their natural line widths $\Gamma_{D_{1,2}}$. The different prefactors of the $\mathcal{D}_{1,2}$ stem from the Clebsch-Gordan coefficients of the corresponding transitions. The equations (2.2) and (2.3) immediately reveal the behavior of the dipole force. While a light field that is blue detuned with respect to a predominant atomic transition, i.e., in the discussed case of the rubidium D-lines, $\omega_{D_{1,2}} > \omega_L$ exerts a repulsive dipole force on the atoms, a red detuned light field with $\omega_{D_{1,2}} < \omega_L$ serves as an attractive potential.

It is important to note that neither the application of the commonly used *rotating wave approximation* for small detunings, i.e., $|\omega_{D_{1,2}} - \omega_L| \ll |\omega_{D_{1,2}} + \omega_L|$ or setting $(\omega_{D_{1,2}} + \omega_L)^{-1} \approx 0$ in Eq. (2.3) nor neglecting the fine structure splitting for large detunings are valid simplifications in the present case. Indeed for the laser wavelengths employed in the experiments presented here, both effects are non-negligible. Other possible, but energetically higher, transitions in rubidium with wavelengths at 420 nm and below are omitted in the considerations as their contribution to the energy shift is well below 1%.

2.2.2 Polarization modes

In Eq. (2.2) we have introduced the polarization of the light field as

$$\mathcal{P}(\mathbf{r}) \equiv \frac{I_{\sigma^+}(\mathbf{r}) - I_{\sigma^-}(\mathbf{r})}{I(\mathbf{r})} \quad (2.4)$$

whereby $\mathcal{P} = 0$ and ± 1 for π and σ^\pm polarization respectively. In the above expression, the light intensity $I(\mathbf{r})$ was split up into separate intensity modes of different polarizations $p = \{\pi, \sigma^+, \sigma^-\}$. They derive from an arbitrary light field according to

$$I_p(\mathbf{r}) = \frac{c\epsilon_0}{2} \int_0^{2\pi/\omega_L} |\mathbf{E}(\mathbf{r}, t) \cdot \boldsymbol{\varepsilon}_p(t)|^2 dt \quad (2.5)$$

where ϵ_0 denotes the vacuum permittivity. Here, the time-dependent electric field was projected onto a basis polarization vector $\boldsymbol{\varepsilon}_p$ before time averaging. The polarization basis is defined with respect to a quantization axis. This preferred direction is commonly provided by a magnetic quantization field $\mathbf{B}(\mathbf{r})$ that is applied to the ensemble of atoms. In the case of a quantization axis pointing along the (Cartesian) z -direction the three polarization basis vectors are given by the three-dimensional Jones vectors [168]

$$\boldsymbol{\varepsilon}_\pi = (0, 0, 1) \quad \text{and} \quad \boldsymbol{\varepsilon}_{\sigma^\pm} = (1, \pm i, 0)/\sqrt{2}. \quad (2.6)$$

For the general description of a quantization field $\mathbf{B}_{\text{qa}}(\mathbf{r})$ pointing in an arbitrary direction, polarization basis vectors can be obtained by transforming the Jones vectors such that the basis vector representing the π -polarization is again aligned in parallel to the quantization axis, i.e., $\boldsymbol{\varepsilon}_\pi \parallel \mathbf{B}_{\text{qa}}(\mathbf{r})$. This transformation can be achieved by a suitable rotation of the basis vectors. Such a rotation in three dimensions is described by the three *Euler angles* α, β, γ [5, 154]. Much alike the aircraft principle axes *yaw*, *pitch* and *roll*, the transformation corresponds to a sequence of elemental rotations by the three-dimensional Cartesian rotation matrices R_i :

$$\boldsymbol{\varepsilon}_{\mathcal{P}} \rightarrow R_z(\gamma)R_x(\beta)R_y(\alpha)\boldsymbol{\varepsilon}_{\mathcal{P}}. \quad (2.7)$$

As a reference for the rotation we set the default orientation of the quantization field along the z -axis, where the Euler angles are $\alpha = \beta = \gamma = 0$. A quantization axis rotated by two of the three Euler angles is illustrated in Fig. 2.3. In section 2.4 as well as chapter 6 and 7 we will elaborate the influence of the direction of the quantization axis further. Finally, the total light intensity $I(\mathbf{r})$ as introduced in Eq. (2.2) and (2.4) is simply given by the sum of all polarization intensity modes $I(\mathbf{r}) = \sum_p I_p(\mathbf{r})$.

2.2.3 Effective magnetic field

For a more intuitive picture of the dipole force, Eq (2.2) can be written as a sum of a state-independent and a state-dependent part, corresponding to the potential landscape of the total intensity $V_{\text{int}}(\mathbf{r}) \propto I(\mathbf{r})$ and the intensity of the circular polarization modes $V_{\text{pol}}(\mathbf{r}) \propto I(\mathbf{r})\mathcal{P}(\mathbf{r})$. Moreover, since the strength of the state-dependent part of the potential depends linearly on the magnetic quantum number m_F , it can be mapped onto an *effective* magnetic field in close analogy to the linear Zeeman effect [5, 75, 154]

$$\begin{aligned} V_{\text{dip}}(\mathbf{r}) &\equiv V_{\text{int}}(\mathbf{r}) + V_{\text{pol}}(\mathbf{r}) \\ &= V_{\text{int}}(\mathbf{r}) + g_F m_F \mu_B B_{\text{eff}}(\mathbf{r}), \end{aligned} \quad (2.8)$$

where μ_B denotes the Bohr-Procopiu-magneton such that the effective magnetic field is

$$B_{\text{eff}}(\mathbf{r}) = -\eta V_{\text{int}}(\mathbf{r})\mathcal{P}(\mathbf{r})/\mu_B \quad (2.9)$$

with

$$\eta = \frac{\mathcal{D}_1 - \mathcal{D}_2}{\mathcal{D}_1 + 2\mathcal{D}_2}. \quad (2.10)$$

From Eq. (2.10) it is immediately evident that the factor η quantifying the contribution of the effective magnetic field to the total potential vanishes for very large detunings where the difference of both predominant atomic transition lines is not resolved and $\mathcal{D}_1 - \mathcal{D}_2 \approx 0$. However, for wavelengths employed in the experiment, e.g., 830 nm in the case of the three-beam lattice laser (see section 2.3) where $\eta \approx 0.13$ the contribution of the state-dependent

potential has a significant influence on the potential landscape. Effects arising from the presence of the effective magnetic field are treated in more detail in section 2.3 and in the chapters 6 and 7.

2.2.4 Optical dipole traps

The starting point of all experiments during this thesis is a Bose-Einstein condensate of ^{87}Rb atoms that is confined in a far detuned optical dipole trap. With a wavelength of 1064 nm the detuning of the laser light that is used for the generation of the dipole trap potential is large compared to all atomic transitions in ^{87}Rb . Thus, the dipole potential can be regarded as conservative in good approximation as well as state-independent. The development of such far-off-resonant dipole traps constitutes a crucial prerequisite for the investigation of physical processes in quantum gases involving the spin degree of freedom. In contrast, magnetic traps only confine atoms in the a low field seeking hyperfine state and yield largely differing trapping potentials for states with differing magnetic quantum number.

Experimentally, dipole traps as well as optical lattice potentials are commonly created by Gaussian laser beams that are focussed on the atomic ensemble. The intensity profile of a radially symmetric Gaussian laser beam propagating along the z -direction with a beam power P and wavelength λ_L is

$$I(\rho, z) = \frac{2P}{\pi w(z)^2} \exp\left(\frac{-2\rho}{w(z)^2}\right) \quad (2.11)$$

where $w(z) = w_0\sqrt{1 + (z/z_R)^2}$ denotes the beam waist along the line of propagation with a minimal waist of w_0 at the focus of the beam. The Rayleigh range $z_R = \pi w_0^2/\lambda_L$ gives the distance from the focus where the cross section of the beam has doubled. As inferred by Eq. (2.11), the trapping potential arising from such a single Gaussian beam is very asymmetric. The intensity gradient along the axis of propagation is generally much smaller than in the radial direction. Within the scope of this thesis experiments were thus performed in *crossed* dipole trap setups that allow for more homogeneous trapping geometries. Here, two perpendicular Gaussian laser beams with wavelengths of 1064 nm intersect in the horizontal plane at their respective focusses. It is ensured that the frequencies of both beams differ by at least 100 MHz in order to avoid interference effects.

Two different crossed dipole trap setups were used throughout this thesis. The first being a circular crossed dipole trap where both Gaussian beams are identical in geometry and of radially symmetric shape as in Eq. (2.11). Assuming equal beam powers and neglecting the axial confinement of each beam as $z \ll z_R$, the resulting intensity profile reads

$$I(\mathbf{r}) = \frac{2P}{\pi w_0^2} \exp\left(\frac{-2y^2}{w_0^2}\right) \left[\exp\left(\frac{-2x^2}{w_0^2}\right) + \exp\left(\frac{-2z^2}{w_0^2}\right) \right]. \quad (2.12)$$

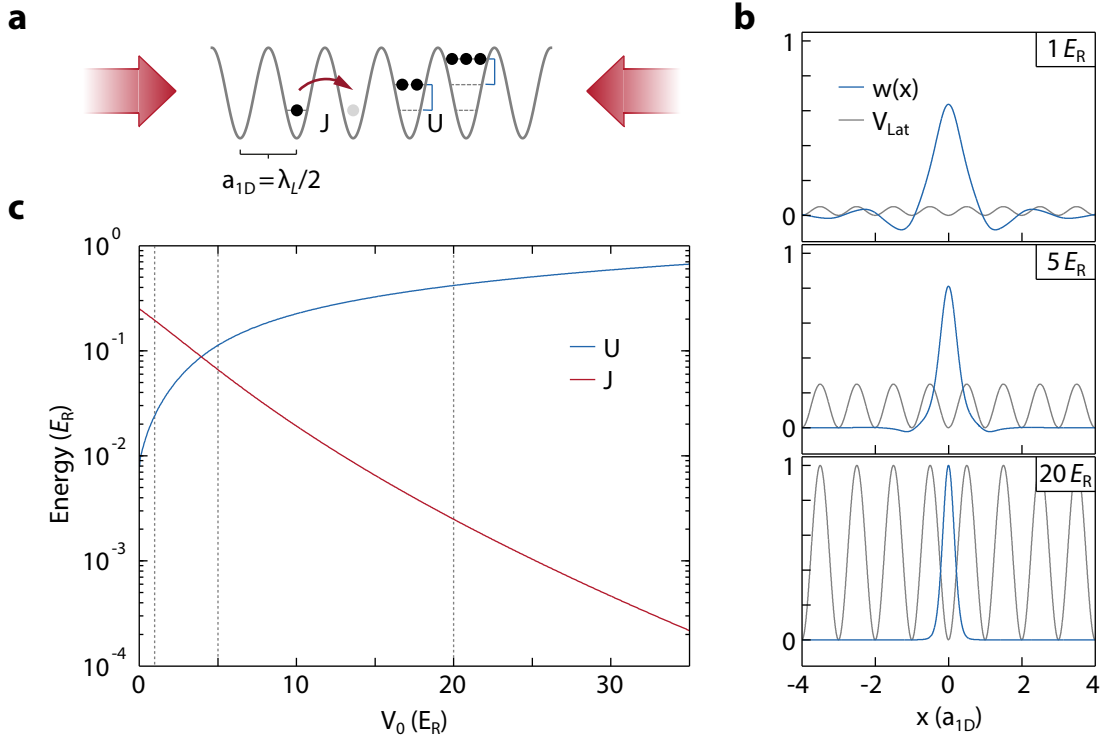


Figure 2.1: Wannier functions and Bose-Hubbard model. **a** illustrates the simple one-dimensional optical lattice. Two counterpropagating laser beams interfere and create a sinusoidal potential with lattice wells separated by half the laser wavelength. In accordance with the Bose-Hubbard model, atoms can tunnel between lattice sites with the tunneling matrix element J . If more than one atom is present at the same lattice site the energy is raised by multiples of the on-site interaction energy U . The additional harmonic confinement is not depicted. Part **b** shows one-dimensional Wannier functions for three different lattice potentials. For increasing lattice depth, the Wannier states localize strongly at a single lattice site and the overlap to adjacent sites vanishes. The subfigure was inspired by Ref. [153]. In **c** the behaviour of the on-site interaction energy and the tunneling matrix element of a one-dimensional lattice are plotted with respect to the lattice depth V_0 .

The Cartesian coordinate system where the dipole trap is aligned in the xz -plane and gravity points opposite to the y -axis is maintained throughout this thesis. For the very weak dipole potentials used here, the gravitational pull on the trapped atoms contributes significantly to the overall potential $V_{tot}(\mathbf{r}) = V_{dip}(\mathbf{r}) + mgy$ leading to a shift of the potential minimum away from the optical axis. This so called gravitational sag results in a lower boundary for the beam power of an optical dipole trap and thus limits the achievable harmonic trap frequencies $\omega_i \equiv \sqrt{\partial_{x_i}^2 V_{tot}(\mathbf{r})/m}$. With minimal beam waists of both $w_0 \approx 37 \mu\text{m}$ the smallest possible trap frequencies of the obtained potential are $\omega_h = 2\pi \times 88 \text{ Hz}$ in the horizontal directions and $\omega_v = 2\pi \times 72 \text{ Hz}$ in the vertical direction.

In general, it is desirable to counteract the effect of the gravitational sag in order

to reach weaker overall harmonic confinements for the realization of more homogeneous quantum gas systems. For this purpose, an elliptical crossed dipole trap has been set up. Here, the two Gaussian laser beams exhibit a strong radial asymmetry. The elliptic beam waists with a minor axis along the vertical direction of $w_{0,v} \approx 82 \mu\text{m}$ and a major axis in the horizontal direction of $w_{0,h} \approx 245 \mu\text{m}$ allow for final trapping frequencies of $\omega_h = 2\pi \times 19 \text{ Hz}$ and $\omega_v = 2\pi \times 48 \text{ Hz}$. The elliptical crossed dipole trap was designed by J. Struck. For a thorough treatment of the subject we refer to his thesis [155] and the review article in Ref. [166].

2.3 Periodic optical potentials

In the previous section, optical potentials were introduced that allow for the trapping of ultracold atoms due to the intensity gradient of Gaussian laser beams. This concept can be extended to periodically varying intensity distributions, the so called optical lattices.

The simplest example of an optical lattice consists of two counterpropagating laser beams with equal frequencies and (linear) polarizations, which can be easily achieved experimentally by retro-reflection of one laser beam with a single mirror. As illustrated in Fig. 2.1a, the interference of both beams results in a standing light wave with a sinusoidal modulation of the light field intensity. Hence, in the case of red-detuned laser light, atoms are confined to the intensity maxima. Due to the additional radial confinement of the Gaussian intensity profiles this setup forms a one-dimensional lattice along the optical axis consisting of a stack of atomic ensembles in disk-shaped ellipsoids with a lattice spacing of $a = \lambda_L/2$. For deep optical potentials that can either be achieved by high laser intensities or small optical detunings the disks are decoupled quasi two-dimensional systems. The potential depth of the lattice scales linearly with the laser power. It is conveniently expressed in units of the recoil energy $E_R = \hbar^2 k_L^2 / (2m)$ that denotes the kinetic energy that is transferred to an atom of mass m by absorbing a lattice photon with wavenumber $k_L = 2\pi/\lambda_L$, where \hbar is the reduced Planck constant.

2.3.1 Non-interacting particles in lattice potentials

A spatially periodic lattice potential is generally invariant under translation by a Bravais lattice vector \mathbf{R} such that $V_{\text{Lat}}(\mathbf{r}) = V_{\text{Lat}}(\mathbf{r} + \mathbf{R})$. The stationary eigenstates of the Schrödinger equation

$$\hat{\mathcal{H}}_{\text{Lat}} |\psi_{\mathbf{q}}^n(\mathbf{r})\rangle = E_{\mathbf{q}}^n |\psi_{\mathbf{q}}^n(\mathbf{r})\rangle \quad (2.13)$$

with a lattice Hamiltonian $\hat{\mathcal{H}}_{\text{Lat}} = \hat{\mathbf{p}}^2 / (2m) + V_{\text{Lat}}(\mathbf{r})$ are given by *Bloch functions* [169, 170]

$$|\psi_{\mathbf{q}}^n(\mathbf{r})\rangle = e^{i\mathbf{q}\mathbf{r}} |u_{\mathbf{q}}^n(\mathbf{r})\rangle \quad \text{where} \quad |u_{\mathbf{q}}^n(\mathbf{r})\rangle = |u_{\mathbf{q}}^n(\mathbf{r} + \mathbf{R})\rangle. \quad (2.14)$$

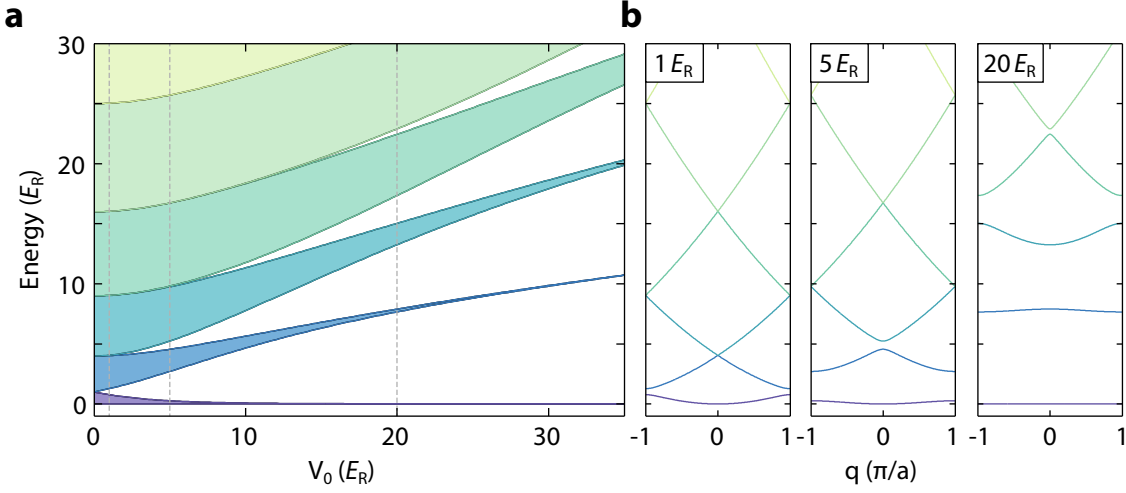


Figure 2.2: Energy spectrum of an optical lattice. In **a** the band gaps of an optical lattice are plotted with respect to the lattice depth. Dashed gray lines mark the lattice depths used for plotting the band structure in **b**. The single-particle dispersion relations in the reduced zone scheme are shown for three different lattice depths. The opening of band gaps and the flattening of bands are clearly visible as the lattice depth is increased.

Here, the index n denotes the discrete energy band of the eigenstate. The quantum number \mathbf{q} is the *quasi-momentum*. Both the Bloch functions $|\psi_{\mathbf{q}}^n(\mathbf{r})\rangle = |\psi_{\mathbf{q}+\mathbf{G}}^n(\mathbf{r})\rangle$ and the eigenenergies $E_{\mathbf{q}}^n = E_{\mathbf{q}+\mathbf{G}}^n$ are periodic in the quasimomentum with respect to a reciprocal lattice vector \mathbf{G} . This periodicity in the reciprocal space allows to reduce the energy spectrum of a particle in a periodic potential to the first Brillouin zone of the lattice as depicted in Fig. 2.2b.

The equations (2.13) and (2.14) infer that particles occupying single Bloch states are completely delocalized over the entire system. For strong lattice potentials, where the atoms tend to be confined at single lattice wells. A more suitable, complete set of localized eigenstates for the description of such systems is provided by Wannier functions [171, 172]. Wannier functions are composed of Bloch functions via the relation

$$w_{n,i}(\mathbf{r} - \mathbf{R}_i) = \frac{1}{\sqrt{N}} \sum_{\mathbf{q}} e^{-i\mathbf{q}\mathbf{R}_i} |\psi_{\mathbf{q}}^n(\mathbf{r})\rangle. \quad (2.15)$$

where $w_{n,i}(\mathbf{r} - \mathbf{R}_i)$ is the Wannier function in the n -th energy band localized at a lattice site with index i . In the same way, Bloch functions can be constructed from a complete set of Wannier functions. For increasing lattice depths, Wannier functions become more and more localized at single lattice site as depicted in Fig. 2.1b.

2.3.2 Bose-Hubbard model

Confining ultracold atoms in optical lattices allows for an unprecedented control over the role of interactions between particles. For shallow lattice potentials, the atomic ensemble

is still well described within the framework of the Gross-Pitaevskii equation [173–175]. With increasing lattice depths and, thus, stronger confinement to lattice sites, interactions between atoms start to play an increasingly important role. A mean-field treatment of interactions breaks down as fluctuations cannot be treated as small perturbations anymore.

A suitable treatment of interacting bosons in a lattice potential is provided by the so called *Bose-Hubbard model* [176]. Here, interactions are restricted to two-particle s -wave scattering processes. At the low energy scales present in ultracold quantum gases this is an appropriate approximation. Furthermore, the s -wave scattering can be modeled as a contact interaction with an interaction potential of

$$V_s(\mathbf{r} - \mathbf{r}') = g\delta(\mathbf{r} - \mathbf{r}') \quad \text{with} \quad g = 4\pi\hbar^2 a_s/m. \quad (2.16)$$

The assumption of a contact potential is justified since the de Broglie wavelength of ultracold atoms is much larger than the (effective) extension of the interaction potential [28]. Here, the s -wave scattering length a_s completely characterizes the interaction processes which are repulsive (attractive) for $a_s > 0$ ($a_s < 0$). Note that, in general, the scattering length depends on the respective spin states of the pair of interacting atoms. For reasons of simplicity, this degree of freedom is omitted in the following.

A gas of N interacting bosons in an external potential can be described by a many-body Hamiltonian in second quantization:

$$\hat{H} = \int \hat{\Psi}^\dagger(\mathbf{r}) \left[\frac{\hat{\mathbf{p}}^2}{2m} + V_{\text{ext}}(\mathbf{r}) \right] \hat{\Psi}^\dagger(\mathbf{r}) \, d\mathbf{r} + \frac{g}{2} \int \hat{\Psi}^\dagger(\mathbf{r}) \hat{\Psi}^\dagger(\mathbf{r}') \hat{\Psi}^\dagger(\mathbf{r}') \hat{\Psi}^\dagger(\mathbf{r}) \, d\mathbf{r} d\mathbf{r}'. \quad (2.17)$$

Hereby, the external potential $V_{\text{ext}} = V_{\text{Lat}} + V_{\text{H}}$ consist of the lattice potential V_{Lat} with an additional confinement V_{H} . In the vicinity of the center of the trap the confinement is well described by a harmonic potential

$$V_{\text{H}}(\mathbf{r}) = \frac{m}{2} \left(\omega_{\text{H},x}^2 x^2 + \omega_{\text{H},y}^2 y^2 + \omega_{\text{H},z}^2 z^2 \right) \quad (2.18)$$

with the harmonic trapping frequencies $\omega_{\text{H},i}$ along the directions i . The bosonic annihilation and creation operators in Eq. (2.17), $\hat{\Psi}$ and $\hat{\Psi}^\dagger$ respectively, fulfill the bosonic commutation relation $[\hat{\Psi}(\mathbf{r}), \hat{\Psi}^\dagger(\mathbf{r}')] = \delta(\mathbf{r} - \mathbf{r}')$. In the case of sufficiently deep optical lattices and low temperatures, where atoms are restricted to the lowest lying energy band one can expand the field operators in the basis of Wannier functions in the lowest band:

$$\hat{\Psi}(\mathbf{r}) = \sum_i \hat{b}_i w_i(\mathbf{r}), \quad (2.19)$$

with \hat{b}_i (\hat{b}_i^\dagger) the annihilation (creation) operator of a particle at lattice site i that, again, obey the bosonic commutation relation $[\hat{b}_i, \hat{b}_j^\dagger] = \delta_{ij}$. As the following considerations remain restricted to the lowest energy band, the band index is omitted here. Additionally, we have introduced the abbreviation $w_i(\mathbf{r} - \mathbf{R}_i) \equiv w_i(\mathbf{r})$ for reasons of clarity. Inserting

(2.19) into Eq. (2.17) leads to the well-known Bose-Hubbard Hamiltonian

$$\hat{\mathcal{H}}_{\text{BH}} = - \sum_{\langle i,j \rangle} J_{ij} (\hat{b}_i^\dagger \hat{b}_j + \hat{b}_j^\dagger \hat{b}_i) + \frac{U}{2} \sum_i \hat{n}_i (\hat{n}_i - 1) + \sum_i \epsilon_i \hat{n}_i \quad (2.20)$$

where $\hat{n}_i = \hat{b}_i^\dagger \hat{b}_i$ is the boson number operator at lattice site i and $\langle i, j \rangle$ denotes the sum over all bonds of nearest-neighboring lattice sites, i.e., $\langle i, j \rangle = \langle j, i \rangle$. The first term of Eq. (2.20) describes quantum tunneling processes between adjacent lattice sites, representing the kinetic part of the Bose-Hubbard Hamiltonian. J_{ij} denotes the tunneling amplitude between a lattice site with index i and a neighboring site j . It is given by

$$J_{ij} = - \int w_i^*(\mathbf{r}) \left[\frac{\hat{\mathbf{p}}^2}{2m} + V_{\text{ext}}(\mathbf{r}) \right] w_j(\mathbf{r}) \, \text{d}\mathbf{r}. \quad (2.21)$$

Note that in condensed matter physics the tunneling matrix element is also often referred to as t instead of J . For the common case of isotropic tunneling along all lattice directions the indexing ij of lattice sites can be omitted. In conventional lattices J is generally positive real-valued. Experimental procedures for the engineering of tunneling matrix elements in optical lattices that can be both negative and complex-valued will be introduced in chapters 3 and 4 respectively.

The second term of the Hamiltonian (2.20) describes two-particle interactions. For sufficiently deep lattice potentials, Wannier functions are well located at single lattice sites. Here, the overlap between particle states at neighboring sites vanishes (see Fig. 2.1b). In this regime, interactions are completely described by on-site processes such that the summation of bosonic number operators can be restricted to single lattice sites. The on-site interaction strength is given by the parameter U with

$$U_i = g \int |w_i(\mathbf{r})|^4 \, \text{d}\mathbf{r} \quad (2.22)$$

and g as in Eq. (2.16). As the integral over Wannier functions is usually independent of the respective lattice site, the index i is dropped in Eq. (2.20). The third term in the Bose-Hubbard Hamiltonian (2.20) incorporates the additional trapping confinement V_{H} that yields a site-dependent energy offset ϵ_i of

$$\epsilon_i = \int V_{\text{H}}(\mathbf{r}) |w_i(\mathbf{r})|^2 \, \text{d}\mathbf{r} \approx V_{\text{H}}(\mathbf{R}_i) \quad (2.23)$$

with V_{H} given in Eq. (2.18).

In the Bose-Hubbard model, the ratio between the tunneling matrix element J and the on-site interaction U determines the physical properties of the system. The behavior of both the amplitude of the tunneling matrix element and the on-site interaction with respect to the optical lattice depth is plotted in Fig. 2.1c. Two distinct quantum phases can be identified [54]. In the case of shallow lattice potentials the tunneling term in Eq. (2.20) dominates and $U/J \rightarrow 0$. Here, the trapped atomic ensemble occupies a superfluid state

with long-range phase coherence. The ground state of the many-body system of N atoms is given by a simple product state of zero-momentum Bloch waves

$$|\Psi_{\text{SF}}\rangle_{\mathbf{q}=0} \stackrel{U \rightarrow 0}{\propto} \left(\sum_{i=1}^M \hat{b}_{i,\mathbf{q}=0}^\dagger \right)^N |0\rangle \quad (2.24)$$

where $|0\rangle$ is the bosonic vacuum state and M denotes the number of lattice sites in the system. In the limit of vanishing interactions the many-body state is equivalent to a coherent state. The expectation value of the particle number on each lattice site thus follows a Poissonian distribution (properties of such a superfluid state in an optical lattice are further discussed in chapter 4).

In the opposite case of deep optical potentials and strong interactions with $U/J \rightarrow \infty$ the interaction dominates the systems behavior. Energetically costly fluctuations of the site occupation numbers are minimized and the ground state many-body wave function is a product of local Fock states. For a homogeneous system with filling $n = N/M$

$$|\Psi_{\text{MI}}\rangle_{n \in \mathbb{Z}} \stackrel{J \rightarrow 0}{\propto} \prod_{i=1}^M (\hat{b}_i^\dagger)^n |0\rangle. \quad (2.25)$$

This so-called Mott-insulating (MI) state exhibits a vanishing phase coherence between lattice sites as well as zero compressibility (see chapter 5).

The two regimes are linked by a zero-temperature second-order quantum phase transition which was first predicted by Fisher *et al.* [54]. Following the proposal by Jaksch *et al.* [55], the transition was first realized in a pioneering experiment with ultracold atoms in an optical lattice by Greiner *et al.* [56].

2.4 Realization of optical lattices with hexagonal symmetry

The first seminal experiments on ultracold atomic ensembles in two- and three dimensional optical lattice potentials were performed in cubic lattices [56, 177]. Corresponding experimental setups relied on perpendicular arrays of counterpropagating laser beams that were generated by retro-reflection. The center piece of all experiments presented in this thesis, the running-wave three beam lattice follows a different approach in order to realize optical lattice potentials with *hexagonal* symmetry. Here, three Gaussian laser beams intersect in a plane under angles of 120° with respect to each other. Furthermore, the lattice beams are not retro-reflected to create standing light waves but rather the running light waves interfere with each other forming a stable intensity modulation. In the following we will elaborate on the properties of this running-wave three-beam lattice.

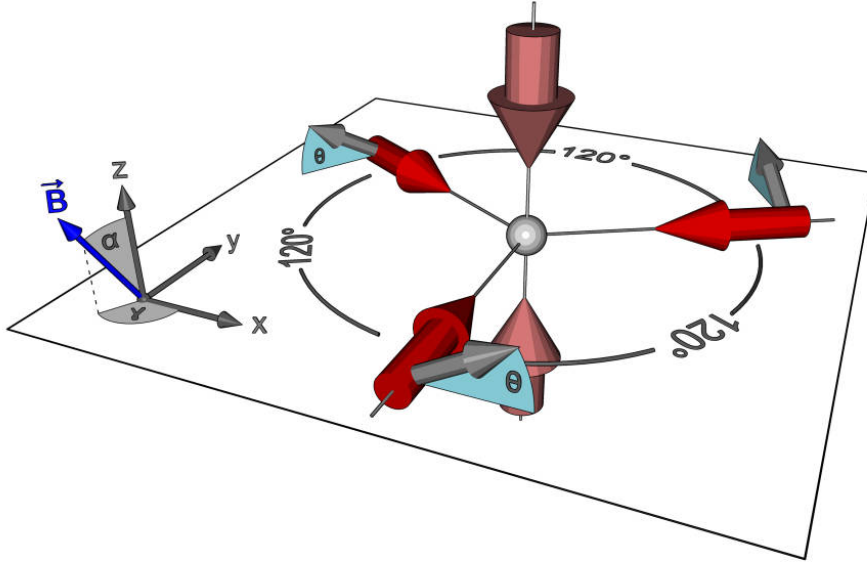


Figure 2.3: Three-beam lattice setup. The optical lattice potential with hexagonal symmetry is created by three laser beams intersecting pairwise under angles of 120° in the xy -plane. The linear polarization vectors all enclose an angle of θ with the xy -plane. In addition to the three beam lattice, a conventional one dimensional lattice can be superimposed that is created by counter-propagating laser beams along the z -axis. Gravity points opposite to the y -axis. The orientation of the quantization field \mathbf{B} in three dimensions can be described within the framework of Euler angles. Here, the quantization field vector depicts a corresponding rotation for the Euler angles α and γ . The figure was inspired by Ref. [154]. A similar figure created by the author appears in Ref. [5].

2.4.1 Three-beam lattice setup

The three-beam lattice setup was first proposed in Refs. [30] and [178] in the context of two-dimensional optical molasses. Both the design and implementation of the three-beam lattice setup at the experiment presented here took place within the PhD thesis of C. Becker [153]. For a thorough treatment of the experimental setup of the lattice and details regarding the corresponding laser system we refer to his thesis.

The Gaussian laser beams that form the three-beam setup are each derived from optical telescopes that are directly coupled to optical fibers. By this, distortions of the beam profiles are reduced to an absolute minimum as the intensity profile of beams exiting an such fibers exhibit an almost perfect Gaussian shape. As depicted in Fig. 2.3, the orientations of the beams, given by their respective wave vectors are

$$\mathbf{k}_1 = k_L (0, 1, 0), \quad \mathbf{k}_2 = \frac{k_L}{2} (\sqrt{3}, -1, 0), \quad \mathbf{k}_3 = \frac{k_L}{2} (-\sqrt{3}, -1, 0). \quad (2.26)$$

Note that the wave vectors given above are merely an approximation of the actual beams present in the experimental setup. The three beams deviate slightly within approximately $\pm 2^\circ$ from the ideal 120° alignment. The exact values for the angles between the lattice

beams were experimentally determined within the Diploma thesis of C. Ölschläger [179] and are given in appendix D. For most experiments presented in this thesis, the influence of the deviations can be neglected. We mention the consideration of the exact lattice vectors whenever necessary.

Close to the waists of the Gaussian beams, the light fields can be approximated by plane waves. Assuming a real-valued amplitude of E_0 for all three beams with individual phases ϕ_i , the total resulting electric field reads

$$\mathbf{E}_{\text{Lat}}(\mathbf{r}, t) = E_0 \sum_{i=1}^3 \boldsymbol{\epsilon}_i e^{i(\mathbf{k}_i \mathbf{r} - \omega_L t + \phi_i)}. \quad (2.27)$$

As it was pointed out in Ref. [30] a d -dimensional optical lattice requires a minimum of $l = d + 1$ laser beams. Furthermore, the resulting interference pattern is determined by the relative phases $\phi_i - \phi_j$ of the incident electric fields. The number of independent relative phases is $l - 1$ and the number of independent possible translations in space is given by d . Hence, for an optical lattice comprised by the minimum number of laser beams, a phase change corresponds to a global translation of the interference pattern in space while the lattice structure itself remains rigid. This condition is obviously fulfilled for the three-beam lattice spanning a two-dimensional Bravais lattice.

On the one hand, random fluctuations of the individual phases ϕ_i result in a randomly moving lattice. As trapped ultracold atoms can be heated by such movements, it is highly desirable to limit the phase-noise to an absolute minimum. For this purpose, an active stabilization of the phases is implemented in the laser system. It relies on beating the incoming laser light of each of the three beam paths with a small percentage of light that is back-reflected at the end of the optical fibers attached to the lattice telescopes [153]. However, the active stabilization was abandoned within the course of this thesis since the free running lattice system appeared to be sufficiently stable within timescales of all experiments that have been performed. This is especially remarkable due to the very long individual path lengths of the three lattice laser beams through the optical fibers that deliver the light from a titanium-sapphire laser system to the science chamber.

On the other hand, a control over the phases ϕ_i allows for the precise and purposeful translation and acceleration of the lattice potential in an experimentally feasible fashion. This experimental technique is central in this work and will be discussed thoroughly in chapter 3.

The reciprocal lattice of the three-beam setup is generated by the possible momentum transfers between the lattice beams. A trapped atom can absorb a photon from the light mode of one beam and re-emit it into another mode. With this consideration, we can define the reciprocal lattice vectors \mathbf{b}_i as

$$\mathbf{b}_i = \varepsilon_{ijk} (\mathbf{k}_j - \mathbf{k}_k) \quad (2.28)$$

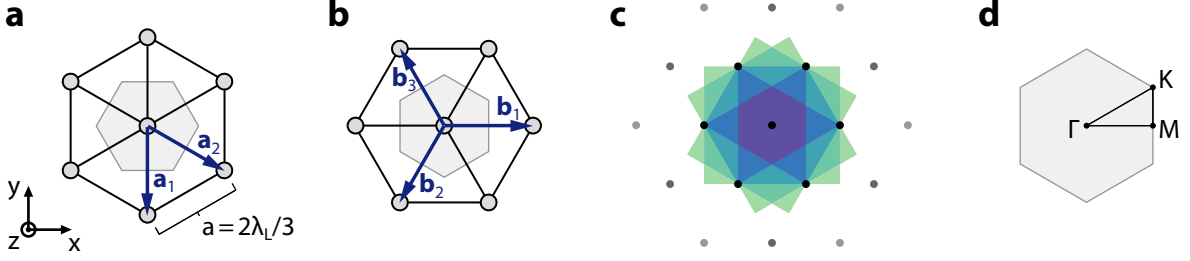


Figure 2.4: Bravais- and reciprocal lattice of the hexagonal lattice. **a** shows the six-fold symmetric real-space Bravais lattice arising from the three-beam running wave setup. Its coordination number, indicating the number of nearest neighboring lattice sites is six. The blue arrows denote a set of Bravais lattice vectors as given in Eq. (2.30) and the gray shaded hexagon indicates the Wigner-Seitz cell. The lattice structure exhibits a lattice spacing of $a = 2\lambda_L/3$. In **b** the corresponding reciprocal Bravais lattice is illustrated with the three reciprocal lattice vectors defined in Eq. (2.29). With respect to the real-space Bravais lattice the reciprocal lattice is rotated by 90° . As in **a**, the gray hexagon corresponds to the Wigner-Seitz cell of the reciprocal lattice, i.e., the first Brillouin Zone. **c** depicts the first five Brillouin zones of the hexagonal lattice. **d** Three distinguished points of high symmetry exist in the first Brillouin Zone. The center Γ at quasimomentum $\mathbf{q} = 0$, the corner K and the middle point of the edges M . Band structures are commonly visualized along a path between the high-symmetry points as in Fig. 2.5 to 2.7.

where ε_{ijk} ist the Levi-Civita symbol¹. Each pair of the three reciprocal lattice vectors

$$\mathbf{b}_1 = b (1, 0, 0), \quad \mathbf{b}_2 = \frac{b}{2} (-1, -\sqrt{3}, 0), \quad \mathbf{b}_3 = \frac{b}{2} (-1, \sqrt{3}, 0). \quad (2.29)$$

with $b = \sqrt{3}k_L$ spans the reciprocal Bravais lattice as depicted in Fig. 2.4b. The real-space Bravais lattice vectors \mathbf{a}_i can be calculated from pairs of the reciprocal Bravais lattice vectors via the relation $\mathbf{a}_i \cdot \mathbf{b}_j = 2\pi\delta_{ij}$ [170]. Fig. 2.4a depicts the two Bravais lattice vectors obtained with \mathbf{b}_1 and \mathbf{b}_2 from Eq. (2.29), that are

$$\mathbf{a}_1 = a (0, -1, 0) \quad \text{and} \quad \mathbf{a}_2 = \frac{a}{2} (\sqrt{3}, -1, 0) \quad (2.30)$$

with a lattice constant of $a = 2\lambda_L/3$.

Inserting Eq. (2.27) into Eq. (2.5) allows for the straightforward calculation of the total intensity distribution for all polarization modes. The resulting optical lattice potential is given by the general description of the dipole potential in Eq. (2.2) and (2.3). As discussed in section 2.2.3 it can be split into a state-independent and a state-dependent part where the latter is determined by the circular polarization modes and can be mapped to an effective magnetic field. For clarity we write in the following

$$V_{\text{Lat}}(\mathbf{r}) = -V_0 [V_{\text{int}}(\mathbf{r}) + V_{\text{pol}}(\mathbf{r})] \quad (2.31)$$

¹Note that the Einstein summation convention is *not* applied in Eq. (2.28).

where V_0 denotes the lattice depths in units of the recoil energy corresponding to a setup created by two counter-propagating laser beams with the same properties as the three-beam lattice lasers [5, 74, 154]. Assuming linear-polarized light with the polarization vectors $\boldsymbol{\epsilon}_i$ in Eq. (2.27) all enclosing an angle of $\theta_1 = \theta_2 = \theta_3 \equiv \theta$ with the xy -plane, the state independent contribution of the potential reads

$$V_{\text{int}}(\mathbf{r}) = 6 + [1 - 3 \cos(2\theta)] \sum_{i=1}^3 \cos(\mathbf{b}_i \mathbf{r} - \Delta\phi_{jk}). \quad (2.32)$$

We have incorporated the three reciprocal lattice vectors \mathbf{b}_i in the above equation such that it can be written as the sum over cosine terms given by each vector. This simplification was the reason for defining an otherwise redundant third reciprocal lattice vector in the first place in Eq. (2.29). The notation for the phase difference $\Delta\phi_{jk} = \phi_k - \phi_j$ accounts for the definition of the reciprocal lattice vectors \mathbf{b}_i in Eq. (2.29) by circular permutation.

For a hyperfine state of $|F, m_F\rangle$ the state-dependent part of the lattice potential is given by

$$V_{\text{pol}}(\mathbf{r}) = \sqrt{3}(-1)^F m_F \eta \cos(\theta) \sum_{i=1}^3 C_i \sin(\mathbf{b}_i \mathbf{r} - \Delta\phi_{jk}) \quad (2.33)$$

with the proportionality factor η defined in Eq. (2.10). Here, the Landé g-Factor for the two ground states of ^{87}Rb is incorporated by the prefactor $(-1)^F$. The coefficients $C_i(\theta, \alpha, \beta, \gamma)$ depend on both the orientation of the polarization vectors and the orientation of the quantization axis as discussed before in section 2.2.3:

$$\begin{aligned} C_1 &= \cos\theta \cos\alpha \cos\beta - 2 \sin\theta \left(\sin\alpha \cos\gamma + \cos\alpha \sin\beta \sin\gamma \right) \\ C_{2,3} &= \cos\theta \cos\alpha \cos\beta + \sin\theta \left(\sin\alpha \cos\gamma + \cos\alpha \sin\beta \cos\gamma \right. \\ &\quad \left. \pm \sqrt{3} [\sin\alpha \sin\gamma - \cos\alpha \sin\beta \cos\gamma] \right) \end{aligned} \quad (2.34)$$

The equations (2.31) to (2.34) fully describe the dipole potential arising from the (ideal) three beam setup considering the aforementioned assumptions of a) negligible harmonic confinement, b) equal beam intensities and c) linear polarized beams with equally aligned polarization vectors $\boldsymbol{\epsilon}_i$ with respect to their corresponding wave vectors \mathbf{k}_i . Effects resulting from a rotation of the quantization field are thoroughly discussed in chapter 6. Until then, we restrict further considerations to the case of the quantization axis pointing along the z -direction, where $C_{1,2,3} = \cos(\theta)$. All experiments in this thesis were performed with a three-beam lattice of wavelength of $\lambda_L = 830$ nm that was derived from a titanium-sapphire laser. In the following, we thus consider a red-detuned light field with $\eta \approx 0.13$.

An important feature of the three-beam lattice setup is the possibility to create one-dimensional lattices with each pair of the three laser beams. Due to the interference arising from two running waves rather than from a retro-reflected laser beam it is experimentally straightforward to move such a one-dimensional lattice along the lattice axis by changing

the phase of one of the laser beams. All three one-dimensional lattices are illustrated in Fig. 2.9a. For the case of polarization vectors aligned perpendicular to the lattice plane, the three possible potentials are

$$V_{1D,i}(\mathbf{r}) = -\frac{V_0}{2} \left[1 + \cos(\mathbf{b}_i \mathbf{r} + \Delta\phi_{jk}) \right]. \quad (2.35)$$

With an angle of $\vartheta_i = \angle(\mathbf{k}_i, \mathbf{k}_j)$ between the lattice laser beams the corresponding lattice constant is

$$a_{1D,i}(\vartheta_i) = \frac{\lambda_L}{2 \sin(\vartheta_i/2)} \approx 479 \text{ nm} \quad (2.36)$$

for the case of $\lambda_L = 830 \text{ nm}$ and $\vartheta_i \approx 120^\circ$ [155]. Note that the experimentally determined exact angles between the three pairs of lattice beams are given in Tab. D.1. The one-dimensional running-wave lattices allow for the pairwise calibration of the lattice depth of the three-beam lattice by intensity modulation [153, 154]. Beyond that, we will present experiments performed in the running-wave 1D-lattice utilizing the control over the position of the lattice in chapter 3.

Taking all three lattice beams into account, the orientation of the polarization vectors ϵ_i , given by the angle enclosed with the xy -plane, allows for the distinction of three fundamentally different potential landscapes: the state-independent triangular lattice, the state-dependent honeycomb lattice and the *purely* state-dependent polarization lattice. We will discuss the properties of these optical lattice types in the following.

2.4.2 Triangular lattice

The resulting potential landscape for the case of all polarization vectors aligned perpendicular to the lattice plane, i.e., $\epsilon_{1,2,3} = \hat{\mathbf{e}}_z$ and $\theta = 90^\circ$ is depicted in Fig. 2.5a. Potential minima are separated by a lattice constant of $a = 2\lambda_L/3$ and form the hexagonally symmetric Bravais lattice already introduced in Fig. 2.4a. For an unambiguous notation, we refer to this lattice as the *triangular* lattice throughout this thesis due to the shape of its upwards and downwards pointing lattice plaquettes. However, in literature this Bravais lattice is also often referred to as the *hexagonal* lattice due to its six-fold symmetry and the shape of its Wigner-Seitz cell.

As immediately evident from Eq. (2.33), the state-dependent part of the potential completely vanishes for $\theta = 90^\circ$. The remaining state-independent potential has a global polarization of π . This peculiarity stems from the fact that the electric field is at all times aligned in parallel with the quantization axis. The corresponding single-particle band structure is plotted in Fig. 2.5b along the paths connecting points of high-symmetry as defined in Fig. 2.4d. It exhibits a large energy gap between the two lowest bands and a Dirac point between the second and third band. A detailed description of the underlying solution of the single-particle eigenvalue problem in the three-beam hexagonal Bravais lattice can be found, e.g., in Ref. [154].

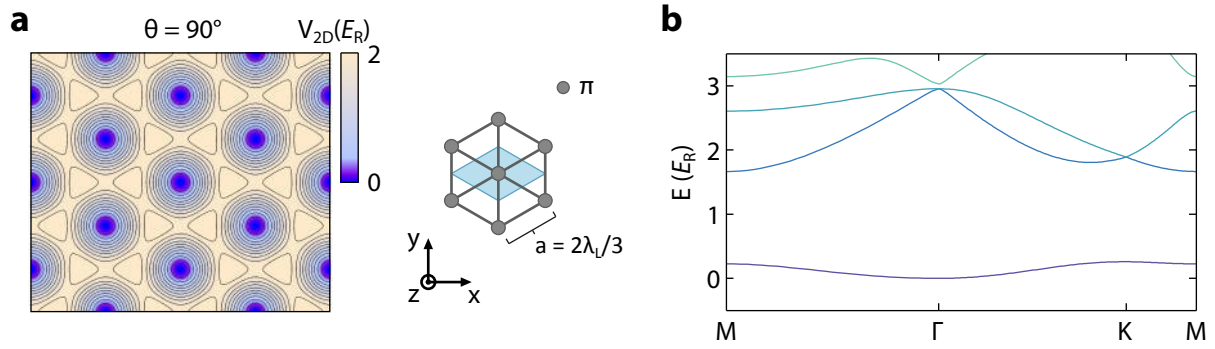


Figure 2.5: Triangular lattice. **a** For polarization vectors aligned perpendicular to the lattice plane, i.e., $\theta = 90^\circ$, the three beam lattice setup forms a state-independent *triangular* lattice with a strong intensity modulation of the potential landscape. A blue rhombus in the illustration of the lattice geometry indicates the unit cell. In part **b** the corresponding energy band structure is plotted along the paths connecting points of high symmetry in the first Brillouin zone as defined in Fig.2.4d. The large energy gap between the two lowest energy bands will be of importance in chapters 3 to 5.

In comparison to a square lattice comprised of similar laser beams the intensity modulation of the triangular lattice is very strong. As a result, tunneling rates decrease much faster with increasing lattice depth.

2.4.3 State-dependent honeycomb lattice

If all polarization vectors lie in the lattice plane, i.e. $\theta = 0$ or $\epsilon_i = R_z(\pi/2) \mathbf{k}_i/|\mathbf{k}_i|$, the dipole potential is inverted as compared to the triangular lattice (see Fig. 2.6a). This is the well-known *honeycomb* lattice resembling graphene. It exhibits large potential maxima and hexagonally arranged minima that are separated by comparably small potential hills. Trapped atoms can easily move by tunneling through this shallow honeycomb channel structure. The underlying Bravais lattice is again the hexagonally symmetric (triangular) lattice discussed in Fig. 2.4a with the difference of having a two-fold atomic basis. In the following, the corresponding two distinct lattice sites in a unit cell are denoted as site \mathbb{A} and \mathbb{B} . Each individual lattice site is separated by $a/\sqrt{3}$ from its nearest neighboring site, where a denotes the lattice constant of the Bravais lattice. With only three nearest neighboring lattice sites, the honeycomb lattice has the smallest possible coordination number in two dimensions. Both triangular and honeycomb lattice structures can be commonly found in all conceivable forms in nature as they describe the close-packing of spheres in two dimensions.

In stark contrast to the triangular lattice, the spin-dependent part of the dipole potential, scaling with $\cos^2 \theta$, is maximally strong. The corresponding polarization pattern of the light field is depicted in the inset of the honeycomb potential plot in Fig. 2.6a. It alternates from pure σ^+ to pure σ^- between adjacent lattice sites (thus, the net polarization of the light field in a unit cell is still π). In accordance with Eq. (2.33) and (2.34) the

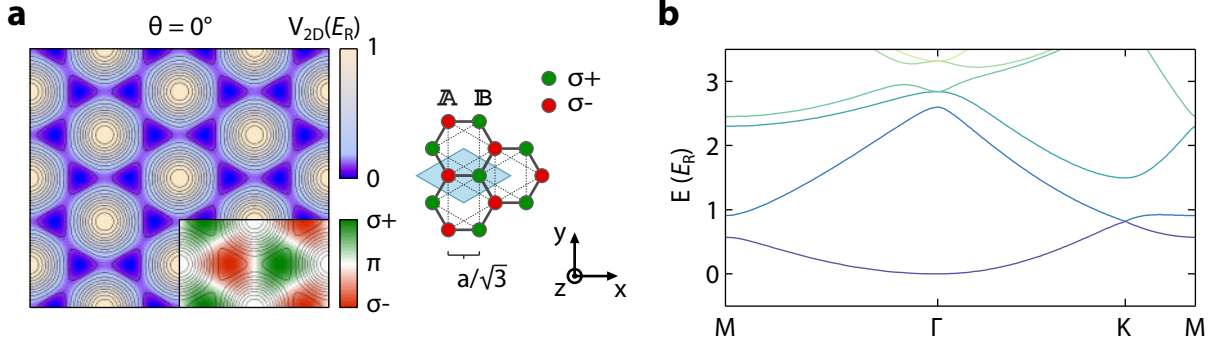


Figure 2.6: Honeycomb lattice. **a** For in-plane polarization, i.e., $\theta = 0^\circ$, the potential is inverted and forms a *honeycomb* structure with shallow channels around large potential maxima. In addition, the circular polarization alternates from pure σ^+ to pure σ^- between adjacent lattice sites. The blue rhombus indicates the unit cell including a site of each sublattice \mathbb{A} and \mathbb{B} . **b** Band structure of the honeycomb lattice plotted for a particle with $m_F = 0$. At the K -point the two lowest energy bands touch forming a Dirac point.

alternation lifts the degeneracy of the two-fold atomic basis for atoms in hyperfine ground states with $m_F \neq 0$. This breaking of the inversion symmetry has a profound influence on the topological properties of the honeycomb lattice. In chapter 6 we will present experiments in the honeycomb lattice where inversion symmetry can be broken in a controllable way. Until then, we will restrict this introduction on the honeycomb lattice to the fully symmetric case for atoms with $m_F = 0$.

The two-fold atomic basis of the honeycomb lattice results in a splitting of the first energy band, leading to the formation of Dirac points between the two lowest bands at the vertices of the Brillouin zone (see Fig. 2.6b). Close to the Dirac point, the dispersion is linear in all directions. Due to the vanishing curvature within these Dirac cones particles have an effective mass of zero and can be described as relativistic particles in the framework of the famous Dirac equation. As each of the six Dirac points is shared by three Brillouin zones, only two Dirac cones are inequivalent in the two-dimensional band structure of the honeycomb lattice. They are commonly referred to as the K and K' points.

2.4.4 Polarization lattice

Eq. (2.32) reveals a third distinct scenario arising from the mere alignment of the linear polarization vectors ϵ_i in the three-beam lattice setup. For a polarization angle of exactly $\theta = \arccos(1/3)/2 \approx 35.26^\circ$, the intensity modulation of the lattice potential vanishes, leaving only a constant energy offset of $-6V_0$.

The remaining modulation of the circular polarization creates a purely state-dependent lattice given by the potential in Eq. (2.33). While atoms in hyperfine states with a magnetic quantum number of $m_F = 0$ experience no lattice potential at all, atoms with $m_F \neq 0$

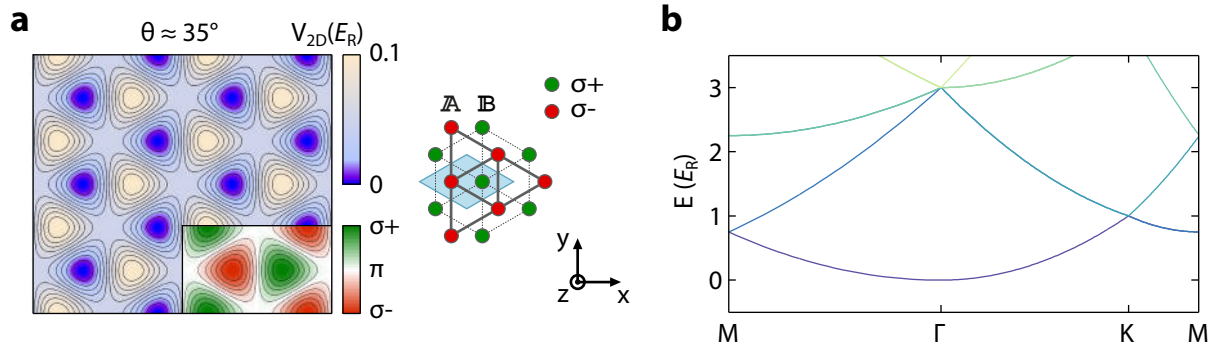


Figure 2.7: Polarization lattice. **a** If the polarization vectors ϵ_i are aligned such that they all enclose an angle of $\theta \approx 35^\circ$ with the lattice plane, the intensity modulation of the three-beam lattice setup vanishes, leaving only a potential modulation for atoms in hyperfine states with $m_F \neq 0$. The potential is calculated for ^{87}Rb -atoms in the $|2, -2\rangle$ state and similar laser parameters as in Fig. 2.5 and 2.6. **b** The shallow potential due to the relatively small proportionality factor $\eta \approx 0.13$ results in an almost free-particle like dispersion relation

are subjected to a triangular lattice (see Fig. 2.7a). For the presented case of relatively far detuned laser light at 830 nm, the potential experienced by the atoms is very shallow due to the small proportionality factor η . In Fig. 2.7a the potential and dispersion is depicted for atoms in the $|2, +2\rangle$ hyperfine state, that are trapped at lattice sites with σ^- polarization. Accordingly, as indicated by dashed lines in the schematic drawing of Fig. 2.7a, atoms that are trapped at the σ^+ -sites, e.g., $|2, -2\rangle$, experience an inverted lattice potential. The corresponding dispersion of such a polarization lattice, depicted in Fig. 2.5, is similar to the triangular lattice. Due to the shallow potential presented here, the band structure in Fig. 2.7b resembles the parabolic dispersion of a free-particle. Laser wavelengths closer to the atomic transitions, however, allow for much stronger confinements in purely state-dependent optical potentials [180]. We will elaborate the peculiarities and experimental prospects of the polarization lattice further briefly chapter 7 with respect to applications for periodic driving schemes. A thorough discussion of the presented polarization lattice potential is provided in Ref. [154].

For reasons of comparability, all potentials and dispersion relations presented in Fig. 2.5, 2.6 and 2.7 have been calculated for the same lattice laser parameters. It is evident that the total intensity modulation of the triangular lattice is twice as strong as in the case of the honeycomb lattice. Note that the and asymmetric and perceptually unadjusted color maps used throughout the potential plots of Fig. 2.5, 2.6 and 2.7 are chosen in order to emphasize the relevant minima of the potential landscapes. A similar figure containing parts of Fig. 2.5, 2.6 and 2.7 that was created by the author also appears in Ref. [5].

The presented description of the running-wave three beam lattice is by far not complete. By considering arbitrarily polarized light beams it is possible to realize a large variety of more complex lattice configurations that are not limited to two dimensions. A promising,

yet comparatively simple expansion of the three-beam lattice should be noted: Retro-reflecting of all three beams allows for the creation of both a kagome lattice [77] as well as a so called \mathcal{T}_3 - or *dice*-lattice [181, 182]. A brief illustration of the potential geometries resulting from such a six-beam setup is provided in chapter 7.

In the following section, we will detail experimental detection techniques applied for ultracold atomic quantum gases in optical lattices.

2.5 Revealing the momentum distribution by time-of-flight measurement

A widely applied detection technique for ultracold quantum gases in general and quantum gases in optical lattices in particular is resonant *time-of-flight* absorption imaging. It relies on a sudden, non-adiabatic switch off of all trapping potentials, such that the atomic ensemble can expand freely for a certain time-of-flight t_{TOF} while it falls under the influence of gravity. The periodicity of the expanding Bloch waves leads to an emergence of sharp Bragg peaks separated by the reciprocal lattice vectors. The resulting real-space density distribution of the expanded matter wave is the density distribution $\tilde{n}(\mathbf{k})$ of the lattice in momentum space [29, 183, 184]

$$\tilde{n}(\mathbf{k}) = \langle \tilde{\Psi}^\dagger(\mathbf{k}) \tilde{\Psi}(\mathbf{k}) \rangle = |\tilde{w}(\mathbf{k})|^2 \sum_{i,j} e^{i\mathbf{k}(\mathbf{R}_j - \mathbf{R}_i)} \langle \hat{b}_i^\dagger \hat{b}_j \rangle. \quad (2.37)$$

The $\tilde{\Psi}(\mathbf{k})$ and $\tilde{w}(\mathbf{k})$ denote the Fourier transform of the bosonic field operators introduced in Eq. (2.19) and the Wannier function defined in Eq. (2.15) respectively. Eq. (2.37) reveals a close connection between the momentum distribution $\tilde{n}(\mathbf{k})$ and the first order correlation function $\langle \hat{b}_i^\dagger \hat{b}_j \rangle$. For increasing lattice depth the long-range phase coherence and, thus, the first order correlation function, decrease rapidly as discussed in section 2.3.2. Accordingly, a Mott-insulating state in a deep optical lattice potential as defined in Eq. (2.25) which exhibits maximally strong phase fluctuations results in an almost featureless momentum distribution $\tilde{n}(\mathbf{k})$ that is governed by the Wannier envelope $|\tilde{w}(\mathbf{k})|^2$. This width of the Fourier transformed Wannier function $\tilde{w}(\mathbf{k})$ determines the extension of the momentum distribution $\tilde{n}(\mathbf{k})$. It increases for increasing lattice depth since the real-space Wannier functions become narrower.

Detection of the density distribution $\hat{n}(\mathbf{r})$ after time-of-flight is achieved by imaging the shadow of a resonant laser beam cast by the atoms. Together with a reference image taken in absence of an atomic cloud this allows for the reconstruction of the *optical density* (OD) along the line of sight. In the experimental setup imaging along two different directions is possible as depicted in Fig. 2.8. Imaging perpendicular to the three-beam lattice, i.e., along the z -axis, reveals the characteristic hexagonally symmetric momentum peaks of a triangular Bravais lattice. In contrast, time-of-flight imaging of a superfluid state in a three-dimensional lattice along the x -axis results in a rectangular momentum structure.

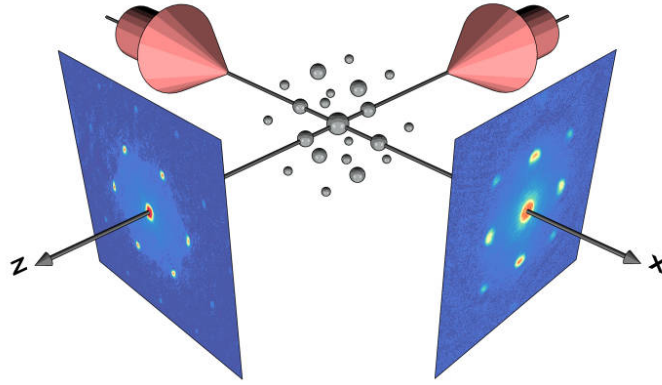


Figure 2.8: Illustration of the time-of-flight absorption imaging setup. In the experimental setup, two imaging systems are implemented along the x - and z axis. By imaging perpendicular to the three-beam lattice the characteristic hexagonally symmetric momentum distribution of a superfluid state in a triangular Bravais lattice can be observed. In a three-dimensional lattice created by the additional counterpropagating 1D lattice a rectangular density distribution is observed along the x -axis. The figure was inspired by Refs. [56] and [153].

Due to the projection of the three beam lattice vectors and the larger wavelength used for the counterpropagating 1D-lattice, the momentum peaks are aligned almost cubically.

A comparison between a pure BEC released from a crossed dipole trap and a superfluid state in an optical lattice is depicted in Fig. 2.10. Here, both the change of the BECs aspect ratio and the expansion of the Bragg momentum peaks for increasing time-of-flight are clearly visible. The parabolic trajectories due to the influence of gravity are used to measure the exact magnification of the imaging system.

As pointed out in Ref. [29] the observed atomic density distribution after time-of-flight $\langle \hat{n}(\mathbf{r}) \rangle_{\text{TOF}}$ deviates from the momentum distribution in the lattice $\langle \tilde{n}(\mathbf{k}) \rangle_{\text{Lat}}$:

$$\langle \hat{n}(\mathbf{r}) \rangle_{\text{TOF}} \approx \left(\frac{m}{\hbar t_{\text{TOF}}} \right)^3 \langle \tilde{n}(\mathbf{k}) \rangle_{\text{Lat}} \quad \text{with} \quad \mathbf{r} = \frac{\hbar t_{\text{TOF}}}{m} \mathbf{k}. \quad (2.38)$$

The main deviation between observed density distribution and actual momentum distribution in the lattice, however, stems from the experimentally finite time-of-flight [185]. In analogy to near-field diffraction known from classical optics, the observed density distribution exhibits a broadening of Bragg peaks. The exact momentum distribution is only recovered in the *far-field* limit for $t_{\text{TOF}} \rightarrow \infty$. A characteristic expansion time where density distribution resulting from time-of-flight and the in-trap momentum distribution become indistinguishable from the ideal far-field solution is given by $t_{\text{FF}} = ml_c R_0 / \hbar$ [185]. Here, l_c is the coherence length of the state and R_0 the in-situ radius of the atomic cloud. For a coherent superfluid state, where $l_c \approx R_0$ and a typical in-trap extension of R_0 the far field regime is reached after $t_{\text{FF}} \approx 300$ ms. In earth's gravitational field this is equivalent to a free-falling distance on the order of 0.5 m, which is unrealistically large with respect

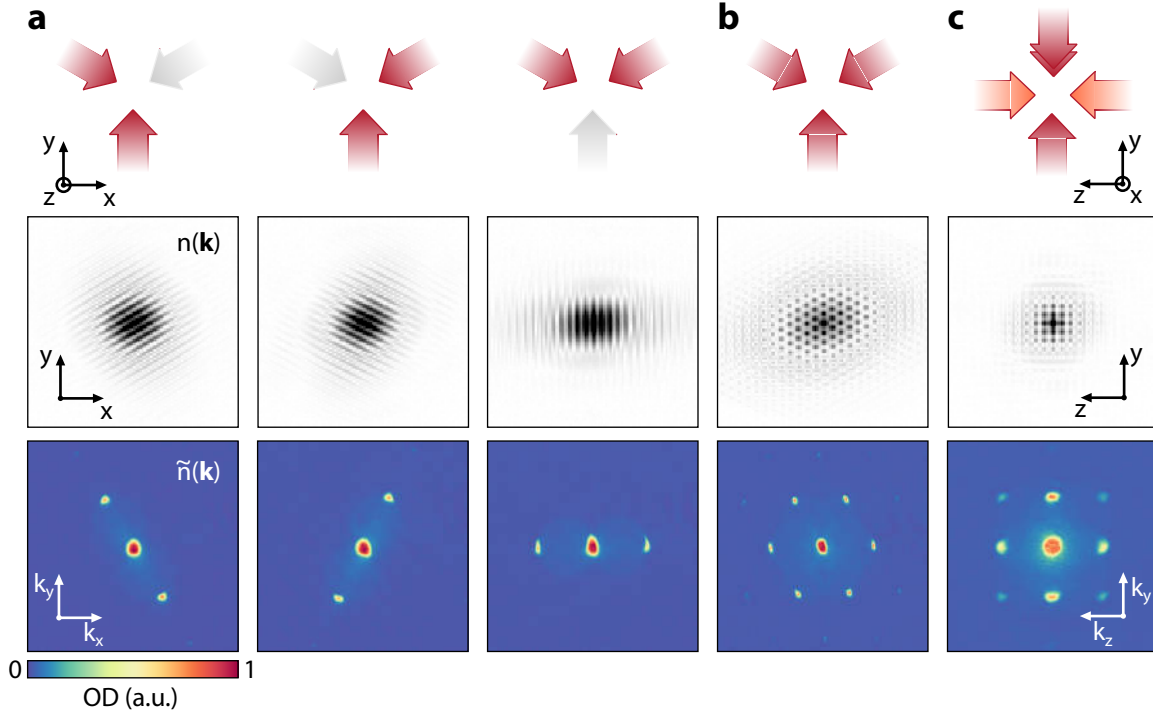


Figure 2.9: Time-of-flight patterns for different lattice setups. **a** shows three possible running-wave 1D lattice setups together with the resulting momentum distribution detected after 40 ms time-of-flight. In the middle row, the Fourier transforms of the optical density distributions are plotted to illustrate the real-space in-trap density distribution. Corresponding images of the three-beam lattice in a triangular configuration are shown in **b**. **c** depicts the imaging along the x -direction after 18 ms TOF. A rectangular momentum distribution appears for a three-dimensional lattice.

to limitations concerning vacuum setups and vanishing optical density. However, several approaches aiming for extending expansion times are subject to current research such as magnetic levitation (see, e.g. [186]) and experiments under microgravity [187].

The time-of-flight imaging technique reveals the momentum distribution by suddenly all trapping potentials. In contrast, it is also possible to observe the *quasimomentum* distribution. For this purpose, the lattice potential is *adiabatically* turned off prior to the free-fall expansion [59, 73]. While preserving the quasimomentum \mathbf{q} a Bloch wave in the n -th energy band is mapped onto the free-particle momentum \mathbf{p} in the n -th Brillouin zone (see Fig. 2.4c). We will utilize this so called *band mapping* technique in chapter 6 in order to measure band populations.

With a lattice spacing on the order of $0.5 \mu\text{m}$, the in-situ density distribution of atoms in the optical lattice cannot be resolved by the imaging systems in our experiment. In recent years, however, the experimental realization of single-site resolving microscope detection setups has sparked tremendous interest [62, 63].

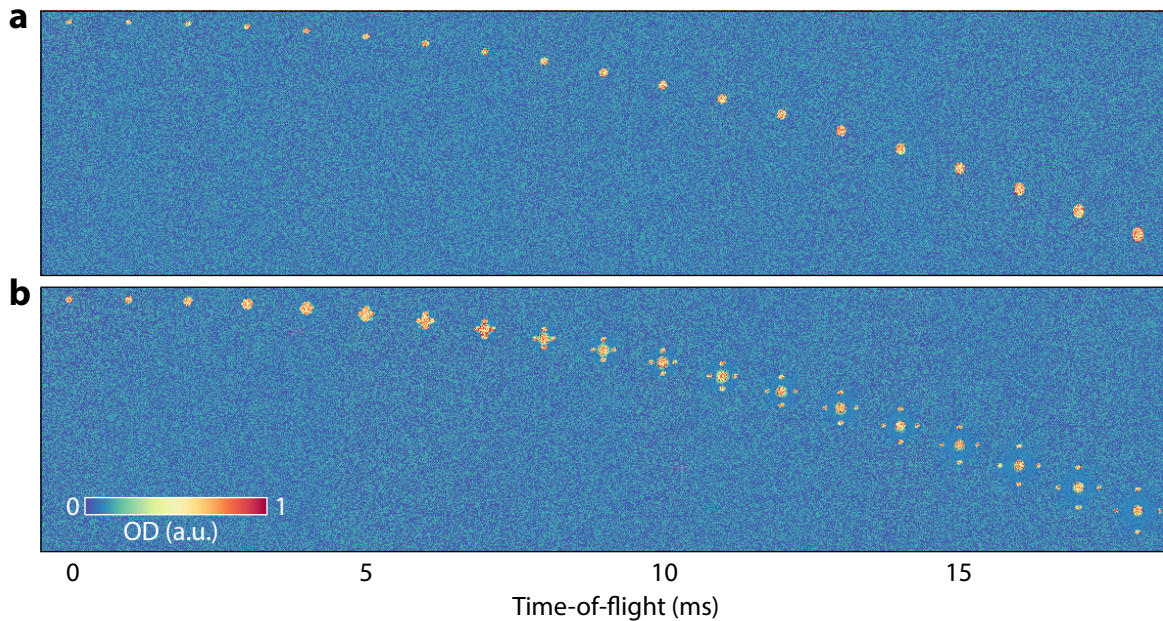


Figure 2.10: Characteristic time-of-flight expansion. **a** A pure BEC is released from a crossed optical dipole trap and falls under the influence of gravity. In contrast to a thermal ensemble, the aspect ratio of the atomic cloud is inverted for increasing TOF. **b** the same experimental sequenced imaged for the release of a superfluid state in a three-dimensional optical lattice.

2.6 Conclusion & outlook

In this chapter we have briefly introduced the concept of periodic optical potentials and described the most important physical aspects for ultracold atomic ensembles confined in such lattices. The running-wave three beam lattice setup has been described with special emphasis on three possible realizations regarding orientation of the linear polarization vectors of the lattice beams. With the time-of-flight absorption technique we have presented the most common detection scheme for ultracold quantum gases which will be of importance throughout all experiments presented here. In the following chapters we will refer to this introductory chapter and elaborate some of the presented concepts further.

3 Bose-Einstein condensates in strongly driven lattices

In this chapter we develop the concept of far off-resonant time-periodic driving of optical lattices. We explain how this technique allows for the experimentally feasible engineering of tunneling matrix elements and, thus, of the dispersion relation in a time-averaged effective picture. Benchmark experiments for the verification of driving schemes are presented and discussed by means of the observed momentum distribution. Beyond that, we investigate the strong driving regime with respect to the occurrence of multi-photon transitions for different lattice dimensionality. We find an excellent agreement with *ab initio* calculations of the transition energies and discuss implications to further experiments.

Tunneling dynamics play a key role in the behavior of quantum many-body systems in periodic potentials. In contrast to solid state systems that are inevitably limited by properties of the underlying atomic composition, ultracold quantum gases in optical lattice potentials provide experimental model systems that allow for the versatile and continuous manipulation and control of tunneling parameters and interactions in general.

A central aspect throughout most experiments performed within this thesis is the manipulation of the tunneling matrix element J_{ij} for ultracold quantum gases in optical lattices as introduced in Eq. (2.20). In the preceding chapter we have discussed the concept decreasing the amplitude of the tunneling matrix element while increasing the on-site interaction energy U by increasing the potential depth of the optical lattice. This allowed for the first observation of the superfluid to Mott insulator quantum phase transition [56].

In order to obtain full control over the tunneling matrix elements concerning not only their amplitude but also their *sign* and, as we will see in chapter 4, their *phase* we utilize the technique of far off-resonant time-periodic lattice driving. This approach does not influence the on-site interaction energy and allows for the versatile manipulation of motional degrees of freedom [92, 188, 189].

Data presented in this chapter have been obtained within the team of J. Simonet, C. Ölschläger, S. Prella and M. Weinberg. The theoretical treatment in section 3.1 and experimental implementation of the lattice driving technique relies on the work of J. Struck [155] and C. Ölschläger [179].

3.1 Tunneling renormalization by periodic driving

In this section the basic concepts of the engineering of tunneling matrix elements by far off-resonant lattice driving are presented. First, we provide an intuitive understanding of the tunneling renormalization in a one-dimensional lattice. A more rigorous treatment of the effective description of such driving is given within the framework of Floquet theory. Here, we will extend the driving schemes to arbitrary forcing functions and lattice systems.

3.1.1 Semiclassical 1D-model

The change of the tunneling parameter due to a time-periodic force acting on the lattice system can be understood in terms of a semiclassical single-particle model. For simplicity, we restrict our considerations to a one-dimensional lattice in the following while the concept can easily be extended to higher dimensions.

In the presence of an external time-dependent force $F(t)$ the lattice system is described by the stationary single particle Hamiltonian $\hat{\mathcal{H}}_{\text{Lat}}(x)$ from Eq. (2.13) with an additional forcing term:

$$\hat{\mathcal{H}}(x, t) = \hat{\mathcal{H}}_{\text{Lat}}(x) - xF(t). \quad (3.1)$$

The solutions of the corresponding Schrödinger equation, the so called *Houston states* [190, 191], exhibit a time-dependent quasimomentum $q_k(t)$ which changes according to

$$\hbar \frac{d}{dt} q_k(t) = F(t). \quad (3.2)$$

Hence, a time-periodic force $F(t) = F(t + T)$ of the form

$$F(t) = F_0 \sin(\Omega t) \quad (3.3)$$

results in a time-dependent shift of the quasimomentum

$$q_k(t) = k - \frac{F_0}{\hbar\Omega} \cos(\Omega t), \quad (3.4)$$

where Ω denotes the driving frequency $\Omega = 2\pi/T$. This time-dependence has a profound influence on the energy dispersion of the lattice system. The lowest band tight-binding dispersion $E(q)$ in a one-dimensional lattice with lattice constant a is given by

$$E(q) = -2J^{\text{bare}} \cos(aq). \quad (3.5)$$

In Eq. (3.5) we have labeled the undisturbed tunneling parameter as J^{bare} in order to distinguish it from the effective tunneling parameter that will be described in the following [192]. Accordingly, the width of the energy band is $\Delta E = 4J^{\text{bare}}$. Bosonic atoms in the ground state occupy the minima of the dispersion at $q_{\min} = 2\pi n_q/a$, $n_q \in \mathbb{Z}$.

Inserting the time-dependent quasimomentum into Eq. (3.5) leads to a time-dependent dispersion. In the limit of high driving frequencies, i.e., in the case of the energy scale associated with the driving being large compared to the typical energy scale of the system given by the tunneling amplitude ($\hbar\Omega \gg J^{\text{bare}}$) the energy of a particle can be approximated by its time-average over one driving cycle. The resulting effective dispersion reads

$$\begin{aligned} E^{\text{eff}}(k) &= \int_0^T E(q_k(t')) dt' \\ &= -2J^{\text{eff}} \cos(ak). \end{aligned} \quad (3.6)$$

Here, we have introduced the effective tunneling matrix element J^{eff} which is a product of the bare tunneling and the zeroth-order Bessel function of the first kind J_{B0} :

$$J^{\text{eff}} = J_{B0}(K) \cdot J^{\text{bare}} \quad \text{with} \quad K = \frac{aF_0}{\hbar\Omega}. \quad (3.7)$$

The Bessel function $J_{B0}(K)$ in dependence to the dimensionless forcing amplitude K is depicted in Fig. 3.1b. As Eq. (3.6) and (3.7) imply, the effective dispersion relation retains its initial shape but exhibits a renormalized width according to the amplitude of the Bessel function. The sign of the effective tunneling parameter and, thus, the effective dispersion can be inverted as the Bessel function becomes negative for forcing amplitudes above $K \approx 2.4$. Now, a superfluid will occupy the new minima of the dispersion at the edges of the Brillouin zone where $q_{\text{min}} = 2\pi(n_q + 1/2)/a$, $n_q \in \mathbb{Z}$.

Moreover, it can be shown that in general any time-periodic forcing leads to an effective dispersion described by

$$E^{\text{eff}}(k) = -2|J^{\text{eff}}| \cos(ak - \theta). \quad (3.8)$$

The realization of a continuous shift of the dispersion by θ/a and its implications will be presented in the following chapter.

An intuitive picture of the inversion of the dispersion relation is illustrated in Fig. 3.1c. Particles oscillating in quasimomentum space around a minimum of the undisturbed dispersion are located for longer times at positions of higher energy. In contrast, atoms oscillating around a maximum of the dispersion at $q = \pm\pi/a$ reside at lower energies for the greater part of every cycle. Therefore, time averaging results in the inversion of the dispersion for sufficiently large amplitudes where such oscillations start to overlap significantly. Accordingly, in the case of even larger amplitudes when oscillations in quasimomentum may span more than one Brillouin zone, the dispersion is inverted again depending on the corresponding turning points of the oscillations.

3.1.2 Effective description of driven systems

The semiclassical model presented in the previous section provides an intuitive understanding of the tunneling renormalization in a time-averaged effective picture. However,

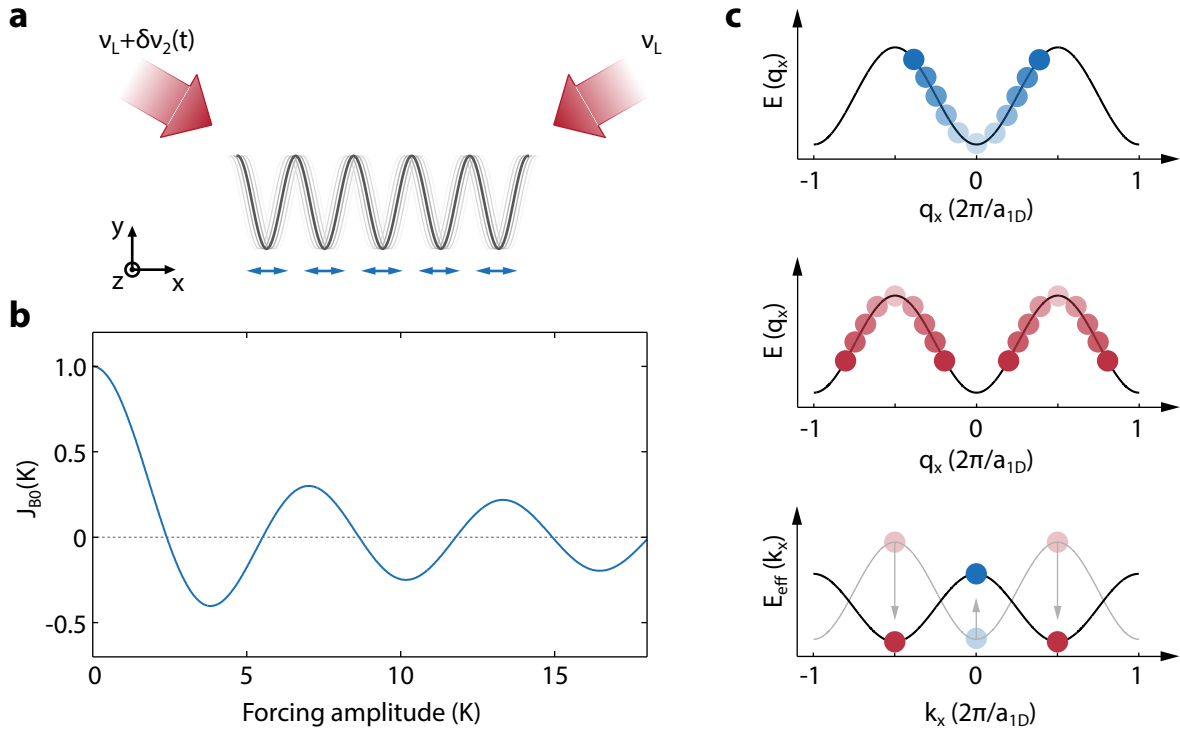


Figure 3.1: Lattice driving in one dimension. **a** Illustration of the periodic driving for the one-dimensional running-wave lattice. The lattice is accelerated by modulating the frequency of one of the running laser beams. **b** Tunneling matrix elements renormalize with the zeroth-order Bessel function of the first kind in dependence of the dimensionless forcing parameter K . **c** Oscillations around minima (maxima) of the dispersion relation depicted by blue (red) circles results in an increase (decrease) of energy and, hence, an inversion of the time-averaged effective dispersion $E^{\text{eff}}(k)$ for suitable forcing amplitudes.

this approach does not constitute a rigorous treatment of time-periodic driving. A theoretical framework for the fully quantum-mechanical description of periodically driven systems is given by Floquet theory [193]. In general, the Floquet theorem [194] can be applied to any periodic linear differential equation. For the present case of time-periodic lattice driving it is used to derive conditions imposed on the forcing of the lattice and the corresponding tunneling renormalization. In the following, we briefly introduce the application of Floquet theory to a time-periodic quantum system. The presented considerations are based on publications by Hemmerich [189], Eckardt *et. al* [92] and Arimondo *et. al* [195]. A comprehensive review regarding the application of the Floquet formalism to the tunneling processes in driven quantum systems is given in Ref. [196].

Applying the Floquet theorem to the Schrödinger equation

$$\hat{\mathcal{H}}(t) |\psi(t)\rangle = i\hbar \frac{\partial}{\partial t} |\psi(t)\rangle \quad (3.9)$$

with a time-periodic Hamiltonian $\hat{\mathcal{H}}(t) = \hat{\mathcal{H}}(t + T)$ leads to time-periodic solutions, the

so-called Floquet-states, of the form

$$|\psi_\alpha\rangle = e^{-i\varepsilon_\alpha t/\hbar} |\phi_\alpha(t)\rangle. \quad (3.10)$$

The *Floquet modes* $|\phi_\alpha(t)\rangle$ exhibit the same periodicity as the time-dependent Hamiltonian $\hat{\mathcal{H}}(t)$. Unsurprisingly, these solutions are in close resemblance of the Bloch-states given in Eq. (2.14) which are periodic in space rather than in time. The connection between Bloch- and Floquet states gives rise to the peculiarity of driven lattice systems being both periodic in space and in time, coined as *spatiotemporal crystals* [97].

With Eq. (3.9) and (3.10) the corresponding eigenvalue problem of the Floquet modes resembles a stationary Schrödinger equation

$$\hat{\mathcal{H}}_{\mathcal{F}} |\phi_\alpha(t)\rangle = \varepsilon_\alpha |\phi_\alpha(t)\rangle \quad (3.11)$$

with the Floquet Hamiltonian $\hat{\mathcal{H}}_{\mathcal{F}} = \hat{\mathcal{H}}(t) - i\hbar\partial_t$. The energy spectrum given by the solutions of Eq. (3.11) is periodic as one can construct infinitely many solutions by adding a phase term to the Floquet modes:

$$|\phi_{\alpha,l}(t)\rangle = e^{-il\Omega t} |\phi_\alpha(t)\rangle \quad \text{with } l \in \mathbb{Z}. \quad (3.12)$$

Hence, the energy spectrum consists of Floquet bands that are separated by $\hbar\Omega$, where $\Omega = 2\pi/T$ denotes the driving frequency:

$$\varepsilon_{\alpha,l} = \varepsilon_\alpha + l\hbar\Omega. \quad (3.13)$$

Again, this so-called *quasienergy* spectrum can be projected onto a reduced zone scheme $\varepsilon_{\alpha,l} \in [-\hbar\Omega/2, +\hbar\Omega/2[$ in analogy to the Brillouin zone of quasimomenta for Bloch bands [92].

The goal is now to obtain an effective, time-independent approximation of the Floquet Hamiltonian $\hat{\mathcal{H}}_{\mathcal{F}}$. For this purpose, one can define the composite Hilbert space $\mathcal{H} \otimes \mathcal{H}_T$ with \mathcal{H} being the Hilbert space of the solutions to the Schrödinger equation (3.9). Accordingly, \mathcal{H}_T denotes the Hilbert space of T -periodic complex-valued functions, referring to the Floquet modes from the eigenvalue problem of Eq. (3.11). The scalar product in $\mathcal{H} \otimes \mathcal{H}_T$ is defined by the time average of the usual scalar product which we write as

$$\langle\langle \cdot | \cdot \rangle\rangle_T \equiv \frac{1}{T} \int_0^T \langle \cdot | \cdot \rangle dt \quad (3.14)$$

in the following. Transformations between the Hilbert space \mathcal{H} and $\mathcal{H} \otimes \mathcal{H}_T$ can be achieved in a very general way [189]. Let $U_l(t) \equiv \exp(-iQ(t) + il\Omega t)$ be a unitary operator with a time-periodic Hermitian operator $Q(t) = Q(t+T)$. A stationary, orthonormal basis $|n\rangle$ in \mathcal{H} transforms to an orthonormal basis $|n(t), l\rangle$ in $\mathcal{H} \otimes \mathcal{H}$ as

$$|n(t), l\rangle = U_l |n\rangle. \quad (3.15)$$

We can now calculate the matrix elements of the Floquet Hamiltonian in the composite Hilbert space [92, 189]:

$$\langle\langle n(t), l | \hat{\mathcal{H}}_{\mathcal{F}} | n'(t), l' \rangle\rangle_T = \delta_{ll'} \langle n | \hat{\mathcal{H}}_{\text{eff}} | n' \rangle + \delta_{ll'} l \hbar \Omega + (1 + \delta_{nn'}) \langle n | \mathcal{V}_{ll'} | n' \rangle \quad (3.16)$$

where we have set $U \equiv U_{l=0}$ such that the time-averaged effective Hamiltonian is defined as

$$\hat{\mathcal{H}}_{\text{eff}} \equiv \left\langle U^\dagger(t) \hat{\mathcal{H}}_{\mathcal{F}}(t) U(t) \right\rangle_T. \quad (3.17)$$

The matrix representation of the Floquet Hamiltonian in Eq. (3.16) is comprised by a block structure with blocks $\langle n | \hat{\mathcal{H}}_{\text{eff}} | n' \rangle + \hbar \Omega$ on the main diagonal, where $l = l'$, that are separated by multiples of the driving energy $\hbar \Omega$ and off-diagonal blocks $\langle n | \mathcal{V}_{ll'} | n' \rangle$ representing an additional perturbation term

$$\mathcal{V}_{ll'} \equiv \left\langle e^{i(l'-l)\Omega t} U^\dagger(t) \hat{\mathcal{H}}_{\mathcal{F}}(t) U(t) \right\rangle_T. \quad (3.18)$$

In the framework of perturbation theory, the perturbation term of Eq. (3.16) vanishes in the limit of high frequency driving where

$$|\langle n | \mathcal{V}_{ll'} | n' \rangle| \ll \hbar \Omega. \quad (3.19)$$

With the criterion that the main-diagonal blocks for different l in the Floquet matrix representation are well separated and do not overlap, i.e., if

$$|\hat{\mathcal{H}}_{\text{eff}}| \ll \hbar \Omega, \quad (3.20)$$

the quasienergy spectrum of the Floquet Hamiltonian in the first energy Brillouin zone is fully described by the energy spectrum of the effective Hamiltonian. In this limit, a suitable choice of the Hermitian operator Q in the unitary transformation of Eq. (3.15) allows for the complete elimination of the time-dependency in the treatment of any periodically driven system.

3.1.3 Application to driven lattices

As introduced in chapter 2, systems of ultracold quantum gases in optical lattices can be described within the framework of the Bose-Hubbard model in good approximation. In addition to the Bose-Hubbard Hamiltonian $\hat{\mathcal{H}}_{\text{BH}}$ given in Eq. (2.20), driven lattice systems in the high-frequency limit are described by an additional forcing term. The complete time-dependent Hamiltonian reads

$$\hat{\mathcal{H}}(t) = \hat{\mathcal{H}}_{\text{BH}} + \hat{\mathcal{H}}_{\text{Force}}(t). \quad (3.21)$$

The time-periodic forcing $\hat{\mathcal{H}}_{\text{Force}}(t) = \hat{\mathcal{H}}_{\text{Force}}(t+T)$ is given by a projection of the inertial force $\mathbf{F}(t) = -m\ddot{\mathbf{R}}_0(t)$, where \mathbf{R}_0 denotes the trajectory of the lattice, onto the respective lattice vectors \mathbf{R}_i for each lattice site:

$$\hat{\mathcal{H}}_{\text{Force}}(t) = \sum_i v_i(t) \hat{n}_i \quad \text{with} \quad v_i(t) \equiv -\mathbf{F}(t) \cdot \mathbf{R}_i. \quad (3.22)$$

In the following, we will restrict our considerations to a time-periodic forcing with vanishing time-average and assume that the lattice system was at rest prior to the acceleration starting at $t = t_0$. The time-dependent momentum shift of each atom in the lattice is then given by

$$\Delta \mathbf{p}(t) = \int_{-\infty}^t \mathbf{F}(t') dt' \quad (3.23)$$

$$= \int_{t_0}^t \mathbf{F}(t') dt' - \frac{1}{T} \int_0^T \int_{t_0}^t \mathbf{F}(t') dt' dt \quad (3.24)$$

$$= -m\dot{\mathbf{R}}_0(t). \quad (3.25)$$

It was shown in Ref. [92] that choosing the Hermitian operator

$$Q(t) = \frac{1}{\hbar} \sum_i W_i(t) n_i \quad (3.26)$$

with the change in momentum projected onto the lattice vectors being

$$W_i(t) = \int_{t_0}^t v_i(t') dt' - \frac{1}{T} \int_0^T \int_{t_0}^t v_i(t') dt' dt \quad (3.27)$$

$$= -\Delta \mathbf{p}(t) \cdot \mathbf{R}_i \quad (3.28)$$

results in the time-averaged effective Bose-Hubbard Hamiltonian

$$\hat{\mathcal{H}}_{\text{eff}} = - \sum_{\langle i,j \rangle} J_{ij}^{\text{eff}} (\hat{b}_i^\dagger \hat{b}_j + \hat{b}_j^\dagger \hat{b}_i) + \frac{U}{2} \sum_i \hat{n}_i (\hat{n}_i - 1). \quad (3.29)$$

This result constitutes a cornerstone for all experiments presented in this thesis that deal with periodically driven lattice systems. Note that we have omitted the external trapping potential in Eq. (3.29). The effective Hamiltonian is similar to the Bose-Hubbard Hamiltonian from Eq. (2.20) with the exception of the renormalized *effective* tunneling matrix elements J_{ij}^{eff} that relate to the bare tunneling matrix elements given in Eq. (2.21) as

$$J_{ij}^{\text{eff}} = J_{ij}^{\text{bare}} \frac{1}{T} \int_0^T e^{iW_{ij}(t)/\hbar} dt \quad \text{where} \quad W_{ij}(t) \equiv W_i(t) - W_j(t). \quad (3.30)$$

With condition (3.20), the effective Bose-Hubbard Hamiltonian is valid for driving frequencies that are much larger than the energy scales in the system, namely the on-site interaction U and the bare tunneling coupling J^{bare} :

$$\max\{U, J^{\text{bare}}\} \ll \hbar\Omega. \quad (3.31)$$

This condition has been verified by a number of numerical simulations in Refs. [92, 197, 198]. However, a second prerequisite for the description of driven lattice systems in terms in the effective Bose-Hubbard picture is the validity of the single band approximation. It is, thus, crucial to avoid couplings of any kind to higher energy bands. Hence, the term *far off-resonant* driving, indicating that the driving scheme discussed here relies on the presence of a comparatively large energy band gap of the lattice system where no excitations are possible. However, this condition is not sufficient due to the strong forcing of the system. In this regime, multi-photon transitions to higher bands may occur with significant probability. We will investigate the excitation spectra of a variety of driven lattice systems with respect to such transitions thoroughly in section 3.3.

As discussed in section 2.5, we rely on the momentum distribution as the main observable for the characterization of the state present in the optical lattice. For a periodically driven system, the momentum distribution $\tilde{n}(\mathbf{k}) \equiv \tilde{n}_{\mathbf{k}}$ in the lattice reference frame is given by Eq. (2.37). Transformation of the observable to the laboratory reference frame can be achieved with the unitary operator [195]

$$U_T = \exp\left(\frac{i}{\hbar}\left[\mathbf{R}_0(t)\hat{\mathbf{p}} - m\mathbf{R}_0(t)\mathbf{r} - \frac{m}{2}\int_0^t \dot{\mathbf{R}}_0^2(t')dt'\right]\right). \quad (3.32)$$

The first term of the unitary operator corresponds to a translation, the second term is a momentum shift and the third term removes the kinetic energy $E_{\text{kin}} = m\dot{\mathbf{R}}_0^2/2$. With $\tilde{n}_{\mathbf{k}}^{\text{Lab}} = U_T\tilde{n}_{\mathbf{k}}U_T^\dagger = \tilde{n}_{\mathbf{k}+\Delta\mathbf{p}(t)/\hbar}$ the observed momentum distribution of the effective state is given by

$$\tilde{n}_{\mathbf{k}}^{\text{Lab}} = |\tilde{w}(\mathbf{k} + \Delta\mathbf{p}(t)/\hbar)|^2 \sum_{i,j} e^{i\mathbf{k}(\mathbf{R}_j - \mathbf{R}_i)} \langle \hat{b}_i^\dagger \hat{b}_j \rangle. \quad (3.33)$$

The obtained equation is similar to Eq. (2.37) with the exception of the Fourier transform of the Wannier function oscillating according to the driving. Measurements revealing a non-trivial motion of this Wannier envelope will be presented in chapter 4. For a superfluid state in the driven system, however, the sharp superfluid momentum peaks at the minima of the effective dispersion remain at fixed positions in the laboratory frame.

3.2 Experimental realization of periodically driven lattices

In this section we will discuss the experimental implementation of periodic driving by means of *monochromatic* driving, i.e., sinusoidal driving with a single driving frequency Ω .

Experimentally, tunneling renormalization by monochromatic periodic driving of ultracold quantum gas lattice systems was first realized by Lignier *et. al* [94] and, for the case of a single particle in a double well potential by Kierig *et. al* [199]. A common method to employ periodic driving in lattice systems comprised of retro-reflected laser beams as in Ref. [94] and more recently, e.g., in Ref. [151] relies on shifting the position of the respective retro-reflecting mirror with piezo-electric actuators. Here, the node of the standing wave at the mirror directly determines the position of the lattice. In contrast, working in the running wave lattice setup permits us do shift the lattice structure in space by modulating the frequency of a laser beam. Frequency modulation can be easily achieved with an acousto-optic modulator that is placed in the branch of the respective laser beam at the laser setup. A modulation of

$$\omega_i(t) = \omega_L + \delta\omega_i(t) \quad (3.34)$$

directly leads to a phase shift of the light field of

$$\phi_i(t) = - \int_{-\infty}^t \delta\omega_i(t') dt'. \quad (3.35)$$

In the following, we will apply the concept of lattice driving to the one-dimensional running-wave lattice that is subject to sinusoidal frequency modulation.

3.2.1 Monochromatic driving of a one-dimensional lattice

The potential of the one dimensional running-wave lattice is given by Eq. (2.35). Let the lattice be comprised of the laser beams with wavevectors \mathbf{k}_2 and \mathbf{k}_3 . The reciprocal lattice vector is given by $\mathbf{b}_1 = b\hat{e}_x$ from Eq. (2.29) such that the lattice is aligned horizontally along the x -axis as depicted in the third row of Fig. 2.9a. This concept is illustrated in Fig. 3.1a.

The phase ϕ_3 is fixed and the condition prior to the start of the modulation at $t_0 = 0$ is set to $\phi_2(t \leq t_0) = 0$. A time-dependent phase $\phi_2(t)$ leads to a global shift of the lattice potential $V_{1D,1} \equiv V_{1D}$ according to

$$V_{1D}(\phi_2(t), x) = V_{1D}(0, x - R_0(t)) \quad (3.36)$$

with $R_0(t)$ denoting the trajectory of a lattice well. Eq. (3.36) yields the connection of phase and trajectory $\phi_2(t) = bR_0(t)$. A frequency modulation as in Eq. (3.34), thus, leads to an inertial force of

$$F(t) = -m\ddot{R}_0(t) = -m\ddot{\phi}_2/b \quad (3.37)$$

where we have used the relation

$$\delta\nu_2 = -\frac{\dot{\phi}_2(t)}{2\pi} = \frac{1}{ma_{1D}} \Delta p(t). \quad (3.38)$$

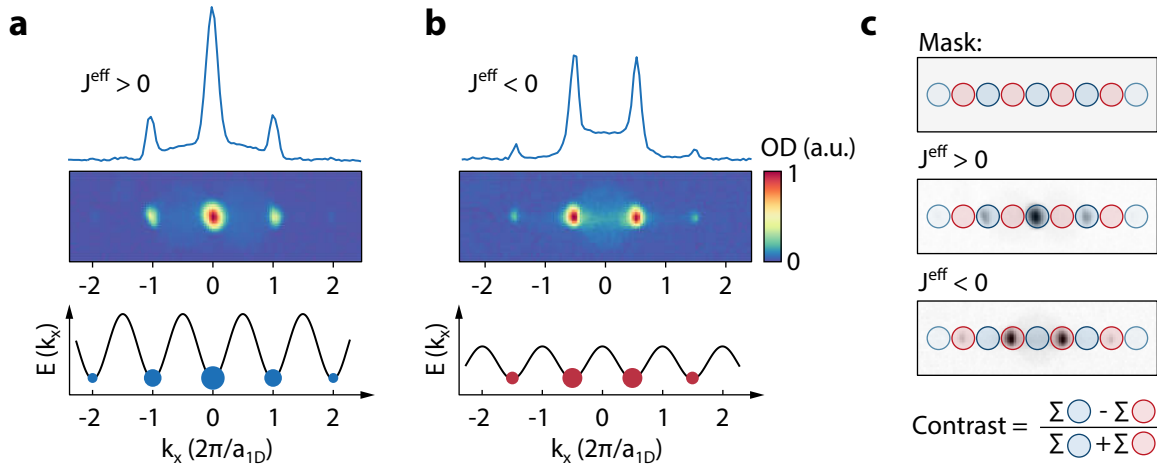


Figure 3.2: Quasimomentum distribution of driven 1D-lattices. **a** Dispersion relation of a lattice with positive tunneling matrix element and corresponding measured momentum distribution for a superfluid state. **b** Effective dispersion and measured momentum distribution for negative tunneling. The inversion of the effective dispersion is clearly visible in the absorption image by the absence of a zero-momentum component as atoms occupy the edges of the Brillouin zone. **c** Definition of the momentum *contrast* for the one-dimensional lattice.

As a result, the periodic frequency modulation of the form $\delta\nu_2(t) = -\nu_0 \cos(\Omega t)$ gives rise to a sinusoidal forcing of

$$F(t) = F_0 \sin(\Omega t) \quad \text{with} \quad F_0 = m\Omega\nu_0 a_{1D}. \quad (3.39)$$

In accordance with the semiclassical picture discussed in section 3.1.1, applying the sinusoidal forcing to Eq. (3.30) results in the renormalization of the tunneling matrix elements following the Bessel function in Fig. 3.1b. The dimensionless forcing amplitude K is given by

$$K = \frac{F_0}{\hbar\Omega} a_{1D} = \frac{m\nu_0}{\hbar} a_{1D}^2. \quad (3.40)$$

The experimental procedure for the driving in the one dimensional running-wave lattice is as follows. First, the Bose-Einstein condensate in the crossed optical dipole trap is adiabatically loaded into the lattice by an exponential ramping of the lattice depth in a ramping time of typically $T_{R,\text{Lat}} = 100$ ms to 500 ms. Subsequently the final lattice depth V_0 is held fixed and the forcing amplitude is linearly ramped up to its final value by increasing the amplitude of the frequency modulation $\tilde{\nu}_0(t) = \nu_0 t / T_{R,\text{drv}}$. Typical ramping times for the driving of the 1D-lattice lie between $T_{R,\text{drv}} = 50$ ms and 150 ms. The driving is maintained at a constant forcing amplitude $K(\nu_0)$ for holding times of $T_{H,\text{drv}} = 20$ ms to 100 ms. By then, bosons have relaxed into the minima of the effective dispersion relation. Finally, a time-of-flight measurement reveals the momentum distribution of the driven system.

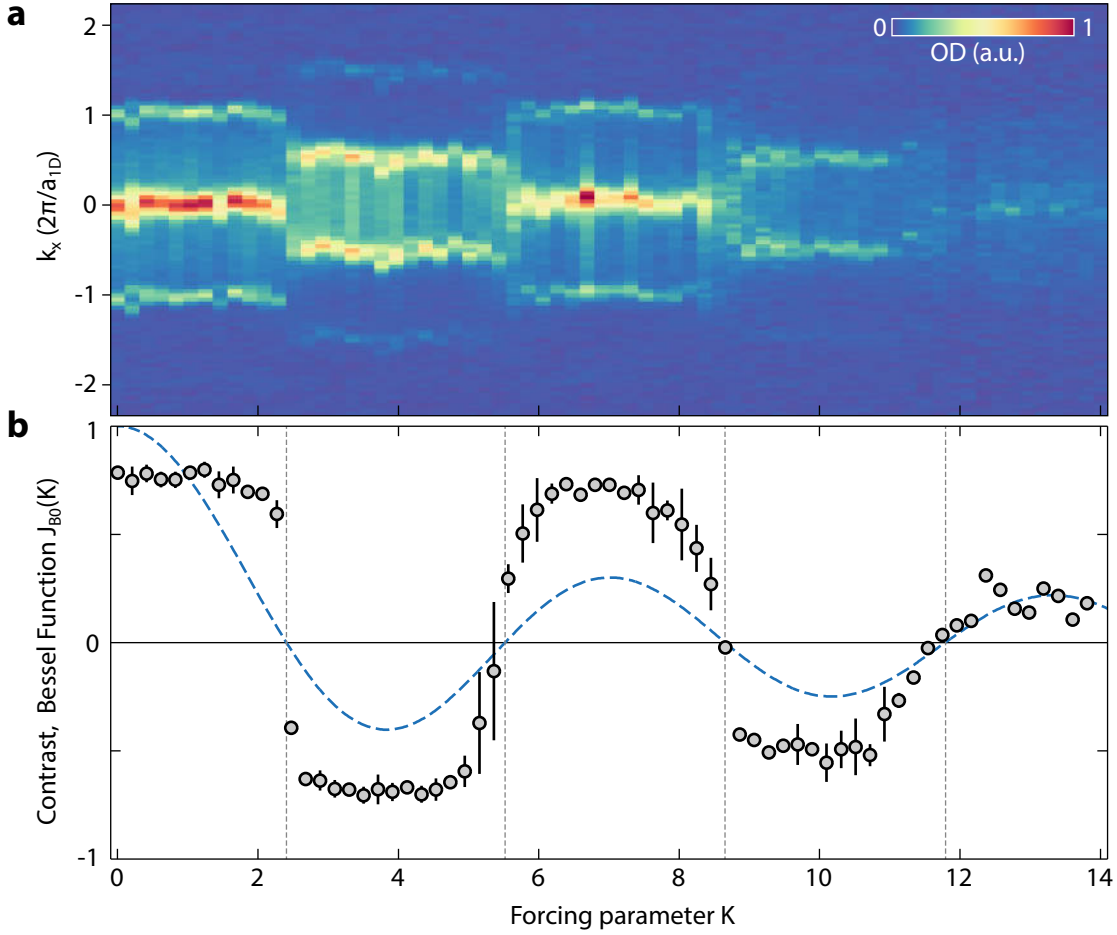


Figure 3.3: Sinusoidal lattice driving with increasing amplitude. **a** Row-sum of measured TOF-images for increasing forcing parameter K . The jump in quasimomentum occupations at the sign-change of the effective tunneling is clearly visible. **b** The zero-crossings of the extracted contrast (black circles) coincide remarkably well with the zero-crossings of the renormalization Bessel function (dashed blue line) that are emphasized by dashed vertical lines. Error bars indicate the standard deviation of the obtained contrast data.

Benchmark experiments for the monochromatic driving in the running-wave 1D lattice are depicted in the figures 3.2 and 3.3. The experimental data in Fig. 3.3 has been obtained by J. Struck and C. Ölschläger without the contribution of the author and is presented in similar fashion in the Refs. [155] and [179]. The results are reproduced here as they provide a crucial understanding of the experimental observation of the effective dispersion and the strength of the applied forcing.

The experiments are performed in a running-wave 1D-lattice with a lattice depth of $V_0 = 8 E_R$ where the atomic ensemble is in a superfluid state. Hereby, the initial BEC is created in the round-crossed dipole trap discussed in section 2.2.4. In the lattice system, the bare tunneling amplitude amounts to $J^{\text{bare}} = 1.2 \times 10^{-2} E_R$. With respect

to the energy gap between the two lowest bands of the initial dispersion relation of $E_{\text{gap}} = 3.6 E_R = h \times 12.1 \text{ kHz}$ the driving frequency is chosen to $\Omega = 2\pi \times 1.5 \text{ kHz}$. Ramping of the lattice depth and the driving amplitude is performed in $T_{R,\text{Lat}} = 100 \text{ ms}$ and $T_{R,\text{drv}} = 20 \text{ ms}$ respectively. Driving is maintained at the final forcing amplitude for another $T_{H,\text{drv}} = 20 \text{ ms}$. Note that, in contrast to the experimental data presented in the previous section, the absorption images in Fig. 3.2 and Fig. 3.3 are obtained after a time-of-flight of 27 ms with a magnification of $M \approx 1$.

In Fig. 3.2 the momentum distributions arising from different effective dispersions are shown. Fig. 3.2a depicts the time-of-flight image and its corresponding column sum for a dispersion with *positive* tunneling matrix elements $J^{\text{eff}} > 0$. Characteristic superfluid momentum peaks are visible at the minima of the dispersion located at zero momentum and multiples of $2\pi/a$ (compare Fig. 2.9). Hereby, the occupation of the momentum peaks is determined by the Wannier envelope centered around $k_x = 0$.

The same scenario is shown in Fig. 3.2b for an effective dispersion with *negative* effective tunneling matrix elements $J^{\text{eff}} < 0$, i.e., a lattice driving amplitude $K(\nu_0)$ resulting in a negative Bessel function. Here, the inversion of the band causes the superfluid momentum peaks to be located at the edges of the Brillouin zone in between the original minima of the dispersion with positive tunneling. It is important to note that the total driving time $T_{\text{drv}} = T_{R,\text{drv}} + T_{H,\text{drv}}$ is experimentally fine-adjusted such that the forcing function completes a full circle in good approximation before all trapping potentials are shut off for the time-of-flight imaging. At this point in time, the condition $\Delta\mathbf{p}(T_{\text{drv}}) = 0$ is fulfilled and the oscillating Wannier envelope from Eq. (3.33) coincides with the Wannier envelope of a system at rest.

In order to extract a quantitative signature for the sign of the effective tunneling matrix element it is useful to define a momentum occupation *contrast* as illustrated in Fig. 3.2c. It is defined as the relative difference of the sum over all pixel values in regions of the respective momentum peaks. The corresponding mask for time-of-flight images is depicted as blue and red circles. Blue (red) regions correspond to atoms residing at the momentum minima of a dispersion with positive (negative) tunneling. Due to the minimum at $k_x = 0$ for $J^{\text{eff}} > 0$, the most outwards lying regions (light blue) each enter only with half their total value in order to ensure a summation over equal surfaces. A positive (negative) tunneling matrix element clearly results in a positive (negative) momentum contrast.

The dependence of the effective tunneling on the driving amplitude is displayed in Fig. 3.3. Here, TOF-images have been taken for an increasing final forcing parameter. The column sum of these images is depicted in Fig. 3.3a, showing a clear and sudden jump between the two distinct cases of positive and negative effective tunneling. This jump is reproduced when extracting the momentum contrast from the images (Fig. 3.3b). Zero crossings coincide extremely well with the *ab initio* calculation of the corresponding Bessel function $J_{B0}(K)$. Note that for the calculation of the Bessel function the *exact* lattice parameters have been used. An approximation of an ideal lattice setup leads to a shift of the Bessel function such that the zero-crossings agree less well with the measured

data. This effect is thoroughly discussed in Ref. [179].

Remarkably, the measurements still exhibits sharp superfluid momentum peaks even after the third zero-crossing of the Bessel function, indicating that the coherence of the system is retained for very strong driving amplitudes. Exemplified, a forcing parameter of $K = 10$ corresponds to a driving amplitude in real-space of approximately five lattice sites [155, 179].

3.2.2 Driving of the triangular lattice

The monochromatic one-dimensional driving scheme discussed in the preceding section can be extended to the full three beam lattice. In this section we consider far off-resonant periodic driving of the state-independent triangular lattice. Prospects of the periodic driving scheme applied to other two-dimensional lattice types such as the honeycomb lattice will be discussed in chapter 7.

Tunneling between lattice sites in the triangular Bravais lattice takes place along three distinct directions. Following a proposal by Eckardt *et al.* [140], monochromatic periodic driving of the triangular lattice on an *elliptical* orbit allows for the tuning of effective tunneling matrix elements as depicted in Fig. 3.4. The corresponding elliptical forcing function $\mathbf{F}(t)$ with forcing amplitudes along the x - and y -axis F_x and F_y respectively is given by

$$\mathbf{F}(t) = -F_x \cos(\Omega t) \hat{\mathbf{e}}_x - F_y \sin(\Omega t) \hat{\mathbf{e}}_y. \quad (3.41)$$

In section 2.4.1 we have discussed that the two independent *relative* phases determine the position of the otherwise rigid triangular interference pattern $V_\Delta(\mathbf{r})$ of the three-beam lattice. Hence, elliptical forcing of the running-wave three beam lattice can be achieved by a suitable frequency modulation of each pair of laser beams. For all experiments presented here, we modulate the beams with wave vectors \mathbf{k}_2 and \mathbf{k}_3 while keeping the frequency of the vertical \mathbf{k}_1 -beam fixed. In analogy to the one dimensional case discussed in the previous section the real-space trajectory $\mathbf{R}_0(t)$ is connected to the time-dependent phases $\phi_2(t)$ and $\phi_3(t)$ via the relation

$$V_\Delta(\phi_2(t), \phi_3(t), \mathbf{r}) = V_\Delta(0, 0, \mathbf{r} - \mathbf{R}_0(t)). \quad (3.42)$$

Using the definition of the relative phases in Eq. (2.32) and (2.33) and setting $\phi_1(t) = 0 \quad \forall t$ leads to

$$\phi_2 = +\mathbf{b}_3 \mathbf{R}_0(t) = \frac{b}{2} \left(-R_x(t) + \sqrt{3}R_y(t) \right) \quad (3.43)$$

$$\phi_3 = -\mathbf{b}_2 \mathbf{R}_0(t) = \frac{b}{2} \left(+R_x(t) + \sqrt{3}R_y(t) \right) \quad (3.44)$$

Considerations similar to the one-dimensional case now yield the expressions for the frequency modulations

$$\delta\nu_{2,3}(t) = \pm \nu_x \sin(\Omega t) + \nu_y \cos(\Omega t) \quad (3.45)$$

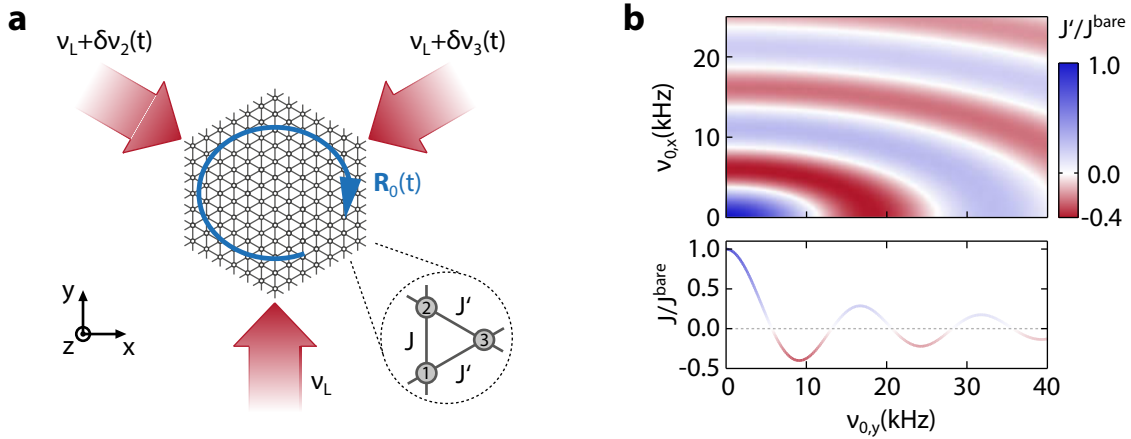


Figure 3.4: Periodic driving of the triangular lattice. **a** Illustration of the experimental realization of periodic driving. A suitable frequency modulation of two laser beams results in an elliptical trajectory $\mathbf{R}_0(t)$ of the rigid lattice structure. Effective tunneling matrix elements along the vertical bond $J \equiv J_{21}^{\text{eff}}$ and the two diagonal bonds $J' \equiv J_{32}^{\text{eff}} = J_{13}^{\text{eff}}$ can be tuned independently. **b** The renormalization of the two independent tunneling parameters J and J' is plotted with respect to the frequency modulation amplitudes ν_x and ν_y .

with the resulting forcing amplitudes given by

$$F_x = \sqrt{3}m\Omega a\nu_x \quad \text{and} \quad F_y = m\Omega a\nu_y \quad (3.46)$$

Here, the prefactor of $\sqrt{3}$ in the expression for F_x stems from the projection onto the diagonal lattice directions. Inserting the obtained forcing in Eq. (3.28) allows for the straightforward calculation of the tunneling renormalization along all three lattice bonds according to Eq. (3.30). These lattice bonds are described by the three Bravais lattice vectors in Eq. (2.30). In order to ensure a clockwise path around a rightwards pointing elementary plaquette of the triangular lattice we define the three lattice plaquette bonds \mathbf{d}_i according to the inset of Fig. 3.4a as

$$\mathbf{d}_{21} \equiv -\mathbf{a}_1, \quad \mathbf{d}_{32} \equiv \mathbf{a}_2, \quad \mathbf{d}_{13} \equiv \mathbf{a}_1 - \mathbf{a}_2 \quad (3.47)$$

in the following. Using Eq. (3.28) yields the expressions

$$W_{21}(t) = -\frac{F_x a}{\Omega} \cos(\Omega t) \quad (3.48)$$

$$W_{32,13}(t) = -\frac{a}{2\Omega} \left(\pm F_x \sin(\Omega t) + F_y \cos(\Omega t) \right). \quad (3.49)$$

Now, the time averaging in Eq. (3.30) is analytically solvable (for a thorough calculation we refer to Ref. [155]). Similar to the one-dimensional case, the resulting tunneling renormalization follows a zeroth order Bessel function of first kind for all lattice bonds. Due to

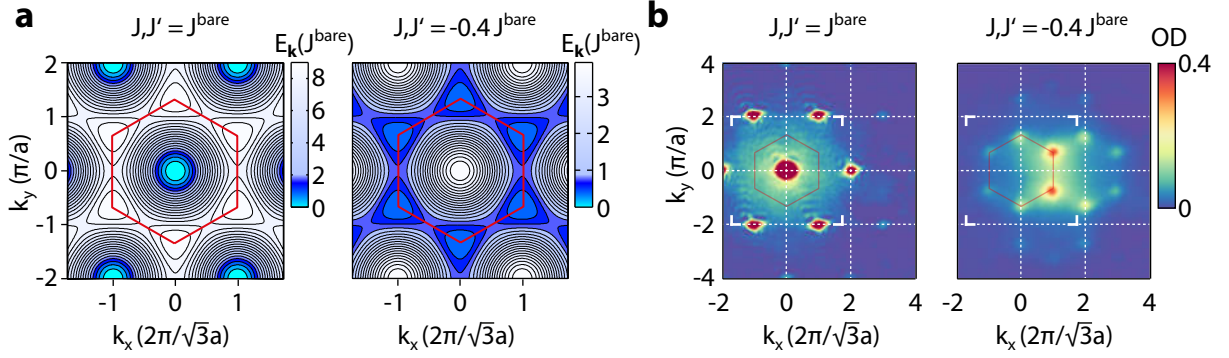


Figure 3.5: Effective dispersion relation of the driven triangular lattice. **a** The effective lowest-band energy dispersion $E_{\mathbf{k}}$ is depicted in dependence of the momenta in the lattice plane. For negative and equally strong effective tunneling matrix elements the dispersion is inverted such that minima are located at the vertices of the Brillouin zone (red hexagon). The asymmetric color map is chosen in order to emphasize the relevant minima of the dispersion. **b** Corresponding TOF-images for the two scenarios. White framing indicates the boundaries of the dispersion plot depicted in **a** and dashed lines facilitate orientation. Color coding is defined relative to the maximum value of the left TOF-image.

the symmetry of the system, the obtained renormalization is equal for the two diagonal tunneling processes. We introduce the notation for the effective tunneling processes

$$J \equiv J_{21}^{\text{eff}} \quad \text{and} \quad J' \equiv J_{32}^{\text{eff}} = J_{13}^{\text{eff}} \quad (3.50)$$

in the following and write

$$J = J_{B0}(K)J^{\text{bare}} \quad \text{and} \quad J' = J_{B0}(K')J^{\text{bare}} \quad (3.51)$$

with the dimensionless forcing parameters

$$K = \frac{F_y a}{\hbar \Omega} = \frac{m a^2}{\hbar} \nu_y \quad (3.52)$$

$$K' = \frac{a}{2\hbar \Omega} \sqrt{3F_x^2 + F_y^2} = \frac{m a^2}{2\hbar} \sqrt{9\nu_x^2 + \nu_y^2}. \quad (3.53)$$

The behavior of both independent tunneling matrix elements with respect to the amplitude of the frequency modulation is plotted in Fig. 3.4b. Obviously, tunneling along the vertical bond J is independent of ν_x as the projection onto the horizontal axis vanishes. The two diagonal bonds depend on both amplitudes ν_x and ν_y , while the renormalization along the x -direction is stronger by the factor of $\sqrt{3}$.

In this chapter we will present experiments performed in the monochromatically driven triangular lattice exclusively for isotropic effective tunneling elements, i.e., $J = J'$. Figure 3.5a depicts the effective lowest-band dispersion relation of the triangular driven lattice in the case of isotropic positive and negative effective tunneling. For the case of positive tunneling, the dispersion is similar to the lowest band shown along the path of symmetry

points in Fig. 2.6b. A single minimum is located at $\mathbf{k} = 0$ in the center of the Brillouin zone. In analogy to the one-dimensional case, the whole dispersion is inverted if the isotropic tunneling becomes negative. Energy minima are located at the six vertices of the Brillouin zone. Since each corner is shared by three Brillouin zones, a total number of two degenerate minima exist in the first Brillouin zone. The appearance of this degeneracy has a striking influence on the physical properties of the system, which will be discussed in detail in the subsequent chapter. Corresponding absorption images of the resulting momentum distributions for a superfluid state taken after 32 ms time-of-flight are shown in Fig. 3.5b. Here, data was obtained by adiabatically loading a BEC into a triangular lattice within $T_{R,\text{Lat}} = 100$ ms with a potential depth of $V_0 = 4.6 \pm 0.1 E_R$. The resulting bare tunneling rate is $J^{\text{bare}} = 4 \times 10^{-3} E_R$ and the energy gap of the undriven dispersion to the first excited band is $E_{\text{gap}} = 3.38 \pm 0.06 E_R = h \times (11.3 \pm 0.2)$ kHz. In the lattice, the driving at a frequency of $\Omega = 2\pi \times 2.791$ kHz is ramped up to its final amplitude in $T_{R,\text{drv}} = 50$ ms and maintained for approximately 3 ms. In similar fashion as in the experiments already discussed for one-dimensional driving, the total holding time is adjusted such that the center of the oscillating Wannier envelope is approximately located on the M -Point of the Brillouin zone. In Fig. 3.5b this corresponds to the momentum $k_x = 2\pi/(\sqrt{3}a)$ and $k_y = 0$. Superfluid momentum peaks are clearly visible at all minima of the effective dispersion, validating the experimental feasibility of the two-dimensional driving scheme.

3.3 Investigating strong-field excitations

In the preceding section we have demonstrated the experimental realization of monochromatic time-periodic driving schemes for one- and two dimensional lattices. An important aspect of this versatile technique is the comparatively *strong* driving of the system which was emphasized by the benchmark experiment of an increasing forcing parameter in Fig. 3.3.

As a result of the strong driving necessary for the inversion of the dispersion, lifetimes of driven systems can decrease by more than an order of magnitude (see Ref. [179]). The limitations due to detrimental excitation processes that are accompanied by a loss of coherence in the sample set an upper bound of the total experimentally accessible timescales for the coherent manipulation of ultracold ensembles. It is, thus, crucial to obtain a comprehensive, quantitative understanding of excitation processes present in strongly driven lattice systems.

On the other hand, as we will see in the following, the strong periodic driving gives rise to the possibility of studying strong field-induced *multi-photon* transitions which are hardly accessible in other physical systems. A quantitative comparison of the presented periodic driving scheme with regular light-matter interaction was discussed by Arlinghaus *et al.* [97]. As demonstrated, e.g., in Fig. 3.3, coherent manipulation of the effective dispersion of an ultracold atomic ensemble in an optical lattice is possible for values of the dimensionless forcing parameter $K = aF/(\hbar\Omega)$ of up to $K \approx 10$. This forcing strength

can be compared to the forcing arising from light matter interaction. As an analogy we consider an atom that is subjected to a strong laser field. Let a light field of photons with energies of $\hbar\omega_L = 5.0$ eV act on a hydrogen atom with a diameter of the Bohr radius. With an electric field strength of $E_L = F/e$ a forcing parameter of $K = 5$ corresponds to a total field strength of $E_L \approx 5 \times 10^{11}$ V/m which is already on the order of the electric field acting on a ground-state electron in hydrogen. In this sense, strong-field physics can be investigated with periodically forced optical lattice systems. A central aspect of such strong driving fields is the occurrence of multi-photon transitions which will be investigated here.

In the following, we employ strongly driven optical lattice systems for the study of excitation spectra of a pure model system. We identify the observed resonances with multi-photon transitions to the first excited band and compare the obtained data with *ab initio* calculations of the transition energies for one- two- and three dimensional lattice geometries.

3.3.1 Strong driving of the one-dimensional lattice

In this section we discuss experiments performed in the driven one-dimensional running-wave lattice as introduced in section 3.2.1. Data presented here has been acquired by adiabatically loading a BEC into the horizontally aligned optical lattice. The lattice potential is exponentially increased to its final value in $T_{R,\text{Lat}} = 150$ ms. Subsequently, the forcing amplitude is ramped up in $T_{R,\text{drv}} = 50$ ms and maintained for another $T_{H,\text{drv}} = 20$ ms at this amplitude. Finally, absorption images of the momentum distribution are taken after 40 ms time-of-flight.

Prior to the periodic forcing, all atoms of the optical lattice occupy the lowest energy band with band index $l = 0$ in good approximation. Multi-photon transitions to excited bands can occur if the condition

$$E_{\text{gap},l}^{\min}(\mathbf{k}) \leq n \times \hbar\Omega \leq E_{\text{gap},l}^{\max}(\mathbf{k}) \quad \text{with} \quad n \in \mathbb{N}^* \quad (3.54)$$

is fulfilled, whereby $E_{\text{gap},l}$ denotes the energy gap between the lowest and the l -th excited band. The momentum transfer of a driving photon of energy $\hbar\Omega$ onto an absorbing atom is negligible compared to the lattice momentum. Therefore, as illustrated in Fig. 3.6b, only transitions with $\Delta\mathbf{k} = 0$ have to be taken into account. The crucial aspect of excitations regarding condition (3.54) is the width of the band gap. An opening of band gaps in the one-dimensional lattice with respect to the lattice depth is already depicted in Fig. 2.2. In Fig. 3.6a the energy differences between the lowest and the first excited band are shown again in dependence of the lattice depth (considering single-photon transitions with $n = 1$) with the additional energy differences corresponding to multi-photon transitions with $n = 2, 3, \dots, 10$. We restrict the following considerations to transitions between the two lowest bands which describe the data presented here in excellent agreement. Furthermore, the increasing width of higher bands prohibits an unambiguous identification of remaining

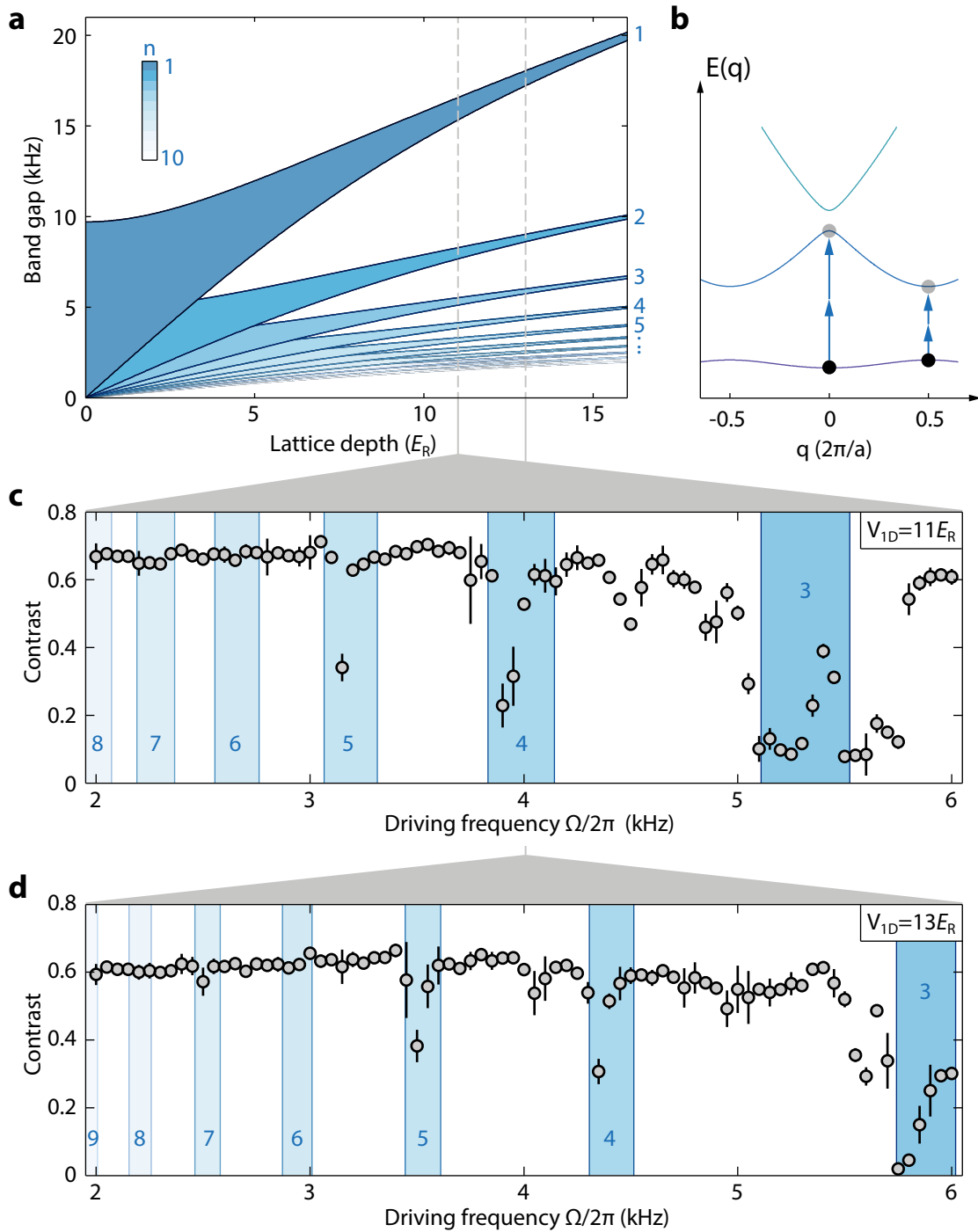


Figure 3.6: Multi-photon transitions in the one-dimensional lattice. **a** The energy gap between the lowest and first excited band ($n = 1$) is plotted in dependence on the lattice depth together with the corresponding energies for multi-photon transitions with E_{gap}/n . **b** Illustration of two-photon transitions for the maximal- and minimal band gap energies at $q = 0$ and π/a . **c** and **d** show excitation spectra obtained at lattice depths of $11 E_R$ and $13 E_R$ respectively. Blue numbers and shaded areas indicate the width and positions of multi-photon transitions obtained from *ab initio* calculations of the band structure.

features in the excitation spectra as the condition (3.54) is always fulfilled for $l > 1$ and $n \gg 1$.

In Fig. 3.6c and d, excitation spectra of the driven 1D-lattice are shown in dependence of the driving frequency for fixed lattice depths of $V_0 = 11 E_R$ and $13 E_R$ respectively. With a final forcing parameter of $K = 3.82$ the renormalizing Bessel function is at its first minimum such that the effective tunneling matrix element is $J = -0.4 J^{\text{bare}}$ as in Fig. 3.2b.

Similar to Fig. 3.3 the data points are the obtained by extracting the contrast defined in Fig. 3.2c with two decisive differences. First, the obtained signal is inverted as the original definition of the contrast would yield negative values. Secondly, the corresponding momentum peak masks are expanded to yet another order. For a lattice at rest, these third-order momentum peaks are clearly negligible concerning the limited extension of the Wannier envelope. However, as the driving frequency is changed, the Wannier envelope, oscillating with the driving frequency, is centered at different momenta. For this data set it is neither experimentally feasible nor necessary to fine-tune the holding-time $T_{H,\text{drv}}$ for each measured frequency to ensure the condition $\Delta p_x(t) = 0$ as it was done, e.g., for the data presented in Fig. 3.2 and 3.3. The extension of the peak mask merely results in a slight decrease of the total amplitude of the contrast due to a smaller relative signal of counted atoms.

In addition to the (extended) contrast data, multi-photon resonance conditions according to Eq. (3.54) are depicted in Fig. 3.6c and d by blue shaded areas. With this, excitation resonances indicated by a loss of coherence and, thus, dips in the contrast signal can be clearly identified for the cases of $n = 3, 4$ and 5 . The slight asymmetry in the resonances tending towards the lower boundary of Eq. (3.54) can be explained by the dynamics in quasimomentum space induced by the driving of the lattice. Due to the oscillation in momentum space, atoms reside for longer times at momenta close to the Brillouin zone edge where the energy gap to the first excited band is minimal for the forcing amplitude at hand (compare Fig. 3.1c). Thus, the excitation probability is higher for transition energies closer to the lower boundary. In conclusion, the resonance positions are in remarkable agreement with the multi-photon transition energies that are calculated without free parameters.

In order to obtain a deeper understanding of the behavior of such strong-field multi-photon transitions we extend the study to a variety of driving amplitudes and observe the dependence of resonances on the lattice depth. Here, the extraction of quantitatively comparable resonance data for various driving amplitudes comes with the problem of a varying contrast signal. As seen in Fig. 3.3, the contrast signal is inverted for a zero-crossing of the Bessel function when the driving amplitude is increased. Accordingly, we have inverted the signal for the data shown in Fig. 3.6. However, the contrast signal does not yield meaningful results at the zero crossing of the Bessel function where the coherence of the system is drastically reduced. We therefore define a new contrast C , as the normalized sum over a number n_{pix} of *maximum* pixels of the absorption image. Thereby, we obtain

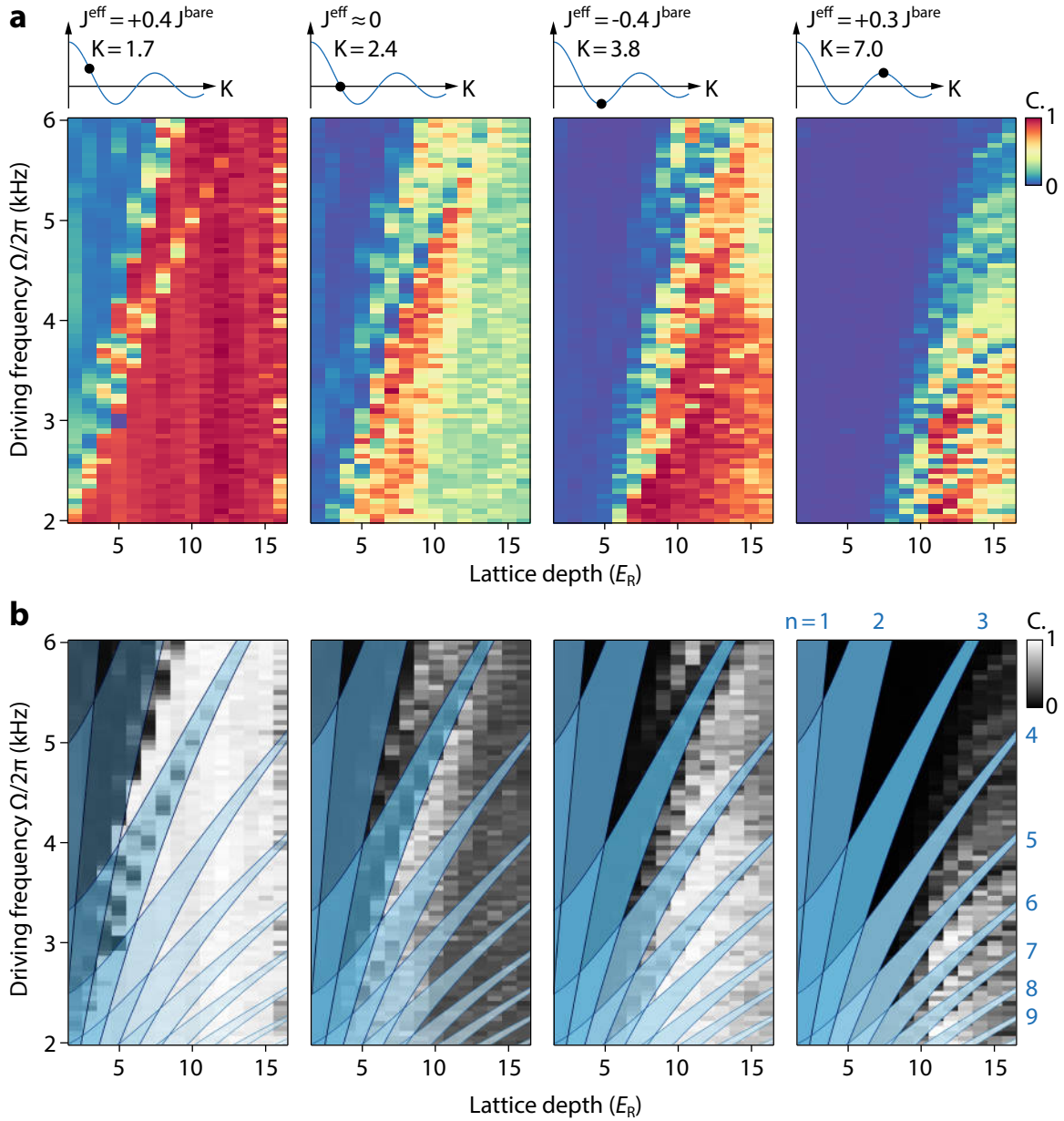


Figure 3.7: Excitation spectra of the driven 1D-lattice for increasing forcing amplitudes. **a** High contrast imaging of the normalized spectra. The forcing amplitude and corresponding tunneling matrix elements are indicated by the position of the black circles on the renormalization Bessel function. Remarkably, a well distinguishable excitation spectrum can be observed with the maximum-pixel contrast even for the case of vanishing tunneling amplitudes. **b** The same data set as in **a** is overlaid by the positions of possible multi-photon transitions. Blue numbers in the lower right corner indicate their respective order. Measured resonance positions are in excellent agreement with the *ab initio* calculations. A slight deviation towards lower transition frequencies for large lattice depths above approximately $13 E_R$ for $n \geq 4$ stem from limitations of the available lattice laser power. Note that the data set for $K = 3.8$ includes the measurements presented in Fig. 3.6.

information about the maximum optical density of the momentum distribution and, thus, the level of coherence maintained in the driven system. The robustness and applicability of this method is discussed in appendix A. Figure 3.7 shows excitation spectra of the driven 1D-lattice obtained for four different driving amplitudes of $K = 1.7, 2.4, 3.8,$ and 7.0 . Preparation and experimental procedure are similar to the data shown in Fig. 3.6. Hereby, the lattice depth has been varied from $2 E_R$ to $16 E_R$ in steps of $1 E_R$ while the driving frequency runs from 2 kHz to 6 kHz as in Fig. 3.6c and d. The maximum-pixel contrast C was extracted from each images for $n_{\text{pix}} = 3$. As this contrast signal is still much smaller for driving amplitudes corresponding to zero effective tunneling the magnitude of each data set belonging to a certain driving amplitude is additionally normalized to a maximum value of $C = 1$. The four data sets are depicted twice: In Fig. 3.7a a high-contrast color map is chosen in order to facilitate the identification of resonances while in 3.7b a conventional grayscale mapping is overlaid by the semi-transparent calculated areas of possible multi-photon transitions similar to Fig. 3.6a. Transitions are indicated in the data set of $K = 7$ according to the respective number n of involved photons. Note that the band gap boundaries were calculated with the *exact* geometric lattice parameters given in appendix D.

For increasing forcing amplitudes excitations are clearly enhanced and higher-order multi-photon resonances appear that can be unambiguously identified up to a total order of $n = 9$. The data exhibit an excellent agreement with the calculated resonance conditions. A slight deviation of the resonance positions for $n \geq 4$ at large lattice depths above $13 E_R$ towards lower excitation frequencies in the two data sets with largest forcing amplitude can be explained. In this regime, the available total laser power for the creation of the lattice potential is already limited, and can lead to a lower total lattice depth than anticipated. Measurements which are not shown here targeting even larger lattice depths confirm this trend.

In addition, the agreement of the calculated resonance positions with the observed data validates a high degree of precision of the employed calibration of the optical lattice depth which relies on parametric heating via a modulation of the lattice amplitude. As the multi-photon resonances observed here are the result of pure single-particle effects we can rule out significant masking effects due to interaction processes for the lattice calibration.

Beyond the assigned multi-photon transitions to the first excited bands weak additional transitions seem to appear for large forcing amplitudes and lattice depths in between the allowed excitation regions with $n = 3$ to 5 . Possible explanations of such features are transitions to even higher excited bands. However, due to the larger width of higher-lying bands, excitation profiles of such transitions should be very broad which does not seem to be the case here. Furthermore, high-order multi-photon transitions with $n \gg 1$ to higher bands necessarily exhibit a much smaller slope in dependence of excitation energy and lattice depth as compared to transitions to the first excited band. Considering, e.g., the additional feature in the upper right corner of the data set obtained for a forcing amplitude

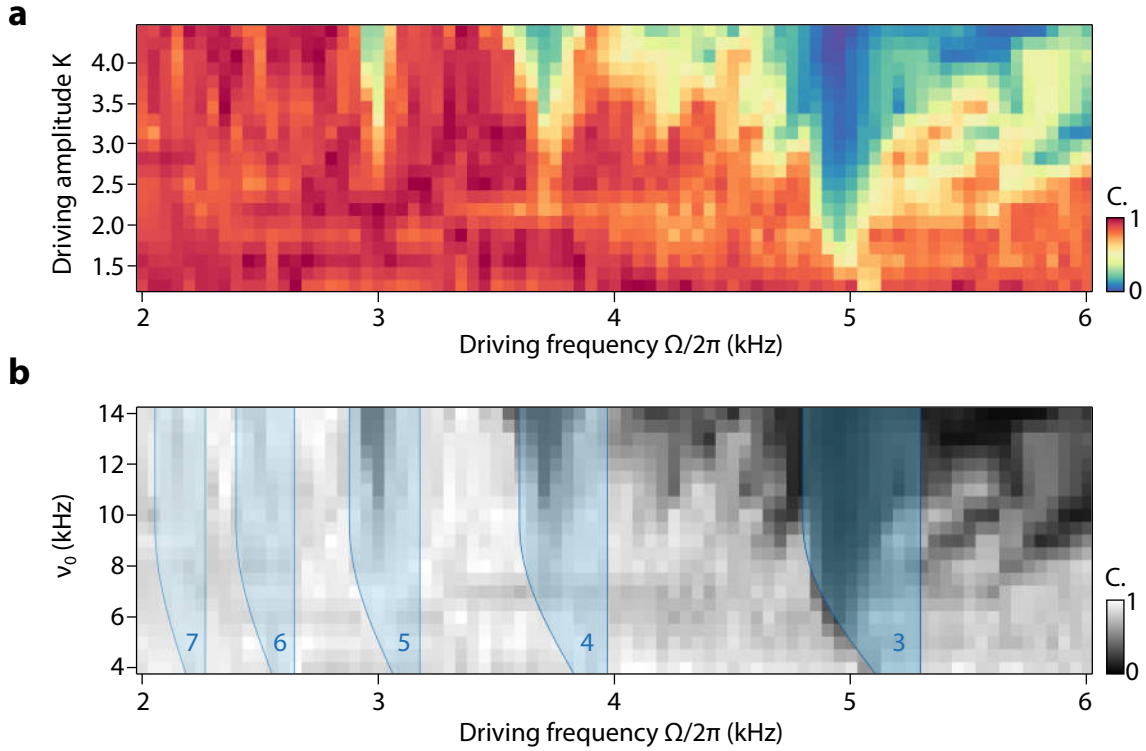


Figure 3.8: Excitation resonances in dependence of the forcing amplitude. **a** High-contrast depiction of the measured spectrum in dependence of the driving frequency and the forcing amplitude K . Data for each second value of the forcing amplitude is interpolated. The excitation spectrum exhibits a rich structure specifically for larger driving frequencies. **b** Several features of the excitation spectra - plotted here in dependence of the frequency modulation amplitude ν_0 can be assigned to multi-photon transitions to the first excited band. Blue-shaded areas indicate the forcing-dependent boundary conditions for multi-photon transitions.

of $K = 7.0$ such a behavior is not observed. Thus, the origin of these additional excitations remains an open question.

With data presented in Fig. 3.8 we continue to investigate the influence of the driving amplitude on the strong-field excitation spectra of the 1D-lattice. Here, both the driving frequency Ω and the driving amplitude K are varied for a *fixed* 1D-lattice depth of $V_0 = 10 E_R$. In analogy to Fig. 3.7 the data set is depicted twice. Note that in part **b** the forcing strength is plotted with respect to the frequency modulation amplitude ν_0 since it is the experimentally adjusted parameter. It is related to the forcing parameter via Eq. (3.40) yielding $1K = 3.18\nu_0$ (kHz). For an improved visualization of the data, every second value for the forcing amplitude is interpolated. Data points for $\nu_0 = 12$ kHz were not recorded and are also interpolated (such interpolation of data does not result in additional artificial features). Finally, unlike the previously discussed data, the maximum-pixel contrast is extracted for a large value of $n_{\text{pix}} = 10^3$ included pixels. The reason for this

rather large averaging over the maximum optical density values is a deviation of the total signal strength for each individually measured forcing amplitude. Nevertheless, the qualitative behavior of the excitation spectra remains unchanged by the inclusion of a large number of pixel values, allowing for easily comparable measurements.

Again, several resonances appearing in the obtained spectrum can be assigned to multi-photon transitions to the first excited band as indicated by the blue shaded areas in Fig. 3.8b. Since the lattice depth was not changed, the positions of such resonances remains fixed. However, condition (3.54) has to be corrected for small driving amplitudes. If the forcing is small, oscillations are limited to small quasimomenta such that particles with initial quasimomenta of $q = 0$ never reach the point of the minimum band gap energy at the edges of the Brillouin zone. This means that the lower boundary for multi-photon transitions thus depends on the forcing amplitude up to the point where the whole Brillouin zone is scanned: $E_{\text{gap}}^{\text{min}} \rightarrow E_{\text{gap}}^{\text{min}}(K)$ for values smaller than $K \approx 3.1$. Blue-shaded areas in Fig. 3.8b include the forcing-dependent lower boundary condition. Even though we have neglected the finite momentum spread of an ultracold bosonic ensemble in the considerations of the forcing-dependent boundary condition, the shape of the resonance with $n = 3$ follows the lower boundary. A widening of the resonance can be observed for increasing driving amplitude. Additional excitation features that are clearly visible for large forcing amplitudes and driving frequencies, however, remain to be understood.

3.3.2 Excitation spectra of the triangular lattice

The striking influence of an elliptical periodic driving scheme on the triangular lattice has already been introduced in section 3.2.2. In chapters 4 and 5 experiments relying on periodic driving of the triangular lattice are presented. For such experiments, a precise knowledge of the corresponding excitations arising in the strong-field limit from periodic driving is a crucial prerequisite. In the following, we thus extend the investigation of excitation spectra to the triangular three-beam lattice and discuss the results in view of further experiments.

Similar to the data shown in Fig. 3.5 the driving is adjusted such that the tunneling renormalization isotropic, i.e., effective tunneling along all lattice bonds amounts to $J, J' = -0.4J^{\text{bare}}$. Here, the final lattice depth ranges from 2 to $6 E_R$. With the shallow confinement along the third axis, the atomic ensemble forms an array of elongated cigar-shaped tubes. Subsequently, the two frequency modulation amplitudes ν_x and ν_y are linearly increased over a ramping time of $T_{R,\text{drv}} = 50$ ms to values of 4.96 kHz and 8.59 kHz respectively. Driving is maintained at these amplitudes for another 2 ms. Hence, the driving timescales are considerably shorter as compared to the driving in the one-dimensional lattice. This choice takes account for the significantly reduced total lifetime of the driven system in the triangular lattice. At a maximum forcing amplitude of $K = 3.83$ it is on the order of 10 ms [155, 179].

In Fig. 3.9 the excitation spectrum of the driven triangular lattice is depicted for values

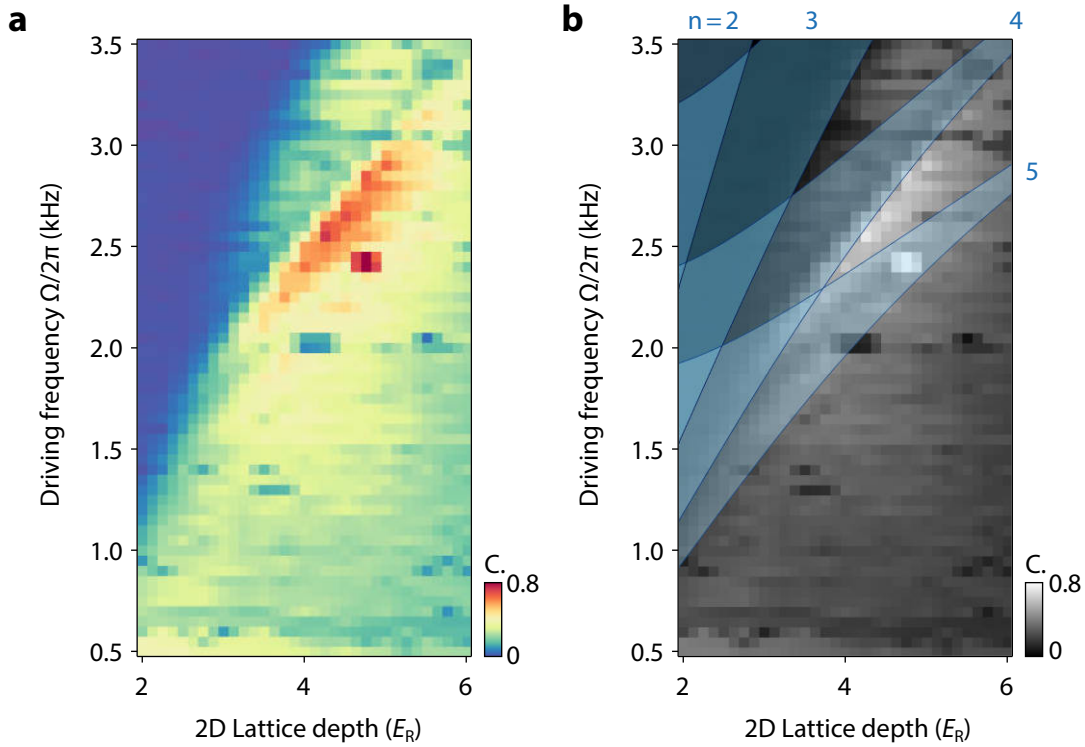


Figure 3.9: Driving resonances in the triangular lattice in dependence of the lattice depth and the driving frequency. Every second value of the lattice depth is interpolated to improve visualization. **a** The excitation spectrum exhibits clearly distinguishable resonance features and a narrow parameter region with a high degree of maintained coherence. **b** Resonances can be assigned with excellent agreement to multi-photon transitions up to the order of $n = 5$.

of the driving frequency between 0.5 and 3.5 kHz. Data was obtained by extracting the maximum-pixel contrast for $n_{\text{pix}} = 3$ from absorption-images taken after 40 ms time-of-flight. The total value of the whole spectrum is normalized to values between 0 and 1. In order to improve the visualization of the observed behavior, the upper bound color axis is limited to 0.8 and data is interpolated for each second value of the triangular lattice depth. Similar to the running-wave 1D-lattice, excitations can be assigned with excellent agreement to multi-photon transitions up to an order of $n = 5$ as depicted in 3.9b. Again, the band gap energies were calculated with the exact lattice parameters given in appendix D. Note that the second and third bands lie closely together in the triangular lattice (compare Fig. 2.5). For the calculation of the minimum and maximum band gap energies, only the second band was considered.

In contrast to the one-dimensional case, however, resonances appear to be narrower as the boundary conditions for multi-photon resonances suggest. This is the case even though the whole Brillouin zone is already scanned for the modulation amplitudes at hand. A possible explanation might again be the varying times that particles in momentum space

are present at different band gap energies and the much shorter total duration of the forcing procedure.

An important feature of the excitation spectrum is the narrow region between the $n = 4$ and $n = 5$ where the periodic driving yields high values of the pixel contrast and, thus, a large degree of maintained coherence of the atomic ensemble in the effective dispersion relation. The time-of-flight image for negative effective tunneling depicted in Fig. 3.5b was obtained precisely in this parameter region. The restriction of the accessible parameter space is a valuable insight for experiments relying on the coherent manipulation of ultracold atomic ensembles in engineered effective dispersion relations in general. Further experiments in the triangular lattice as discussed in the subsequent two chapters were performed exclusively in this parameter region. In particular, such restrictions in the parameter space of periodic driving play a crucial role for experiments presented in chapter 5.

3.3.3 Periodic driving in the 3D-lattice

As discussed in chapter 2, the three-beam lattice can be superimposed with an additional retro-reflected one-dimensional lattice in order to form a three-dimensional lattice system by slicing up the elongated condensate tubes. The 3D-lattice is an important prerequisite for the study of strongly correlated many-body systems with a small number of particles per lattice site. A paradigm example of the application of periodic driving to such systems is the mapping to the so-called *quantum XY model* [140] that will be discussed in chapter 5.

Three dimensional driven systems have been realized, e.g., by Zenesini *et al.* [95] where cubic lattices formed by three perpendicular pairs of counterpropagating laser beams was sinusoidally modulated with piezoelectric actuators in order to drive the quantum phase transition from a superfluid to a Mott-insulating state. In contrast, we perform periodic driving solely in the triangular lattice in the presence of the additional perpendicular *static* lattice. The study of the coherence properties of the driven three-dimensional lattice system serves as a benchmark for the reaching of the strongly correlated regime in tailored effective dispersion relations.

Figure 3.10 shows a comparison of excitation spectra obtained in the triangular lattice with- and without the presence of an additional perpendicular 1D-lattice. For both cases, the three-beam lattice was exponentially ramped to a final value of $V_0 = 4.5 E_R$ in 50 ms. Here, the driving amplitude was linearly increased in 5 ms and maintained for another 5 ms at a fixed driving frequency of $\Omega = 2\pi \times 2.55$ kHz. In analogy to the two-dimensional driven triangular lattice, the short ramping procedure was chosen to take account for the lifetime of the coherently engineered superfluid state in the three-dimensional lattice which is limited to the order of a few ms. For black data points in Fig. 3.10, the additional 1D-lattice was exponentially ramped up *prior* to the ramping of the three beam lattice to a potential depth of $V_{0,1D} = 30 E_R$ in 500 ms. With this large potential depth, tunneling

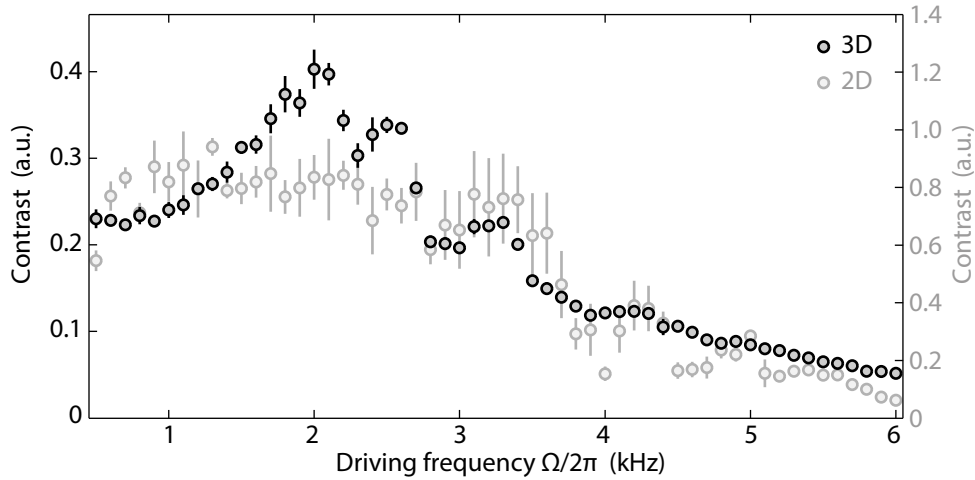


Figure 3.10: Comparison of driving in the 2D- and 3D lattice. Excitation spectra obtained by the maximum-pixel contrast for n_{pix} for the triangular three-beam lattice are depicted with (black data points) and without (gray data points) an additional perpendicular 1D-lattice. The absolute level of coherence is significantly lowered by the presence of an additional lattice along the line of sight. However, the qualitative behavior of both spectra is quite similar. Error bars denote the standard deviation.

processes between the formed layers are suppressed for experimentally relevant timescales.

The extreme difference between the two investigated many-body systems manifests itself in a large difference of the absolute value of the contrast extracted from the TOF-images while the qualitative behavior of the excitation spectrum remains relatively similar for both cases. However, by comparing the spectra above driving frequencies of 3.5 kHz, it is evident that several clearly distinguishable multi-photon resonances in the two-dimensional lattice are not resolved in the three-dimensional system. This circumstance can be attributed to the fact that the total duration of forcing was chosen to be substantially shorter in the three-dimensional case.

In principle, additional excitations resulting from the periodic forcing in the lattice plane could appear due to the fact that the 1D-lattice is not aligned precisely perpendicular to the three-beam lattice plane but encloses a horizontal angle of approximately 2° with the z -axis (Note that this inclination is intended in order to avoid the appearance of super-lattices due to residual reflections at surfaces of the science cell.) Nevertheless, the projection of the forcing onto the 1D-lattice, i.e., the sine of the inclination angle, yields a negligible amount of the forcing amplitude $K_\perp \approx 0.1$ along this direction, such that additional multi-photon resonances bridging the large 1D-lattice band gap of $E_{\text{gap}}^{1\text{D}} = 32$ kHz can be ruled out.

In Fig. 3.11 we verify the assumption of negligible excitations in the perpendicular lattice further by investigating the excitation spectra of the driven 3D-lattice in dependence

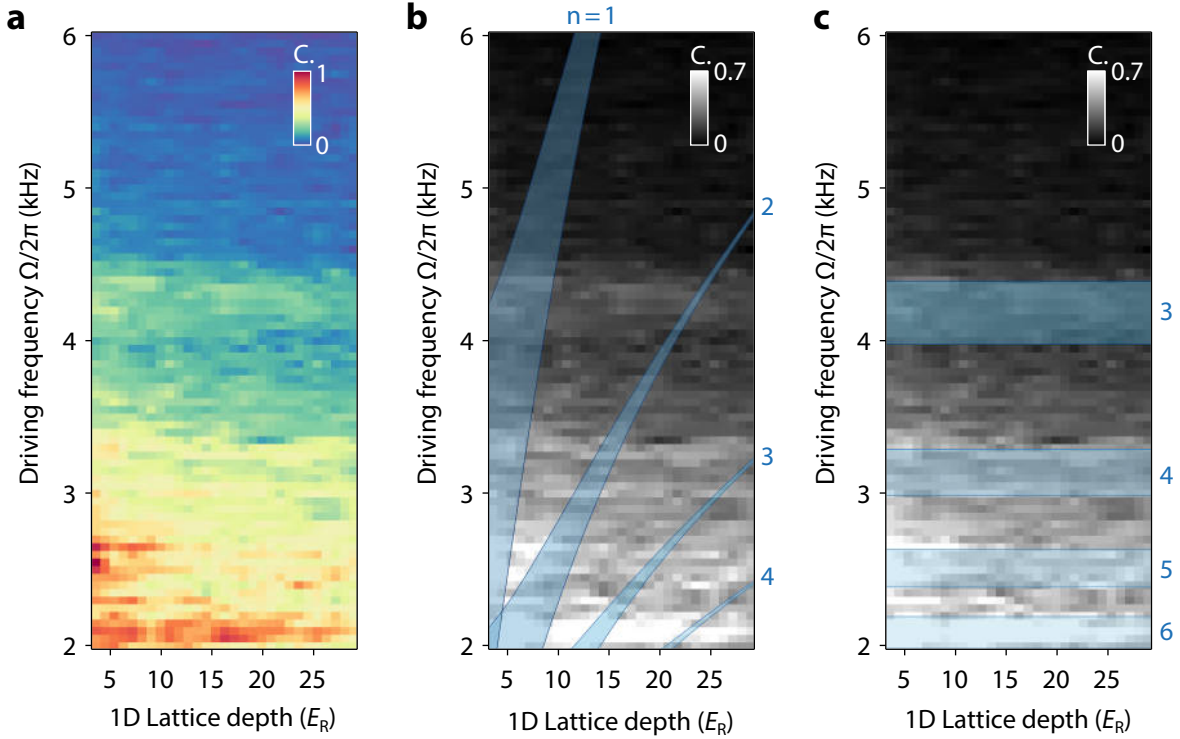


Figure 3.11: Excitation spectrum of the three-dimensional lattice in dependence of the driving frequency and the one-dimensional lattice depth. For an improved visualization, every second value of the 1D-lattice depth is interpolated. The excitation spectrum depicted in **a** appears to be constant with respect to the 1D-lattice depth. Transitions to excited bands of the additional lattice as indicated by blue-shaded areas in **b** are not observed while the congruence with in this case constant transitions in the triangular lattice is also less clear as shown in **c**.

of the 1D-lattice depth while the triangular lattice depth is held fixed at $V_0 = 4.25 E_R$. Clearly, as shown in 3.11b the excitation spectrum does not show the characteristic excitation spectrum corresponding to multi-photon transitions for the one-dimensional lattice. In contrast to the behavior of the excitation spectrum with respect to the triangular lattice depth (compare Fig. 3.9), the excitation spectrum retains its shape for a varying 1D-lattice depths.

In Fig. 3.11c, a comparison of the excitation spectrum to possible multi-photon transitions in the triangular lattice is shown. Apparently the observed resonances are shifted in this case, which can be attributed to interaction effects in the now strongly confined three-dimensional system.

As the main result of the measurements in Fig. 3.11 we can clearly state that no additional driving excitations arise due to the presence of a strong 1D-lattice on the comparatively short timescales investigated here. Limitations arising from the short lifetime and low level of coherence in the strongly confined driven three-dimensional lattice will be of importance for experiments presented in chapter 5.

3.4 Conclusion & outlook

To conclude, we have verified the experimental technique of time-periodic lattice driving for the engineering of effective tunneling matrix elements. With this, both driving in the running-wave 1D-lattice and the triangular lattice allows for the coherent engineering of an effective time-averaged dispersion relation. We have furthermore established an analog of periodic lattice driving to strong-field processes arising from a comparison of the forcing amplitude to the strength of light-matter interactions. In accordance with this notion we indeed observe multi-photon transitions up to an order of $n = 9$ that are in excellent agreement with corresponding energies calculated without free parameters. While these results connote an important prerequisite for the accessible parameter space of experiments discussed in the following, additional features in the excitation spectra as well as the influence of excitations in a strongly interacting three-dimensional lattice have yet to be fully understood.

4 Engineering artificial gauge fields

Here, we experimentally realize complex-valued tunneling matrix elements in optical lattices by a time-asymmetric far off-resonant driving technique that allows for the emulation of artificial gauge fields. The feasibility of this approach is verified with excellent agreement to *ab initio* calculations in a proof-of-principle experiment on a one-dimensional lattice. We extend the concept to the triangular lattice, creating fully tunable gauge invariant staggered fluxes. This system represents the geometrically frustrated Ising-XY model that constitutes a generic spin model involving two coupled symmetries. Their associated order parameters are derived and analyzed with respect to the staggered flux strength and the temperature of the atomic ensemble.

The concept of gauge fields was first introduced in the context of classical electrodynamics. Since then, a large variety of accurate theories have been developed in many branches of physics that rely on gauge-invariances and their underlying symmetries. Ultracold quantum gases provide an ideal testing ground for the study of gauge fields in specifically tailored scenarios.

For the investigation of ultracold quantum many body systems comprised of neutral atoms in analogy to charged particles, it is necessary to artificially engineer the effects of electric or magnetic fields. In this chapter we present an experimentally feasible method for the creation of fully tunable gauge fields in driven optical lattice systems. By engineering complex-valued tunneling matrix elements it is possible to adjust the corresponding phases, the so called Peierls phases, to all possible values ranging from 0 to 2π . In comparison to techniques relying on laser-assisted tunneling processes, this far off-resonant driving allows for the creation of an easily adjustable strength of the artificial gauge field. In order to validate our approach, we extract the value of the Peierls phase on a one-dimensional lattice in excellent agreement with *ab initio* calculations.

We extend the driving technique to the triangular lattice realizing the geometrically frustrated XY model. Here, the combination of Peierls phases for each individual lattice plaquette gives rise to staggered magnetic fluxes. With an elementary flux quantum per lattice plaquette the strength of the artificial magnetic field corresponds to the strong field regime. We observe a (spontaneous) symmetry breaking between the two-fold degeneracy of ground states in the case of maximal staggered field strengths. Furthermore, this discrete \mathbb{Z}_2 - or Ising symmetry can be broken on purpose by tuning the staggered flux strength. We investigate the Ising order parameter with respect to the flux and entropy of the system. A statistical data analysis reveals a thermally driven phase transition from

an ordered ferromagnetic- to an unordered paramagnetic state.

With the long-range phase coherence in accordance with Bose-Einstein condensation, the system also exhibits a spontaneously broken continuous $U(1)$ symmetry. Observed changes in the long-range phase coherence in dependence of the staggered flux strength hint towards a strong coupling of both the $U(1)$ and the \mathbb{Z}_2 order parameters.

Parts of this chapter have been published in [1] and [3] as well as in the PhD thesis of J. Struck [155]. Experiments presented here were performed within the team of J. Struck, C. Ölschläger, J. Simonet and M. Weinberg. Analysis of data depicted in Fig. 4.3 and 4.4 was performed by C. Ölschläger.

4.1 Realization of tunable Peierls phases

In the preceding chapter we have introduced the concept of monochromatic far off-resonant driving in order to manipulate tunneling matrix elements. In the following, we will generalize this approach to more complicated driving schemes allowing for the engineering of complex-valued tunneling parameters that emulate the presence of vector gauge potentials.

4.1.1 Peierls substitution in the tight-binding model

In electromagnetism, the kinetic part of the Hamiltonian for a particle with charge q is modified in the presence of the vector potential $\mathbf{A}(\mathbf{r})$ according to

$$\frac{1}{2m}\hat{\mathbf{p}}^2 \rightarrow \frac{1}{2m}(\hat{\mathbf{p}} - q\mathbf{A}(\mathbf{r}))^2. \quad (4.1)$$

This purely quantum mechanical influence of the vector potential is impressively demonstrated by the Aharonov-Bohm effect, where the phase of a particle's wave function is altered despite no residual electromagnetic fields being present along its path [98, 99]. In close resemblance, the effect of a gauge potential acting on a charged particle in a tight binding lattice can be described in the framework of the so-called *Peierls substitution* [200]. The Peierls substitution replaces real-valued tunneling matrix elements with complex ones

$$J_{ij} \rightarrow |J_{ij}| e^{i\theta_{ij}} \quad (4.2)$$

where the Peierls phase θ_{ij} between the lattice sites with indices i and j is connected to the vector gauge potential via the integral

$$\theta_{ij} = \frac{q}{\hbar} \int_{\mathbf{R}_j}^{\mathbf{R}_i} \mathbf{A}(\mathbf{r}) d\mathbf{r}. \quad (4.3)$$

As the acquired phase is not independent of the path taken by the particle, the integral is evaluated along the straight lattice bond connecting the two sites. In analogy to Eq. (4.1)

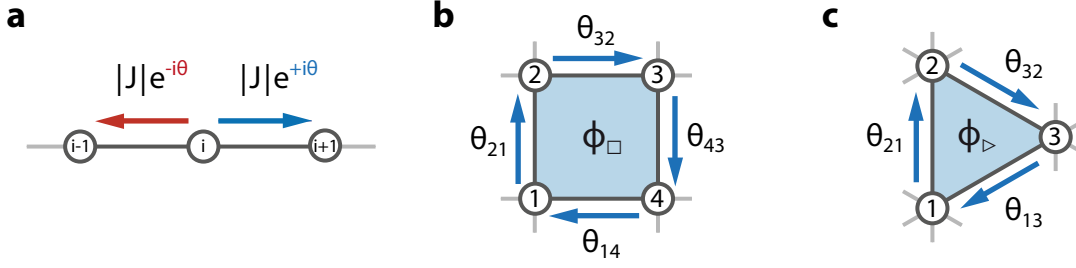


Figure 4.1: Illustration of Peierls phases and gauge invariant fluxes. **a** Complex-valued tunneling matrix elements introduce a directionality to the tunneling. For each tunneling process from site j to site i , a phase of θ_{ij} is imprinted onto particle's wave function. A gauge invariant quantity is given by the fluxes through elementary lattice plaquettes, shown here for **b** a square lattice and **c** a triangular lattice. The figure was modeled after Ref. [155].

the kinetic part of the Bose-Hubbard Hamiltonian from Eq. (2.20) is altered due to the complex tunneling:

$$\hat{\mathcal{H}}_{\text{BH}} = - \sum_{\langle i,j \rangle} |J_{ij}| \left(e^{i\theta_{ij}} \hat{b}_i^\dagger \hat{b}_j + e^{i\theta_{ji}} \hat{b}_j^\dagger \hat{b}_i \right) + \frac{U}{2} \sum_i \hat{n}_i (\hat{n}_i - 1). \quad (4.4)$$

Hence, the presence of a gauge field causes a directionality of tunneling processes with the trivial exceptions of $\theta_{ij} = 2\pi \times n, n \in \mathbb{Z}$. As depicted in Fig. 4.1a, tunneling in opposite directions inverts the Peierls phases, such that

$$\theta_{ji} = -\theta_{ij}. \quad (4.5)$$

The values of the Peierls phases depend on the specific gauge chosen, i.e., a global phase of the wave function. For a one-dimensional lattice the introduction of Peierls phases leads to a global shift of the dispersion relation. Here, a specific gauge, i.e., a suitable choice of the reference frame, can always be found that counteracts this shift.

In contrast, as illustrated in Fig. 4.1b and c, lattices of higher dimensionality exhibit a gauge invariant quantity: the magnetic flux Φ of a field $\mathbf{B}(\mathbf{r})$ through an elementary lattice plaquette \mathcal{P} . In accordance with Stokes' theorem it is given by the sum over all Peierls phases around a lattice plaquette

$$\Phi_{\mathcal{P}} = \frac{q}{\hbar} \iint_{S_{\mathcal{P}}} \mathbf{B}(\mathbf{r}) dS_{\mathcal{P}} = \frac{q}{\hbar} \oint_{\mathcal{P}} \mathbf{A}(\mathbf{r}) d\mathbf{r} = \sum_{\mathcal{P}} \theta_{ji} \quad (4.6)$$

where $S_{\mathcal{P}}$ denotes the surface of the plaquette and we have used $\mathbf{B}(\mathbf{r}) = \nabla \times \mathbf{A}(\mathbf{r})$.

Having established the connections between gauge fields, Peierls phases and the complex tunneling parameters we can, so to say, put the cart before the horse: in the following, we will discuss how to create complex-valued tunneling matrix elements in optical lattices by employing the far off-resonant driving techniques introduced in the preceding chapter. This allows us to directly engineer the Hamiltonian (4.4) and, thus, use neutral ultracold atoms in order to emulate the effects of an artificial gauge field $\mathbf{A}(\mathbf{r})$ acting on charged particles.

4.1.2 Symmetry constraints of the forcing

In section 3.1.3 we have derived a general expression of the renormalized effective tunneling matrix element for arbitrary forcing (see Eq. (3.30)). In order to obtain complex-valued tunneling, the imaginary part of Eq. (3.30) must not vanish, i.e.,

$$\text{Im} \left(J_{ij}^{\text{eff}} / J_{ij}^{\text{bare}} \right) = \frac{1}{T} \int_0^T \sin \left(W_{ij}(t) / \hbar \right) dt \neq 0. \quad (4.7)$$

This condition is only fulfilled if the underlying driving functions $v_{ij} \equiv v_i - v_j$ introduced in Eq. (3.22) break two fundamental symmetries: the shift (anti)symmetry

$$v_{ij}(t) = -v_{ij}(t - T/2) \quad \forall t \quad (4.8)$$

with respect to the driving period $T = 2\pi/\Omega$ and the reflection-, or time-reversal symmetry

$$v_{ij}(t - \tau) = v_{ij}(-t - \tau) \quad \forall \tau \in [0, T[. \quad (4.9)$$

In the case of a rigid lattice potential, the above conditions necessarily apply to the forcing function itself as the $v_{ij}(t)$ denotes the forcing projected onto the lattice vectors [1, 155]. However, this is only the case for a rigid lattice potential. In general, lattice geometries with time-dependent bonds can also be generated, e.g., by shifting superlattices with respect to each other [2]. In chapter 7 we will briefly discuss another approach for the creation of time-dependent lattice bonds. Experiments presented in this chapter, however, are restricted to rigid lattice potentials.

In order to break both symmetries in Eq. (4.8) and (4.9), a forcing function inevitably exhibits more than a single Fourier component. Hence, driving schemes leading to complex-valued tunneling can be labeled as *multichromatic* forcing in contrast to the purely sinusoidal- or *monochromatic* forcing employed in experiments that were presented in the preceding chapter. As the driving itself still relies on the strong-field like forcing of the system, the accessible parameter regime lacking multi-photon resonances is more restricted as compared to monochromatic driving schemes.

4.1.3 Complex-valued tunneling in the one-dimensional lattice

In the following, we demonstrate the realization of a fully tunable vector gauge potential by engineering complex-valued tunneling parameters in the one-dimensional running-wave lattice.

With the constraints on the driving scheme established in the previous section, we choose a function that is comprised of a train of sinusoidal pulses. It is defined over a period as

$$F_x(t) = \begin{cases} F_0 \sin(\Omega_1 t) & \text{for } 0 < t < T_1 \\ 0 & \text{for } T_1 < t < T. \end{cases} \quad (4.10)$$

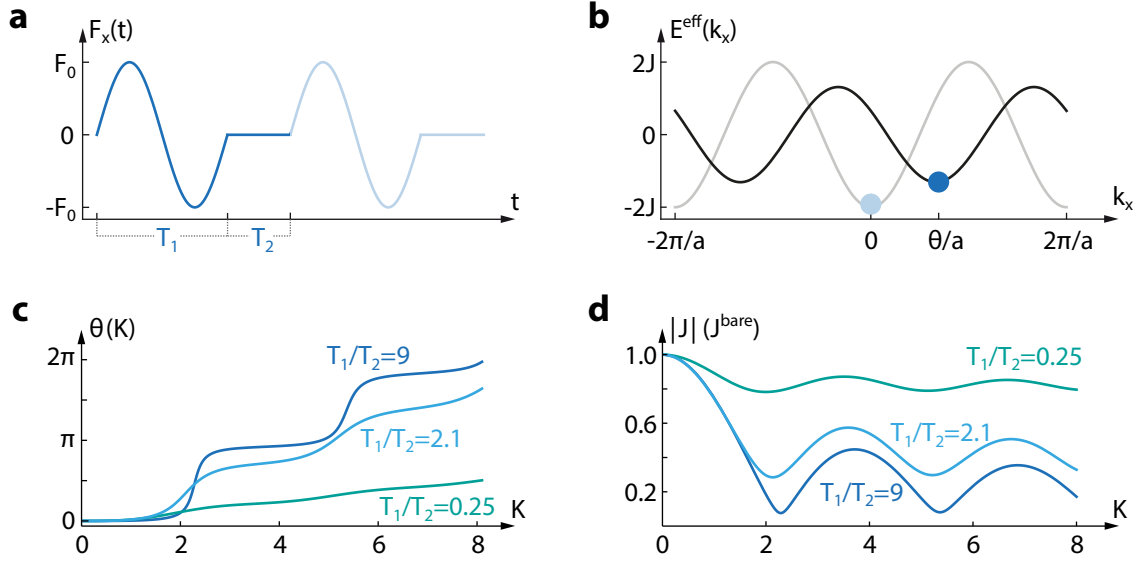


Figure 4.2: Engineering of Peierls phases by asymmetric driving. **a** A forcing function comprised of trains of sine pulses allows for the creation of complex-valued tunneling matrix elements on a one-dimensional lattice. **b** A finite Peierls phase θ results in the shift of the dispersion relation by θ/a . The asymmetry parameter T_1/T_2 modifies the behavior of tunneling renormalization both for **c** the Peierls phase and **d** the total tunneling amplitude. The figure is modeled after Ref. [1] and appears in similar fashion in Ref. [4]. The plots in **c** and **d** have been calculated by J. Struck.

As depicted in Fig. 4.2a, $T_1 = 2\pi/\Omega_1$ is the period of the sine pulse. T_2 denotes the time separating the sine pulses where no force is applied to the system. Accordingly, $T = T_1 + T_2$ is the total period of the forcing function. It is straightforward to verify that the forcing (4.10) breaks the two symmetry conditions (4.8) and (4.9), thus allowing for the generation of complex-valued tunneling. Even though this forcing function has an infinite number of Fourier components, the amplitude of higher-order components decreases rapidly such that unwanted multi-photon transitions for these frequencies only occur with negligible probability.

The resulting renormalization of the tunneling matrix elements can be derived with the above forcing function according to Eq. (3.30), leading to

$$\frac{J_{i,i-1}^{\text{eff}}}{J_{\text{bare}}} = \frac{T_2}{T} e^{+iKT_1/T} + \frac{T_1}{T} e^{-iKT_2/T} J_{B0}(K), \quad (4.11)$$

where again K is the dimensionless forcing parameter and $J_{B0}(K)$ denotes the zeroth-order Bessel function as in the monochromatic case. For the case of $T_2/T \rightarrow 0$ the monochromatic driving as described in chapter 3 is recovered. A thorough calculation of the effective renormalized tunneling elements and the frequency modulation of the laser beams corresponding to the forcing function in Eq. (4.10) can be found in Ref. [155]. The directionality of the tunneling is indicated by the indices in $J_{i,i-1}^{\text{eff}}$, describing the tunneling from the

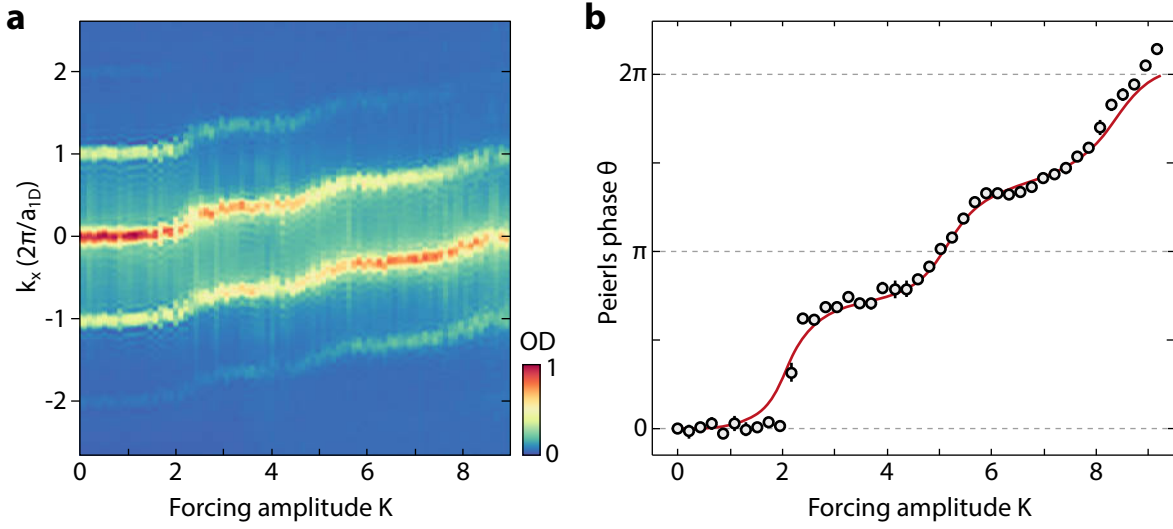


Figure 4.3: Realization of a fully tunable Peierls phase in the one-dimensional lattice. **a** Row-sums of the momentum distribution of the 1D-lattice after time-of-flight. An increase of the asymmetric forcing amplitude results in a shift of quasimomentum peaks. **b** Values of the Peierls phase θ (black data points) extracted from the images in **a** span the full range between 0 and 2π and exhibit an excellent agreement with *ab initio* calculations of the expected value (solid line). Error bars denoting the standard deviation of data almost entirely lie within the data points. Similar figures appear in Refs. [1], [4] and [155].

$(i - 1)$ -th to the i -th lattice site. Tunneling in the opposite direction is described by the complex-conjugate of the expression (4.11). In the following we write

$$J_{\rightarrow} \equiv J_{i,i-1}^{\text{eff}} \quad \text{and} \quad J_{\leftarrow} \equiv J_{i,i+1}^{\text{eff}} \quad (4.12)$$

for tunneling processes to the right and left respectively (compare to Fig. 4.1a). We define the Peierls phase θ as the argument of tunneling to the right:

$$\theta = \arg(J_{\rightarrow}), \quad (4.13)$$

such that the effective Bose-Hubbard Hamiltonian (4.4) simplifies to

$$\hat{\mathcal{H}}_{\text{BH}} = -|J| \sum_i \left(e^{+i\theta} \hat{b}_i^\dagger \hat{b}_{i-1} + e^{-i\theta} \hat{b}_i^\dagger \hat{b}_{i+1} \right) + \frac{U}{2} \sum_i \hat{n}_i (\hat{n}_i - 1). \quad (4.14)$$

In the above equation we have used the fact that the amplitude of the directional tunneling is always equal for both directions, hence, $|J_{\rightarrow}| \equiv |J_{\leftarrow}| \equiv |J|$.

As depicted in Fig. 4.2c and d, the renormalization of the tunneling matrix element depends heavily on the asymmetry parameter T_1/T_2 of the sine pulse forcing. While for large values $T_1/T_2 \gg 1$ the Peierls phase is modulated strongly with increasing forcing parameter K , the absolute value of the tunneling decreases. In the opposite case of shorter

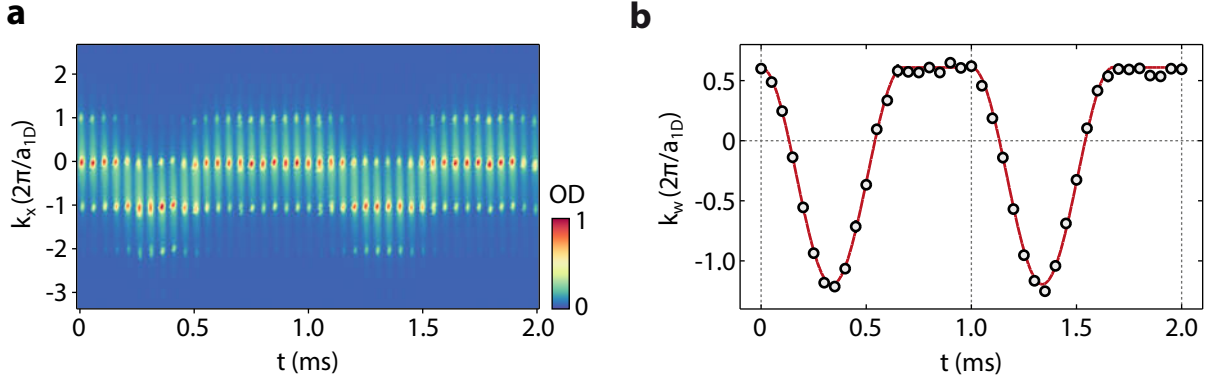


Figure 4.4: Time-resolved measurement of the momentum distribution over two complete driving cycles. **a** Momentum distribution of atoms depicted as a succession of TOF-images rather than row-sums. While the Wannier envelope oscillates, the positions of the quasimomentum peaks remain fixed. **b** Extracted time-dependent position of the Wannier envelope (black data points) with a standard deviation denoted by error bars that lie almost always within the data points. The theoretically expected behavior is indicated by the solid line. A similar figure is also depicted in Ref. [155] and in the supplementary material of Ref. [1].

sine pulses and longer resting times, or $T_1/T_2 < 1$ the tunneling amplitude remains relatively constant with respect to the forcing amplitude. However, tuning of the Peierls phase to comparable values requires stronger forcing parameters. In order to span the full parameter range for the Peierls phase between 0 and 2π while avoiding large heating losses accompanied by strong forcing amplitudes we compromise between the two extremes to a value of $T_1/T_2 = 2.1$ (see Fig. 4.2).

Experiments presented in the following are performed in the one dimensional running-wave lattice similar to the monochromatic forcing scheme discussed in chapter 3. A BEC confined in the elliptical dipole trap (see section 2.2.4) is loaded into the lattice with a final lattice depth of $V_0 = 10 \pm 1 E_R$. Here, the tight-binding conditions are well satisfied and the bare tunneling amplitude amounts to $J^{\text{bare}} = 0.7 \times 10^{-2} E_R$. With a minimal energy gap between the two lowest bands of $E_{\text{gap}} = h \times 14.4 \text{ kHz}$ the driving frequency is set to $\Omega = 2\pi \times 1 \text{ kHz}$, corresponding to a forcing period of $T = 1 \text{ ms}$.

In the lattice, the driving amplitude is ramped to its final value in 120 ms and retained for another 20 ms before all trapping potentials are switched off and absorption images of the resulting momentum distribution are taken after 27 ms time-of-flight. Hereby, the ramping of the forcing amplitude $K(t)$ is adjusted such that it partially compensates the nonlinearity of the Peierls phase $\theta(K)$ depicted in Fig. 4.2c.

In section 3.1.1 we have already argued that the presence of a finite Peierls phase results in a shift of the effective dispersion relation

$$E^{\text{eff}}(k) = -2|J^{\text{eff}}| \cos(ak - \theta) \quad (4.15)$$

as illustrated in Fig. 4.2b. We investigate the shift of the dispersion minima with respect

to the forcing parameter K in Fig. 4.3. The positions of the superfluid quasimomentum peaks at the minima of the effective dispersion is depicted as row-sums over the obtained TOF images in Fig. 4.3a. They directly relate to the Peierls phase introduced via the lattice driving according to $k_{\min} = \theta/a$. In Fig. 4.3b the Peierls phases, extracted by Gaussian fits of the momentum peaks to the row sums of the TOF images, are plotted in dependence of the forcing amplitude in the full range of possible values $\theta \in [0, 2\pi[$. The obtained data show an excellent agreement with the theoretically expected value that is calculated without free parameters. A systematic deviation for small driving amplitudes around $K = 2$ can be understood by means of a dynamical instability of the system at a critical quasimomentum. The dynamical response of the system to the asymmetric driving scheme is described in detail in Ref. [1]. Special emphasis on the understanding of the dynamical instability arising for a critical quasimomentum is given in Ref. [155]. As sharp momentum peaks are visible in the data presented in Fig. 4.3a up to a forcing parameter of $K = 9$, we can conclude that the asymmetric driving scheme does not result in significant heating processes. Note that the discussed scheme even allows for the tuning of the Peierls phase way beyond values of 2π for even stronger forcing without a significant loss of coherence. However, as these values have no physical meaning, such measurements are not discussed here.

In order to rule out time-dependent shifts of the quasimomentum peaks due to the forcing, a time-resolved measurement of the momentum distribution for a fixed forcing parameter is presented in Fig. 4.4. Spanning two complete driving cycles, it is clearly demonstrated by the TOF-data depicted in Fig. 4.4a that the positions of the quasimomentum peaks remain constant while the Wannier envelope oscillates, subjected to the momentum change $\Delta p_x(t)$ (compare Eq. (3.33)). The extracted time-dependent position of the Wannier envelope $k_w(t)$, obtained by a broad Gaussian fit to the row-sum of the images is plotted in Fig. 4.4b. It shows an excellent agreement with the theoretically expected behavior according to $k_w(t) = k_0 + \Delta p_x(t)/\hbar$, proving that the superfluid system accurately responds to the inertial forcing of the lattice.

4.2 Tunable gauge-invariant fluxes on the triangular lattice

In the preceding section we have proven the experimental feasibility of engineering complex valued tunneling matrix elements in optical lattices by multichromatic time-periodic driving. The Peierls phase could be continuously tuned over the full range between 0 and 2π . In the following, we will extend this technique to the triangular lattice, allowing for the generation of artificial staggered magnetic fields.

The presence of Peierls phases in two dimensional Bravais lattices is already sketched in Fig. 4.1b and c. As a gauge invariant quantity, the sum of Peierls phases around a lattice plaquette \mathcal{P} corresponds to a magnetic flux $\Phi_{\mathcal{P}}$. From the directionality of the

complex tunneling created by periodic lattice driving according to Eq. (4.5) it is immediately evident that the summation over pairwise-parallel plaquette bonds as in the square lattice (Fig. 4.1b) always leads to a vanishing flux through the plaquette. In contrast, the summation of Peierls phases around a triangular lattice plaquette (Fig. 4.1c) can result in a finite magnetic flux, as the plaquette bonds are not parallel.

This can be understood in terms of a symmetry argument: as the described global periodic driving of the rigid lattice potential does not break the translational symmetries of the Bravais lattices and thus, the induced magnetic flux through a primitive lattice cell must vanish. Unlike in the square lattice, the primitive cell of the hexagonal Bravais lattice consists of two lattice plaquettes (see Fig. 2.4), namely one triangle pointing leftwards and one pointing rightwards, the flux through a single plaquette can have a non-zero value as long as the flux in the complementary plaquette exhibits the same flux amplitude but opposite sign. The result is a *staggered* magnetic flux pattern maintaining the periodicity of the underlying Bravais lattice.

In recent years, many efforts for the creation of homogeneous fluxes in optical lattice systems have been made in order to, e.g., study the quantum Hall regime with ultracold atomic model systems. Such a *rectification* of staggered fluxes mostly rely on laser-assisted tunneling processes as, e.g, in [120, 121, 201]. However, more sophisticated periodic driving schemes involving the time-dependent breaking of lattice symmetries by superlattice potentials may also allow for the creation of homogeneous fluxes or different topological band structures [2]. In the following, we demonstrate the creation of artificial staggered magnetic fluxes on a triangular lattice by using global time-asymmetric periodic lattice driving similar to the scheme discussed in the foregoing sections.

4.2.1 Time-asymmetric elliptical forcing

In analogy to the elliptic driving scheme introduced in section 3.2.2 we choose the following forcing function

$$\mathbf{F}(t) = -F_x \cos(\omega t) \hat{\mathbf{e}}_x - F_y \left(\sin(\Omega t) + \delta \sin(2\Omega t) \right) \hat{\mathbf{e}}_y \quad (4.16)$$

with a corresponding frequency modulation of two of the three lattice beams

$$\delta\nu_{2,3} = \pm \sin(\Omega t) \nu_x + \left(\cos(\Omega t) + \delta \cos(2\Omega t)/2 \right) \nu_y. \quad (4.17)$$

The forcing is similar to the purely elliptical one except for the additional first higher-harmonic term $\delta \sin(2\Omega t)$. A control parameter of $\delta \neq 0$ breaks the two symmetry conditions in Eq. (4.8) and (4.9), thus, enables the creation of complex-valued tunneling along the lattice bonds. The time averaging integrals for the tunneling renormalization according to Eq. (3.30) can only be solved numerically. Similar to the monochromatic driving of the triangular lattice, the renormalization is always equal for the diagonal plaquette bonds. Hence, we simplify the notation of the Peierls phases along the lattice bonds depicted in

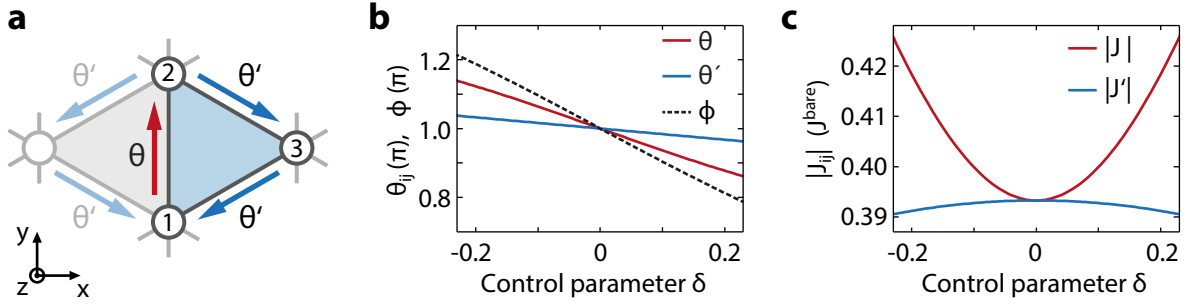


Figure 4.5: Peierls phases and fluxes on the triangular lattice. **a** Illustration of Peierls phases on a primitive cell of the triangular lattice. **b** Numerically calculated values of the two independent Peierls phases and the staggered flux strength in dependence of the control parameter δ introduced in Eq. (4.16) and (4.17) for forcing parameters of $K = K' \approx 3.62$. **c** Corresponding absolute values of the independent renormalized tunneling matrix elements J and J' . Parts **b** and **c** of the figure are also featured in Ref. [155] and the supplementary material of [3].

Fig. 4.1c to

$$\theta \equiv \theta_{21} \quad \text{and} \quad \theta' \equiv \theta_{32} = \theta_{13} \quad (4.18)$$

in accordance with the notation of J and J' given in Eq. (3.50) and Fig. 3.4a. With this, the flux through a lattice plaquette is given by

$$\Phi_{\triangleright} = \theta_{21} + \theta_{32} + \theta_{13} = \theta + 2\theta' = -\Phi_{\triangleleft}, \quad (4.19)$$

where Φ_{\triangleright} and Φ_{\triangleleft} denote the flux through the rightwards and leftwards pointing triangular lattice plaquettes respectively. As the relation $\Phi_{\triangleright} = -\Phi_{\triangleleft}$ holds, we refer to the magnetic flux as the flux strength $\Phi \equiv \Phi_{\triangleright}$ in the following. In Fig. 4.5a the defined Peierls phases are illustrated again for a primitive lattice cell consisting of both rightwards and leftwards pointing lattice plaquettes. Fig. 4.5b and c depict the numerically calculated behavior of the Peierls phases θ, θ' , the flux strength Φ and the amplitude of the renormalized tunneling matrix elements $|J|$ and $|J'|$.

Experiments presented in the following were all performed in a triangular lattice with a lattice depth $4.6 \pm 0.1 E_R$. Perpendicular to the lattice plane, only the weak harmonic trapping confinement was present. The corresponding bare single-particle tunneling rate is $J^{\text{bare}} = 4 \times 10^{-3} E_R$. In this regime, the ensemble is in a superfluid state with a well defined quasimomentum. We drive the system with a frequency of $\Omega = 2\pi \times 2.791$ kHz (and its first higher-harmonic of 2Ω). With a minimal energy gap of $E_{\text{gap}} = h \times (11.3 \pm 0.2)$ kHz between the two lowest bands the choice of the driving frequency results only in minimal heating processes due to multi-photon resonances. In the lattice, the two driving amplitudes K and K' introduced in Eq. (3.52) and (3.53) are linearly increased within $T_{R,\text{drv}} = 50$ ms to a final value of both $K = K' \approx 3.62$. Note that, in the limit of vanishing forcing asymmetry $\delta \rightarrow 0$, the chosen value of the homogeneous driving corresponds to the first

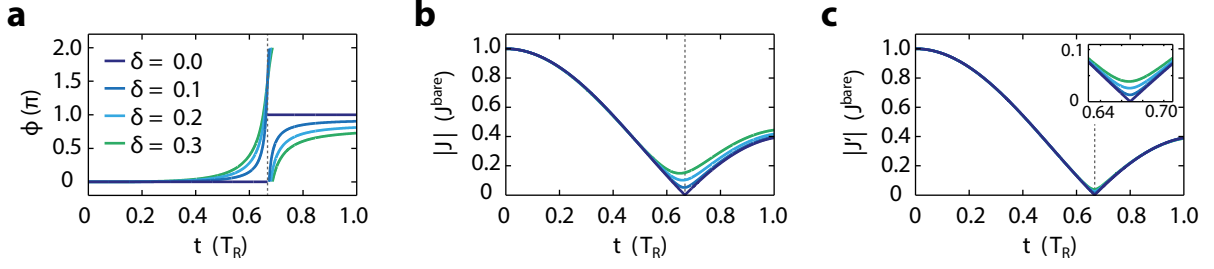


Figure 4.6: Time-resolved evolution during the ramping procedure of the asymmetric forcing. During the linear increase of the forcing parameters to their final values of $K, K' \approx 3.62$ both the staggered flux strength shown in (a) and the magnitudes of the tunneling parameters J shown in b and J' shown in c vary strongly. All parameters are plotted for varying control parameter δ . Vertical dashed lines mark the sudden jump of the flux strength at the zero-crossing of the renormalization Bessel function for the case of $\delta = 0$. The inset in c magnifies the behavior of $|J'|$ in the vicinity of the minima. The figure is also featured in Ref. [155] and the supplementary material of [3].

minimum of the renormalizing Bessel function. Driving is maintained at the maximum amplitudes for a few milliseconds, before all trapping potentials are suddenly switched off and absorption images are taken after 32 ms time-of-flight.

The time-resolved behavior of the magnetic flux strength Φ and the magnitudes of the two independent tunneling parameters $|J|$ and $|J'|$ during the ramping procedure is shown in Fig. 4.6 for different values of the control parameter δ . Due to the linear increase of the driving amplitudes, all parameters vary strongly during the ramp. In particular, the tunneling magnitudes decrease strongly before recovering to the final value around $|J|, |J'| \approx 0.4J^{\text{bare}}$. Vanishing tunneling rates are accompanied with diverging timescales of the system. Hence, the ramping process is highly non-adiabatic and coherence is completely lost during the increase of the forcing parameters as the dispersion becomes completely flat. However, for increasing tunneling amplitudes atoms fully recondense into a superfluid state at the newly formed minima of the inverted dispersion until the ramping procedure is finished.

The control parameter δ is experimentally varied over a small parameter range $\delta \in [-0.2, +0.2]$. As depicted in Fig. 4.5c, the final amplitudes $|J|$ and $|J'|$ of the effective tunneling matrix elements only deviate by a few percent within this range.

For the present lattice depth the system is well approximated by the tight binding limit. Here, the effective dispersion relation including the presence of Peierls phases reads

$$E^{\text{eff}}(\mathbf{k}) = -2J \cos(\mathbf{d}_1 \mathbf{k} - \theta) - 2J' \cos(\mathbf{d}_2 \mathbf{k} - \theta') - 2J' \cos(\mathbf{d}_3 \mathbf{k} - \theta'), \quad (4.20)$$

where we have defined the lattice bonds \mathbf{d}_i forming a clockwise path around a rightward pointing triangular plaquette as

$$\mathbf{d}_1 = -\mathbf{a}_1, \quad \mathbf{d}_2 = \mathbf{a}_2, \quad \text{and} \quad \mathbf{d}_3 = \mathbf{a}_1 - \mathbf{a}_2 \quad (4.21)$$

with the Bravais lattice vectors given in Eq. (2.30).

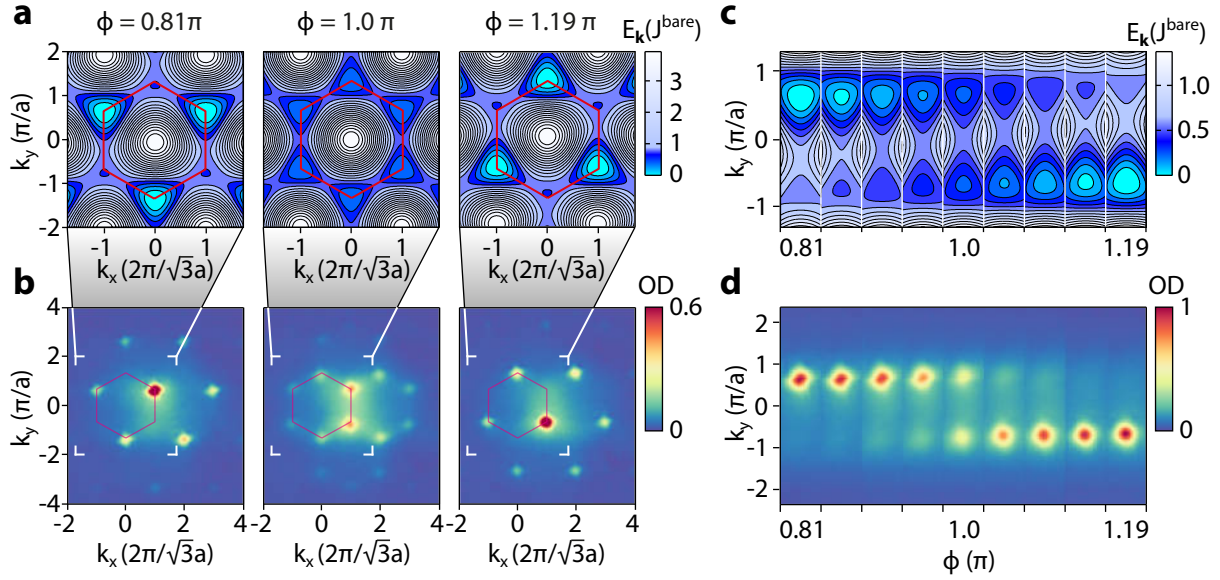


Figure 4.7: Tunability of staggered fluxes. **a** Calculated tight-binding dispersion relation for three values of the staggered flux strength according to Eq. (4.20). The red hexagon indicates the borders of the first Brillouin zone. Either one of the degenerate minima at the vertices of the Brillouin zone can be favored for a flux strength different from π . **b** Corresponding TOF-images averaged over approximately 200 experimental realizations for the three flux strengths. The white framing indicates the region of the dispersion plotted in **a**. For all images the Wannier envelope is centered at approximately $k_x = 2\pi/\sqrt{3}a$ and $k_y = 0$. The optical density is scaled with respect to the maximum value of the three shown images. In **c** and **d**, a section of the calculated dispersion and the corresponding TOF-images around the two minima of the Brillouin zone along $k_x = 2\pi/\sqrt{3}a$ is plotted for different values of the flux strength. Similar depictions are shown in Ref. [3] and [155].

4.2.2 Tuning of staggered fluxes

The deformation of the two-dimensional effective dispersion relation resulting from the driving has been depicted already in Fig. 3.5 for the homogeneous case of $\delta = 0$ and $\theta = \theta' = \pi$. Here, the dispersion is exactly inverted, resulting in two degenerate minima at the vertices of the first Brillouin zone. On average, both minima are equally populated as indicated by the averaged absorption image in Fig. 4.7b. However, single-shot measurements reveal a statistically fluctuating occupation, favoring either one of the two minima. This peculiar behavior will be discussed in detail in the following section.

The introduction of complex-valued tunneling to the system with a nonzero value of the control parameter δ allows for the tuning of the flux strength away from its maximum value of π . For a flux strength of $\Phi \neq \pi$ the degeneracy of the two minima is lifted, resulting in a global- and a metastable minimum as depicted for reduced fluxes of $\phi = (1 \pm 0.19)\pi$ in Fig. 4.7a that arise for a control parameter of $\delta = \pm 0.2$. As can be seen from the corresponding averaged TOF-images shown in Fig. 4.7b, atoms only occupy the global

minimum of the dispersion. However, in the intermediate regime of flux strengths close to π , significant occupations of the metastable minima can also be observed which result from the non-adiabatic ramping process. In Fig. 4.7c and d, the tunability of the flux strength and the corresponding occupations of the two minima in the first Brillouin zone are demonstrated. Data are shown close to the Brillouin zone edge at $k_x = 2\pi/\sqrt{3}a$. The slight distortion of the superfluid momentum peak occupying the upper minimum for $\Phi < \pi$ in Fig. 4.7d is an artifact of image processing: for an improved visualization, the initial TOF-images were tilted by approximately 2° due to an imperfection in the imaging setup. The occupation of the two minima is in good agreement with the expected shape of the band structure.

4.3 Emulation of the Ising-XY model

In the previous section we have demonstrated the tunability of the staggered flux strength Φ in a triangular lattice. The resulting dispersion relation exhibits two degenerate minima for the homogeneous case of $\Phi = \pi$ which correspond to two energetically equivalent configurations of the staggered flux pattern (see Fig. 4.8). This symmetry is broken for flux strengths differing from π where either one of the flux configuration is energetically favorable as one of the minima becomes a global minimum. We will, thus, investigate the relevant symmetries of the staggered-flux system in the following.

4.3.1 Mapping to the classical XY model

The driven system is well described by the time-averaged effective Bose-Hubbard Hamiltonian of Eq. (4.14) as the presence of the triangular lattice with only weak perpendicular confinement results in an array of elongated tubes. Additional spatial degrees of freedom have been omitted in Eq. (4.14) under the assumption of phase stiffness for each lattice site. This implies that each lattice site i can be described in terms of the number-phase representation of a coherent state

$$\langle \hat{b}_i \rangle = \sqrt{N_i} e^{i\varphi_i} \quad (4.22)$$

which is characterized by its well-defined phase φ_i and the on-site particle number N_i . In the case of equal effective tunneling matrix elements, i.e., for a homogeneous forcing with $\delta = 0$ and Peierls phases of $\theta = \theta' = \pi$, the energy of the entire system in this regime can be expressed in terms of the local phases of the coherent state as

$$E(\{\varphi_i, N_i\}) = - \sum_{\langle i,j \rangle} J_{ij} \sqrt{N_i N_j} \cos(\varphi_j - \varphi_i) + \frac{U}{2} \sum_i \hat{n}_i(\hat{n}_i - 1) + \sum_i \epsilon_i \hat{n}_i. \quad (4.23)$$

The local phases correspond to two-dimensional vector spins $\mathbf{s}_i \equiv (\cos \varphi_i, \sin \varphi_i)$ which represent classical vector spins in the sense that they can continuously point in any direction within the xy -plane [96, 155]. The Thomas-Fermi density distribution of the atomic

ensemble in the harmonic trap together with the density-weighting of spins in Eq. (4.23) results in a reduced influence of spins close to the lattice boundary. This fading-like effect allows the approximation of the energy expression with a homogeneous counterpart: Substituting the site-dependent particle numbers N_i with a homogeneous mean particle number per lattice site \bar{N} while neglecting the on-site interaction term and the external potential results in an energy expression of

$$E_{\text{XY}}(\{\varphi_i\}) = -2\bar{N} \sum_{\langle i,j \rangle} J_{ij} \mathbf{s}_i \cdot \mathbf{s}_j. \quad (4.24)$$

This so-called classical XY model also serves as an intuitive illustration of the long-range ordered phase distribution of the atomic ensemble in the superfluid regime: for the case of a homogeneous Peierls phase of π , i.e., negative effective tunneling matrix elements J_{ij} throughout the lattice, the local phases (XY-spins) minimize their energy by aligning at an angle of 180° with respect to each other. Such an alternating pattern resembles the Néel ordering of antiferromagnetically interacting spins which is present in the case of negative absolute tunneling in the one-dimensional lattice as discussed in chapter 3 (see Fig. 3.2). However, the antiparallel Néel-alignment of vector spins is inhibited in the triangular lattice: While pairs of adjacent lattice sites tend to align antiparallel, this condition cannot be satisfied for all bonds of the triangular lattice plaquette at the same time. Such a conflict between the minimization of energy and constraints imposed on the system due to the lattice geometry is known as *geometrical frustration*.

As illustrated in Fig. 4.8b, the resulting ground state of long-range phase ordering in the fully frustrated triangular lattice is a compromise: all XY-spins arrange at an angle of 120° with respect to each other. This ground state is doubly degenerate, corresponding to the two possible staggered flux patterns discussed before. Again, by tuning the staggered flux strength away from its maximum value of π , the degeneracy is lifted and one of the phase configurations becomes energetically favorable.

Already for real-valued tunneling matrix elements the mapping of local phases to the XY-vector spins enables the investigation of magnetism in a rich phase diagram: As the vector spins can be treated as classical magnets, the independent tunability of tunneling parameters allows for the emulation of ferromagnetic and antiferromagnetic interactions along the lattice bonds leading to a large variety of spin configurations and phase transitions [96].

4.3.2 Symmetries of the Ising-XY spin model

It is straightforward to show that the Hamiltonian (4.4) is invariant under the global transformation

$$\hat{b}_i \rightarrow \hat{b}_i e^{i\gamma} . \quad (4.25)$$

In terms of the XY-spin representation discussed previously, this transformation corresponds to a rotation of each spin $\{\varphi_i\} \rightarrow \{\varphi_i + \gamma\}$ by an arbitrary angle γ . Such a

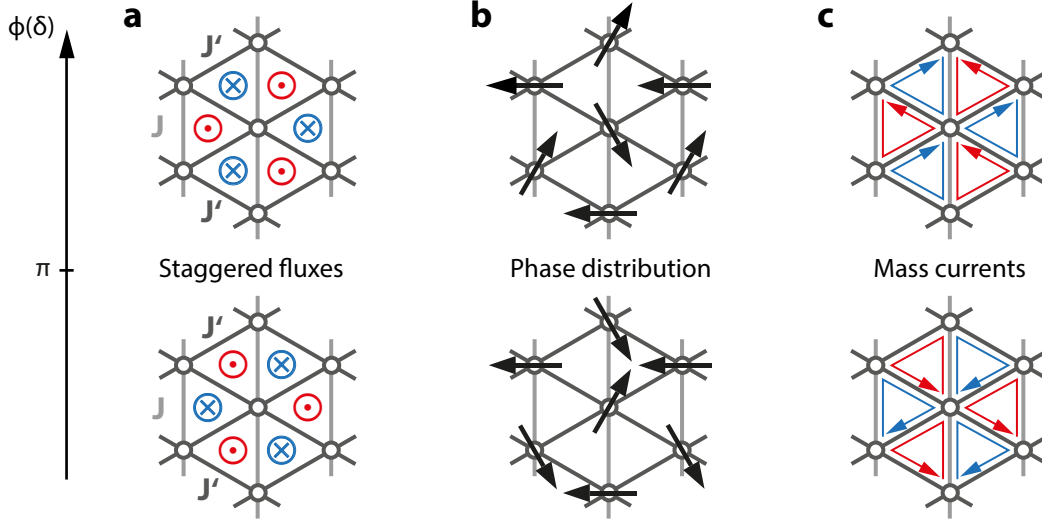


Figure 4.8: Staggered fluxes and order parameters of the coupled Ising-XY model on the triangular lattice. **a** The control over the staggered flux strength Φ enables the breaking of the discrete \mathbb{Z}_2 symmetry. Only for flux strengths of $\Phi = \pi$ the two configurations of the staggered fluxes are degenerate. **b** Resulting long-range ordered phase distribution of the on-site wave functions in the XY-vector spin representation as the order parameter of the continuous $U(1)$ symmetry. **c** Corresponding cyclotron-like mass currents with a discrete \mathbb{Z}_2 , or Ising symmetry. Blue and red arrows indicate the alternating pattern of clockwise and anticlockwise flowing currents. Similar figures appear in Ref. [3] and [155].

continuous rotational, or $U(1)$ symmetry is spontaneously broken at the onset of Bose-Einstein condensation where the local phases φ_i acquire a fixed, long range order. We define this long-range phase coherence as the order parameter for the quantification of the $U(1)$ symmetry.

A second symmetry is present in the system for the case of a staggered flux strength of $\Phi = 0$ or π : the Hamiltonian (4.4) is invariant under a local inversion transformation

$$\hat{b}_i \rightarrow \hat{b}_i^\dagger \quad (4.26)$$

which corresponds to a local inversion of all phases $\{\varphi_i\} \rightarrow \{-\varphi_i\}$. This discrete \mathbb{Z}_2 , or Ising symmetry is broken for flux strengths differing from 0 or π as the kinetic part of the Bose-Hubbard Hamiltonian transforms as

$$\hat{\mathcal{H}}'_{\text{BH}} \stackrel{\hat{b}_j \rightarrow \hat{b}_j^\dagger}{=} - \sum_{\langle i,j \rangle} |J_{ij}| \left(e^{-i\theta_{ij}} \hat{b}_i^\dagger \hat{b}_j + e^{+i\theta_{ji}} \hat{b}_j^\dagger \hat{b}_i \right) \quad (4.27)$$

where we have used the bosonic commutation relation and the directionality $\theta_{ji} = -\theta_{ij}$ of the complex tunneling. Hence, the local inversion leads to an inversion of the Peierls phases and, thus, an inversion of the staggered flux.

An order parameter quantifying the \mathbb{Z}_2 symmetry of the system is closely related to the staggered gauge fluxes: The conflict between the imprinted Peierls phases θ_{ij} and the orientation of the XY-spins results in a mass current \hat{j}_{ij} along each lattice bond given by

$$\langle \hat{j}_{ij} \rangle = -\frac{2|J_{ij}|}{\hbar} \text{Im} \left(e^{i\theta_{ij}} \langle b_i^\dagger b_j \rangle \right) \quad (4.28)$$

$$= -\frac{2|J_{ij}|}{\hbar} \sqrt{N_i N_j} \sin(\theta_{ij} + \varphi_j - \varphi_i). \quad (4.29)$$

The derivation of the above expression relies on the evaluation of the current operator with the Ehrenfest theorem applied to the Bose-Hubbard Hamiltonian (4.4) [155]. In the triangular lattice this results in a staggered pattern of cyclotron-like mass currents around each lattice plaquette as depicted in Fig. 4.8c. These currents exhibit a well-defined chirality of either clockwise or anti-clockwise orientation for the rightwards and leftwards pointing triangular plaquettes respectively. The total staggered current \mathcal{J}_{tot} of the lattice system is then given by

$$\langle \mathcal{J}_{\text{tot}} \rangle = \frac{2|J|}{\hbar} \sum_s^M \sum_{i=1}^3 \langle \hat{j}_{\mathbf{d}_i} \rangle. \quad (4.30)$$

In the above equation the first summation is carried out over all lattice sites M . The second summation denotes the clockwise summation of the mass current over the three plaquette bonds \mathbf{d}_i as defined in Eq. (4.21). Furthermore, we have assumed isotropic tunneling amplitudes $|J_{ij}| = |J|$ for simplicity [3]. By evaluating Eq. (4.30) for the current operator expressed in terms of a basis in reciprocal space the total mass current \mathcal{J}_{tot} can be linked to the experimentally observed time-of-flight momentum distribution of the atomic ensemble:

$$\langle \mathcal{J}_{\text{tot}} \rangle = \frac{2|J|}{\hbar} \sum_{\mathbf{k}} \langle \tilde{n}_{\mathbf{k}} \rangle \mathcal{X}(\theta, \theta', \mathbf{k}) \quad (4.31)$$

with the momentum-space observable $\langle \tilde{n}_{\mathbf{k}} \rangle$ and a weighting function in momentum space $\mathcal{X}(\theta, \theta', \mathbf{k})$ depending on both independently engineered Peierls phases:

$$\mathcal{X}(\theta, \theta', \mathbf{k}) = \sin(\mathbf{d}_1 \mathbf{k} - \theta) + \sin(\mathbf{d}_2 \mathbf{k} - \theta') + \sin(\mathbf{d}_3 \mathbf{k} - \theta'). \quad (4.32)$$

The derivation of Eq. (4.31) and (4.32) is thoroughly described in the PhD thesis of J. Struck [155]. Examples of the gauge-dependent weighting mask $\mathcal{X}(\theta, \theta', \mathbf{k})$ for three different staggered flux strengths are shown in Fig. 4.9 for a section in momentum space that corresponds to the evaluated absorption images.

With the experimentally observable expression of the total mass current we have acquired an order parameter of the discrete \mathbb{Z}_2 symmetry: the chirality, or handedness of the cyclotron mass currents around each triangular lattice plaquette. The ordering of alternating fluxes, namely clockwise for rightwards pointing plaquettes and anticlockwise for

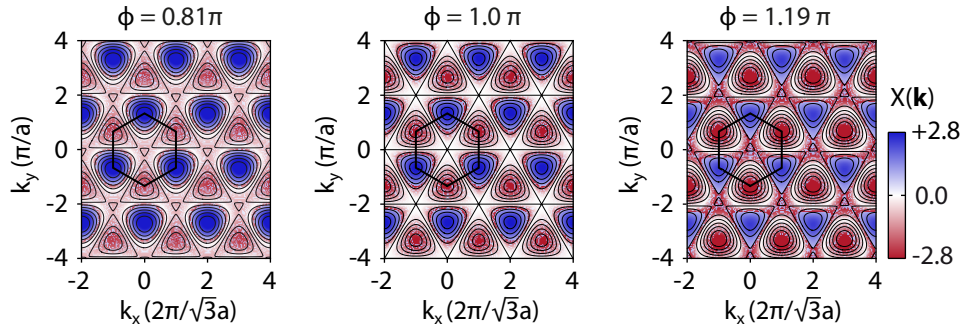


Figure 4.9: Gauge-dependent weighting mask of the total staggered mass currents evaluated for three different flux strengths. The depicted section in momentum space corresponds to the evaluated region of absorption images. In analogy to Fig. 3.5 and 4.7 the black hexagon indicates the borders of the first Brillouin zone. A similar figure is presented in Ref. [155].

leftwards pointing plaquettes or vice versa defines the orientation of an Ising-type spin. Similar to the staggered flux pattern, the two possible orientations of cyclotron currents are degenerate for the case of a maximum flux strength of π . By tuning the flux away from π , the Ising symmetry can be broken on purpose.

The relation between the local phase ordering, the Peierls phases and the cyclotron currents indicated by Eq. (4.29) suggests a strong link between the continuous $U(1)$ and the discrete \mathbb{Z}_2 symmetries. Due to the mapping of the phases onto classical XY-spins and the Ising-type \mathbb{Z}_2 order parameter, the tunable staggered flux system can be regarded as a coupled Ising-XY spin model.

4.3.3 Thermally driven phase transition

For the case of classical XY models on geometrically frustrated lattice systems the question whether the discrete \mathbb{Z}_2 and the continuous $U(1)$ symmetries are broken simultaneously and, thus, whether the two corresponding phase transitions occur at the same temperature has been controversially debated for the case of two-dimensional systems [202–210] as already pointed out in Ref. [3] and [155]. Here, the breaking of the continuous $U(1)$ symmetry is described by a Berezinsky–Kosterlitz–Thouless transition that is characterized by a diverging correlation length. Only very recently, two closely lying but separated phase transitions could be resolved by Monte-Carlo simulations of fully frustrated two-dimensional lattice systems [211, 212].

In the following, we will, thus, investigate properties of the Ising-XY model with special emphasis on the continuous $U(1)$ and the discrete Ising symmetry under a thermally driven phase transition. For this purpose, we observe the behavior of the two order parameters under the influence of a varying flux strength for three values of entropy.

The initial entropy of the system is adjusted by leaving the atomic ensemble in the optical lattice for three hold times of $t_1 = 0$ ms, $t_2 = 80$ ms and $t_3 = 160$ ms prior to the

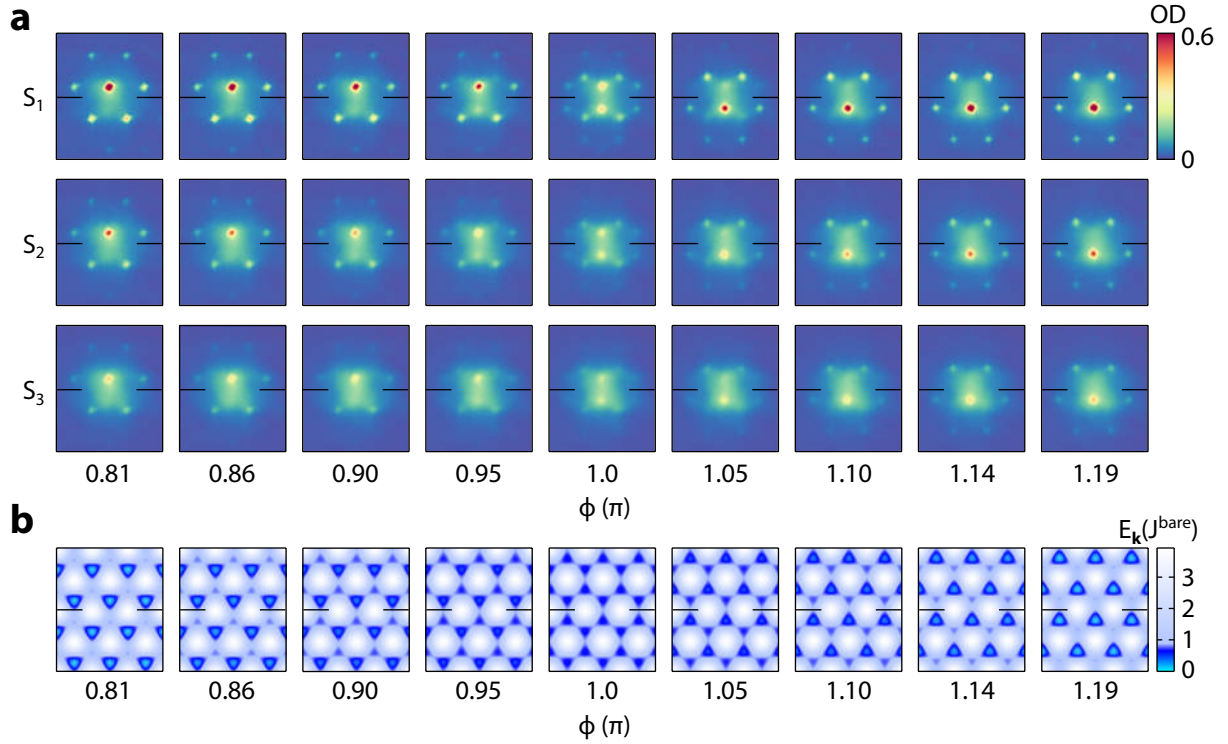


Figure 4.10: Measurement series for increasing entropy. **a** Time-of-flight absorption images for increasing initial entropy $S_1 < S_2 < S_3$ and different values of the staggered flux strength Φ . Each image consists of an average of approximately 200 individual measurements. **b** Calculated tight-binding dispersion relation for the different values of the staggered flux strength. Horizontal lines in the images serve as a guide to the eye for the relative position of the momentum peaks at the minima of the dispersion. Similar figures are also shown in Ref. [155] and the supplementary material of Ref. [3].

initialization of lattice driving. Heating effects due to technical noise leads to increasing values of the initial entropies $S_1 < S_2 < S_3$ respectively. In Fig. 4.10a resulting averaged absorption images are shown from the three obtained data sets for a selection of staggered flux strength values in analogy to Fig. 4.7b, where three of the absorption images for the smallest initial entropy were already shown. The corresponding tight-binding dispersion for the different fluxes according to Eq. (4.20) is depicted in Fig. 4.10b. An increase in entropy is clearly visible as contrast of the superfluid momentum peaks reduces. In the following we will analyze both order parameters quantitatively for these data sets, each resulting from more than 2500 individual measurements.

As a measure of the total cyclotron mass currents induced by the staggered fluxes we extract the normalized total current

$$\mathcal{M} = \sum_{\mathbf{k}} \langle \tilde{n}_{\mathbf{k}} \rangle \mathcal{X}(\theta, \theta', \mathbf{k}) / \sum_{\mathbf{k}} \langle \tilde{n}_{\mathbf{k}} \rangle \quad (4.33)$$

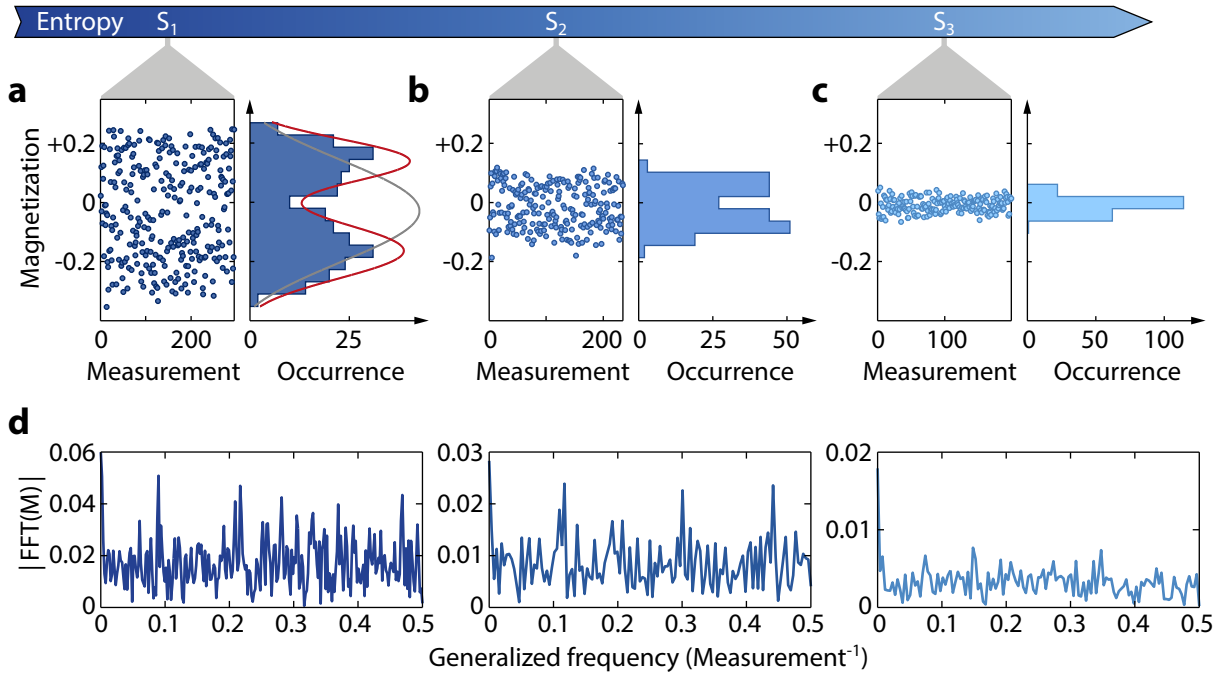


Figure 4.11: Statistical distribution of the magnetization. **a** Consecutive measurements of the magnetization at lowest entropy S_1 and maximum flux strength of $\Phi = \pi$. A clear bimodal fluctuation with a strongly suppressed signal at zero magnetization is observed. The solid gray (red) line indicates the unimodal (bimodal) fitted Gaussian probability distribution. **b** For increasing entropy, the spontaneous magnetization decreases and the bimodal distributions merge at the highest entropy S_2 as shown in **c**. Fourier spectra of the magnetization data, shown in **d** are in accordance with white noise. Similar figures are featured in Ref. [3] and [155].

from each individual absorption image. We call this scalar value the magnetization of the system in analogy to the magnetization of an Ising ferromagnet.

In contrast to the averaged depiction of absorption images, the extracted magnetization and, thus, the occupation of the two minima of the dispersion exhibits strong shot-to-shot fluctuations for low entropy (S_1) at flux strengths of $\Phi = \pi$. This results in a bimodal statistical distribution shown for roughly 200 consecutive measurements in Fig. 4.11a where the system predominantly occupies one of the two possible degenerate configurations depicted in Fig. 4.8, thus, breaking the \mathbb{Z}_2 symmetry. Occurrences of zero magnetization are significantly suppressed as indicated by the corresponding histogram. In appendix C the first 99 single-shot images of Fig. 4.11 are shown in Fig. C.2, C.3 and C.4 for all three initial entropy values and a flux strength of π as a demonstration of the fluctuations.

This bimodal behavior favoring the occupation of one of the minima in the dispersion relation is expected in such a system. The simultaneous occupation of both degenerate ground states for the few measured cases of zero magnetization likely occurs due to the formation of spatial domains with different long range phase coherence patterns. The

formation of such domains may result from the highly non-adiabatic ramping procedure through a completely flat dispersion relation. At the boundaries of two domains consisting of phase patterns as depicted in Fig. 4.8b, the additional domain wall energy of the system is given by the local phases which cannot align themselves in the optimal angle of 120° with respect to each other (compare Eq. (4.24)). Indeed, domain formation in a similar one-dimensional model system emulating ferromagnetic interactions has recently been observed by Parker *et al.* [213]. In principle, a coherent single-particle superposition of atoms in both quasimomentum states may also explain the occurrence of zero magnetization in the low-entropy measurements. However, such a state would exhibit a density modulation in real space which is energetically highly disfavored due to repulsive interactions [155].

The discussed breaking of the \mathbb{Z}_2 symmetry leading to a finite spontaneous magnetization of the system is analogous to ferromagnetism described by the classical Ising model. An increase of entropy (S_2) in the system leads to a significant reduction of fluctuations (see Fig. 4.11b). Finally, for even larger entropy (S_3) the bimodal distribution merge, preserving the \mathbb{Z}_2 symmetry as in Fig. 4.11c. In the Ising model, this behavior of the spontaneous magnetization in dependence of the entropy corresponds to a thermally driven phase transition from an ordered-ferromagnetic state to an unordered-paramagnetic state.

In order to exclude systematic fluctuations or long-term drifts of the experimental apparatus as the origin of the symmetry breaking, Fourier spectra of the magnetization data are shown in Fig. 4.11d. No significant features can be identified in the Fourier spectra which are in full agreement with white noise. However, this observation does not exclude technical noise as the origin of the symmetry breaking process. Thus, the question whether the symmetry is spontaneously broken or induced by technical fluctuations is impossible to answer. Nonetheless, we demonstrate that the magnetic susceptibility is significantly larger at lower entropies.

4.3.4 Statistical data analysis of symmetry breaking

In Fig. 4.11 the bimodal distributions of the extracted magnetization values are visualized as histograms. Here, the suppression of zero magnetization measurements for the entropies S_1 and S_2 is evident while no such suppression can be observed for the largest initial entropy S_3 . However, the bin size of the histograms is an arbitrary choice. Different bin sizes may reveal different features present in the data. Two trivial cases of bin sizes exemplify this problem: First, the choice of a single bin for a number of n data points obviously results in a unimodal distribution. Second, the bin size can also be chosen small enough, such that each data point is assigned to an individual bin. In order to reliably distinguish between the number of occupied modes in the distribution of magnetization values it is, thus, crucial to employ a robust statistical data analysis that does not depend on additional preprocessing constraints.

Finding an optimal partitioning of data sets is a widespread problem for a large variety

of applications in data mining and still a matter of current research. A commonly employed solution is the k -means clustering method [214–216]. The k -means algorithm aims to partition a multivariate data set into a number of k clusters by minimizing the sum of squares within each cluster. This allows for a division of the data space into Dirichlet-Voronoi cells [217] where each centroid of a cluster serves as a *generator* (also referred to as *seed*) of the Voronoi diagram [218].

Although the k -means problem is computationally difficult (NP-hard) it can be readily solved with standard data analysis software for the rather trivial case of the one-dimensional magnetization data space. However, observations belonging to a certain mode can be expected to vary with a Gaussian probability distribution. As a number such distributions is likely to overlap with each other, we extend the statistical analysis of the obtained magnetization data to a *fuzzy* clustering method [219]. In contrast to hard clustering, where each data point is allocated unambiguously to a distinct cluster, fuzzy- or soft clustering allows for the allocation of data points to more than one cluster in analogy to fuzzy logic. Hereby, a certain membership level of each data point indicates the association with a particular cluster.

As a special case of fuzzy clustering, we fit a Gaussian mixture probability distribution with $k_M = 1, 2, \dots$ modes to the one-dimensional magnetization data. With this, the optimal number of modes describing each data set can be determined by comparing the information criteria of the fitted probability models [3]. Information criteria provide a measure for the likelihood of a model fitted to a data set with respect to the number of free parameters, i.e., they weigh the goodness of the applied fit against the complexity of the used model. In this sense, information criteria can be regarded as the statistical equivalent to Occam’s razor.

For the comparison of models fitted to the magnetization data we rely on the Schwarz-Bayes information criterion (SBC) extracted from the respective fits [220]. In comparison with the also commonly used Akaike information criterion [221] the Schwarz-Bayes criterion tends to penalize the number of free parameters more strongly. An application of Akaike information criteria to the measured magnetization distributions did not allow for a clear distinction between the optimal number of modes. Other information criteria such as the Hannan–Quinn- or the Deviance information criteria were not considered in the data analysis.

The optimal model is indicated by the smallest value of the SBC_{k_M} for a k_M -modal fit. In Fig. 4.11a the fitted Gaussian probability distributions are plotted for $k_M = 1$ (gray solid line) and $k_M = 2$ (red solid line) together with the magnetization histogram. In this case, the extracted information criteria clearly favor the bimodal distribution with $SBC_1 > SBC_2$. As the initial parameters of the probability clustering algorithm are chosen randomly, each Gaussian mixture fit is reiterated ten times. Out of these fit parameters the most likely fit is selected for each k_M (i.e., the one with the smallest SBC). Furthermore, the obtained parameters and information criteria are averaged ten times in order to rule out residual fluctuations of the fitted results due to the initial randomness of

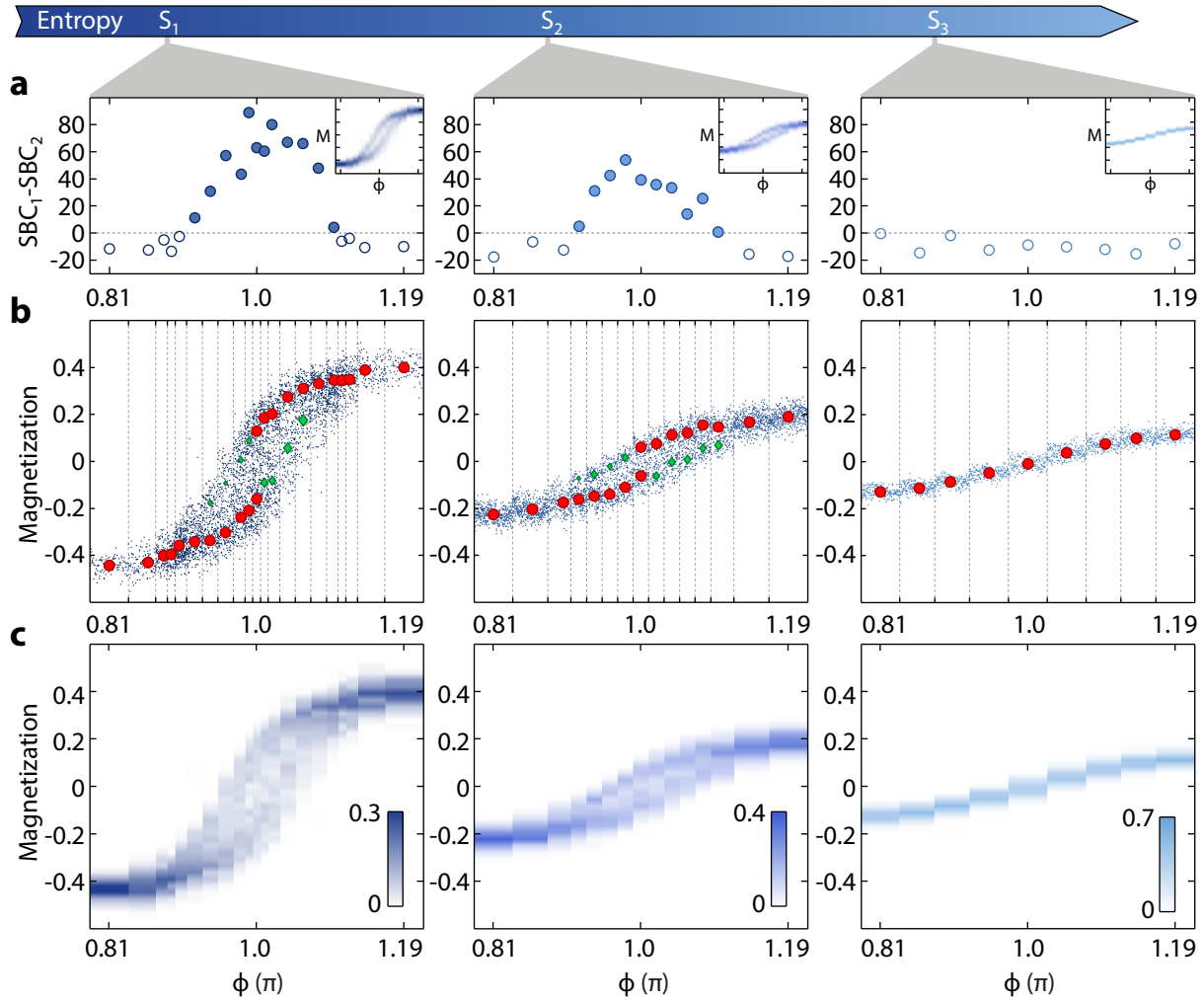


Figure 4.12: Magnetization behavior for the thermally driven phase transition for three increasing values of the initial entropy $S_1 < S_2 < S_3$. **a** Differences of Schwarz-Bayes information criteria for uni- and bimodal Gaussian probability distributions fitted to the magnetization data sets. Negative (positive) values indicated by open (filled) circles favor a unimodal (bimodal) distribution. Insets depict the resulting optimal Gaussian fits. **b** Raw magnetization data (tiny dots) with the stable and metastable maxima of the fitted Gaussian mixture distributions indicated by red circles and green diamonds respectively. The size of the diamonds is a measure of the relative occupation of the metastable mode. For the lowest entropy, the metastable- and stable positions overlap for the last two bimodal distributions at $\Phi > \pi$. No bimodal distributions can be observed for the largest entropy, hinting towards a crossing of the phase transition to a paramagnetic state. **c** Histograms for each flux value. Each column corresponds to a histogram of the magnetization data for a certain flux value as depicted for $\Phi = \pi$ in Fig. 4.11. All histograms are normalized with respect to the maximum number of occurrences in a single bin for the whole data set. Hence, the different color axes. Data are presented in similar fashion in Ref. [3] and [155].

the algorithm. Throughout all measured data sets, multimodal probability models with $k_M \geq 3$ exhibit a worse likelihood compared to unimodal or bimodal fits and are omitted from the following considerations.

In Fig. 4.12a the differences $SBC_1 - SBC_2$ of information criteria between a unimodal and a bimodal Gaussian probability distributions are plotted for all measured flux values and initial entropies. Values above zero (filled circles) indicate a bimodal distribution as the optimal model, while values below zero (open circles) favor the unimodal distribution. While for the entropies S_1 and S_2 bimodal distributions are clearly favored in the vicinity of the maximum flux strength $\Phi = \pi$, no bimodal distribution of the magnetization data can be observed for the largest initial entropy S_3 . Insets in the upper right corner of the plots depict the corresponding optimal Gaussian mixture fits. In Fig. 4.12b the extracted magnetization data, roughly 2500 individual measurements for each entropy value, are depicted as consecutive measurements similar to Fig. 4.11. Red circles indicate the positions of the fitted Gaussian mixture distribution corresponding to the occupation of the global minimum in the effective dispersion relation. In the case of a remaining bimodal distribution for flux strengths different from π , green diamonds indicate the position of the smaller Gaussian mode which corresponds to the occupation of the metastable state in the dispersion. Hereby, the size of the diamonds illustrates the relative strength of the metastable mode as compared to the stable one. Histograms of the data are plotted in Fig. 4.12c.

A slight asymmetry of the magnetization curves towards negative values can be observed. However, this is merely an artifact which stems from a misalignment of the Wannier envelope position. As the final envelope position lies slightly below the central vertical position at $k_y = 0$, negative valued regions of the weighting function shown in Fig. 4.9 are favored over the positive ones for the given size of the Wannier envelope.

With the statistically robust data analysis, the flux-dependent measurements depicted in Fig. 4.12 substantiate the notion of the staggered flux system undergoing an Ising-type thermal phase transition: A tuning of the staggered flux strength away from $\Phi = \pi$ breaks the \mathbb{Z}_2 symmetry of the system and emulates the presence of an external longitudinal magnetic field in a classical Ising model. This artificial external field results in a net magnetization of the system. For flux strengths far enough detuned from π the system can be completely magnetized in a single mode. Intermediate fluxes and low enough entropies (S_1 and S_2), however, allow for an occupation of the metastable magnetization mode which stems from the non-adiabatic preparation process of the effective dispersion and is a clear signature of non-equilibrium dynamics in the ferromagnetic phase. The metastable state is stabilized against decay into the global minimum by repulsive atomic interactions which inhibit the fragmentation of the condensate [3].

The flux-dependent data presented in Fig. 4.12b and c resembles the hysteresis behavior known from the classical Ising model below the Curie temperature. However, with the non-adiabatic preparation procedure of ramping directly to the desired flux value, the occupation of metastable states in the staggered flux system is of an entirely different

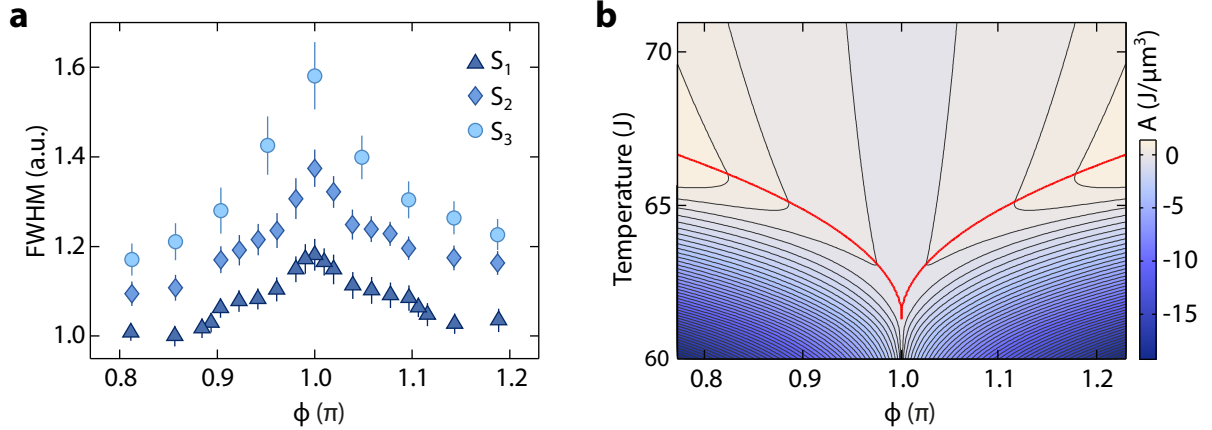


Figure 4.13: Momentum peak widths and free energy of the Ising-XY system. **a** Full-width-half-maximum values extracted from the time by Gaussian fits to the central peaks of the averaged TOF-images as depicted in Fig. 4.10 for the three initial entropies $S_1 < S_2 < S_3$. Error bars denote the residuals of the Gaussian fits. **b** Free energy in units of the effective tunneling amplitude per cubic micrometer. The phase boundary between a thermal Bose gas and a BEC is indicated by the red line. Here, the free energy exhibits a non-analytic behavior. The figure also appears in Ref. [3] and [155]. The free energy data was provided with kind permission of L. Mathey.

origin as compared to the continuous change of an external field leading to hysteresis curves in Ising magnetism.

4.3.5 Analysis of long-range phase coherence - $U(1)$ symmetry

The previously discussed analysis of the magnetization gives insight into the long-range order of mass currents and, thus, the discrete Ising- or \mathbb{Z}_2 symmetry of the staggered flux system. In the following, we will investigate the continuous $U(1)$ symmetry for the same set of measurements.

As we have mentioned before, the order parameter associated with the $U(1)$ symmetry is the long-range phase coherence. This long-range order signifies the breaking of the $U(1)$ symmetry as expected for Bose-Einstein condensation and corresponds to the occupation of a single quasimomentum state. The widths of the imaged superfluid momentum peaks will therefore be used as a measure for the degree of phase coherence. It should be noted that in principle the fraction of condensed atoms is a more suitable observable for the quantification of long-range phase coherence. This parameter, however, is difficult to extract from the obtained density profiles: for higher entropies fitting routines do not allow for a reliable discrimination between the relatively large incoherent background and the remaining coherent peak structure.

In Fig. 4.13a the full width at half maximum (FWHM) of the momentum peaks is plotted for the three initial entropies $S_1 < S_2 < S_3$ with respect to the staggered flux strength. Values are obtained by fitting a combination of Gaussians to the row-sum of

the central peaks (compare Fig. 4.7d). A broad Gaussian fit to the background eliminates the influence of the Wannier envelope and residual occupations due to thermal atoms or quantum depletion. A second Gaussian is fitted directly to the predominantly occupied peak.

Two crucial observations can be made: First, an increase of entropy leads to the expected broadening of the momentum peaks for every data set. With this, the condition $S_1 < S_2 < S_3$ is confirmed for all values of the staggered flux strength.

Second, the sharpness of momentum peaks depends strongly on the staggered flux strength for all three initial entropies. The tuning of the flux strength away from its maximum value results in sharper peaks as already indicated in Fig. 4.10. Intuitively, this effect can be understood by the behavior of the single-particle dispersion of Eq. (4.20). For an increasing flux strength the curvature of the dispersion minima decreases leading to an increase of the density of states and, thus, to a lower critical temperature for Bose-Einstein condensation [155]. The critical temperature can be determined by calculating the free energy of the system with respect to the staggered flux strength as depicted in Fig. 4.13b: a non-analytic behavior of the free energy, depicted as a red line, indicates the phase transition between a thermal Bose gas and a BEC. Similar to the FWHM-values, the critical temperature exhibits a pronounced cusp at the maximum flux strength $\Phi = \pi$ [3].

However, in section 2.5 we have argued how the experimentally observed peak width is actually not equal to the actual width of the momentum spread: As the time-of-flight is not sufficiently long to reach the far-field regime, the momentum peaks are significantly convoluted with the in-situ trap size. While the sharpness of momentum peaks still serves as a qualitative measure for the long-range phase coherence, a quantitative analysis is difficult. Whether the entropies at which the phase transitions related to the breaking of the $U(1)$ and \mathbb{Z}_2 symmetries occur coincide remains an open question.

4.4 Model-free statistical data analysis

In the preceding section we have utilized tools of statistical data analysis in order to verify the presence of (spontaneous) symmetry breaking and the occupation of metastable modes. Although the outcome of the statistical analysis does not rely on further interpretations, the treated observable itself is a model-based quantity, implying an *a priori* knowledge of the model system leading to Eq. (4.33). Furthermore, the constraint to a very small data set, i.e., the single scalar values - the magnetization - that are extracted from each image consisting of thousands of pixels only utilizes a tiny fraction of information contained in the data.

In general, both the reliance on such *model-based inference* and an *a priori* knowledge of the observed physical processes as well as the limitation to a small set of parameters extracted from experimental data are major weaknesses in the analysis and interpretation of measurements.

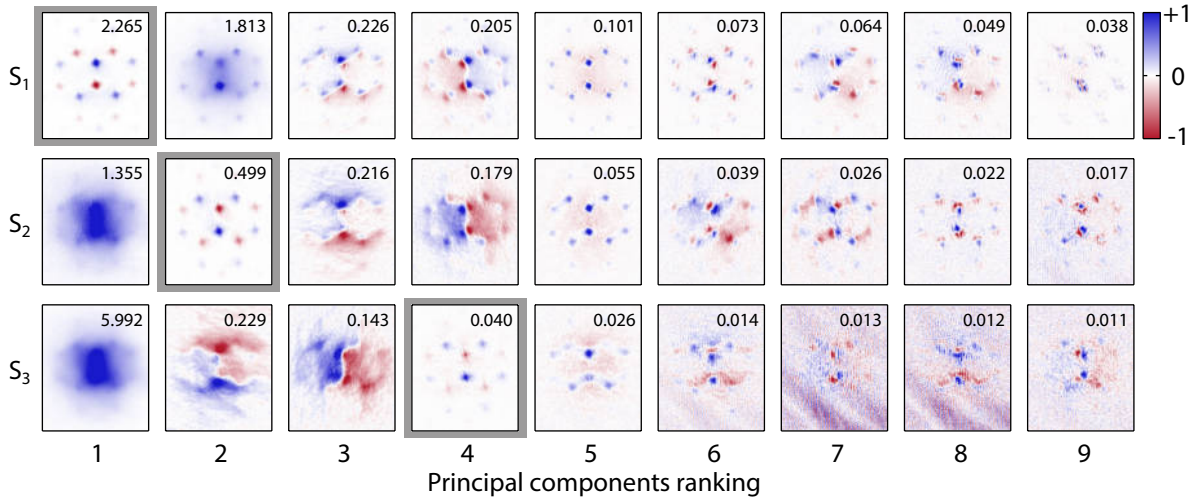


Figure 4.14: Principal component analysis of symmetry breaking for the three initial entropies. The nine largest principal components obtained from data sets at maximum flux strength of $\Phi = \pi$ are sorted by decreasing eigenvalue (numbers in the upper corners of the images). Principal components accounting for the symmetry breaking are highlighted by a gray framing.

Thus, in order to exploit the entire information contained in the images without relying on any *a priori* knowledge of the observed atomic state we pursue an additional approach of a model-free statistical data analysis for the quantification of the symmetry breaking behavior discussed above. Even though model-free analysis methods are solely based on statistical concepts such as independence, entropy extremization and maximum-likelihood (as for the information criteria discussed above), the interpretation of outcomes of course still relies on the comparison with expected models by the experimenter [222].

4.4.1 Principal component analysis

We apply the multivariate statistical analysis techniques of *principal component analysis* (PCA) and *independent component analysis* (ICA) to the data sets of images belonging to a single initial entropy value S_i and staggered flux strength Φ . These methods are well established and successfully used in signal- and image processing over a wide spectrum of applications such as the analysis of neural networks and artificial intelligence, classification of galaxies, electroencephalography, face recognition, stock market predictions and blind source separation in general [223–227], only to name a few. To the best of our knowledge, principal- and independent component analysis methods were first used by Segal *et al.* [222] in the context of quantum gas experiments and the implementation of PCA and ICA for the analysis of symmetry breaking was sparked by their publication. We will briefly sketch the underlying principles of the two algorithms in the following. Interestingly, a strong link between the PCA and *k*-means clustering algorithms discussed in the previous section has been discovered rather recently [228, 229].

The principle component analysis aims to express a set of multivariate data in terms of a set of uncorrelated variables [230]. The magnetization measurements for each initial entropy and staggered flux strength are obtained for a comparatively large number $n \approx 200$ of individual time-of-flight absorption images with a number of $p \approx 2.7 \times 10^4$ pixels in the experimentally relevant region around the Wannier envelope. Each CCD-pixel can be regarded as a variable. Accordingly, we have n observations for p correlated variables x . The images can be written into vectors $\mathbf{x}_i = (x_1, x_2, \dots, x_p)$ in order to construct the centered $n \times p$ data matrix

$$D = \begin{bmatrix} \mathbf{x}_1 - \mathbf{x}_M \\ \mathbf{x}_2 - \mathbf{x}_M \\ \vdots \\ \mathbf{x}_n - \mathbf{x}_M \end{bmatrix} \quad \text{with} \quad \mathbf{x}_M = \frac{1}{n} \sum_{i=1}^n \mathbf{x}_i. \quad (4.34)$$

PCA relies on the finding of eigenvalues of the $p \times p$ covariance matrix $Q = D^T D / (n - 1)$ where D^T denotes the transpose of D . A diagonal element Q_{jj} of the covariance matrix corresponds to the sample variance σ_j^2 of the j -th pixel. An off-diagonal element Q_{jk} , where $k \neq j$, is the covariance of the j -th and the k -th pixel. Hence, if $Q_{jk} = 0$, the pixels j and k are uncorrelated. The matrix Q is generally hard to diagonalize as the number of pixels can be very large. The problem of finding the eigenvectors \mathbf{y}_i to the matrix Q can be circumvented by first computing the eigenvectors \mathbf{z}_i of the $n \times n$ matrix $G = DD^T / (n - 1)$ as $n \ll p$. It is straightforward to show that eigenvectors of Q are related to the n eigenvectors of G via $\mathbf{y}_i = D^T \mathbf{z}_i$ [231]. These eigenvectors are the principal components of the data set. They are orthogonal (since Q is real and symmetric) and *per definitionem* statistically uncorrelated. For both a large number of images and a large number of pixels, the diagonalization is hard to compute. However, standard PCA algorithms allow for an efficient calculation of the most significant principal components with the largest eigenvalues.

Each original image vector \mathbf{x}_i can now be expressed in terms of the mean image \mathbf{x}_M and a linear combination of the n principal components:

$$\mathbf{x}_i = \mathbf{x}_M + \sum_{j=1}^n C_{ij}^P \mathbf{y}_j. \quad (4.35)$$

The eigenvalue of a principal component \mathbf{y}_j is given by the variance of its coefficients C_{ij}^P . It is often referred to as the *strength* of the principal component and reflects its relative importance. The diagonalization of the covariance matrix Q implies that the set of coefficients for any basis image \mathbf{x}_i is statistically uncorrelated with the set of coefficients of any other basis image $\mathbf{x}_{k \neq i}$ [222], or:

$$\sigma_{ik}^2 = \frac{1}{n-1} \sum_{j=1}^n C_{ij}^P C_{kj}^P \stackrel{!}{=} 0. \quad (4.36)$$

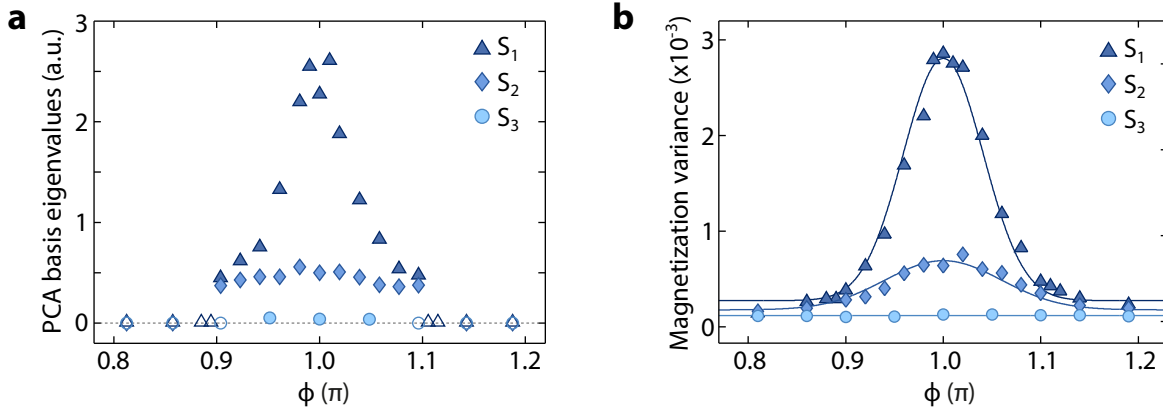


Figure 4.15: Symmetry breaking components and variance of the magnetization. **a** Strengths (eigenvalues) of the principal components related to symmetry breaking are plotted for each initial entropy $S_1 < S_2 < S_3$ and staggered flux strength. Open markers at a value of zero denote data sets where no principal components associated with symmetry breaking could be identified. **b** Corresponding variances of the magnetization data shown in Fig. 4.12. Solid lines are Gaussian fits to the data as a guide to the eye. Part **b** of the figure also appears in the supplementary material of Ref. [3].

In Fig. 4.14 the calculated nine strongest principal components of the image sets for the three initial entropies at maximum flux strength $\Phi = \pi$ are shown in descending order of their eigenvalues. A principal component representing symmetry breaking can be clearly identified as the first- second- and fourth component for the entropies S_1 , S_2 and S_3 respectively (highlighted by gray frames). Here, the two possible coherent momentum occupations exhibit opposite signs. According to Eq. (4.35) this always results in a single mode being predominantly occupied for every linear combination of principal components.

Besides the symmetry breaking component several other principal components can be assigned to a variety of origins in Fig. 4.14. For example, the secondly ranked component of the initial entropy S_1 and the strongest components of both S_2 and S_3 represent fluctuations in the total particle number. Furthermore, the fifth principle component of all three data sets is likely related to a small variation of the relative strength of all superfluid momentum peaks. Finally, principal components exhibiting domain-like patterns such as the third and fourth components of S_1 and S_3 as well as the second and third components of the data set for S_3 can be attributed to fluctuations of the overall position of the momentum distribution in different directions.

Even though we have argued in the preceding section that the \mathbb{Z}_2 symmetry of the system is restored for the largest initial entropy S_3 , a component associated with symmetry breaking is present in the principal components, indicating that the phase transition to a paramagnetic state may not have been crossed entirely. With this, an important advantage of statistical image processing is exemplified: as the PCA algorithm does not necessarily rely on the prerequisite of a sufficient signal-to-noise ratio. Residual symmetry breaking may very well be present in the magnetization data for the largest initial entropy as well.

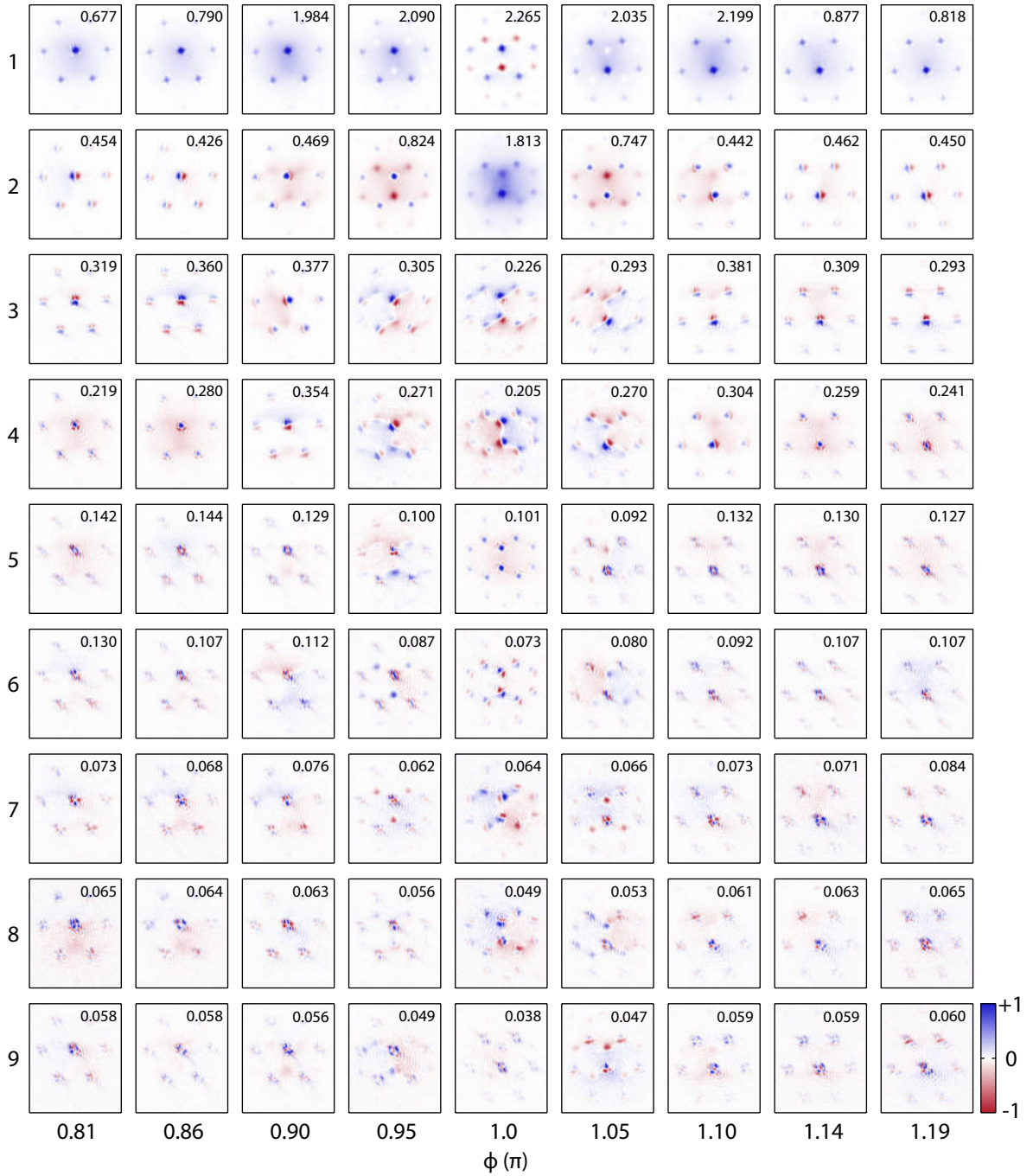


Figure 4.16: First nine principal components and eigenvalues for the lowest initial entropy S_1 and selected values of the staggered flux strength Φ . The eigenvalues decrease rapidly. Above the fourth or fifth ranked place the principal components represent different forms of technical fluctuations, e.g., residual changes of the absorption image position. While the symmetry breaking component is the predominant component for a flux strength of π , its contribution rapidly decays for smaller flux strengths.

If, however, the fluctuation of data overwhelms the spread of each individual mode, the distinction of both modes is impossible. On the contrary, the variance of the remaining symmetry breaking component is extremely small (less than a percent compared to the largest eigenvalue) such that the residual symmetry breaking can safely be neglected and the notion of the phase transition from a ferromagnetic to a paramagnetic Ising-system holds.

The level of symmetry breaking that is present in each subset of data according to the principal component analysis is depicted in Fig.4.15a. Here, the eigenvalues of the principal components associated with symmetry breaking are plotted as filled markers for each measured entropy and flux value, while open markers indicate the absence of a clearly identifiable symmetry breaking component in the nine largest principal components. A distinct rise of the symmetry breaking strength towards the maximum flux of π can be observed for the lowest initial entropy. This behavior is reproduced, although less pronounced, for the intermediate entropy S_2 . As discussed, the contribution of symmetry breaking is extremely small for the largest entropy S_3 . In Fig.4.16 the corresponding strongest principal components of the data set S_1 are shown for a selection of different flux values as an example of the decline and eventual vanishing of the symmetry breaking basis.

For comparison, Fig.4.15b shows the variance of the magnetization data sets from Fig.4.12. A similar rise of fluctuations can be observed in the vicinity of $\Phi = \pi$ for the two lowest entropies while the fluctuation strength for S_3 remains constantly small for every value of the staggered flux. The similarity of the fluctuation behavior of the relevant principal components and the magnetization data confirms the previous interpretations of the occupation of different modes in dependence of the staggered flux strength as well as the phase transition from a spontaneously magnetized ferromagnetic state to an unordered paramagnetic state.

4.4.2 Independent component analysis

The second widely applied technique in signal and image processing, the independent component analysis, applies a higher order test to the statistics of its basis coefficients C_{ij}^I as compared to Eq.(4.36) for the PCA. This *statistical independence* for the ICA coefficients of any two images \mathbf{x}_i and \mathbf{x}_k is defined as the condition

$$\frac{1}{n} \sum_{j=1}^n f(C_{ij}^I) g(C_{kj}^I) - \frac{1}{n^2} \left[\sum_{j=1}^n f(C_{ij}^I) \right] \left[\sum_{j=1}^n g(C_{kj}^I) \right] \stackrel{!}{=} 0 \quad (4.37)$$

where f and g are any integrable functions [222]. Statistically independent coefficients are, thus, also uncorrelated since the condition of Eq.(4.36) can be recovered by $f(x) = g(x) = x$. While the higher-order decorrelation of ICA may result in more reliable signal extraction, it is not superior compared to PCA for every task: the independent component basis is not necessarily orthogonal. This implies that the total variance in this basis is not

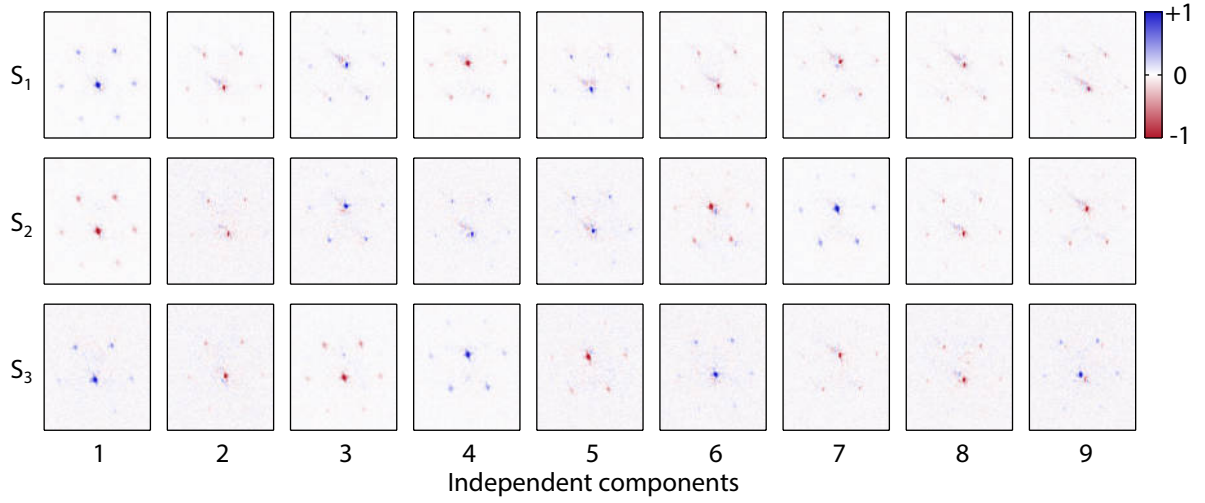


Figure 4.17: Independent components for the three measured initial entropies at a staggered flux strength of $\Phi = \pi$. In contrast to the principal component basis, all nine calculated individual basis images present fractions of one of the two momentum modes and do not allow for the distinction of different physical processes.

conserved as it is the case for PCA. As a consequence, independent component images cannot be ranked by their variance. Furthermore, suitable algorithms for the calculation of the independent component basis for large data sets, such as the *FastICA* algorithm [232] are sensitive to outliers in the data.

In Fig. 4.17, bases of nine independent components calculated with *FastICA* are shown for the three data sets at maximum flux strength of π and each initial entropy, in analogy to the principal component basis depicted in Fig. 4.14. Here, every basis image represents only fractions of one momentum mode. This indicates that the ICA is in fact not a suitable tool for the analysis of the presented symmetry breaking measurements as the similarity of basis images does not allow for a distinction of different fluctuation processes. The complete partitioning of basis components into separate modes can likely be attributed to the residual shot-to-shot movements of the entire momentum distributions which are more significant due to the higher-order decorrelation condition.

In appendix B we will present an additional method of statistical image processing for the quantification of the shot-to-shot fluctuations of mode occupations that relies on a correlation analysis.

4.5 Conclusion & outlook

In conclusion, we have demonstrated the realization of fully tunable-complex valued tunneling matrix elements by time-asymmetric periodic driving of a one-dimensional lattice. The presence of a Peierls phase, given by the argument of the tunneling parameter em-

ulates the presence of a vector gauge potential for the neutral atoms in analogy to a charged particle in a magnetic field. The method could be extended to the triangular lattice, where the two distinct elementary plaquettes without pairwise-parallel bonds give rise to tunable gauge invariant staggered magnetic fluxes. Hereby, the presence of more than one distinct minimum in the effective dispersion of the triangular lattice results in geometrical frustration.

The staggered flux system exhibits both a discrete Ising-type \mathbb{Z}_2 symmetry as well as a continuous $U(1)$ phase symmetry that can be mapped onto classical XY-spins. This coupled Ising-XY spin model system allows for the study of phase transitions related to the two fundamental symmetries with respect to their order parameters of chiral mass currents and a long-range phase coherence. A thermal phase transition from an ordered to an unordered state, mimicking ferromagnetism and paramagnetism respectively, could be observed. As a non-equilibrium signature of the phase transition, a significant occupation of metastable states with chiral currents opposing the staggered flux directions could be evidenced. The interpretation of the phase transition, symmetry breaking and the presence of metastable modes could be confirmed by model-free multivariate statistical data analysis. A strong interplay between the discrete \mathbb{Z}_2 and the continuous $U(1)$ symmetry is indicated by the dependence of the long-range phase coherence on the staggered flux strength.

Although quantitative statements about the relative position of the two phase transitions could not be extracted from the presented data due to experimental limitations, the coupled Ising-XY model system may provide an opportunity to do so in future experiments. Furthermore, the periodic driving scheme can be extended into the strongly correlated regime where exotic quantum phases such as a chiral Mott insulator are expected to emerge [233–235]. In the subsequent section we will focus on the strongly correlated regime for the case of monochromatic driving where the occupation number of lattice sites can be mapped onto a spin- $1/2$ XY model of quantum magnetism [140].

5 Frustrated quantum antiferromagnetism in a triangular lattice

In this chapter we investigate the possibility of emulating frustrated quantum antiferromagnetism on the triangular optical lattice. In the hard-core boson limit of strong repulsive interactions the mapping of classical XY spins continuously approaches a quantum spin- $1/2$ XY model. On-site interactions are increased by an additional perpendicular optical lattice. We discuss limitations of the accessible parameter space for the harmonic lattice driving in the strongly correlated regime and probe the transition from a weakly interacting superfluid to a Mott-insulating state in both the static and the driven system. An analysis of quantum noise correlations reveals the feasibility of our approach. First hints towards an order-by-disorder effect in the frustrated system are observed.

Quantum magnetism describes the exchange coupling of quantum mechanical spins which is an essential element for a larger variety of fundamental condensed matter systems. In particular, an antiferromagnetic coupling between spins that are ordered on a regular lattice structure can give rise to a manifold of intriguing physical phenomena. Here, the energetically favored Néel-ordering of spins is inhibited due to the lattice geometry. As discussed in the previous chapter, this impossibility of fulfilling several conflicting constraints for the minimization of energy results in geometrical frustration. The study of such frustrated quantum antiferromagnets promises to yield valuable insights. For example, quantum antiferromagnetism is believed to be strongly connected to high- T_c superconductivity as an antiferromagnetic phase always exists close to a superconducting phase in the complex ordered cuprates [128, 129]. Furthermore, novel highly nontrivial quantum phases are expected to appear for certain frustrated quantum antiferromagnets.

A paradigm example of such an exotic phase is the quantum spin liquid. The highly disordered spin liquid states possess no local order parameter and are comprised by resonating valence bonds, where two antiparallel spins couple to a coherent superposition of a spin-0 singlet. Beyond the absence of local order, quantum spin liquids are expected to exhibit a hidden topological order. The robustness of this order against local perturbations together with the anyonic character of excitations may allow for the utilization of such states for quantum information processing [131].

In the last decade, indications of spin liquids have been observed in triangular lattices comprised of a Mott-insulating organic salt of κ -(BEDT-TTF)₂Cu₂(CN)₃ [132–136]. More recently, strong hints towards a spin-liquid ground state in the kagome-ordered mineral herbertsmithite ZnCu₃(OH)₆Cl₂ were evidenced in the form of spin-state fractionalization [138]. However, the realization and characterization of such compounds is extremely demanding: samples have to be cooled down to mK-temperatures and are probed by neutron- or myon scattering.

A different approach of investigating quantum antiferromagnetic many-body systems in a clean and well-controllable environment is the emulation of such systems with ultracold atoms in optical lattices. Here, the natural realization of a quantum magnet is given by a fermionic Mott insulator with two different internal hyperfine states. However, a major disadvantage of this implementation is the demand for ultra-low temperatures below the exchange energy. Short-range quantum magnetism could be emulated in such a system of an ultracold potassium fermi-gas by redistributing entropy along the bonds of a dimerized cubic lattice [139]. However, the realization of long-range (dis)ordered quantum magnets with fermionic Mott insulators appears to be extremely difficult.

In contrast, the manipulation of motional degrees of freedom by periodic lattice driving, can also be utilized to emulate frustrated quantum magnetism with bosonic atoms in suitable regimes where the temperature is low compared to the relevant energy scales of the tunneling and the on-site interaction [140]. In the preceding chapter we have shown that a system of antiferromagnetically coupled bosons on a triangular lattice can be mapped to a geometrically frustrated *classical* XY model.

Experiments presented in this chapter have been performed within the team of J. Simonet, C. Ölschläger, S. Prella and M. Weinberg.

5.1 Quantum XY model

In this section, we will describe how the *classical* XY model approaches the *quantum* spin-1/2 XY model in the hard-core boson limit of strong repulsive interaction on the basis of Eckardt *et al.* [140] and discuss implications of the resulting high degree of geometric frustration that is accompanied with a hugely degenerate ground state of the system.

5.1.1 Inverse Holstein-Primakoff mapping

In chapter 3 we have described how time-averaging over the fast periodic lattice driving results in an effective Bose-Hubbard Hamiltonian (3.29). In the weakly interacting regime, where $U \ll |J|$, the number-phase representation of a coherent state at each lattice site $\langle \hat{b}_i \rangle = \sqrt{N_i} \exp(i\varphi_i)$ with the local phases φ_i can be mapped onto a classical XY model. Here, two-dimensional vector spins with a continuous rotational degree of freedom represent the orientation of classical magnets. By neglecting the additional harmonic confinement of the trapping potential, a homogeneous density $N_i = \bar{N}$ at all lattice sites

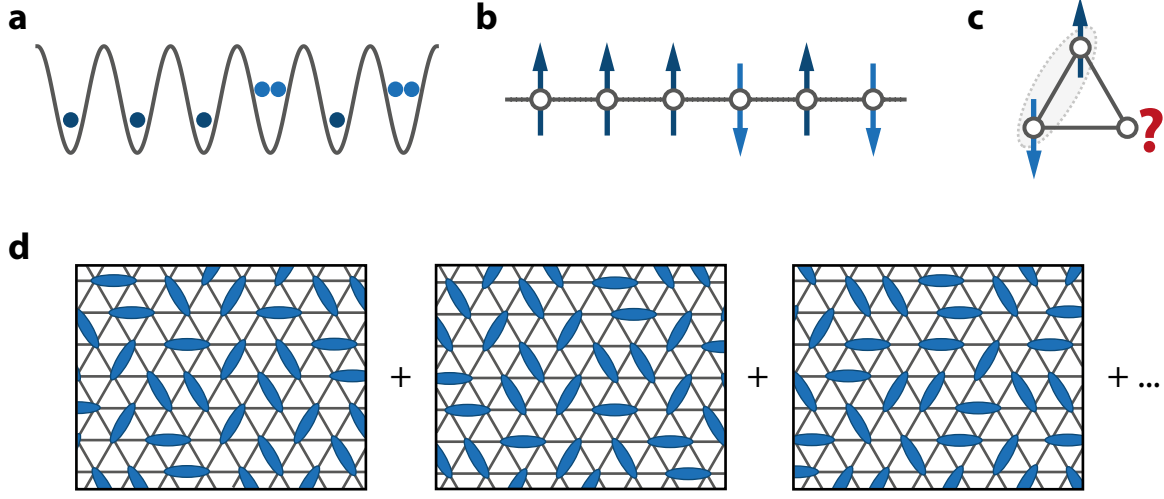


Figure 5.1: Mapping of the quantum spin- $1/2$ XY model. **a** In the strongly interacting regime, the two possible on-site occupation numbers, depicted here for $N_i = 1$ and $N_i = 2$ can be associated with the two spin- $1/2$ states $|\uparrow\rangle$ and $|\downarrow\rangle$ shown in **b**. In the case of a triangular lattice depicted in **c**, geometrical frustration arises for antiferromagnetic coupling. For a single plaquette, the ground state is already six-fold degenerate. **d** Illustration of the degeneracy of a valence bond spin liquid, where each oval represents a singlet state comprised of a coherent superposition of two spin states.

is energetically favorable.

In the opposite limit of strong repulsive interactions, where $U \gg |J|$, two site occupation numbers $N_i = n$ and $N_i = n + 1$ are possible with $n \equiv [\bar{N}]$ being the largest integer smaller than the average on-site particle number \bar{N} . As the central aspect of the mapping towards the quantum XY model, we associate these two possible occupation states $|n\rangle_i$ and $|n + 1\rangle_i$ with “spin-up” and “spin-down” respectively [140, 236]. An illustration of the mapping for the case of $n = 1$ is given in Fig. 5.1a and b. With this, each site can be expressed in the Bloch-sphere representation as

$$|\vartheta_i, \varphi_i\rangle \equiv \cos(\vartheta_i/2) |n\rangle_i + \sin(\vartheta_i/2) e^{i\varphi_i} |n + 1\rangle_i. \quad (5.1)$$

By applying an inverse Holstein-Primakoff transformation [237] to the bosonic annihilation and creation operators \hat{b}_i and \hat{b}_i^\dagger , i.e. mapping them onto spin lowering- and raising operators \hat{S}_i and \hat{S}_i^\dagger respectively according to

$$\frac{2}{\sqrt{n+1}} \hat{b}_i \rightarrow \hat{S}_i \equiv \hat{\sigma}_i^x - i\hat{\sigma}_i^y \quad \text{and} \quad \frac{2}{\sqrt{n+1}} \hat{b}_i^\dagger \rightarrow \hat{S}_i^\dagger \equiv \hat{\sigma}_i^x + i\hat{\sigma}_i^y \quad (5.2)$$

in the effective Bose-Hubbard Hamiltonian (3.29) yields the quantum XY Hamiltonian

$$\hat{\mathcal{H}}_{\text{XY}} = -\frac{n+1}{4} \sum_{\langle i,j \rangle} J_{ij}^{\text{eff}} (\hat{\sigma}_i^x \hat{\sigma}_j^x + \hat{\sigma}_i^y \hat{\sigma}_j^y + \hat{\sigma}_j^x \hat{\sigma}_i^x + \hat{\sigma}_j^y \hat{\sigma}_i^y) + \frac{1}{2} \sum_i (\mu_i + nU) \hat{\sigma}_i^z \quad (5.3)$$

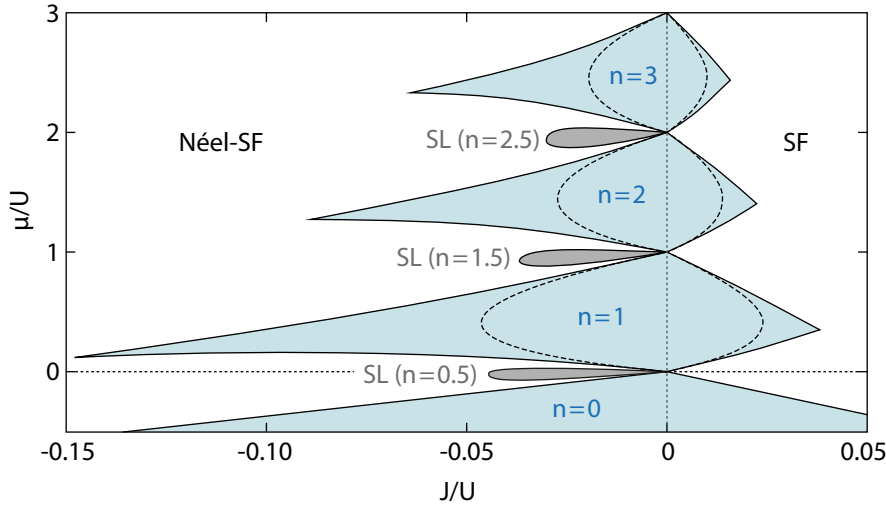


Figure 5.2: Phase diagram for ferromagnetic and antiferromagnetic coupling for a slightly asymmetric triangular lattice. The superfluid phase with negative tunneling matrix elements is labeled a *Néel*-superfluid. Due to geometric frustration, the characteristic Mott insulator lobes with integer filling (blue shaded regions) extend further into the antiferromagnetic region. Dashed lines in the lobes indicate the corresponding results of a mean-field calculation. In between the Mott lobes, spin-liquid phases with half-odd-integer fillings are expected to appear for antiferromagnetic coupling (gray bubbles). The figure was modeled after Ref. [140] with kind permission of A. Eckardt.

where the $\hat{\sigma}_i^x$, $\hat{\sigma}_i^y$ and $\hat{\sigma}_i^z$ denote the spin-1/2 Pauli operators at lattice site i . The harmonic trapping potential is incorporated by the site-dependent chemical potential μ_i . In contrast to the weakly interacting regime, the local ground state of the quantum XY system cannot be expressed as a product state since $|\vartheta_i, \varphi_i\rangle$ cannot simultaneously be an eigenstate of $\hat{\sigma}_i^x$ and $\hat{\sigma}_i^y$.

5.1.2 Frustration and ground-state degeneracy

The mapping of occupation numbers to quantized spins has a profound influence on the ground state of the triangular lattice. In analogy to the rotor model of phases in the classical XY model discussed in the preceding chapter, the spins on a triangular plaquette cannot all be aligned antiparallel with respect to each other. In the weakly interacting regime, this geometric frustration results in a compromised alignment of local vector spins at 120° and a two fold degenerate global ground state. In contrast, the quantized nature of the mapping to a spin-1/2 representation in the strongly interacting regime inhibits such a compromise as depicted in Fig. 5.1c. Instead, the ground state of a *single* lattice plaquette is already six-fold degenerate as the energetically unfavorable alignment of spins can be located at all three bonds in two different combinations, namely $|\uparrow\uparrow\rangle$ and $|\downarrow\downarrow\rangle$. The number of degenerate ground states W grows exponentially with the number of lattice sites N_{sites} according to $W = \exp(\mathcal{S}N_{\text{sites}}/k_B)$ where \mathcal{S} denotes the *extensive* entropy per

lattice site and k_B is the Boltzmann constant [238]. The extensive entropy of the triangular lattice can be calculated as

$$\mathcal{S} = \frac{2k_B}{\pi} \int_0^{\pi/3} \ln(2 \cos \phi) d\phi \approx 0.323 k_B. \quad (5.4)$$

Note that, compared to the triangular lattice, the extensive entropy of the *kagome* lattice is even larger as it exhibits a particularly high degree of frustration. The large degree of degeneracy strongly enhances fluctuations in the frustrated system and can suppress magnetic ordering of individual spins even at zero temperature. Instead, pairs of antiferromagnetically interacting spins $|\uparrow\rangle$ and $|\downarrow\rangle$ can form spin-0 singlet states comprised of a coherent superposition $(|\uparrow\downarrow\rangle + |\downarrow\uparrow\rangle)/\sqrt{2}$ in analogy to valence bonding. A fixed spatial order of such singlets breaks the translational symmetry of the lattice and forms a so-called valence bond solid. In contrast, quantum fluctuations may give rise to a superposition state of a large variety of partitionings which preserves both translational and spin-rotational symmetries. Such an exotic, highly disordered state - the so-called *resonating valence bond spin liquid* [127, 239], illustrated in Fig. 5.1d - is suggested to be a possible explanation for high- T_c superconductivity in cuprates [128].

5.1.3 Quantum phases on the frustrated triangular lattice

The phase diagram of bosons on the triangular lattice incorporating both ferromagnetic and antiferromagnetic coupling can be mapped by studying quantum fluctuations in a generalized Bogoliubov approach [140, 240]. For moderately larger fillings than $n = 1$ the bosonic annihilation and creation operators can already be approximated by the well-known number-phase representation incorporating quantum fluctuations of both the local phases and the local particle numbers:

$$\hat{b}_i \approx \sqrt{N_i + \delta N_i} e^{i(\varphi_i + \delta\varphi_i)} \quad \text{and} \quad \hat{b}_i^\dagger \approx \sqrt{N_i + \delta N_i} e^{-i(\varphi_i + \delta\varphi_i)}. \quad (5.5)$$

The calculated phase diagram of Ref. [140] resulting from a second-order expansion of the fluctuations in the effective Bose-Hubbard Hamiltonian for a triangular lattice with slightly asymmetric tunneling amplitudes $J'/J = 1.3$ is shown in Fig. 5.2. As a striking feature, the characteristic Mott insulator lobes [241] with integer filling extend way further into the antiferromagnetic coupling region. This behavior is a direct consequence of geometric frustration. In between the Mott lobes, spin-liquid phases, indicated by gray bubbles, are expected on the antiferromagnetic coupling region for half-odd-integer fillings.

In contrast to the clearly distinguishable momentum peaks in absorption images of the Néel-superfluid which was treated in the preceding chapters, experimental time-of flight signatures of both the frustrated Mott insulator and the spin-liquid phases are harder to detect as the first order correlation function vanishes (see section 2.5). In the following, we will focus on the superfluid to Mott insulator transition for ferromagnetically and

antiferromagnetically coupled bosons and will attempt to evidence the presence of a Mott-insulating state in both regimes by means of quantum noise correlations. An unambiguous distinction between a Mott-insulating state and a quantum spin liquid in optical lattice systems, however, should in principle be achievable by single-site resolved measurements [62–65] of number fluctuations.

5.2 Characterization of the Mott-insulating phase

The main goal of experiments presented in this chapter is the realization and study of the strongly-correlated antiferromagnetic Mott insulator (MI) phase in the triangular lattice. Hereby, monochromatic lattice driving is used to engineer the amplitude and sign of the coupling in accordance with the experimental techniques described in chapter 3. It is, thus, crucial to first characterize the Mott insulator quantum phase in the static lattice before investigating the driven lattice further. In the following section we will investigate properties and experimental signatures of the superfluid to Mott insulator transition and the Mott-insulating phase for a stack of decoupled, two-dimensional triangular lattice planes.

The discussed Holstein-Primakoff mapping of particle number occupations onto quantum spin- $1/2$ states is valid only in the hard-core boson limit of strong interactions, i.e. $U \gg |J|$. In order to reach this regime in the triangular three-beam lattice we utilize a strongly confining retro-reflected one dimensional lattice that is aligned perpendicular to the triangular lattice plane. For sufficiently deep 1D-lattice depths, the resulting atomic ensemble consists of a stack of non-interacting two-dimensional layers of triangular lattices. Note that we have already briefly discussed such a three-dimensional lattice array in the context of multi-photon excitations in section 3.3.3.

5.2.1 Superfluid to Mott insulator transition

Experimentally, the strongly interacting triangular lattice layer system is prepared by first adiabatically loading a BEC from the elliptical crossed dipole trap into the retro-reflected 1D-lattice with an exponential ramp of the lattice depth to its final value of typically $V_{0,1D} = 30 E_R$ to $50 E_R$ in $T_{R,1D} = 500$ ms. Subsequently, the three-beam lattice depth is increased with a similar ramping shape in $T_{R,2D} = 100$ ms to its final lattice depth. This experimental sequence was chosen after various other ramp shapes such as linear and sigmoidal ramps have been tested as well as different timescales and ordering of the ramping procedure. It yields the optimal results concerning the adiabatic preparation with minimum heating processes involved.

We investigate the superfluid to Mott insulator transition by varying the final triangular lattice depth and, thereby, the ratio between the on-site interaction U and the tunneling amplitude J . In order to account for the dimensionality of the three-dimensional system it is convenient to describe the transition in terms of this dimensionless ratio while weighting

the tunneling amplitudes with their respective coordination number, i.e. $n_c = 6$ for the triangular lattice and $n_c = 2$ for the retro-reflected 1D-lattice.

In Fig. 5.3a, time-of-flight images are shown for an increasing triangular lattice depth and, hence, an increasing ratio between the on-site interaction U and the weighted tunneling $6J_{2D} + 2J_{1D}$. As interactions become more and more dominant, the coherence of the atomic ensemble is lost, finally leading to a featureless Gaussian density distribution. A common observable for the quantification of the first order correlation of the time-of-flight momentum distribution according to Eq. (2.37) is the *visibility*. In close analogy to the previously introduced superfluid peak contrast of the one-dimensional lattice (see Fig. 3.2) it is defined as the normalized difference of the number of atoms at the positions of the first-order superfluid momentum peaks and regions in between the peaks, which have the same distance from the center of the momentum distribution (see inset in Fig. 5.3b).

Measurements of the visibility for an increasing lattice depth are shown as blue markers for a variety of initial atom numbers and two different 1D-lattice depths of $V_{0,1D} = 30 E_R$ and $50 E_R$ in Fig. 5.3b. In the superfluid regime, the visibility is close to unity as the incoherent background density is negligible. A slight depletion of the visibility signal can be attributed to deviations from the ideal quasimomentum distribution resulting from the finite system size and time-of-flight as discussed in section 2.5. The visibility signal decreases as the 2D-lattice depth and with it the ratio $U/(6J_{2D} + 2J_{1D})$ is increased. Values of the bare tunneling amplitudes J_{2D} and J_{1D} as well as the three-dimensional on-site interaction energy U are calculated by evaluating the respective Wannier integrals of Eq. (2.21) and (2.22). The smooth transition of the visibility as the phase boundary to the MI-state is crossed stems from the inhomogeneity of the system. Harmonic confinement of the atomic ensemble results in a site-dependent chemical potential which leads to the continuous formation of various Mott shells in the characteristic *wedding cake* pattern with superfluid regions in between Mott insulator shells with integer particle numbers per lattice site that increase towards the center of the trap (compare vertical lines, i.e., increasing chemical potential, in Fig. 5.2) [55, 242–244]. For a deep triangular lattice the phase coherence has vanished completely in accordance with the product of local Fock states given in Eq. (2.25).

A transition point from the superfluid to the Mott-insulating state is often defined at the ratio of U/J where the superfluid order parameter vanishes. Due to the harmonic confinement and simultaneous presence of Mott-insulating shells and superfluid states, the transition to a Mott-insulating state is continuous and the visibility signal exhibits a smooth shape. It is, thus, convenient to define the transition point by the zero-crossing of a linear fit to the region with maximal slope of the visibility signal. For the presented data this yields a value of $U/(6J_{2D} + 2J_{1D})_{\text{SFMI}} \approx 60$. In contrast, we define the transition at the ratio where the visibility signal starts to decrease linearly, since we rely on the appearance of coherent interference peaks as the main observable for the superfluid Néel ordering in the system. Hence, the transition point is defined at a value of $U/(6J_{2D} + 2J_{1D})_{\text{SFMI}} \approx 4$ to 5 in the following. A detailed discussion of the superfluid to Mott insulator transition in

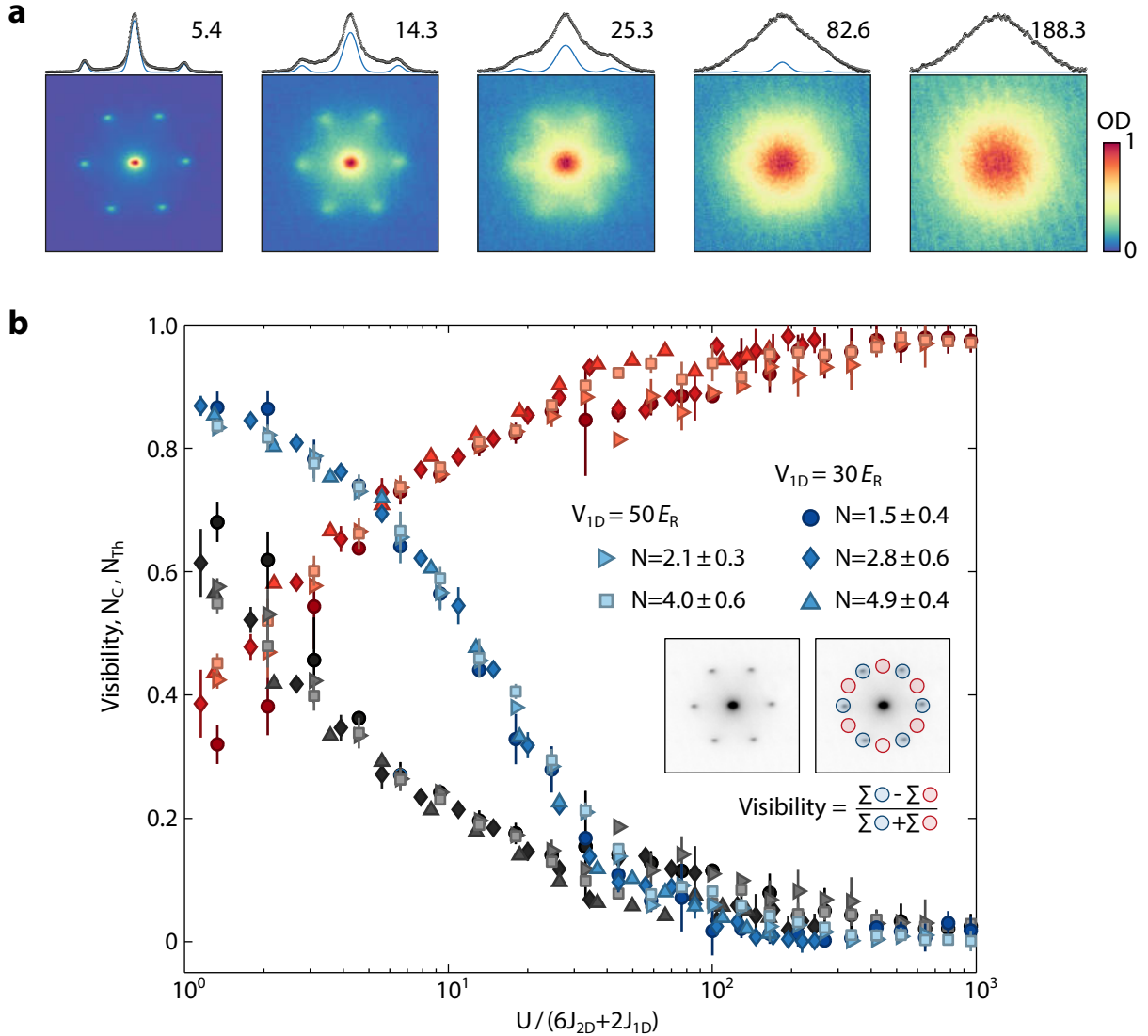


Figure 5.3: Superfluid to Mott insulator transition in the 2D-layer triangular lattice. **a** Time-of-flight images of the quasimomentum distribution for increasing ratio of $U/(6J_{2D} + 2J_{1D})$. The respective values are shown in the upper right corners of each image, together with their central density profiles. The decrease of condensate fraction (blue solid lines) and the degree of coherence is clearly visible. For dominating interactions the density profile is well described by a single Gaussian distribution. The optical density of each image has been normalized to its maximum value. **b** Visibility (blue), condensate fraction N_C (black) and incoherent thermal fraction N_{Th} (red) are plotted against the logarithmic ratio of on-site interaction and tunneling $U/(6J_{2D} + 2J_{1D})$ for a variety of initial atom numbers and two different values of the perpendicular 1D-lattice depth (see legend). Error bars denote the standard deviation of the averaged values. The definition of the visibility is exemplified in the inset for an absorption image in the superfluid regime. Regardless of total particle number $N \times 10^5$ or 1D-lattice depth, all individual measurements coincide.

the 2D-layered triangular lattice and its difference from the isotropic 3D-system is given by Becker *et al.* [74].

Together with the visibility, the coherent condensate fraction N_C and the incoherent (thermal) fraction of the absorption images are plotted. Both values are obtained by extracting integrals of bimodal Gaussian fits from individual absorption images. As a central result of the depiction in Fig. 5.3b, all data coincide regardless of the systems particle number or confining 1D-lattice depth.

5.2.2 Lifetime of the Mott-insulating state

In order to be able to investigate the time-averaged effective quantum XY model in the hard-core boson limit of strong interactions it is crucial to ensure that the Mott-insulating state is long-lived. Indeed, possible heating mechanisms due to technical noise as well as scattering of lattice photons might destroy the Mott-insulating state.

However, due to the maximized phase fluctuations of the local Fock states, the time-of-flight momentum distribution of a MI-state is a featureless Gaussian density profile that cannot be distinguished from a density distribution of a thermal gas. We thus probe the MI-lifetime for different maximum lattice depths by ramping the lattice back to a fixed shallow 2D-lattice depth of $4.0 E_R$ in the superfluid regime as plotted in Fig. 5.4a. As a consequence, long-range phase coherence is rapidly restored over the entire lattice on the order of a tunneling time $\tau_{\text{Th}} = \hbar/J$ [56]. The corresponding tunneling time along the shallow triangular lattice is $\tau_{\text{Th}} \approx 7.6$ ms for $V_{0,2D} = 4.0 E_R$. In contrast, incoherent parts of the atomic ensemble which are excited from the Mott-insulating state due to technical heating do not contribute to the recovery of coherence. Hence, the resulting decay of recovered visibility is a direct measure of the MI-lifetime.

Results shown in Fig. 5.4b exhibit an exponential decay of visibility with respect to the holding time in the deep MI-lattice. Furthermore, the corresponding decay constant increases rapidly for larger lattice depths above $8.0 E_R$, corresponding to values of $U/(6J_{2D} + 2J_{1D}) > 150$ (see inset in Fig. 5.4b). Nevertheless, the extracted MI-lifetimes remain at values well above 100 ms even for deep lattice depths and strong interactions.

As a result, the finite lifetime of the Mott-insulating state is not a limiting factor for the study of the quantum spin-1/2 XY model: as we will see in the following, technical heating processes associated with far off-resonant periodic lattice driving are generally an order of magnitude larger in the three-dimensional lattice.

5.2.3 Detecting on-site excitations

In the strongly interacting limit of $U \gg |J|$ the excitation spectrum of an atomic ensemble in an optical lattice is significantly altered. The lowest lying excitation for a Mott-insulating state is the creation of a particle-hole pair corresponding to an additional energy of U [56, 241, 245]. Thus, in contrast to the smooth gapless excitation spectrum

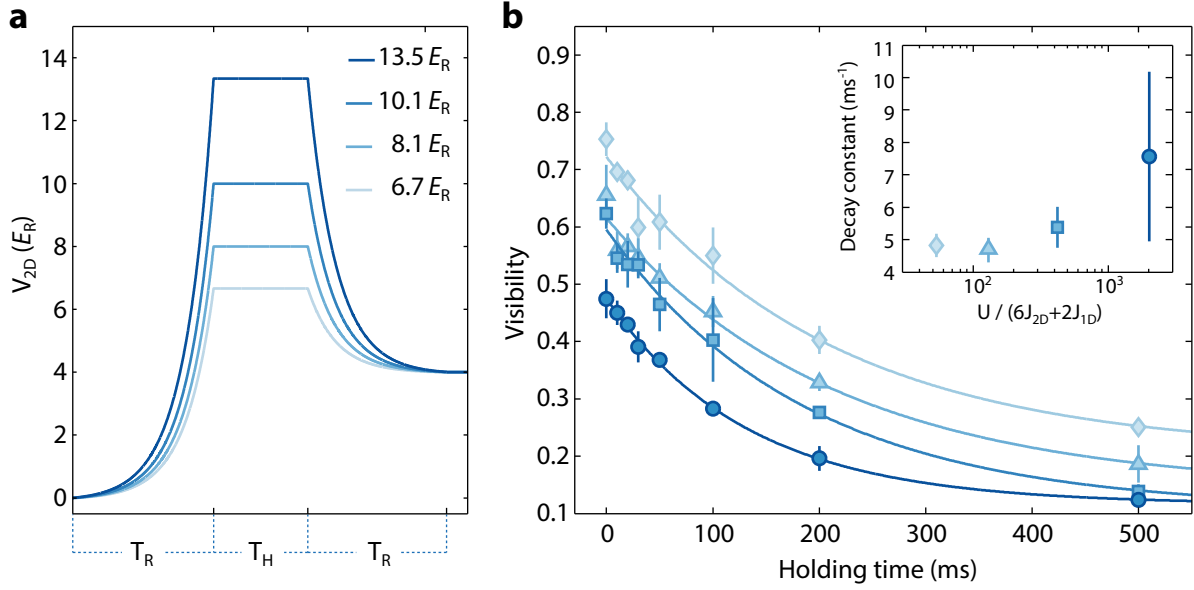


Figure 5.4: Mott insulator lifetime measurement. **a** The lifetime of the Mott-insulating state is determined for four different lattice depths in the Mott-insulating regime by holding the system at these depth for a variable time T_H before ramping the lattice down again into the superfluid regime at a fixed depth of $4.0 E_R$. **b** The recovered visibility is plotted in dependence of the holding time. Error bars denote the standard deviation of averaged data. Solid lines are exponential fits to the data. An increase of the decay constant with an increasing maximum lattice depth and, thus, ratios of $U/(6J_{2D} + 2J_{1D})$ can be observed (see inset). Error bars of the decay constant values indicate the 95% confidence interval of the exponential fits.

of a superfluid state, the Mott-insulating state exhibits a gapped energy spectrum with resonances at multiples of U . The emergence of such resonances that were detected using potential gradients between lattice wells in order to facilitate particle-hole creation was the first unambiguous evidence for the presence of the MI-state of an ultracold bosonic quantum gas in a deep optical lattice [56].

Here, we probe the excitation spectrum of the MI-state by using amplitude modulation of the lattice potential. Starting from a deep optical lattice, the lattice depth is periodically modulated for a time between 20 ms and 40 ms with an amplitude of approximately 10% to 20% of the maximum lattice depth. The frequency of the modulation is varied from shot to shot. For modulation frequencies matching a multiple of the on-site interaction energy U excitations are expected due to the induced creation of particle-hole pairs. Subsequently, we ramp down the lattice potential completely, allowing the system to form a BEC. We detect the amount of excitations generated in the system by extracting the remaining condensate fraction with respect to an incoherent background with a bimodal Gaussian fit.

In Fig. 5.5a excitation spectra are shown for three different modulation parameters for an intermediately deep optical lattice of $5 E_R$ and an additional perpendicular 1D-lattice

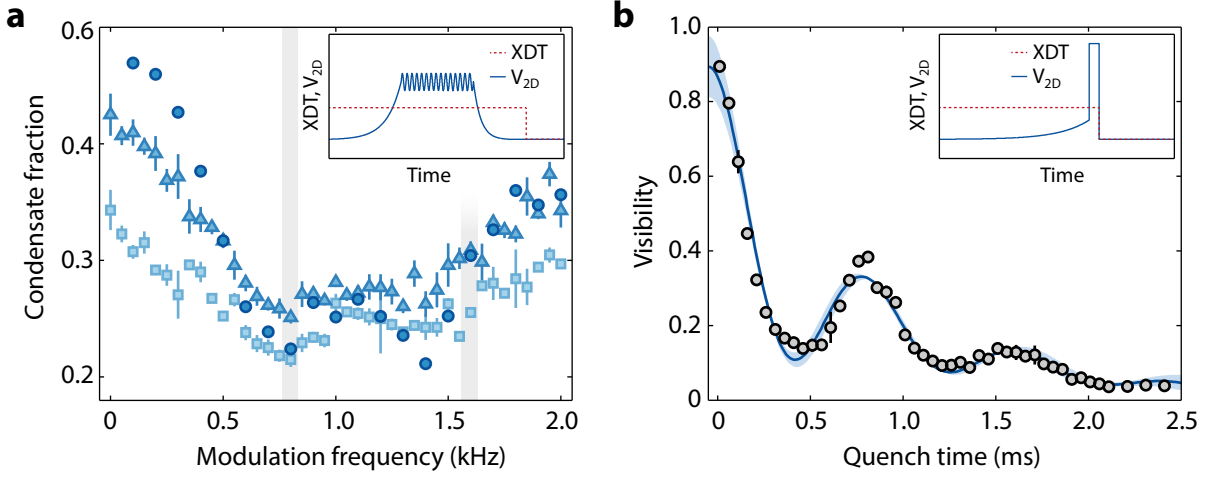


Figure 5.5: Experimental detection of the on-site interaction energy U in the Mott-insulating state. **a** Excitation spectra obtained with amplitude modulation as illustrated in the inset. The lattice amplitude was modulated by: 20% for 20 ms (circles), 10% for 40 ms (triangles) and 20% for 40 ms (squares). Gray vertical lines indicate the expected resonance positions at U and $2U$. **b** Collapse-and-revival measurement of the bosonic matter wave field. A sudden quench into the deep Mott-insulating regime (see inset) results in dynamic revivals of coherence on timescales of $t_{\text{rev}} = h/U$ due to the rephasing of local coherent states that can be detected as an increase of visibility (black circles). The solid blue line is a fit to the data consisting of an exponentially decreasing cosine with an additional linearly decreasing offset. Blue shaded areas around the line indicate the 95% confidence interval of the fit.

of $30 E_R$. An excitation resonance at the expected value of $U \approx 798$ Hz can clearly be identified. However, the spectrum is significantly broadened due to the strong modulation. A second resonance peak as in Ref. [56] is not evident. In conclusion, the limited quality of the amplitude modulation spectra together with the need for strong perturbations of the robust Mott-insulating state on timescales of tens of milliseconds likely renders the amplitude modulation technique impractical for the detection of particle-hole excitations in the antiferromagnetic MI.

A different approach of experimentally detecting the on-site interaction energy of a deep optical lattice is given by the dynamic behavior of a matter-wave field [246]. As discussed in section 2.3.2, the local eigenstates of N_i atoms confined to deep optical lattice wells i with governing on-site interaction $U \ll |J|$ are Fock number states $|N_i\rangle$. According to the Bose-Hubbard Hamiltonian (2.20) the corresponding local eigenenergies are $E_i = N_i(N_i - 1)U/2$. With this, the time evolution of $|N_i\rangle$ is simply given by

$$|N_i(t)\rangle = e^{-iE_i t/\hbar} |N_i(0)\rangle. \quad (5.6)$$

In contrast, the local wave functions can be expressed as coherent states $|\alpha_i\rangle$ in the superfluid regime that exhibit a Poissonian particle number distribution. In the Fock

basis such coherent states can be expressed as

$$|\alpha_i\rangle = e^{-|\alpha|^2/2} \sum_{n=0}^{\infty} \frac{\alpha^n}{\sqrt{n!}} |n\rangle, \quad (5.7)$$

where α is a complex amplitude linked to the average atom number per site $\bar{N} = |\alpha|^2$. By suddenly quenching the optical lattice potential from the superfluid regime into a deep lattice, the initially coherent states will evolve in time as a superposition of the new Fock eigenstates according to

$$|\alpha_i(t)\rangle = e^{-|\alpha|^2/2} \sum_{n=0}^{\infty} \frac{\alpha^n}{\sqrt{n!}} e^{-in(n-1)Ut/2\hbar} |n\rangle. \quad (5.8)$$

This time evolution has a profound effect on the coherence properties of the atomic matter wave field. The different time evolutions of atom number states result in a fast collapse of long-range phase coherence. However, all phase factors in the above equation rephase for integer multiples of a revival time t_{rev} that is solely determined by the on-site interaction energy $t_{\text{rev}} = \hbar/U$ [246–248].

In Fig. 5.5b, such measurements of initial collapse and subsequent revival of coherence are depicted. Hereby, the optical lattice was suddenly quenched from an initially superfluid regime at $3.2 E_R$ to a value of $16.2 E_R$ and held there for a variable quench time before all confining potentials are shut off and the interference visibility is evaluated after time-of-flight. The characteristic revival behavior is observed, although less distinct as in Ref. [246]. A fit to the data, consisting of an exponentially decreasing cosine squared with an additional linearly decreasing background yields a revival time of $t_{\text{rev}} = 788 \pm 17 \mu\text{s}$, which corresponds to an on-site interaction energy of $U = 1.27 \pm 0.03 \text{ kHz}$. This result is significantly smaller as the theoretically expected value at the present lattice depths of $U = 1.59 \pm 0.05 \text{ kHz}$. However, the remaining discrepancy likely stems from imperfections of the lattice intensity regulation on such small timescales.

From the experiments discussed above we conclude that a robust Mott-insulating state can be prepared in the three beam lattice with additional perpendicular confinement of a deep one-dimensional lattice. In the following section we will investigate, whether the antiferromagnetic side of the phase diagram of Fig. 5.2 can be investigated by means of periodic lattice driving.

5.3 Realization of the antiferromagnetic Mott insulator by lattice driving

Experimentally, a Mott-insulating state can also be prepared using the far off-resonant time-periodic driving scheme presented in chapter 3. The ability to tune the tunneling amplitude independently from the on-site interaction energy enables the experimenter to reach the strongly interacting regime of $U \gg |J|$ without increasing the lattice depth

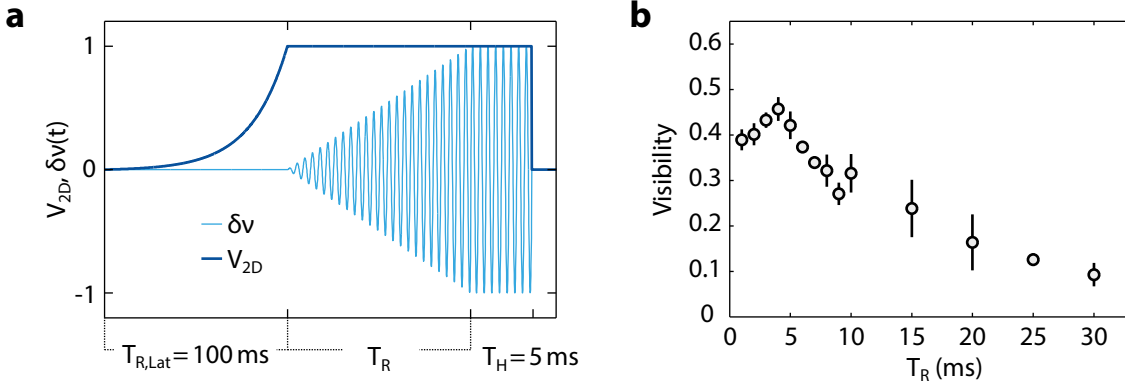


Figure 5.6: Ramping timescales of the lattice driving in the strongly confined 3D-lattice are investigated for lattice parameters of $V_{1D,0} = 30 E_R$ and $V_{2D,0} = 4.25 E_R$. **a** Illustration of the ramping procedure: After the 2D-lattice is ramped up (dark blue line) the driving (light blue) is linearly ramped up (not to scale). While the linear ramping time of the driving is modified, driving is maintained at the maximum amplitude of $K = 3.82$ for 5 ms. **b** A clear maximum in the remaining visibility of the momentum distribution can be identified at a ramping time of 4 ms.

[94, 95]. Here, we explore the feasibility of this technique for the creation of an antiferromagnetic Mott insulator and the mapping of the phase diagram of Fig. 5.2. As the striking consequence of the induced geometric frustration in the quantum spin- $1/2$ XY model, the Mott lobes extend to larger values on the antiferromagnetic side of the phase diagram. Hence, the observation of a shift in the transition point from an antiferromagnetic Mott insulator to the Néel-superfluid as compared to the conventional superfluid to Mott insulator transition discussed in the previous section represents a *smoking-gun* of the high degree of degeneracy arising from geometric frustration.

5.3.1 Limitations of the parameter space

The coherent engineering of tunneling matrix elements by periodic driving imposes several constraints onto the optical lattice system. In chapter 3 we have identified the emergence of multi-photon resonances for lattice driving as the main source of detrimental heating processes. As a consequence, time-averaged effective model Hamiltonians can only be created in systems with a sufficiently large energy gap between the two lowest bands such that atoms subjected to strong forcing cannot be coupled to higher energy bands. For a homogeneous forcing amplitude of $K = 3.82$, yielding the largest negative tunneling matrix element along all lattice bonds of the triangular lattice, the narrow experimentally feasible parameter space has been mapped out in Fig. 3.9. As a central result, the coherent engineering of maximally negative effective tunneling matrix elements is possible only above a critical lattice depth of $V_{2D,c} \approx 4.0 E_R$ in the triangular lattice.

Furthermore, experiments carried out in the strongly confined three-dimensional lattice have to take account for the limited lifetime of the driven system on the order of a

few milliseconds. The optimal linear ramping time of the periodic driving in the strongly confined three-dimensional lattice is investigated in Fig. 5.6. In addition, coherence levels are significantly reduced in the 3D-system (compare Fig. 3.10). This circumstance can be attributed to the absence of two beneficial mechanisms in the strongly confined three-dimensional lattice system: First, additional entropy introduced into the atomic ensemble by the strong forcing cannot be redistributed along the axis perpendicular to the triangular lattice as it is the case for the array of elongated tubes that is present without an additional 1D-lattice. Second, the actual tunneling rates in the three-dimensional system along the triangular lattice plane are significantly reduced in comparison to a triangular lattice of the same potential depth comprised of an array of tubes. This peculiarity stems from the additional Bose enhancement of tunneling between elongated tubes with a large occupation number. Moreover, in contrast to the three-dimensional array of tubes, the Mermin-Wagner-Hohenberg theorem explicitly forbids the formation of true long-range phase ordering due to short-range interactions in pure two-dimensional systems [249, 250]. As a consequence, a coherent Néel-ordered superfluid as treated in chapter 4 is not expected for the stacked array of 2D-triangular lattice that is created by a strongly confining perpendicular 1D-lattice.

The necessarily short timescales of the driving combined with relatively long tunneling times of $\tau_{\text{Th}} > 5$ ms along the triangular lattice plane render the engineering of a frustrated Mott-insulating state in the quantum spin- $1/2$ XY model and the mapping of the phase diagram of Fig. 5.2 a difficult task to undertake. It should, however, be noted that, regardless of the limited timescales, MI-states have been successfully prepared by periodic driving techniques in non-frustrated cubic lattice geometries [95]. In the following, we discuss the feasibility of creating a frustrated Mott insulator and the investigation of the quantum phase transition to a Néel superfluid on the antiferromagnetic side of the phase diagram depicted in Fig. 5.2.

We aim for the realization of a frustrated Mott insulator in the hard-core boson limit of strong interactions by starting with an array of non-interacting two-dimensional superfluids in the triangular lattice that is created by a strong perpendicular confinement of a 1D-lattice on the order of $V_{1\text{D},0} = 30 E_{\text{R}}$ to $50 E_{\text{R}}$.

Effects of the tuning of the tunneling amplitude by periodic lattice driving are exemplified in Fig. 5.7a. Here, the triangular lattice depth is plotted against the forcing parameter K and resulting ratio of $U/(6J_{2\text{D}} + 2J_{1\text{D}})$ for a confining 1D-lattice of $V_{1\text{D},0} = 30 E_{\text{R}}$. The dashed red line indicates the position of maximally negative tunneling at a forcing parameter of $K = 3.82$ and the gray solid lines mark triangular lattice depths of $2 E_{\text{R}}$, $4.25 E_{\text{R}}$ and $8 E_{\text{R}}$. It is evident that an increase of the forcing amplitude and the resulting decrease of the tunneling amplitude in the triangular lattice $J_{2\text{D}}$ easily allows for the creation of dominating on-site interactions as values of $U/(6J_{2\text{D}} + 2J_{1\text{D}}) > 100$ can be reached for all initial triangular lattice depths. Yet, the weakly interacting superfluid regime is hard to reach for negative tunneling matrix elements: Already for an initial triangular lattice depth of $4.25 E_{\text{R}}$, where the driving scheme yields the best results (compare Fig. 3.9), the

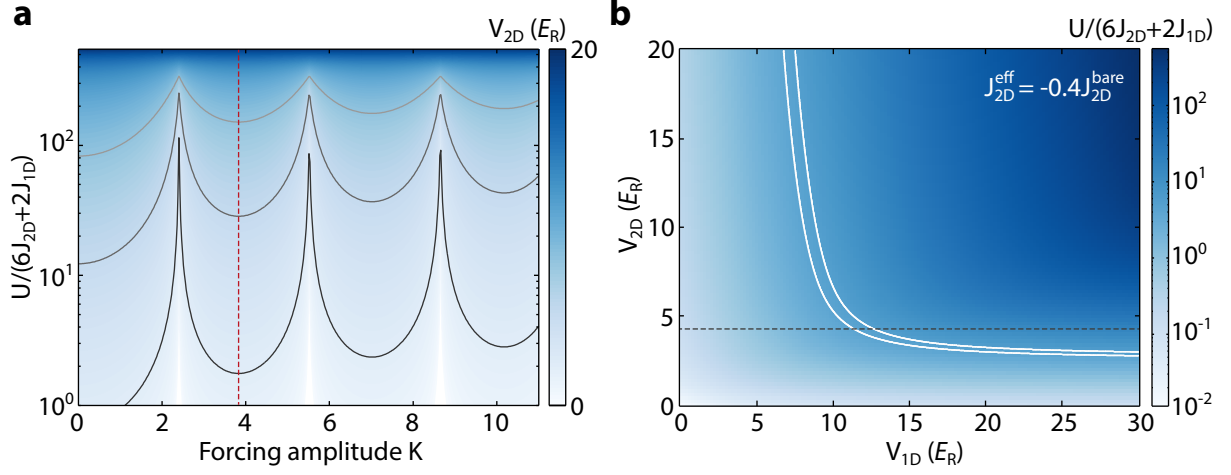


Figure 5.7: Lattice driving parameters in the strongly interacting regime. **a** 2D-lattice depth in dependence of the dimensionless forcing amplitude K and the ratio of on-site interaction to tunneling $U/(6J_{2D} + 2J_{1D})$ for a 1D-lattice depth of $30 E_R$. The dashed red line indicates the position of maximally negative effective tunneling. Solid gray lines mark values for the V_{2D} of 2, 4.25 and $8 E_R$. **b** The ratio of on-site interaction to tunneling is plotted in dependence of both 1D- and 2D-lattice depth for an effective tunneling amplitude of $0.4J_{2D}^{\text{bare}}$. The dashed black line marks $V_{2D} = 4.25 E_R$ and white lines indicate the boundaries for $U/(6J_{2D} + 2J_{1D}) = 4$ and 5. Here the atomic ensemble is expected to be in the Néel superfluid.

total reduction of the tunneling amplitude to $|J_{2D}^{\text{eff}}| = 0.4J_{2D}^{\text{bare}}$ at the minimum of the renormalizing Bessel function gives a minimum value of $U/(6J_{2D} + 2J_{1D}) = 16.1$ that is still on the Mott-insulating side of the phase diagram.

In Fig. 5.7b we explore the resulting ratio of $U/(6J_{2D} + 2J_{1D})$ for the maximally negative tunneling amplitude in dependence of both the perpendicular 1D- and the triangular 2D-lattice depth. Here, the dashed black line indicates the optimal 2D-lattice depth of $4.25 E_R$ while the two white lines mark the boundaries of the on-site interaction to tunneling ratios of $U/(6J_{2D} + 2J_{1D}) = 5$ and $U/(6J_{2D} + 2J_{1D}) = 4$ where the appearance of a superfluid is expected.

As a result of the previous considerations, the mapping of the quantum phase transition from a strongly interacting antiferromagnetic Mott insulator to the Néel-superfluid by increasing the periodic driving of the triangular lattice should only be possible for rather shallow depths of the confining 1D-lattice below $V_{1D} \approx 12 E_R$. The system cannot be treated as individual two-dimensional triangular lattice layers anymore in such a regime as tunneling perpendicular to the lattice planes becomes significantly large.

However, assuming that the relatively short achievable timescales of the lattice driving do not constitute a fundamental problem according to Ref. [95], the realization of the strongly interacting antiferromagnetic Mott insulator appears to be an experimentally feasible task.

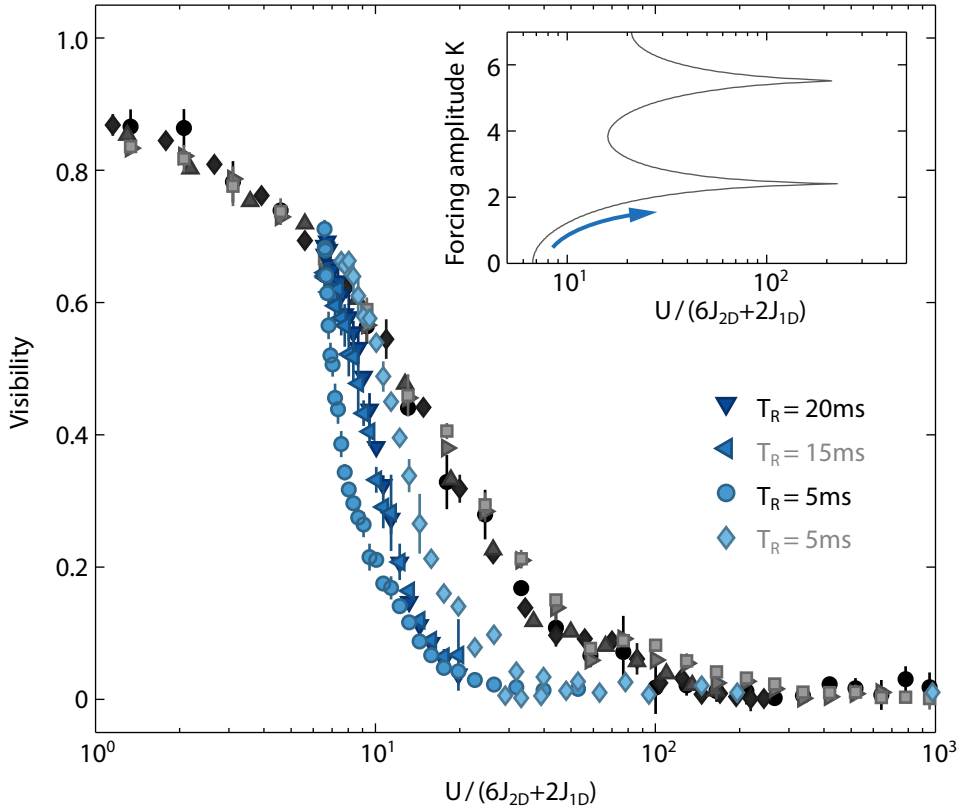


Figure 5.8: Superfluid to Mott insulator transition in the driven lattice. By increasing the periodic forcing amplitude the ratio of on-site interaction and tunneling amplitude (see inset). The measured visibility for different ramping times and procedures (blue data points) decreases significantly faster as compared to the static superfluid to Mott insulator transition (black and gray data points).

5.3.2 Superfluid to Mott insulator transition in the driven lattice

As we have reasoned in the preceding section, the antiferromagnetic Mott-insulating state of dominating on-site interaction energy U can be reached in the three-dimensional lattice system by employing the far off-resonant periodic driving technique to tuning the tunneling matrix elements of the triangular lattice to small negative values. For this purpose, we prepare the atomic ensemble close to the Mott-insulating regime at a triangular lattice depth of $4.25 E_R$, where the driving in the purely triangular lattice has yielded the optimal results in terms of preserved coherence. The presence of a strong perpendicular 1D-lattice of $30 E_R$ results in a stack of two-dimensional superfluid states. Here, the ratio between on-site interaction energy and (bare) tunneling is $U/(6J_{2D} + 2J_{1D}) = 6.7$.

For the data presented in Fig. 5.8 the ratio $U/|J|$ is gradually increased by increasing the periodic forcing amplitude K while the lattice depths are held fixed (see ramping procedure in the inset). Blue data points show the observed visibility for several linear ramping times of the driving in an atomic ensemble with in total $N = (4.9 \pm 0.7) \times 10^5$

particles. For comparison, black and gray data points depict the visibility measurements performed in the static 3D lattice as shown in Fig. 5.3. Ideally, data obtained for the driving should coincide with the static case as the relevant parameter is given in both cases by the ratio between on-site interaction and tunneling. However, it is evident that the lattice driving scheme results in a faster decrease of visibility as compared to the static measurements. This is also the case if the periodic driving is linearly decreased to a value of zero before the time-of-flight imaging. In Fig. 5.8 these measurements are indicated by a gray legend entry.

The observed behavior of the visibility puts the experimental feasibility of reaching the antiferromagnetic Mott-insulating regime with periodic lattice driving into question. Nevertheless, in order to prove or disprove the presence of a Mott-insulating state in the driven system a more reliable observable than the extracted visibility is needed. Greiner *et al.* have observed the appearance of a discrete excitation spectrum at integers of the on-site interaction energy U as the unambiguous verification of a Mott-insulating state. The excitation spectrum could be reproduced by Zenesini *et al.* [95] in the driven Mott insulator by modulating the tunneling amplitude itself with an additional modulation of the driving amplitude. This technique has the advantage of leaving all other lattice parameters unchanged. In contrast, the lattice amplitude modulation employed for the detection of the on-site interaction energy in the static lattice (see Fig. 5.5b) is impractical for the driven system for two reasons: First, comparatively long timescales are needed for the modulation that exceed the lifetime of the driven system. Second, as we have extensively demonstrated in chapter 3, the driven system is extremely sensitive to a change of the lattice depth which may give rise to additional multi-photon transitions.

On these grounds we have employed the modulation of the effective tunneling amplitude used in Ref. [95] in order to detect the gapped excitation spectrum. Yet, no distinguishable signal could be observed on the short timescales of the lattice driving. On the one hand, the absence of such a signal could be interpreted as the absence of a Mott-insulating state in general. On the other hand the failure of the tunneling modulation method can also be attributed to the short timescales of the driving: as the final forcing amplitude can only be maintained for 5 ms, the detection of an on-site interaction energy at the calculated value of $U = 720$ Hz corresponds to a modulation of merely 3.6 cycles, which may not be enough to introduce a significant amount of excitations to the system.

5.4 Quantum noise correlation analysis of the Mott-insulating state

In the preceding section we have argued that the detection of the Mott-insulating state in the driven system is generally difficult. Moreover, due to the absence of phase coherence accompanied by vanishing first order correlations, the momentum distribution of such a strongly correlated atomic ensemble does not exhibit any interference structures after the

ballistic time-of-flight expansion. Instead, the density distribution is solely determined by the structureless Wannier envelope in Eq. (2.37) which can be well approximated by a Gaussian distribution in the limit of deep lattice potentials. However, the initially featureless single-shot Gaussian column density distributions contain additional information hidden in fluctuations around their average values that originates from correlations of intrinsic quantum noise [57, 251]. In the following, we will discuss the underlying principles of such quantum noise correlations and utilize them in order to verify the presence of a Mott-insulating state in both the static and the driven strongly correlated 3D lattice system. For a thorough treatment of the application and implementation of the noise correlation analysis technique in the field of ultracold atomic gases we refer to Ref. [252] and [253].

5.4.1 Hanbury Brown-Twiss interferometry

Time-of-flight imaging relies on the sudden release of an ensemble of particles and a subsequent ballistic expansion before an integrated column density profile is obtained by detecting the shadow cast by the expanded cloud onto a CCD camera. Considering a bosonic Mott-insulating state consisting of atoms strongly confined to a deep optical lattice, this corresponds to the simultaneous detection of many independent, incoherent sources of bosons with many independent detectors, i.e., the individual CCD pixels.

Such a scenario was first investigated in the formalism of classical electromagnetic fields in 1956 for the case of the detection of astronomical radio waves as well as visible light sources in seminal experiments by Hanbury Brown and Twiss [254, 255]. Their findings were soon supported by Purcell [256] and sparked the broader application of quantum electrodynamics to many physical systems. In the initial experiments, the observed statistical bunching of photons could be used to determine properties of the light source, namely the angular size of stars. Since then, Hanbury Brown-Twiss intensity interferometry is used for a large variety of applications.

The effect relies on the indistinguishability of particles and the interference of different detection paths between two detectors. As a central result, the probability to simultaneously detect two (bosonic) particles that are emitted from two independent sources with two independent detectors depends on the relative distance d of the two detectors. This peculiarity can be understood by considering possible trajectories of particles for a simultaneous detection. In Fig. 5.9a the two paths of two independent particles from their sources, in this case the sites of an optical lattice, to the two detectors A and B are illustrated as solid black and dashed gray arrows. As the individual probabilities of both trajectories have to be summed due to the indistinguishability of particles, they can interfere both constructively and destructively, depending on the relative phase between the paths and, hence, the different path lengths.

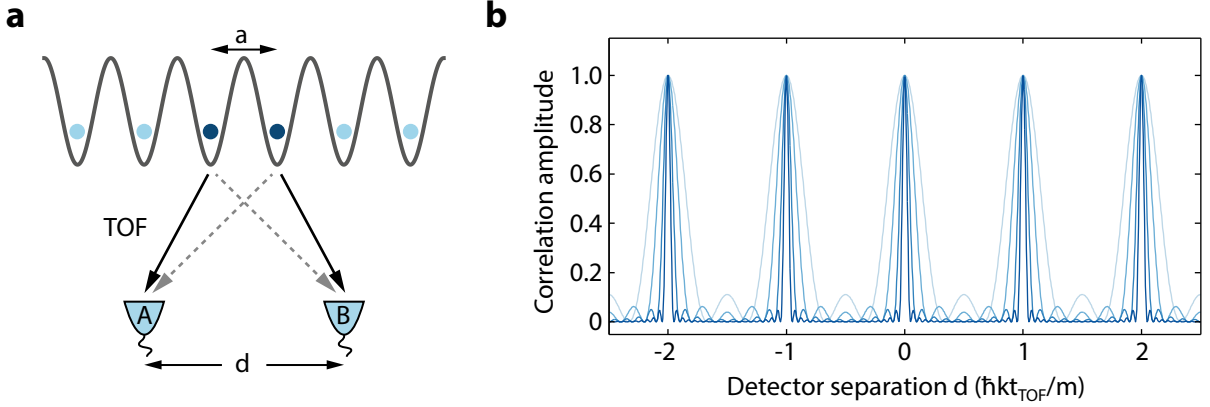


Figure 5.9: Hanbury Brown-Twiss correlations for atoms released from an optical lattice. **a** For the case of a simultaneous detection of two atoms that are released from individual lattice sites two possible trajectories, depicted as solid black and dashed gray arrows, exist to the detectors A and B. These trajectories may interfere constructively or destructively, depending on their relative phase factor that is determined by the distance d between the two detectors. **b** Correlation amplitudes for a one-dimensional chain of N particles calculated for $N = 3, 5, 10$ and 20 plotted in ascending darkness of blue coloring respectively.

5.4.2 Noise correlation observable in time-of-flight images

For the two-dimensional optical density images obtained after time-of-flight such spatial correlations can be analyzed by calculating the second-order density-density autocorrelation function $\mathcal{C}_D(\mathbf{d})$ in dependence of the detector distance vector \mathbf{d} according to

$$\mathcal{C}_D(\mathbf{d}) = \int \langle \hat{n}(\mathbf{r} - \mathbf{d}/2) \hat{n}(\mathbf{r} + \mathbf{d}/2) \rangle d^2\mathbf{r}, \quad (5.9)$$

where $\hat{n}(\mathbf{r}) = \hat{b}^\dagger(\mathbf{r})\hat{b}(\mathbf{r})$ denotes the density operator at position \mathbf{r} [57, 253]. The expression $\mathcal{C}_D(\mathbf{d})$ is conveniently scaled by the expectation value for uncorrelated particles

$$\mathcal{C}_U(\mathbf{d}) = \int \langle \hat{n}(\mathbf{r} - \mathbf{d}/2) \rangle \langle \hat{n}(\mathbf{r} + \mathbf{d}/2) \rangle d^2\mathbf{r} \quad (5.10)$$

such that the normalized observable for spatial noise correlations can be defined as

$$\mathcal{C}_N(\mathbf{d}) = \frac{\mathcal{C}_D(\mathbf{d})}{\mathcal{C}_U(\mathbf{d})} - 1. \quad (5.11)$$

With this, a value of $\mathcal{C}_N > 0$ indicates density-density correlations in the image noise, while $\mathcal{C}_N < 0$ corresponds to anti-correlations in analogy to the bunching (antibunching) of bosons (fermions) in the Hanbury Brown-Twiss effect. By expressing the density operator $\hat{n}(\mathbf{r}) = \hat{b}^\dagger(\mathbf{r})\hat{b}(\mathbf{r})$ in terms of the local wave functions that can be well approximated by spherically-symmetric Gaussians in strongly confining three-dimensional lattice

potentials, a calculation of the normalized correlation function yields the result

$$\mathcal{C}_N(\mathbf{d}) = \frac{1}{N^2} \left| \sum_{j=1}^{N_{\text{sites}}} e^{im\mathbf{R}_j \cdot \mathbf{d}/(\hbar t)} N_j \right|^2, \quad (5.12)$$

where \mathbf{R}_j denotes the position of lattice site j with local particle number N_j [253]. As the positions of lattice sites is *per definitionem* periodic, the above expression represents a Fourier sum with a periodicity of the reciprocal lattice vectors. The resulting correlation signal is plotted in Fig. 5.9b for a one-dimensional lattice with a single atom at each site for different total numbers of lattice sites, while the detector distance d is scaled according to the time-of-flight t_{TOF} . The emergence of extremely sharp peaks for an increasing system size is evident.

5.4.3 Experimental implementation of the noise correlation analysis

In order to extract the spatial quantum noise correlations from a set of typically 50 to 100 CCD images, one has to evaluate the integrals of Eq. (5.9) and (5.10). Hereby, the corresponding density-density autocorrelation function of each image matrix M_{I} has to be determined according to

$$\mathcal{C}_{\text{I}}(\mathbf{d}) = \int M_{\text{I}}(\mathbf{r} - \mathbf{d}/2) M_{\text{I}}(\mathbf{r} + \mathbf{d}/2) d^2\mathbf{r} = (M_{\text{I}} * M_{\text{I}})(\mathbf{d}), \quad (5.13)$$

where the $*$ denotes the convolution of two functions. The computationally hard procedure of the above equation can be significantly simplified by substituting the convolution integral with corresponding Fourier transformations according to the relation

$$\mathcal{F}(f * g) = \mathcal{F}(f) \cdot \mathcal{F}^*(g) \quad (5.14)$$

which yields the easily computable consecutive Fourier transformations

$$\mathcal{C}_{\text{I}} = \mathcal{F}^{-1} \left(|\mathcal{F}(M_{\text{I}})|^2 \right). \quad (5.15)$$

With this, the numerator of Eq. (5.11) is given by the sum over all individual autocorrelation functions. Accordingly, the denominator of Eq. (5.11) can be determined by calculating the autocorrelation function of the average of all individual images.

For extracting the quantum noise correlations from a set of optical density images, several requirements have to be met: First, the level of uncorrelated noise that is fundamentally limited by photon shot noise should be smaller than the correlated noise [251]. For optical densities close to unity and a large quantum efficiency of the CCD camera (which is on the order of 90% for imaging of the triangular lattice plane) this condition is readily fulfilled for the experimental setup. Second, all additional sources of correlated noise beyond the atomic quantum noise correlations should be as small as possible. Origins of such correlated noise include fluctuations in the detected particle number and detection

intensity, residual movements of the atomic cloud and interference fringes in the optical density image. Typically, residual interference signals result from slight variations of the imaging setup, e.g., vibrations, in between the absorption imaging of the atomic cloud and the recording of the corresponding reference image without atoms.

In order to minimize fluctuations in particle number, detection intensity and position, the obtained images are thoroughly pre-processed before the autocorrelation function of each image is calculated: The first step in preprocessing the images is to cancel intensity variations by normalizing each image with its individual intensity offset. This offset is extracted from a rectangular frame outside the respective region of interest containing an atomic signal. Secondly, a Gaussian is fitted to the featureless atomic density distribution. The image is then divided by its integral in order to normalize the observed particle numbers. Hereby, images yielding a deviation in the width of the obtained Gaussian above $\pm 10\%$ from the total mean value of all images are excluded from the analysis. Furthermore, the cloud is shifted to a fixed, centered position according to the position of the fitted Gaussian such that residual movements of the atomic cloud are compensated. A commonly employed practice for noise correlation image preprocessing is the *manual* exclusion of images that exhibit residual interference fringes and other periodic noise [57, 58]. In principle, however, it is desirable to avoid such choices made by the experimenter for reasons of reproducibility of results and applicability to large data sets. Instead, we solely rely on automated processing of data in order to reduce the influence of unwanted periodic noise. For this purpose, each individual image is filtered by a high-pass Hamming-window function prior to the calculation of the autocorrelation function. Nonetheless, the finally obtained correlation signal matrix \mathcal{C}_N still exhibits unwanted high-frequency noise components. The strongest components of such noise are additionally filtered out by applying a series of Gaussian notch filters to each pixel value above a certain amplitude threshold in the spectral density of the correlation signal. This procedure is exemplified Fig. A.3 of appendix A.

In Fig. 5.10 obtained correlation signals are shown for a Mott-insulating state in the static three dimensional lattice at lattice depths of $V_{2D,0} = 10 E_R$ and $V_{1D,0} = 30 E_R$, corresponding to a ratio of $U/(6J_{2D} + 2J_{1D}) \approx 190$. Here, Fig. 5.10a and c depict examples of an optical density image along both imaging directions of the experimental setup (compare Fig. 2.8 and 2.9). Clearly, no residual first order correlations due to superfluid interference are present in the density distributions along both directions. The featureless Gaussian density profile resulting from the absence of phase ordering of local Fock states is exemplified by the blue line profiles at the sides of the optical density images that depict the pixel values along the respective hair crosses in the images. The red lines are Gaussian fits to the data, emphasizing the presence of noise fluctuations around the mean value. Note that the difference in size of the images stems from the fact that the xy -plane in Fig. 5.10a was imaged after $t_{\text{TOF}} = 38$ ms of ballistic expansion while the zy -plane is imaged after $t_{\text{TOF}} = 18$ ms. The relative strength of the correlation signal is expected to increase quadratically with the time-of-flight [57].

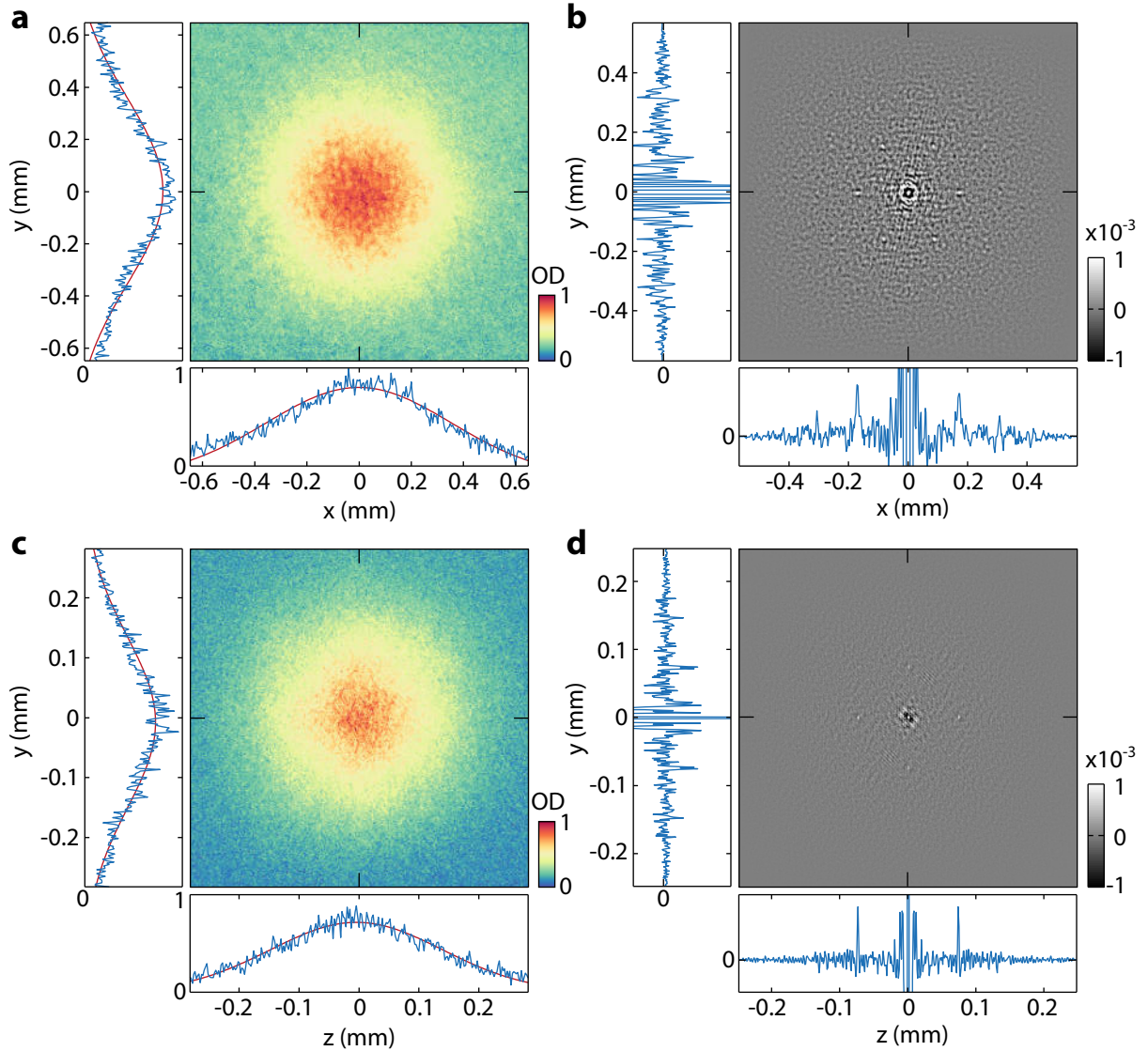


Figure 5.10: Quantum noise correlations in the static Mott insulator at $U/(6J_{2D} + 2J_{1D}) \approx 190$. **a** and **c** show examples of optical density images of the Mott insulator along both implemented imaging directions, i.e., the z -axis and the x -axis respectively. In addition, the featureless Gaussian density profiles are depicted by the blue line plots at the sides of the images that correspond to the pixel values along the hair crosses in both images. Red lines indicate a Gaussian fit to the data, emphasizing the statistical noise around the mean value. In **b** and **d** the corresponding correlation signals are shown that were extracted from a data set of approximately 100 individual images. Beyond the strong autocorrelation peak, the noise correlations at the expected positions of the reciprocal lattice vectors are clearly visible. The line plots at the sides of the correlation images depict the correlation signal along the hair crosses. Hereby, the correlations along the deep one-dimensional lattice (z -direction in **d**) are the most pronounced as well as the most narrow signal due to the larger lattice depth of $V_{1D,0} = 30 E_R$ along this direction as compared to $V_{2D,0} = 10 E_R$ in the triangular lattice plane. Note that in the vertical direction of the correlation signal of **b**, noise correlations are expected only at the second order momentum positions.

The corresponding correlation matrices \mathcal{C}_N obtained from an initial data set of approximately 100 individual images for each imaging direction are shown in Fig. 5.10b and d. As expected, both images feature a strong autocorrelation peak at zero distance as well as clearly distinguishable quantum noise correlation peaks at the positions of the reciprocal lattice vectors. The positive correlation signals are also visible in the respective line profiles of the correlation signal at the sides of the images. Hereby, correlations along the perpendicular 1D-lattice (z -direction) are the most prominent as well as narrow features. This is due to the fact that the confining lattice is significantly deeper in this direction: As it was pointed out in Ref. [257], the width of the correlation peaks rapidly decreases for a decreasing of the ratio $U/|J|$. Indeed, as $U/|J|$ increases, larger Mott-shells form and more atoms contribute to the density-density correlations. In analogy to Fig. 5.9b this leads to a decrease of the width of correlation peaks.

A strong oscillation of the correlation amplitude can be observed around the noise correlation peaks as well as the autocorrelation peak at zero position, yielding *negative* values of \mathcal{C}_N . This behavior can be attributed to residual fluctuations of the position of the atomic cloud that were not compensated in the pre-processing of images. However, the signal-to-noise ratio of the correlation peaks is of limited quality as, e.g., compared to the results presented by Fölling *et al.* [57]. Moreover, correlation signals spanning larger distances than a single reciprocal lattice vector are significantly reduced in amplitude. Ideally, such correlation signals should span the entire region of the analyzed image (see Fig. 5.9b) as the Fourier sum of Eq. (5.12) is not spatially limited by any envelope function. The extension of the correlation peaks is, thus, only limited by the ratio of correlated atom noise to residual photon shot noise which appears to decrease rather rapidly for larger distances in the analyzed images.

5.4.4 Noise correlations in the antiferromagnetic Mott insulator

In order to investigate the strongly interacting many-body state in the quantum spin-1/2 regime of antiferromagnetic interactions, we have applied the analysis of quantum noise correlations to the driven three-dimensional lattice. Thereby, lattice driving is performed at potential depths of $V_{2D,0} = 4.55 E_R$ and $V_{1D,0} = 30 E_R$ while the periodic forcing amplitude is chosen as $K = 2.57$ such that the homogeneous effective tunneling renormalizes to $J^{\text{eff}} = -0.08 J^{\text{bare}}$. Similar to the investigated static system, these parameters yield a ratio of $U/(6|J_{2D}^{\text{eff}}| + 2J_{1D}) \approx 190$.

In Fig. 5.11 the resulting quantum noise correlation signal, extracted from a data set of 100 individual images, is depicted for the imaging of the 2D-lattice plane (compare Fig. 5.10a and b). Similar to the static system, the density distribution shown for a single image in Fig. 5.11a is well described by a featureless Gaussian already after the short timescales of the periodic driving. The calculated quantum noise correlations are also clearly visible. They exhibit comparable amplitudes and the same positions of the reciprocal lattice vectors as in the static lattice.

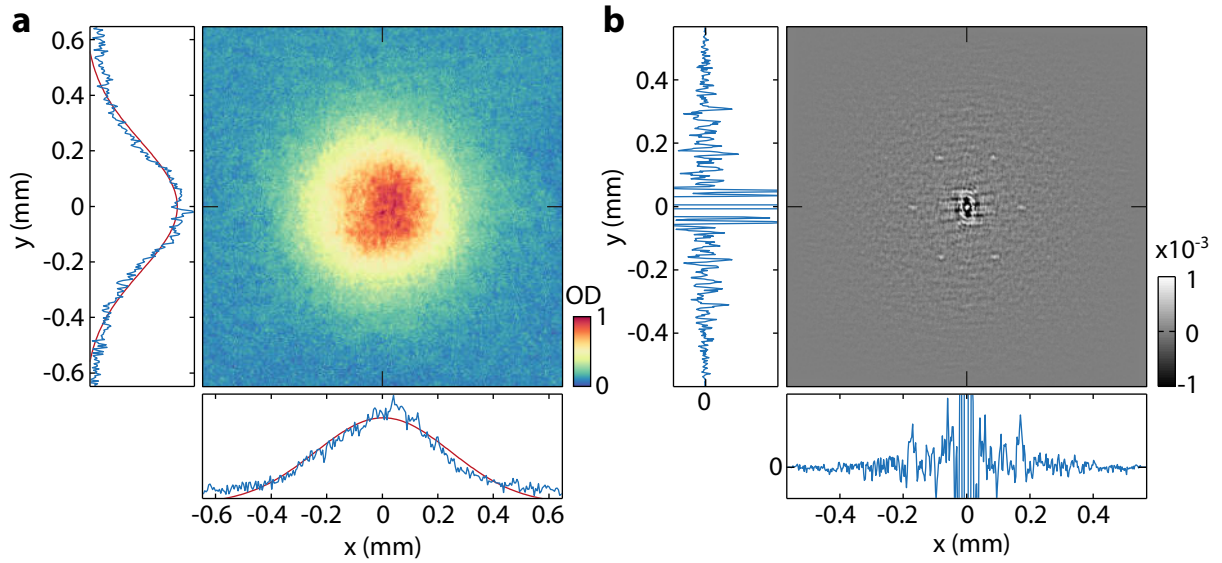


Figure 5.11: Quantum noise correlations in the antiferromagnetic Mott-insulating regime of the driven three-dimensional lattice for a ratio of on-site interaction to (effective) tunneling of $U/(6|J_{2D}^{\text{eff}}| + 2J_{1D}) \approx 190$. **a** Individual absorption images, shown here in the triangular lattice plane again correspond to a featureless Gaussian density distribution with additional noise. **b** Extracted noise correlations reveal the same peak structure as in the static lattice.

In conclusion, the characteristic quantum noise correlations presented in Fig. 5.10 and 5.11 verify the presence of an ensemble of *incoherent* sources of bosons confined to the three-dimensional lattice sites. On the one hand, this observation agrees perfectly with the Mott-insulating state. In principle, however, such noise correlations could also appear in the case of an incoherent thermal gas such that the observation of second-order correlations alone is ambivalent.

With the ability to restore coherence from the investigated strongly interacting system, the presence of a thermal gas as the source of noise correlations can be ruled out for the static lattice. Due to the strong forcing of the lattice and the absence of the beneficial Bose enhanced tunneling and redistribution of entropy along additional dimensions in the three-dimensional lattice, such restoration of coherence could not be observed in the driven system owing to the lifetime being limited to a few milliseconds. Together with the observed rapid decrease of visibility for increasingly dominant on-site interactions (see Fig. 5.8) we have argued that the experimental feasibility of the realization of an antiferromagnetic Mott insulator by lattice driving is at least questionable. Yet, we do not observe any quantum noise correlations in a similar data set for an initially thermal gas (a result that is also reported in Ref. [57]). Therefore, the observed correlation signal in Fig. 5.11 likely stems from a Mott-insulating state.

Nonetheless, more observations are needed for an unambiguous verification of the antiferromagnetic Mott insulator. What can, however, be concluded from the *positions* of

correlation peaks in the driven system is that the symmetry of the lattice is preserved in this state: An ordered occupation of sites which breaks the translational symmetry of the triangular lattice would give rise to additional correlation peaks at half the reciprocal lattice vectors which we do not observe. The appearance of such additional correlation peaks due to a larger lattice unit cell were, e.g., reported in Ref. [141] for a one-dimensional lattice with alternating occupation number corresponding to a Néel ordering of antiferromagnetic spins. Even though it breaks the translational symmetry, a valence-bond solid, however, should not lead to additional peaks owing to the entanglement of pairs of pseudo-spin states.

5.5 Order-by-disorder signature of the frustrated antiferromagnet

As discussed before, an unambiguous signature of the frustrated antiferromagnetic Mott insulator in the second-order correlations of time-of-flight images is inherently elusive. In the following, we will investigate whether signatures of geometric frustration can be detected in absorption images by considering a so-called *order-by-disorder* effect.

Following Eckardt *et al.* [140], the general idea is that the occupation of the dispersion relation with its two degenerate minima of the driven system with negative, real valued tunneling matrix elements (see Fig. 3.5 and 4.7) changes as interactions become dominant. An increase of interaction is accompanied by an increase of quantum fluctuations. In the weakly interacting regime, this circumstance is well described within the framework of Bogoliubov theory as an increase of *quantum depletion*, i.e., the fraction of the many-body wave function that is not represented by the macroscopic single-particle wave function of a Bose-Einstein condensate [258].

For a wave function occupying one of the two possible minima of the dispersion relation small quantum fluctuations towards momenta with higher energies will be distributed symmetrically in momentum space. For larger fluctuations, however, their shape will become increasingly asymmetric, tending towards the neighboring minimum: Here, the dispersion relation is less steep, such that fluctuations require fewer energy along this direction. As a consequence, the total wave functions will tend to join the two minima for increasing quantum fluctuations. In the extreme case of sufficiently strong quantum fluctuations the wave functions will merge at the position in between the minima. With only a single possible occupation in the first Brillouin zone, this system does not exhibit any frustration but rather a regular 180° Néel-ordering of local vector spins in a *rhombic* pattern (compare Ref. [96]). With this, an increase in fluctuations should lead to the ordering of a previously frustrated system, hence the term “order by disorder”. In Ref. [140] these findings are supported by thorough numerical calculations based on the variational ansatz sketched in section 5.1.3.

We investigate this effect by analyzing residual peak positions of the driven three-

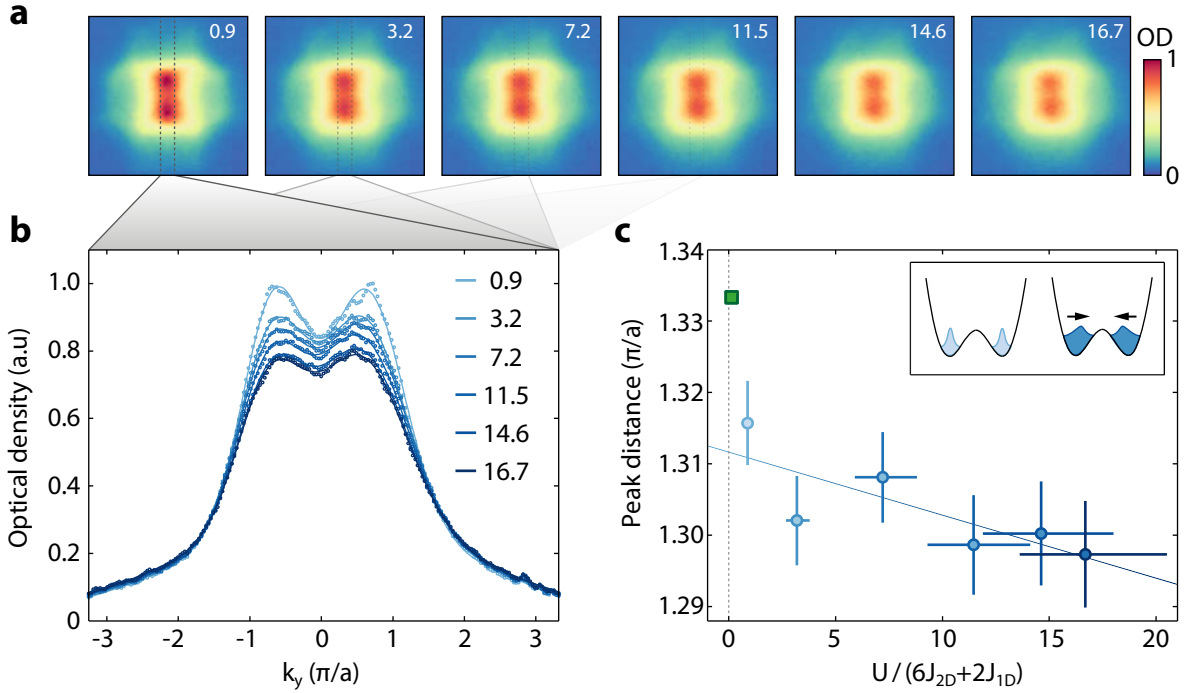


Figure 5.12: Order-by-disorder behavior for increasing interactions. **a** Time-of-flight images of the frustrated 3D-system for increasing ratios of $U/(6|J_{2D}^{\text{eff}}| + 2J_{1D})$ indicated by numbers in the images. **b** Extracted central intensity profiles of the images (small circles) are fitted with three Gaussians (solid lines) in order to extract the distances between the central peaks. **c** The resulting distances are plotted against the ratio of on-site interaction and tunneling $U/(6|J_{2D}^{\text{eff}}| + 2J_{1D})$. Vertical error bars indicate the 95% confidence intervals of the fit in **b**. Horizontal error bars reflect an estimated uncertainty of the lattice depths of 5% for the calculation of the tunneling amplitudes and the on-site interaction. The solid line is a linear fit to the data and the green square indicates the distance of degenerate minima in the ideal dispersion relation of $3\pi/(2a)$. The peak shift due to increased quantum fluctuations is illustrated in the inset.

dimensional system in a regime of intermediately strong interactions where a first-order correlation peak structure in the three-dimensional lattice can still be identified. With a triangular lattice depth of $V_{2D,0} = 4.25 E_R$ the driving is ramped to its maximally negative value, yielding a homogeneous effective tunneling matrix element of $J^{\text{eff}} = -0.4J^{\text{bare}}$. Different interaction strengths are chosen by varying the perpendicular 1D-lattice depth from $V_{1D,0} = 5 E_R$ to $30 E_R$ in steps of $5 E_R$ such that all other parameters remain unchanged. The corresponding time-of-flight images, averaged over many individual realizations, are shown in Fig. 5.12a in ascending order of the ratio $U/(6|J_{2D}^{\text{eff}}| + 2J_{1D})$. Central profiles, depicted in Fig. 5.12b, are extracted from the images by a summation over vertical stripes. The distance between the two central peaks is analyzed by fitting the line profiles with three Gaussians - a broad background and one for each residual peak. The resulting distances are depicted in Fig. 5.12c together with the expected peak distance of $2\pi/(3a)$ for

an ideal superfluid state.

Here, uncertainties for the calculated ratio between on-site interaction energy and tunneling is indicated by horizontal error bars. They are determined for an assumed precision of the calibrated lattice depth of $\pm 5\%$. This value is a quite conservative estimate, as the measurements of multi-photon resonances presented in chapter 3 verify an excellent agreement with the calculated band structure. As predicted, all extracted peak distances are smaller than the theoretical value and a decrease of the distance can be observed for increasing interactions. However, the observed effect is extremely weak as compared to the error margins of the fit given by the corresponding 95% confidence intervals. Furthermore, the validity of the fitting function with as many as nine free parameters remains to be tested.

It should also be noted that the directionality of the expected peak shift is initially not distinguished: As shown in Fig. 3.5 and 4.7 the two minima of the dispersion relation are located at the six vertices of the first Brillouin zone and, thus, have three nearest neighboring minima. Accordingly, the observation of the vertical minima in Fig. 5.12 is an arbitrary choice that was made due to the position of the Wannier envelope. Hence, in contrast to the simplified explanation of a two-well system used above (see inset in Fig. 5.12c), the shift in the wave function due to quantum fluctuations should also be present along the other two possible directions connecting each two minima. A distinction of these directions can, however, be induced by slight asymmetries of the lattice potential. Indeed, as the angles of the three-beam lattice are not aligned at exactly 120° with respect to each other (see appendix D) such asymmetries do appear in the dispersion as described in Ref. [96] and may result in a preferred directionality of the peak shift. In order to investigate the directionality of the shift it is necessary to evaluate the peak positions along the other possible directions for images with a suitably adjusted position of the oscillating Wannier envelope.

Numerical calculations presented in Ref. [140] indicate that the merging of peaks due to quantum fluctuations should become stronger for asymmetric effective tunneling parameters $J' > J$ as the energy barrier between the two minima becomes shallower in this case (this effect is thoroughly described in Ref. [96]).

5.6 Conclusion & outlook

The investigation of the strongly correlated regime in the layered triangular lattice system presented in this chapter has yielded the following results: First, the creation of a robust Mott-insulating state in deep static lattice potentials could be demonstrated. Second, the realization of an antiferromagnetic Mott-insulating state by far off-resonant lattice driving should be experimentally feasible. An analysis of quantum noise correlations provides quantitatively similar results of spatial density-density correlations for static as well as strongly driven systems, hinting towards the successful engineering of a frustrated Mott insulator with unbroken translational symmetry. In addition, first signatures of an order-

by-disorder effect resulting from an increase in quantum fluctuations could be observed.

However, further measurements are necessary in order to verify the profound influences of the high degree of frustration arising from the mapping to a quantum spin- $1/2$ model in the hard-core boson limit of strong interactions and to map out the corresponding phase diagram for antiferromagnetic interactions. A promising experimental technique for the investigation of this phase transition is the *melting* of the Mott insulator by adiabatically lowering the chemical potential, i.e., transferring the system into a very shallow trapping potential. An additional method of reaching the Néel superfluid in sufficiently deep lattices is the continuous lowering of the interaction strength by using Feshbach resonances. Due to the absence of experimentally applicable Feshbach resonances in ^{87}Rb , this approach should be more suitable for, e.g., a system comprised of ^{39}K .

Finally, a systematic dependence of the peak distance on the interaction strength as well as the asymmetry of the tunneling directions remains to be investigated in the driven lattice, promising deep insights into order-by-disorder effects and geometric frustration.

6 Probing Dirac points in the state-dependent honeycomb lattice

Here, we present a novel method of controlling the geometry of a state-dependent honeycomb lattice: The energy offset between the two sublattices of the honeycomb structure can be tuned by rotating the atomic quantization axis. This enables us to continuously tune between a homogeneous graphene-like honeycomb lattice and a triangular lattice and to open an energy gap at the characteristic Dirac points. We probe the symmetry of the lattice with microwave spectroscopy techniques and investigate the behavior of atoms excited to the second energy band. We find a striking influence of the energy gap at the Dirac cones onto the lifetimes of atoms in the excited band.

The honeycomb lattice structure can be found in a large variety of manifestations in nature as it represents the two-dimensional close-packing of spheres. It is the basis of many intriguing systems of condensed matter. The most prominent example thereof is graphene, a flat monolayer of carbon with sp^2 hybridization bonding. Since its first realization in 2004 [142], graphene has opened a completely new field of research and already represents a promising candidate for revolutionary technological applications. In 2010 the Nobel prize in physics was awarded to A. Geim and K. Novoselov “for groundbreaking experiments regarding the two-dimensional material graphene” [259, 260].

The two dimensional honeycomb structure of graphene gives rise to an unusual electronic spectrum of massless, ultra-relativistic electrons as the two lowest energy bands touch at the vertices of the hexagonal Brillouin zone such that the dispersion relation becomes linear. For low energies this results in the formation of new quasiparticles that are accurately described by the 3-dimensional Dirac equation [146]. The touching point of the bands, the so-called Dirac point exhibits a topological singularity, resulting in a localized Berry flux of π . Together with its extremely strong bonding and two-dimensional nature, the extraordinary topology of graphene gives rise to a large variety of fascinating phenomena, such as the anomalous quantum Hall effect and exceptional charge, heat and spin transport characteristics, only to name a few [143, 261].

Ultracold atoms in unconventional optical lattices provide an ideal testing ground for many of such intriguing aspects. Here, the clean environment and high degree of control of internal and external system parameters allow for the engineering of model systems aim-

ing at a deeper understanding of the behavior of single- and many particle systems with respect to symmetry and topology. For example, Klein-tunneling has been demonstrated for the presence of a Dirac point in a one-dimensional lattice [147] and the relativistic *zitterbewegung* was evidenced in a Bose-Einstein condensate [148]. The complex interplay of symmetry and interactions allowed for the observation of a Néel ordering of spin components in the state-dependent honeycomb lattice with striking influences on the superfluid to Mott insulator quantum phase transitions [75]. Moreover, ensembles of quantum degenerate fermionic atoms in a *brick* lattice, that is topologically equivalent to a honeycomb lattice, have been used to study the merging of Dirac cones [76]. Recently, the singular Berry flux in an optical honeycomb lattice could be mapped using interferometric methods [149] and the Haldane model was engineered with periodic driving techniques similar to those discussed in the preceding chapters [151].

In this chapter we investigate a graphene-like honeycomb lattice with a state-dependent component that allows us to continuously tune the symmetry of the lattice structure. The change of the lattice symmetry is accomplished by adjusting the energy offset between the diatomic basis of the honeycomb lattice. As one of the two sublattice sites becomes energetically favorable the inversion symmetry of the lattice is broken and changed from a homogeneous honeycomb lattice to a triangular one. With this, an energy gap can be created and tuned at the aforementioned Dirac cones. Thus, in contrast to experiments presented in the chapters 3, 4 and 5, the band structure is altered by a change of the lattice structure in real space rather than engineering effective time-averaged potentials.

In the following, we will present experiments probing the state-dependent honeycomb lattice with respect to the opening of the band gap at the Dirac point. We explain the method used to control the lattice symmetry and, thus, the band structure by rotating the magnetic quantization field. We verify the effect of the rotation on the lattice structure by performing band-selective microwave spectroscopy that is in good agreement with theoretical calculations. Finally we utilize this spectroscopy technique to excite the atomic ensemble to the second lowest energy band, enabling us to probe the dynamic behavior of the atomic ensemble with respect to the presence of an energy gap at the Dirac cones. Time-resolved measurements of the population of the excited band reveal a striking influence of the presence of a Dirac point.

Experiments presented in this chapter have been performed within the team of C. Staarman, C. Ölschläger, J. Struck, J. Simonet and M. Weinberg. The leitmotif of manipulating the inversion symmetry of the state-dependent honeycomb lattice by changing the orientation of the quantization axis as well as the numerical mean-field treatment of interaction effects relies on the work of P. Soltan-Panahi [154]. Parts of this chapter have been published in Ref. [5].

6.1 State-dependent honeycomb lattice

In chapter 2 we have already briefly introduced the basic properties of the state-dependent honeycomb lattice that is generated for an in-plane alignment of the linear polarization vectors $\boldsymbol{\epsilon}_i$ of the three-beam lattice setup, i.e., for the case of $\theta = 0$. The orientation of the polarization vectors gives rise to an alternating pattern of circular polarization in the resulting light field (compare Fig. 2.6) which stems from the projection of the oscillating electric field onto the quantization axis as defined in Eq. (2.5). In chapter 2 we have described the orientation of the quantization axis by means of the three *Euler angles* that unambiguously define the orientation of a rigid body in three dimensions. In this section we will investigate the basic properties of the state-dependent potential for the case of a quantization axis aligned perpendicular to the lattice plane along the z -axis, corresponding to Euler angles of $\alpha, \beta, \gamma = 0$. For this case the total lattice potential, comprised of a state-independent and a state-dependent part, reads

$$V_{2D}(\mathbf{r}) = 2V_0 \sum_{i=1}^3 \cos(\mathbf{b}_i \mathbf{r}) - \sqrt{3}V_0 (-1)^F m_F \eta \sum_{i=1}^3 \sin(\mathbf{b}_i \mathbf{r}), \quad (6.1)$$

where the relative strength of the state-dependent potential is given by the proportionality factor η that is determined by the detuning of the lattice light with respect to the atomic transitions. In chapter 2 we have argued that, due to its linear dependency on the magnetic quantum number m_F , the state-dependent part of the potential, represented by the second term in the above equation, can be expressed as an effective magnetic field resembling the linear Zeeman effect:

$$V_{2D}(\mathbf{r}) = V_{\text{Int}}(\mathbf{r}) + g_F m_F \mu_B B_{\text{eff}}(\mathbf{r}). \quad (6.2)$$

Hence, for magnetic quantum numbers different from zero, the alternating pattern of circular polarizations results in the potential energy of one of the two sublattice sites being lifted while the other one is lowered. Whether an atom in a hyperfine state $|F, m_F\rangle$ is predominantly confined at a lattice site with σ^+ or σ^- polarization depends on the sign of its magnetic quantum number and the respective Landé factor g_F . The sign change of the Landé factor in the ground-state manifold of ^{87}Rb is incorporated in Eq. (6.1) by the prefactor $(-1)^F$. Accordingly, an atom in the hyperfine state $|1, -1\rangle$ experiences the same potential as an atom in the state $|2, +1\rangle$.

In Fig. 6.1 the state-dependency of the honeycomb lattice is depicted for the three cases of $m_F = 0, \pm 1$. In analogy to Fig. 2.6 the respective potentials are shown in Fig. 6.1a, b and c. The underlying lattice geometry, together with a calculation of the absolute square of the lowest-band Bloch function at zero quasimomentum and a cut through the two sublattice sites are depicted in the parts d, e and f. The resulting band structure is plotted in g, h and i. The potential is clearly unaffected by the polarization light field for $m_F = 0$ and the two distinct sublattice sites are degenerate, preserving the honeycomb structure. The corresponding Bloch function of the lowest energy band is evenly distributed on all lattice

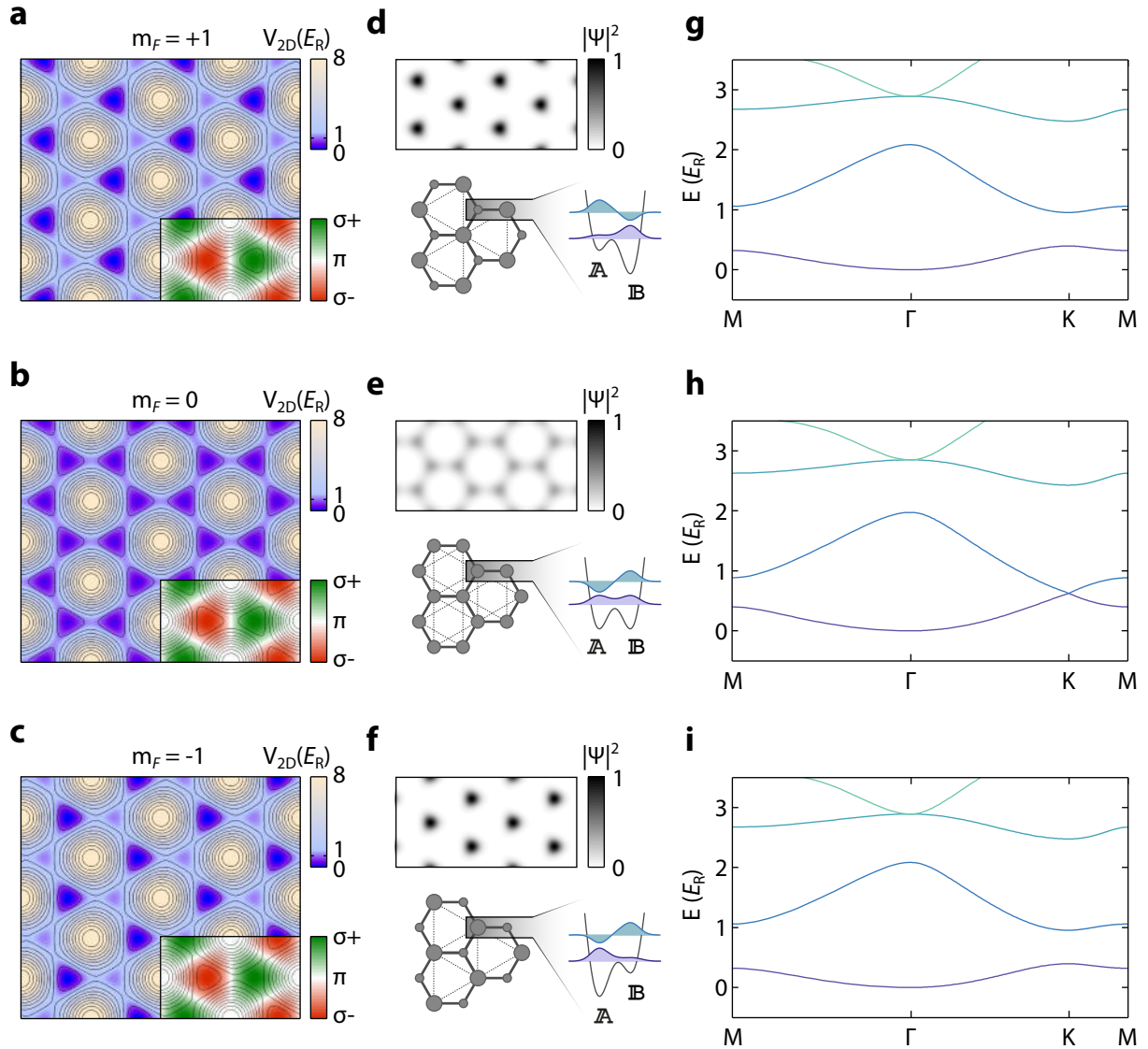


Figure 6.1: State-dependency of the honeycomb lattice for three magnetic quantum numbers $m_F = 0, \pm 1$. Parts **a**, **b** and **c** depict the state-dependent honeycomb lattice potential for ^{87}Rb atoms in the three hyperfine states $|F = 1, m_F = 0, \pm 1\rangle$ respectively. While the lattice is symmetric for zero magnetic quantum number, the degeneracy between the two sublattices is clearly lifted for $m_F = \pm 1$ where atoms are either trapped at the sites with σ^+ or σ^- light. In parts **d**, **e** and **f** the absolute squares of the corresponding lowest-band Bloch functions are plotted together with an illustration of the lattice geometry and a one-dimensional cut through the potential at the two sublattice sites \mathbb{A} and \mathbb{B} . Dashed lines in the illustration of the lattice geometry indicate next-nearest neighbor tunneling processes along the occupied sublattices. The influence of the energy offset between the sites is clearly reflected in the shape of the two lowest lying Bloch functions shown in purple and cyan. The corresponding band structures are shown in parts **g**, **h** and **i**. While the two lowest bands of the symmetric honeycomb lattice touch at the K-points of the first Brillouin zone forming a Dirac point, an energy gap opens up at the K-point for the asymmetric cases. Illustrations in parts **d**, **e** and **f** are based on Ref. [68].

sites and a finite density along the honeycomb channel structure can still be observed. At the corners of the first Brillouin zone the two lowest lying energy bands touch, forming a Dirac point surrounded by a linear dispersion relation.

In contrast, the potential is strongly affected by the circular polarized light field for the cases of magnetic quantum numbers $m_F = \pm 1$, where each state is trapped at the sublattice sites with σ^+ or σ^- light respectively, thereby forming a triangular lattice with occupations at every second honeycomb lattice site with shallow local minima in between. Accordingly, the band-structure exhibits an energy gap at the K-point. The strong confinement of the lowest-band Bloch function (first band), accompanied by an increased density at the deeper lattice sites is clearly evident. In addition, the Bloch function in the first excited band (second band) exhibits a larger amplitude at the shallower lattice site.

Note that we have changed the notation of the potential lattice depth in comparison to chapter 2: the tunneling processes in the honeycomb lattice take place along the shallow channel structure rather than through the large potential hills in the middle of each hexagon. Therefore, we define the honeycomb lattice depth as the potential barrier height along the channel structure between the minima of the symmetric honeycomb lattice. As indicated in Fig. 6.1, this physically relevant lattice depth amounts to one eighth of the initial lattice depth that was defined as the difference between the minima and the global maximum of the potential. Accordingly, the potentials and band structures plotted in Fig. 6.1 correspond to a physical lattice depth of $V_{2D,0} = 1 E_R$ rather than $8 E_R$. This convention is used throughout the chapter.

6.2 Inversion symmetry breaking by rotating the quantization axis

In the preceding section we have discussed the inversion symmetry breaking in the state-dependent honeycomb lattice for the cases of non-vanishing magnetic quantum numbers. The band structure is strongly influenced by the energy offset between the twofold atomic basis due to the presence of an alternating circularly polarized light field. Mixtures of different hyperfine states loaded into the state-dependent honeycomb lattice are profoundly influenced by this effect. For example, repulsive interactions between a mixture of two hyperfine states that are trapped at different basis sites leads to a strong *tunneling blockade* in both triangular sublattices [75]. In addition, such binary spin mixtures can give rise to a new quantum phase in the superfluid regime. It is characterized by a phase twist of the complex superfluid order parameter and results in a symmetry breaking in momentum space [68].

The mechanism responsible for the inversion symmetry breaking of the lattice potential, however, is discrete as it scales with the integer differences between the magnetic quantum number m_F . In the following, we will present an elegant and experimentally feasible method to continuously as well as dynamically control the energy offset between lattice

sites and discuss the implications on the band structure.

6.2.1 Effective magnetic quantum number

From section 2.2.2 we can recall that the three polarization modes $p = \{\pi, \sigma^+, \sigma^-\}$ of the laser light field arise from the projection of the oscillating electric field onto the three-dimensional Jones vectors according to

$$I_p(\mathbf{r}) \propto |\mathbf{E}(\mathbf{r}) \cdot \boldsymbol{\varepsilon}_p|^2. \quad (6.3)$$

The Jones vectors $\boldsymbol{\varepsilon}_\pi$ and $\boldsymbol{\varepsilon}_{\sigma^\pm}$, given in Eq. (2.6), are determined by the orientation of the systems quantization axis. Experimentally, this axis is defined by a homogeneous magnetic field $\mathbf{B}_{\text{qa}}(\mathbf{r})$ with a strength of 1 G. A change in orientation of the quantization axis requires a transformation of the Jones vectors, as the Jones vector $\boldsymbol{\varepsilon}_\pi$ always has to be aligned in parallel to the quantization field. In section 2.2.2 we have described the orientation of the quantization axis in terms of the three Euler angles α , β , and γ . The corresponding rotational transformations of the Jones vectors have led to the general description of the three-beam lattice potential for arbitrary orientations of the quantization field given in Eq. (2.32) and (2.33). Here, the shape of the state-dependent part of the potential is determined by the three coefficients C_i of Eq. (2.34) that only depend on the Euler angles and the angle θ of the linear laser polarization with respect to the lattice plane. Previously, we have discussed the case of a quantization axis aligned in parallel to the z -axis, i.e., perpendicular to the three-beam lattice plane and $\alpha, \beta, \gamma = 0$. In the following, we will treat the orientation of the quantization axis with respect to the variable Euler angle α , while we set $\beta = 0$. As the honeycomb potential is created for $\theta = 0$, all three coefficients of Eq. (2.34) are then given by $C_i = \cos(\alpha)$. Note that the honeycomb potential is unaffected by the third Euler angle as all components of the coefficients in Eq. (2.34) incorporating γ also scale with $\sin \theta$. However, as imperfections in the alignment of the polarization angles θ and the lattice beams cannot be ruled out completely, we also set $\gamma = 0$ such that the rotation of the quantization axis takes place in the xz -plane. This allows to re-formulate the expression for the state-dependent potential of Eq. (6.2) in terms of an *effective* magnetic quantum number \tilde{m} that incorporates the magnetic quantum number, the respective Landé-factor and the rotation of the quantization field:

$$\tilde{m} = (-1)^F m_F \cos(\alpha). \quad (6.4)$$

As the central result, the strength of the energy offset between the twofold basis of the honeycomb lattice can be continuously tuned for a single hyperfine state by rotating the quantization field by the Euler angle α around the y -axis.

6.2.2 Opening of Dirac points

The effect of the rotation of the quantization field onto the total lattice potential and its band structure is shown in Fig. 6.2 for the case of the ^{87}Rb hyperfine states $|1, +1\rangle$ or

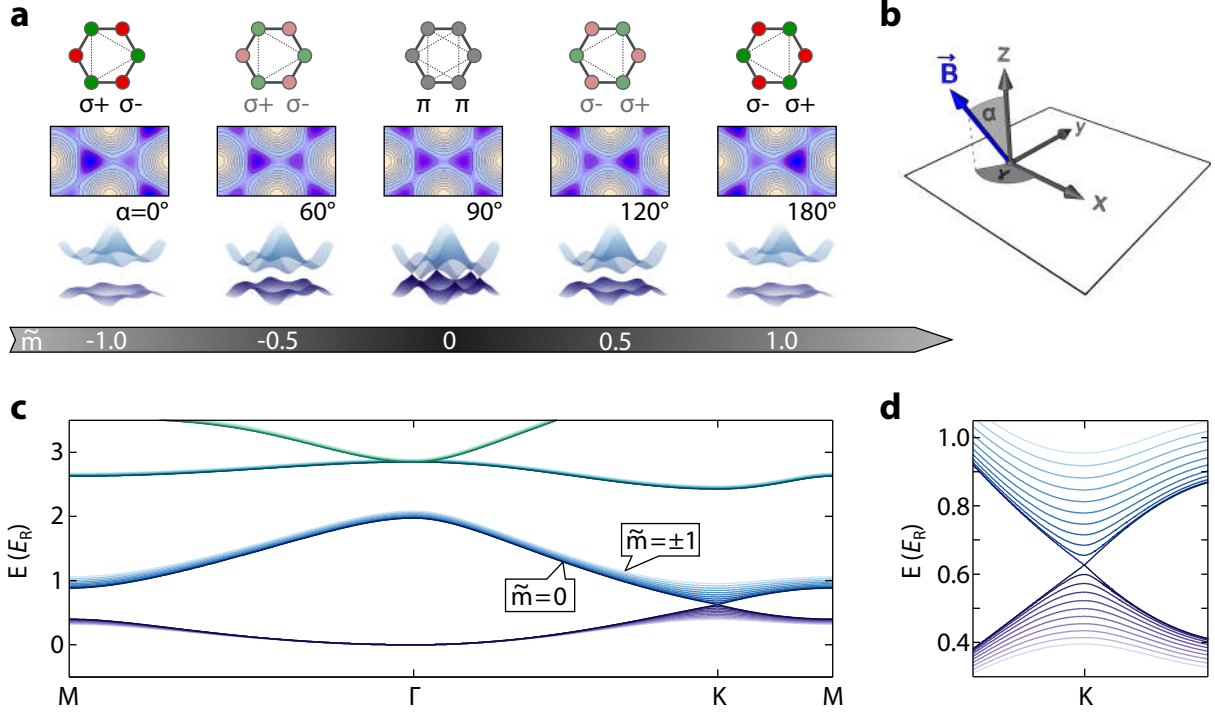


Figure 6.2: Effective magnetic quantum number and continuous opening of Dirac points. **a** A rotation by the Euler angle α continuously changes the effective magnetic quantum number \tilde{m} allowing for the precise adjustment of the circular polarization component of the light field and, thus, the energy offset between sublattice sites. **b** Illustration of the quantization field in the defined coordinate system with two Euler angles α and γ . The three-beam lattice is aligned in the xy -plane. Parts **c** and **d** depict the continuous opening of the Dirac point at the K-point of the Brillouin zone for a lattice depth of $1 E_R$. A similar figure can be found in Ref. [5].

$|2, -1\rangle$. As depicted in Fig. 6.2a, the potential energy for these states is always lowered for σ^+ . Now, by rotating the quantization field $\mathbf{B}_{\text{qa}}(\mathbf{r})$ away from its initial orientation parallel to the z -axis for an angle of $\alpha = 0$ (see part b of the figure) the strength of the circular polarization components in the light field decreases as, e.g., for the case of $\alpha = 60^\circ$ and $\tilde{m} = -0.5$. With this, both the energy differences between the twofold basis of the honeycomb lattice decreases as well as the energy gap between the two lowest bands. If the quantization field is exactly aligned in the xy -plane of the lattice, i.e., $\alpha = 90^\circ$ and $\tilde{m} = 0$, the polarization of the light field is everywhere π . Now the two sublattices are energetically degenerate such that the perfectly symmetric honeycomb lattice is restored and the two lowest energy bands touch at the vertices of the first Brillouin zone forming Dirac cones. Rotating the quantization field further re-opens the energy gap while the circular polarization pattern is interchanged: Sites with previously σ^+ polarization exhibit a σ^- polarization and vice versa.

The corresponding band structure and opening of the Dirac points in dependence of the effective magnetic quantum number is plotted in Fig. 6.2b and c for a lattice depth of

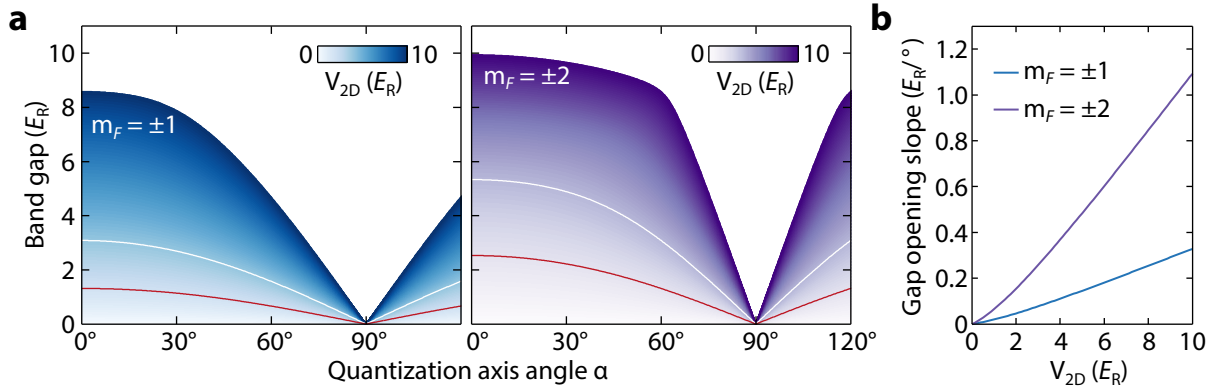


Figure 6.3: Opening of the band gap for increasing lattice depths. **a** The band gap at the K-point is plotted for increasing lattice depths with respect to the Euler angle α . Red and white solid lines indicate a lattice depth of $2 E_R$ and $4 E_R$ respectively. While the band gap scales linearly with m_F for shallow lattice depths, a clear cusp emerges in the behavior of the energy gap for $m_F = \pm 2$ for deeper potentials that is not reproduced for $m_F = \pm 1$. **b** The linear slope of the band gap opening close to $\alpha = 90^\circ$ is plotted in dependence of the lattice depth in units of E_R per degree.

$V_{2D,0} = 1 E_R$. While the energy gap is perfectly closed for an effective quantum number of $\tilde{m} = 0$ it amounts to $E_{\text{gap}} \approx 0.6 E_R$ for $\tilde{m} = \pm 1$ which corresponds to approximately 2 kHz.

It is evident that the opening of the band gap is quite sensitive to the orientation of the quantization axis as the presented case is calculated for a comparatively shallow total lattice depth. We explore the quantitative behavior of the energy gap opening with respect to the Euler angle α in Fig. 6.3. In part 6.3a the calculated band gap at the K-points of the Brillouin zone are plotted for increasing lattice depths up to $10 E_R$ in dependence of α for initial magnetic quantum numbers of $m_F = \pm 1$ and $m_F = \pm 2$. Hereby, white and red lines indicate a lattice depth of $2 E_R$ and $4 E_R$ respectively. For relatively small potentials the band opening scales linearly with the magnetic quantum number, i.e. the energy gap is always twice as large for $m_F = \pm 2$ as compared to $m_F = \pm 1$. For deeper potentials, however, a clear cusp in the behavior of the band gap emerges around $\alpha = 60^\circ$ for $m_F = \pm 2$ that is not observed for $m_F = \pm 1$.

Nevertheless, the band gap increases linearly close to angles of $\alpha = 90^\circ$ for all lattice depths. The corresponding slope of the band opening is plotted for both initial magnetic quantum numbers in Fig. 6.3b in units of E_R per degree of α for increasing lattice depths. Once more, the sensitivity of the band gap on the angle of the quantization axis becomes notable. For example, a lattice depth of $4 E_R$ results in a band opening slope of $0.11 E_R/^\circ$ and $0.37 E_R/^\circ$ for $m_F = \pm 1$ and $m_F = \pm 2$ respectively, corresponding to values of $368 \text{ Hz}/^\circ$ and $1223 \text{ Hz}/^\circ$. For an accurate control over the opening and closing of the dirac cone it is, thus, crucial to be able to precisely adjust the Euler angle α . The quantization field is experimentally aligned by a set of Helmholtz coils. Residual stray fields can be

compensated fairly well up to the order of mG with an additional set of Helmholtz coils similar to the three pairs of quantization coils [153]. As can be deduced from Fig. 6.3b, a stray field of 1 mG perpendicular to the lattice plane corresponds to a band gap of approximately $20 \text{ mHz}/E_R$ for a hyperfine state with $m_F = \pm 1$ at a quantization angle of $\alpha = 90^\circ$.

6.2.3 Experimental realization of the rotation

The three pairs of Helmholtz coils used for the rotation of the quantization field in the experiment are aligned along the x , y and z -axis and have inductances of $L = 115 \mu\text{H}$, $L = 440 \mu\text{H}$ and $L = 150 \mu\text{H}$ respectively and a resistance of $R \approx 0.6 \Omega$. With this, the timescale for a rotation of the magnetic field around the y -axis by $\pi/2$ was chosen to $t_{\pi/2} = 550 \text{ ms}$. The experimental limitation of the timescales for the rotation procedure due to the finite inductances of the Helmholtz coils is by far not close to the fundamental limitation defined by the Larmor precession frequency of ^{87}Rb in the given magnetic field that is on the order of $0.77 \text{ MHz}/G$.

Nevertheless, we investigate the possibility of any residual influences of the rotation procedure onto the hyperfine state. For this, an atomic ensemble in the $|1, -1\rangle$ state is adiabatically loaded into the state-dependent honeycomb lattice with a depth of $V_{2D,0} = 3 E_R$ and an additional perpendicular one-dimensional lattice of $V_{1D,0} = 10 E_R$. Here, a full rotation of the quantization field that is initially aligned parallel to the z -axis is performed by $\alpha = 360^\circ$ around the y -axis in $4t_{\pi/2} = 2.2 \text{ ms}$. Thereby, the field is rotated by changing the current through the Helmholtz coils aligned along the z -axis and the y -axis according to

$$I_y(\alpha) = \sin(\alpha), \quad I_z(\alpha) = \cos(\alpha) \quad \text{with} \quad \alpha(t) \in [0, 2\pi]. \quad (6.5)$$

Subsequently, the hyperfine state is probed by a Stern-Gerlach separation in time-of-flight. Measurements showed no influence of the rotation procedure onto the population of the hyperfine states. A similar procedure of rotating the quantization axis by 180° and back to $\alpha = 0^\circ$ yields the same results. Hence, it could be verified that the atomic ensemble adiabatically follows the rotation of the quantization field.

6.3 Band-selective microwave spectroscopy

The influence of the orientation of the quantization axis onto the lattice geometry can be elegantly probed by a band-selective microwave spectroscopy. This versatile technique was previously applied to investigate interaction effects and the spatial ordering of spin-mixtures in the state-dependent honeycomb lattice [75]. For a thorough discussion of the mechanism and implications we refer to the PhD thesis of P. Soltan-Panahi [154]. In the following, we briefly describe the basic principles and experimental procedure of band-

selective microwave spectroscopy in the state-dependent honeycomb lattice and apply the method to investigate the tunability of the effective magnetic quantum number \tilde{m} .

6.3.1 Theoretical description

A microwave pulse can drive transitions between the two ground-state hyperfine manifolds $F = 1, 2$ of ^{87}Rb . The corresponding energy structure for the twofold atomic basis in the state-dependent honeycomb lattice is shown in Fig. 6.4a. While the two manifolds are separated by approximately 6.8GHz, the Zeeman splitting due the external quantization field between adjacent magnetic sublevels amounts to 0.7 MHz. In order to understand the resulting spectroscopy we have to consider the preparation and initial state of the atomic ensemble in the state-dependent lattice.

The atomic ensemble in an initial hyperfine state $|F, m_F\rangle$ is adiabatically loaded into a relatively shallow optical lattice of $V_{2D,0} = 3 E_R$ to $4 E_R$ with an additional perpendicular 1D-lattice of $V_{1D,0} = 10 E_R$. As the ensemble is still in the superfluid regime, it occupies the lowest Bloch band of the lattice at zero quasimomentum $\psi_{\mathbf{q}=0}^0(\mathbf{r})$ (see section 2.3.1). In the following, we use the notation $\psi_s^n(\mathbf{r})$ for the n -th Bloch wave function at zero quasimomentum in the hyperfine state $s \equiv |F, m_F\rangle$. In Fig. 6.4a and previously in Fig. 6.1 these states are indicated by the purple density distribution in the one-dimensional sketch of the two-fold atomic basis. From the initial state in the zeroth Bloch band $\psi_s^0(\mathbf{r})$ transitions can be driven to other Bloch bands $\psi_{s'}^n(\mathbf{r})$. According to the Franck-Condon principle best known from vibronic transitions in molecules, the probability of these transitions is determined by the overlap between initial and final wave functions.

As the Bloch bands are well separated close to zero quasimomentum and, similar to the multi-photon transitions discussed in chapter 3, the momentum transfer onto atoms by microwave photons can safely be neglected in comparison to the reciprocal lattice momentum. Hence, the microwave spectroscopy can be treated as a two-level problem such that transitions are described as a Rabi oscillation between the initial state $\psi_s^0(\mathbf{r})$ and the final state $\psi_{s'}^n(\mathbf{r})$. The ratio of transferred atoms is then given by

$$\frac{N'(\omega_{\text{MW}}, t)}{N} = \frac{|\Omega_{\text{FC}}|^2}{|\Omega_{\text{FC}}|^2 + \Delta\omega^2} \cdot \sin^2\left(\sqrt{|\Omega_{\text{FC}}|^2 + \Delta\omega^2} \cdot t/2\right) \quad (6.6)$$

where the frequency detuning $\Delta\omega = \omega_{\text{MW}} - \Delta\omega_{\psi',\psi}$ is determined by the microwave frequency ω_{MW} and the frequency difference $\Delta\omega_{\psi',\psi}$ between the initial and the final hyperfine state in its respective Bloch band. Ω_{FC} denotes the Rabi-frequency of the transition that relates to the on-resonance Rabi-frequency of free atoms Ω_R according to

$$\Omega_{\text{FC}} = \Omega_R \int \psi_{s'}^{n*}(\mathbf{r}) \psi_s^0(\mathbf{r}) d^3r. \quad (6.7)$$

The spatial integral in the above equation defining the overlap between initial and final wave function is known as the Franck-Condon factor.

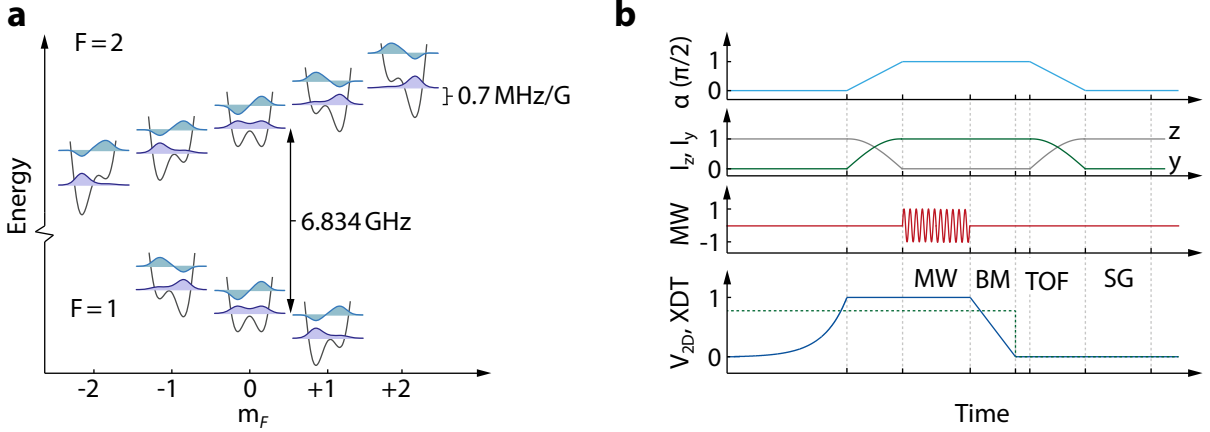


Figure 6.4: Microwave spectroscopy. **a** The energy level structure of the two ground-state hyperfine manifolds is shown for the twofold atomic basis in the state-dependent honeycomb lattice. The two lowest Bloch bands are plotted for each magnetic substate. **b** Experimental procedure of the microwave spectroscopy and rotation of the magnetic field (not to scale). After the lattice (dark blue line) is ramped to its final intensity in 100ms the quantization axis angle (light blue) is rotated in approximately 0.5ms by changing the currents I_y (green) and I_z (gray) through the Helmholtz coils. Subsequently, a microwave pulse (red) is applied to the atomic ensemble. Before the dipole trap (dashed green line) is shut off the lattice is completely ramped down in 1 ms, transferring the quasimomentum distribution into real momenta (band mapping). The quantization axis is rotated back to its initial orientation during the time-of-flight before a Stern-Gerlach gradient field is applied for 12 ms that separates the spin components.

6.3.2 Experimental procedure

The experimental procedure for the band-selective microwave spectroscopy in the honeycomb system including the rotation of the quantization axis is illustrated in Fig. 6.4b. Note that the time axis is plotted not to scale with the actual durations of subsequent experimental steps used in the experiment for clarity. First, a Bose-Einstein condensate is prepared in a single hyperfine state in the crossed dipole trap. Prior to this, the RF-evaporation in the magnetic trap is performed in the $|1, -1\rangle$ state (see section 2.1). If necessary, the atomic ensemble can be completely transferred into all other magnetic substates of the ground state hyperfine manifold by a combination of microwave pulses and radio frequency sweeps (adiabatic passages). Details concerning the initial state preparation technique can be found in Refs. [153, 158, 262]. Note that, in contrast to experiments discussed in the preceding chapters 3 to 5 experiments are performed in the *round* crossed dipole trap (see section 2.2.4).

After the initial state preparation in the dipole trap the lattice is adiabatically ramped up to a final potential depth between $V_{2D,0} = 3 E_R$ and $4 E_R$ in 100 ms. Simultaneously to the three-beam lattice, the perpendicular 1D-lattice (not depicted in the figure) is ramped to a depth between $V_{1D,0} \approx 10 E_R$ and $50 E_R$. In the three-dimensional lattice,

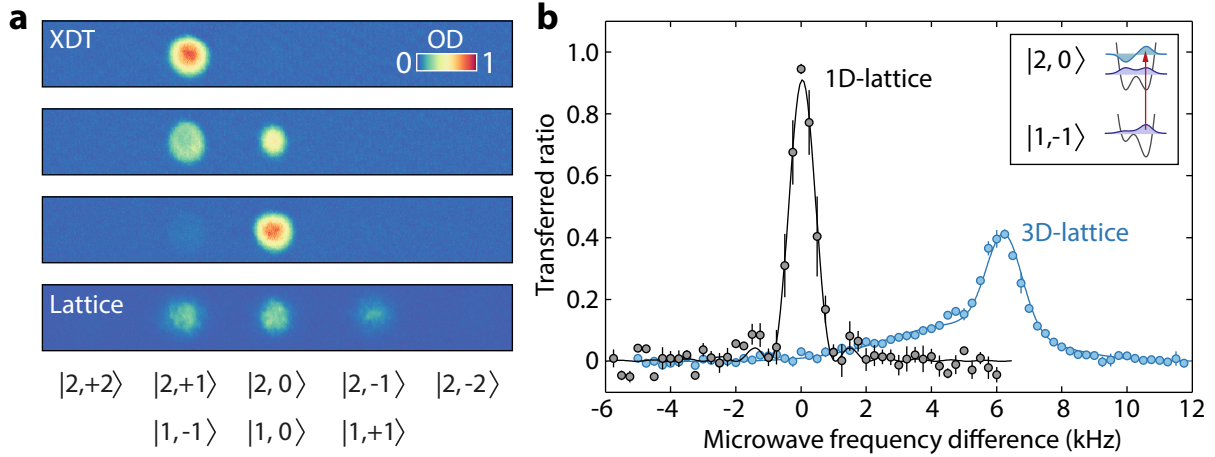


Figure 6.5: Microwave spectroscopy and spin dynamics. **a** Time-of-flight images of magnetic substates separated by a Stern-Gerlach field. The efficient transfer from the initial $|1, -1\rangle$ state into the $|2, 0\rangle$ state is demonstrated in the crossed dipole trap (first three images). The increased density in the optical lattice gives rise to additional hyperfine components due to spin-changing collisions (last image). **b** Microwave spectra for the transition obtained in the 1D and the 3D-lattice. While the transition in the state-independent 1D-lattice is exactly at the same position as for the free dipole trap (zero position of the frequency difference) the transition in the state-dependent potential is clearly shifted to larger frequencies.

the quantization axis is rotated around the y -axis. The angle α is linearly tuned to its final value (light blue line) as depicted for the case of $\alpha = 90^\circ$ by changing the currents I_y and I_z (gray and green lines) in the respective Helmholtz coils according to Eq. (6.5).

Following the rotation of the quantization field, a rectangular microwave pulse is applied for a typical duration of 1 ms. Before the dipole trap (green dashed line) is switched off, both lattice potentials are quickly ramped down. Thereby, it is possible to project the occupation of the final Bloch state onto real momenta in the corresponding Brillouin zone. For this *band mapping* technique the duration of the ramp T_{BM} has to be small compared to the external trapping frequencies ω_h and ω_v such that a redistribution of momenta during the ramping procedure can be neglected. However, it is also required that the ramping timescale is much larger than the minimum band gap between the observed energy bands in the lattice as shorter ramping times will not allow the atomic state to adiabatically follow the eigenstate of the decreasing lattice potential such that other Bloch bands are populated [53, 73, 263]. Hence, the constraints onto the timescale of the ramping can be formulated as

$$\hbar\omega_{h,v} \ll h/T_{\text{BM}} \ll E_{\text{gap}}. \quad (6.8)$$

For experiments presented here, we employ a ramping time of $T_{\text{BM}} = 0.5$ ms which satisfies the above condition for the given trapping frequencies and lattice depths.

After the lattice potentials are completely ramped down the crossed dipole trap is

switched off and the atoms fall freely under gravity. During the time-of-flight the quantization axis is rotated back to its initial orientation parallel to the z -axis. Now, a magnetic field gradient is applied to the atoms that spatially separates the different magnetic substates in analogy to the well known Stern-Gerlach experiment. Hereby, the additional rotation of the quantization field is required since the gradient field is applied along the z -axis of the coordinate system such that a different orientation of the quantization field would result in an unwanted projection of the obtained hyperfine states onto the direction of the field gradient.

Absorption imaging of the separated hyperfine states allows to easily determine the relative transferred particle number of the final state. Note that the Stern-Gerlach separation along the z -axis and the subsequent imaging in the yz -plane does not allow for the observation of the actual band populations in the honeycomb lattice. For the microwave spectroscopy presented here, we are primarily interested in the transferred percentage of atoms. The band mapping is applied nonetheless as it allows for an easier way of comparing the initial and final particle numbers.

6.3.3 Spin-changing collisions

In Fig. 6.5 an example of the Stern-Gerlach separation is shown together with obtained microwave spectra for the transition from the initial state $|1, -1\rangle$ to $|2, 0\rangle$. The first three time-of-flight images in Fig. 6.5a depict the Stern-Gerlach separation for a microwave pulse applied to a free atomic ensemble in the crossed dipole trap. Here, the frequency-dependent transfer of atoms from the $|1, -1\rangle$ to $|2, 0\rangle$ state is clearly visible. If the microwave frequency is on-resonance with the atomic transition, the entire atomic ensemble can be transferred to the $|2, 0\rangle$ state (third image from above). In the last Stern-Gerlach image of Fig. 6.5a a similar situation is depicted for the three-dimensional lattice where a significant population of a third magnetic substate can be observed. However, this population cannot result from any additional microwave transition as the energy differences between the different substates are large compared to the width of the microwave pulse. Instead, the additional component represents a population of the $|2, -1\rangle$ state that stems from spin-changing collisions between atoms that were transferred into the $|2, 0\rangle$ state. As this state is not *stretched*, such spin changing collisions, i.e.,

$$2 \times |F', m_{F'}\rangle \rightarrow |F', m_{F'} - 1\rangle + |F', m_{F'} + 1\rangle \quad (6.9)$$

can occur with finite probability. This effect is not observed in the crossed dipole trap as on the timescales used in the experiment collisions are less frequent due to the much lower density as compared to an optical lattice system [74]. In order to determine the actual ratio of the transferred atoms the additional spin component has to be taken into account. As indicated in Fig. 6.5a, atoms in the $|2, +1\rangle$ state as the complementary product of the spin-changing collisions are hidden in the residual $|1, -1\rangle$ component due to the opposite signs of their respective Landé-factors, the total number of transferred

atoms N' is determined by $N' = N(|2, 0\rangle) + 2N(|2, -1\rangle)$. As other spin changing collision processes such as $2 \times |2, 0\rangle \rightarrow |2, -2\rangle + |2, +2\rangle$ and $2 \times |2, \pm 1\rangle \rightarrow |2, 0\rangle + |2, \pm 2\rangle$ may also occur in the lattice system, the additional Stern-Gerlach components for $N(|2, \pm 2\rangle)$ are also included in the evaluation of the transferred particle number.

The resulting microwave spectra of the transition from $|1, -1\rangle$ to $|2, 0\rangle$ are shown in Fig. 6.5b for the cases of only the state-independent 1D-lattice present and for the total three-dimensional lattice setup including the state-dependent honeycomb lattice with a quantization axis aligned along the z -axis. The ratio of transferred particles in the case of the 1D-lattice shows a single resonance and follows the sinc-function of Eq. (6.6) as shown by the black solid line. Note that the resonance position is exactly the same as for the free atomic ensemble in the crossed dipole trap indicated by the zero frequency difference. In contrast, the resonance position in the 3D-lattice is clearly shifted due to the state-dependency of the potential and exhibits a bimodal structure. This shift can be attributed to a transition of $\psi_{|1,-1}^0 \rightarrow \psi_{|2,0}^1$ into the first excited Bloch band of the lattice as indicated by the inset in Fig. 6.5b with a residual transfer into the lowest Bloch band. In the following, we will investigate the microwave spectra in the honeycomb lattice systematically with respect to the orientation of the quantization axis and the resulting Franck-Condon overlaps.

6.3.4 Microwave spectra in the tunable honeycomb lattice

With the established band-selective microwave spectroscopy technique the rotation of the quantization axis or, in other words, the influence of the effective magnetic quantum number \tilde{m} onto the state-dependent honeycomb lattice can be probed. In Fig. 6.6 two different scenarios are investigated with respect to the orientation of the quantization axis. The spectra presented in Fig. 6.6a are obtained for an initial state with magnetic quantum number $m_F = 0$ that is independent of any circular polarization of the lattice light field while the final state with $m_{F'} = -1$ is strongly influenced by the rotation of the quantization field. Hereby, the honeycomb lattice depth amounts to $V_{2D,0} = 4.0 E_R$ and the additionally confining 1D-lattice depth is $V_{1D,0} = 9.6 E_R$. In contrast, the spectra shown in Fig. 6.6b are obtained for the opposite case of a state-independent final hyperfine state and a state-dependent initial state. While the honeycomb lattice depth is also set to $V_{2D,0} = 4.0 E_R$, the 1D-lattice potential of $V_{1D,0} = 46.3 E_R$ significantly increases on-site interaction effects.

Nonetheless, the spectroscopy signal of both cases is the same for the quantization axis being aligned exactly in the lattice plane, i.e, for $\alpha = 90^\circ$. Indicated by the respective insets, both the initial and final state are similar as the twofold atomic basis of the honeycomb lattice is completely degenerate and the effective magnetic quantum number is always $\tilde{m} = 0$. Here, only a single resonance is observed that corresponds to a transition into the lowest Bloch function of the final state. Another resonance at larger frequency, corresponding to a transition into the second Bloch state is not observed as the Franck-

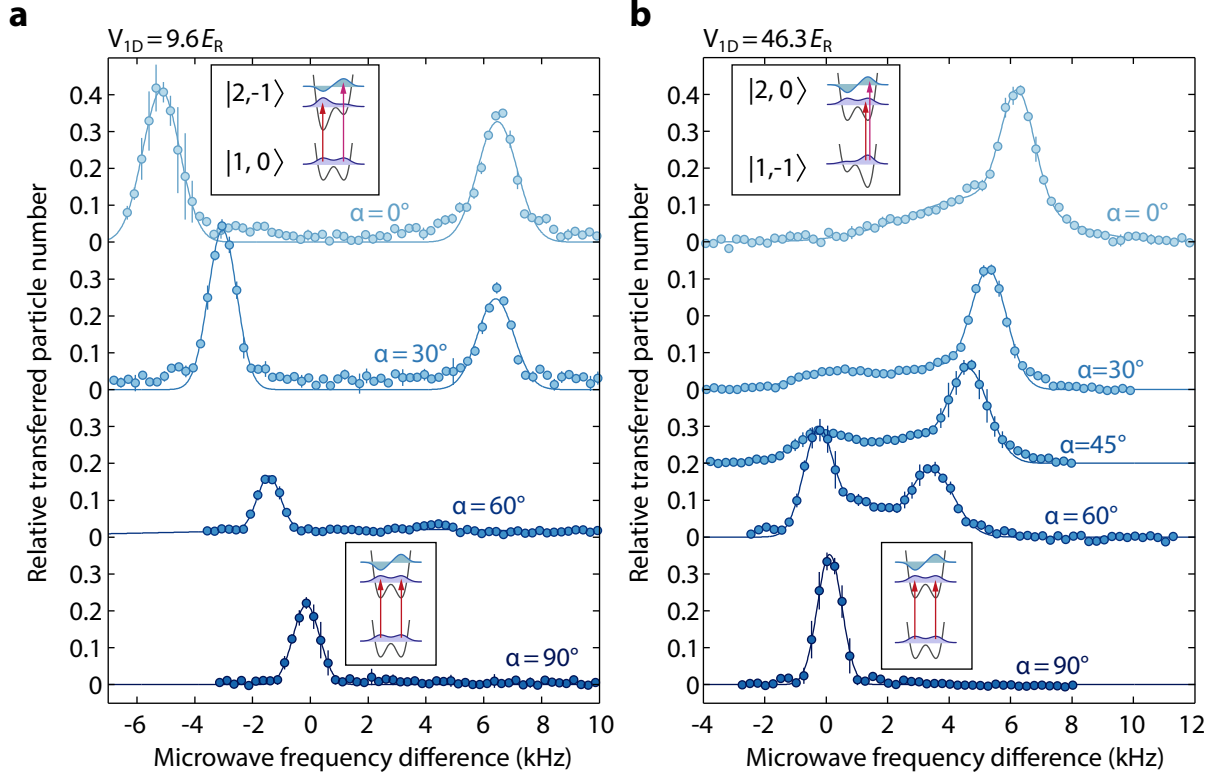


Figure 6.6: Microwave spectra of the tunable honeycomb lattice. **a** The transition from $|1, 0\rangle$ to $|2, -1\rangle$ is shown for a honeycomb lattice depth of $V_{2D,0} = 4.0 E_R$ and an additional 1D-lattice of $V_{1D,0} = 9.6 E_R$. A shift of the transition between lowest Bloch state towards smaller frequencies can clearly be observed for increasing energy offset between the final two-fold atomic basis. In addition, a second transition into the first excited Bloch state appears for a strong energy difference (see red arrows in the inset). **b** A transition from $|1, -1\rangle$ to $|2, 0\rangle$ is shown for the same honeycomb lattice depth but a strong 1D-lattice of $V_{1D,0} = 46.3 E_R$. Again, a transition to the first excited Bloch state emerges for increasing energy offset while a residual transition to the lowest Bloch state remains.

Condon overlap between the initial and final wave functions vanishes as both potentials are similar. This circumstance, however, significantly changes for an effective magnetic quantum number different from zero.

Let us first consider the transition $|1, 0\rangle \rightarrow |2, -1\rangle$ in Fig. 6.6a. If the quantization axis is rotated out of the lattice plane the resonance position for the transition between lowest bands first gets shifted towards smaller frequencies as evident for the case of $\alpha = 60^\circ$. This behavior can be understood as the final Bloch state $\psi_{|1,-1\rangle}^0$ becomes more deeply trapped at the now stronger confining sublattice site. Hence, the energy difference between initial and final state decreases due to the light shift. For even larger energy offsets between the twofold atomic basis this behavior continues and the resonance is shifted further towards smaller frequencies as observed in the spectra for $\alpha = 30^\circ$ and 60° . In addition, a second resonance appears that indicates a transition into the second Bloch state. This transition

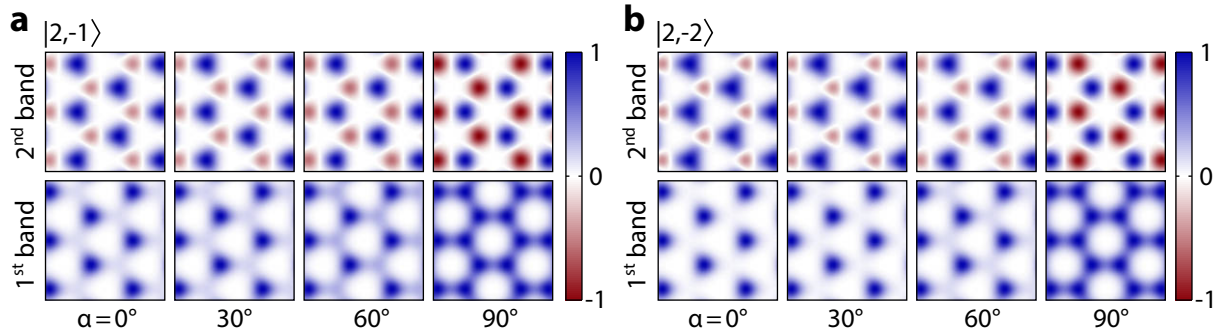


Figure 6.7: Bloch functions of the two lowest bands. **a** The first two Bloch functions of the final state $|2, -1\rangle$ from Fig. 6.6a are plotted for various angles α . The continuous transition from a asymmetric triangular state to a symmetric honeycomb state is evident. The influence of the rotation of the quantization axis on the shape of the Bloch functions is even stronger for larger magnetic quantum number as depicted in **b**. Note that the small imaginary components of the initially complex wave function have neglected in the depiction in order to illustrate the sign change and nodes of the second band.

emerges since the initial and final potentials now strongly differ such that the respective Bloch functions of initial and final state are no longer orthonormal. In Fig. 6.7a the two final Bloch states are plotted for various values of α . Here, the change from an asymmetric triangular state to a symmetric honeycomb state is evident as the energy offset between the sublattice sites decreases. Similar Bloch functions for the even more asymmetric state $|2, -2\rangle$ are shown in Fig. 6.7b.

The corresponding microwave spectra of the investigated $|1, -1\rangle \rightarrow |2, 0\rangle$ transition are shown in Fig. 6.6b. A similar emergence of a transition to the second Bloch state can be observed for an increasing energy offset. Moreover, an expected shift of this resonance towards higher transition frequencies is evident. This shift that can be understood as now the energetically lower *initial* state of the $F = 1$ hyperfine manifold rather than the final state becomes increasingly confined such that the transitions are further separated. Strikingly, a similar shift of the transition to the first Bloch state is not reproduced. While the resonance position remains relatively constant for an increasing energy offset, it quickly becomes broader and vanishes. In contrast to the previously discussed $|1, 0\rangle \rightarrow |2, -1\rangle$ transition such a behavior cannot be understood in a simple single-particle picture. In the following, we will therefore include interaction effects between the initial and the final state in the interpretation of the obtained excitation spectrum.

6.3.5 Interaction effects

The microwave spectroscopy process involves at least two atomic states, i.e., an initial state ψ_s^0 and a final state ψ_s^n , which interact repulsively with each other. Already for the moderate lattice depths at the presented experiments, such interaction effects can strongly

influence the energy spectrum of these states. Here, we employ a mean-field ansatz to investigate such interaction effects. This numerical method is based on the interpretation of excitation spectra in the state-dependent honeycomb lattice by P. Soltan-Panahi. For a comprehensive discussion of the employed algorithms and extensive applications we refer to his thesis [154]. In the following, the principle of the mean-field approach is briefly sketched and numerical calculations are applied to the observed excitation spectra of $|1, -1\rangle \rightarrow |2, 0\rangle$.

The influence of interactions can be described in the weakly interacting regime by an *effective* potential that arises from the mean-field interaction between the involved spin states:

$$V_{\text{eff}}^s(\mathbf{r}) = \sum_{s'} g_{s,s'} |\psi_{s'}^n|^2 \quad \text{with} \quad g_{s,s'} = \frac{4\pi\hbar^2}{m} a_{s,s'}. \quad (6.10)$$

In analogy to the single-component case of Eq. (2.16) the interaction strength $g_{s,s'}$ between the hyperfine states s and s' is determined by the respective scattering length $a_{s,s'}$. With this, the system for the spin-state s is described by the effective Hamiltonian

$$\hat{\mathcal{H}}^s = \hat{\mathcal{H}}_0^s + V_{\text{eff}}^s(\mathbf{r}), \quad \text{with} \quad \hat{\mathcal{H}}_0^s = -\frac{\hbar^2}{2m}\Delta + V_{\text{Lat}}^s(\mathbf{r}) \quad (6.11)$$

that represents the time-independent Gross-Pitaevskii equation [175, 192]. For the microwave spectroscopy discussed here, the final state is initially not occupied such that the contribution of $\psi_{s'}^n(\mathbf{r})$ to the mean-field interaction can be neglected [154]. The corresponding equations then simplify to

$$\left[-\frac{\hbar^2}{2m}\Delta + V_{\text{Lat}}^s(\mathbf{r}) + g_{s,s} |\psi_s^0(\mathbf{r})|^2 \right] \psi_s^0(\mathbf{r}) = E_s \psi_s^0(\mathbf{r}) \quad (6.12)$$

$$\left[-\frac{\hbar^2}{2m}\Delta + V_{\text{Lat}}^{s'}(\mathbf{r}) + g_{s,s'} |\psi_s^0(\mathbf{r})|^2 \right] \psi_{s'}^n(\mathbf{r}) = E_{s'} \psi_{s'}^n(\mathbf{r}) \quad (6.13)$$

such that the initial state $\psi_s^0(\mathbf{r})$ is not influenced by the final state $\psi_{s'}^n(\mathbf{r})$. In this case, the additional repulsive interaction term of Eq. (6.12) only results in a small broadening of the initial wave function. In contrast, the final state is strongly influenced by the effective potential arising from the repulsive interaction with the initial state. This result is confirmed by the unexpected behavior of the excitation spectra for the transition $|1, -1\rangle \rightarrow |2, 0\rangle$ depicted in Fig. 6.6b. As the initial state exhibits a strong asymmetric confinement to a single lattice sites for a significant amount of the circular polarized light field, also the final state is strongly influenced. In contrast, the excitation spectrum of the transition $|1, 0\rangle \rightarrow |2, -1\rangle$ shown in Fig. 6.6a is not influenced by interaction effects as the initial state with $m_F = 0$ is always distributed homogeneously over the twofold atomic basis.

As the effective potential in Eq. (6.10) is determined by the periodic spatial density distribution of the atoms in the lattice it can be expanded in a discrete Fourier series in

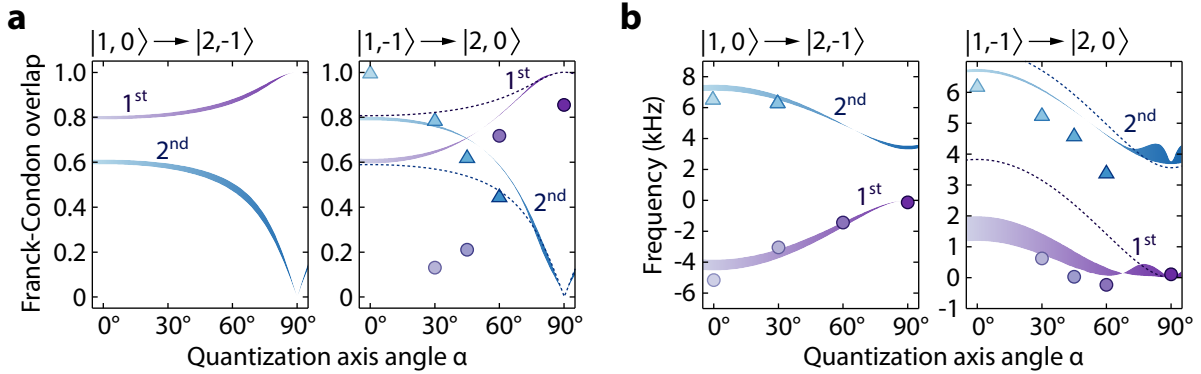


Figure 6.8: Quantitative investigation of microwave spectra. **a** Calculated Franck-Condon factors for the two investigated transitions (and the extracted values for the strongly interacting system) are plotted in dependence of α . As expected the Franck-Condon overlap for the transitions to the second Bloch state vanishes for both cases in the symmetric honeycomb lattice at $\alpha = 90^\circ$ where initial and final states are similar. **b** *Ab initio* calculations of the resonance positions reproduce the extracted values (circles and triangles). While interaction effects are omitted for the calculations of the $|1, 0\rangle \rightarrow |2, -1\rangle$ transition, the $|1, -1\rangle \rightarrow |2, 0\rangle$ transition is investigated by the iterative Gross-Pitaevskii method described in the text. Dashed lines indicate the calculated resonance positions neglecting interaction effects for the transition $|1, -1\rangle \rightarrow |2, 0\rangle$.

order to solve the Gross-Pitaevskii equations. The exact numerical solution can be obtained by an iterative calculation of the effective potential with the initial condition $V_{\text{eff}}^s(\mathbf{r}) = 0$. For each iteration i , the ground-state wave function is calculated such that the interaction term can be determined:

$$\left[\hat{\mathcal{H}}_0^s + V_{\text{eff},i}^s(\mathbf{r}) \right] \psi_s^0(\mathbf{r}) = E_s \psi_s^0(\mathbf{r}) \longrightarrow V_{\text{eff},i+1}^s(\mathbf{r}), V_{\text{eff},i+1}^{s'}(\mathbf{r}) \quad (6.14)$$

$$\left[\hat{\mathcal{H}}_0^{s'} + V_{\text{eff},i}^{s'}(\mathbf{r}) \right] \psi_{s'}^n(\mathbf{r}) = E_{s'} \psi_{s'}^n(\mathbf{r}) \quad (6.15)$$

iteration $i + 1$

In Fig. 6.8 the calculated Franck-Condon factors and the resonance positions of the first two Bloch states are shown for the transitions $|1, 0\rangle \rightarrow |2, -1\rangle$ and $|1, -1\rangle \rightarrow |2, 0\rangle$ together with the data extracted from the microwave spectra in Fig. 6.6. Note that the Franck-Condon overlaps for $|1, 0\rangle \rightarrow |2, -1\rangle$ are not depicted: Spectra shown in Fig. 6.6a have been obtained for varying pulse durations and microwave intensities such that a comparison of Franck-Condon overlaps that are given by the respective areas under the resonance curves is not possible. In Fig. 6.8a the characteristic vanishing of the Franck-Condon factor in the case of similar initial and final potentials, i.e., $\alpha = 90^\circ$ is reproduced for both transitions. Hereby, numerical calculations for the $|1, 0\rangle \rightarrow |2, -1\rangle$ transitions did not include any interaction effects. The finite spread of the calculated wave function overlap and the resonance positions indicate an assumed uncertainty of the calibrated

lattice depths by $\pm 5\%$. As we have discussed in the preceding chapter, this is a quite conservative assumption. The observed resonance positions, indicated by circles (triangles) for the transition to the first (second) Bloch state are in good agreement with the *ab initio* calculations.

Franck-Condon overlaps and resonance positions for the $|1, -1\rangle \rightarrow |2, 0\rangle$ transition were calculated using the iterative Gross-Pitaevskii approach discussed above due to two reasons: First, with a potential depth of $V_{1D,0} = 46.3 E_R$ the additional confining 1D-lattice was chosen to be significantly stronger as compared to the $|1, 0\rangle \rightarrow |2, -1\rangle$ transition ($9.6 E_R$). Second, the interaction-dependent effective potential acting on the final state is significantly stronger as the initial state is confined to a single lattice site for quantization axis angles different from $\alpha = 90^\circ$. For the calculations, homogeneous average filling of $N = 2.5$ to 3.5 particles per lattice site was estimated while the calibrated lattice depths were assumed to be exact. This initial occupation number strongly affects the influence of the effective interaction potential giving rise to the areas of uncertainty in the depicted calculations. The qualitative behavior of both the Franck-Condon overlaps can be reproduced although the observed strong decrease of the transition to the first Bloch state is not recovered by the calculations. Nonetheless, in comparison to calculations neglecting interaction effects (dashed lines) the obtained values represent a significant improvement. Moreover, the observed shift of resonance frequencies for an increasing site-offset is confirmed by the iterative mean-field method in stark contrast to the non-interacting case.

In conclusion, the investigated microwave spectra are in excellent agreement with the expected behavior of atomic ensembles in the state-dependent honeycomb lattice under the rotation of the quantization axis. Thus, the experimental technique of continuously tuning the band structure by altering the potential in real-space could be verified. Moreover, strong influences of interaction effects could be reproduced by means of an additional effective mean-field potential that is calculated by an iterative Gross-Pitaevskii approach.

6.4 Probing inter-band dynamics

In the decade following the first realization of ultracold atoms in optical lattices, experiments have primarily concentrated on the Bose-Hubbard regime of atoms in the lowest energy band. However, orbital degrees of freedom - especially for topologically non-trivial systems - constitute an important aspect to many intriguing physical effects in solid state materials such as the colossal magnetoresistance, high-temperature superconductivity or topological semimetals.

Ultracold atom systems provide an ideal playground for the study of novel effects related to multiorbital systems that may give rise to supersolid quantum phases [264, 265], quantum stripe ordering in the triangular lattice [266], incommensurate superfluidity [267] and, specifically in the honeycomb lattice, flat bands and Wigner crystallization [268] only to name a few.

So far, experiments with bosonic quantum gases in optical lattice have successfully achieved the addressing of excited bands where Bose-Einstein condensation at nonzero quasimomenta could be observed in a three-dimensional cubic lattice [269] as well as in a bipartite chequerboard lattice [66, 67]. In the latter case, evidence for a complex valued chiral order parameter was found and a topologically avoided band transition could be investigated [270, 271]. Moreover, an unconventional twisted superfluid phase has been observed for spin mixtures in the state-dependent honeycomb lattice that arises due to an interaction-induced admixture of higher bands to the ground state wave functions.

Simultaneously, higher energy bands could also be populated in fermionic systems by interaction-induced transitions between Bloch bands [59] and momentum-resolved modulation spectroscopy [80] that allowed the investigation of particle-hole dynamics [82]. Moreover, Landau-Zener-Stückelberg transitions between the two lowest bands of a brick lattice were used in order to probe tunable Dirac cones and [76] and topological phases [151].

While the interest in multi-orbital systems of ultracold atoms has increased tremendously in recent years, corresponding investigations of decay channels are relatively sparse and interband relaxation processes still lack a deeper understanding in quantum gas systems. For example, Heinze *et al.* [82] report a striking influence of the scattering length on the lifetime of a particle-like excitation in the second energy band of single-component fermi gas. In contrast to solid state systems where a variety of mechanisms may induce band decay processes (e.g., charge carrier multiplication or exchange of energy with spin degrees of freedom), only two possible decay channels have been identified in (bosonic) quantum gas systems until now: First, a collision of atoms in the excited band can lead to one atom being promoted into a higher energy band while the other atom decays into the lowest band [272], thus, conserving energy and momentum. Second, both atoms may decay into the lowest band if the excess energy can be redistributed into an available degree of freedom [273].

In the following, we aim to investigate decay mechanisms of excited bands in the tunable honeycomb lattice with respect to the presence of Dirac cones by utilizing the possibility to continuously alter both the real-space lattice potential as well as the energy band structure.

6.4.1 Excitation mechanism

In the preceding section the potential structure of the state-dependent honeycomb lattice has been investigated by a band-selective microwave spectroscopy. Transition resonances to the two lowest Bloch states corresponding to distinct energy bands of the optical lattice could be observed. We now employ this experimental technique and the knowledge about the respective transition properties in order to probe the dynamics of atoms in excited Bloch bands. By applying the previously discussed band mapping procedure, information of the momentum-resolved band population can be obtained. In the preceding

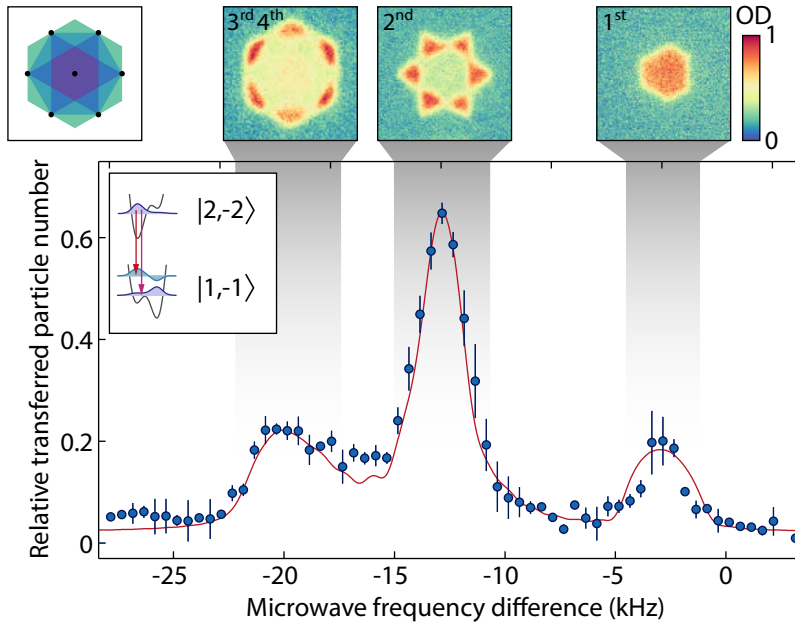


Figure 6.9: Microwave transition to excited bands. The microwave spectrum of the transition from the $|2, -2\rangle$ to the $|1, -1\rangle$ state (see inset) exhibits three distinct resonances that can be attributed to the four lowest energy bands. Band mapping images reveal the characteristic shape and population of the corresponding Brillouin zone, where the third and fourth band are simultaneously populated as they are degenerate at the Γ point. The solid red line indicates a theoretical calculation of the transition spectrum with the only free parameter being the absolute height of the transition.

investigations of microwave spectra, band mapping was primarily used to facilitate the determination of the relative final state population: The decrease of the lattice depths on sufficiently large timescales inhibits the expansion of the atomic cloud with its initial quasimomentum components as the eigenstates of the ensemble adiabatically follow the lattice potential.

We will investigate the band population of the state-dependent honeycomb lattice in more detail in the following. Hereby, in contrast to the preceding measurements, the atomic ensemble is imaged perpendicular to the three-beam lattice plane, thus, allowing a direct observation of the band populations after time-of-flight. Note that the Stern-Gerlach field gradient for the separation of magnetic substates in time-of-flight is now applied along the y -axis.

In Fig. 6.9 a microwave spectrum of the transition from the $|2, -2\rangle$ state into the $|1, -1\rangle$ state is shown for a large frequency range in the case of a maximum energy offset between the respective sites, i.e., a quantization field aligned along the z -axis. It is obtained at lattice depths of $V_{2D,0} = 3.0 E_R$ and $V_{1D,0} = 4.0 E_R$. Here, a variety of transitions to different Bloch bands can be identified that we will use in the following experiments. As the final state is energetically lower as the initial state, the largest observed resonance is the transition to the lowest Bloch band. In analogy to the microwave spectra treated

in section 6.3 it is shifted towards lower transition frequencies in comparison with the free transition in the crossed dipole trap: Initial and final state are shifted closer to each other in the state-dependent lattice as the confinement to a single lattice site that is accompanied by a lowering of potential energy is larger for the energetically higher state (see inset). The corresponding band mapping image clearly reproduces the hexagonal shape of the first Brillouin zone as introduced in Fig. 2.4. A schematic drawing of the first four Brillouin zones is again shown in Fig. 6.9.

While the transition to the lowest Bloch state is relatively weak due to the small spatial overlap between the wave functions that are primarily confined to different lattice sites, the transition to the second Bloch state is strongly pronounced. Here, the band mapping image shows the characteristic hexagram (depicted in blue in the schematic drawing). For even smaller transition frequencies, a broad transition into both the third and the fourth energy band can be observed. These transitions occur simultaneously as they are always degenerate at zero quasimomentum (see Fig. 6.1). Again, the time-of-flight band mapping image clearly shows the population of the respective Brillouin zones. Note that, in contrast to the spectroscopy signal itself, the shown images were obtained by a *sweep* of the microwave frequency over the resonance (indicated by gray areas). With this, an optimal transfer into the given state can be achieved.

The solid red line in Fig. 6.9 indicates a theoretical calculation of the transition spectrum. Despite the relatively small lattice depths, mean-field interaction effects have been taken into account, whereby the initial on-site occupation number has been weighted according to the in-trap Thomas-Fermi density profile. In order to reproduce the shape of the transition, sinc-profiles determined by Eq. (6.6) have been summed for all four lowest transitions at every evaluated frequency. With the absolute height of the transition being the only free parameter in the numerical calculations the obtained signal is in excellent agreement with the experimental data.

6.4.2 Time-resolved band decay

By sweeping the microwave pulse frequency through a transition to a final Bloch state, we have described a suitable technique to transfer an atomic ensemble with high efficiency into excited Bloch bands of an optical lattice. In the following, we employ this method in order to investigate the dynamical behavior of atoms excited to the second Bloch band with respect to the presence of Dirac cones between the two lowest bands that can be adjusted by the discussed rotation of the quantization axis. Thereby, the dynamical occupation of the bands can be observed by performing the band-mapping procedure described above.

In Fig. 6.10a time-dependent occupations of the first two Brillouin zones are shown for the two fundamentally different scenarios: First, a maximally opened band gap at the K-point of the Brillouin zone is created by the inversion symmetry breaking between the sublattices due to the strong energy offset for a perpendicularly aligned quantization axis, i.e., for the final states of $|1, -1\rangle$ and $|2, -1\rangle$ with an angle of $\alpha = 0^\circ$. Second, a

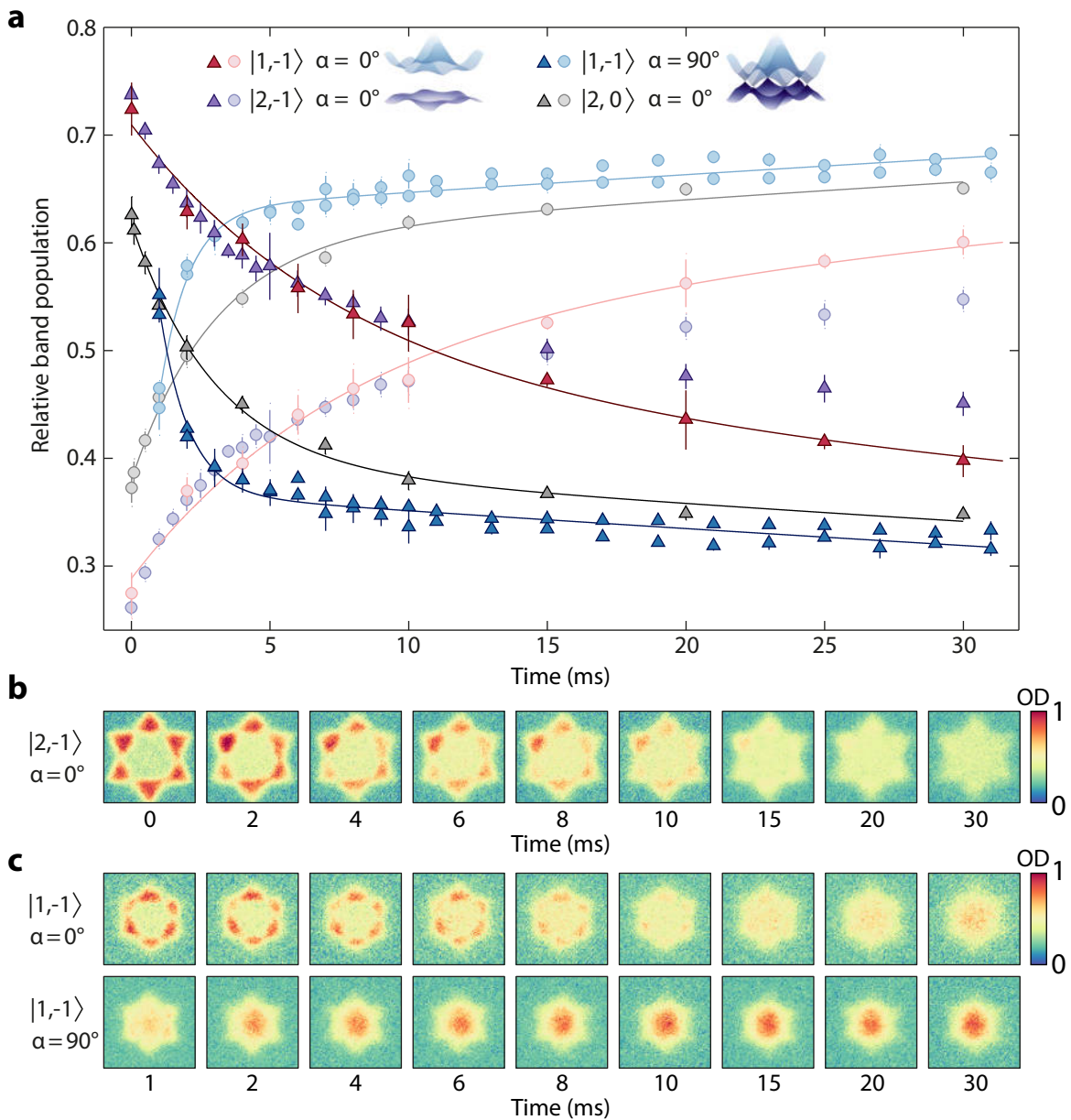


Figure 6.10: Band decay dynamics in the presence of Dirac cones. **a** The time-dependent relative population of the first (second) Brillouin zone is depicted by circles (triangles) for the two fundamentally different scenarios of a maximally opened band gap (red and purple markers) and closed Dirac points (blue and gray markers). Data is obtained by summing the atom numbers in the respective Brillouin zones. A striking difference of the lifetimes in the first excited Bloch band can be observed: While for both cases a finite fraction of atoms remains in the second Brillouin zone at all times, the initial decay to the first Brillouin zone is roughly an order of magnitude larger in the case of closed Dirac points. Error bars correspond to the standard deviation of multiple measurements. The two sets of blue markers stem from two independent measurement series. Solid lines represent double-exponential fits to the data. **b** Corresponding time-of-flight images of the observed band populations for the opened band gap and final state $|2, -1\rangle$. **c** Comparison of time-of-flight images of the final state $|1, -1\rangle$ for opened (closed) Dirac points at $\alpha = 0^\circ$ (90°).

completely intersecting Band structure with Dirac cones at both K-points is investigated where the energy offset between the two sublattices is zero as the effective magnetic quantum number vanishes (here, for $|1, -1\rangle$ and $\alpha = 90^\circ$). In addition, a similar system with a perpendicular quantization axis but zero magnetic quantum number ($|2, 0\rangle$ and $\alpha = 0^\circ$) is also investigated. Measurements were performed in the three-dimensional lattice with potential depths of $V_{2D,0} = 3.0 E_R$ and $V_{1D,0} = 3.7 E_R$. The time axis depicted in the figure corresponds to the waiting time in the lattice system following the microwave sweep of 1 ms duration before the band mapping procedure. Band populations are counted by summing over the area of the respective Brillouin zone (see Fig. 6.9). Hereby, the boundaries of the respective Brillouin zone in the experimental time-of-flight images can be determined with high accuracy by the position of the superfluid quasimomentum peaks that arise for a sudden switch-off of the lattice potential.

The two scenarios exhibit a strikingly different behavior. While atoms transferred to the excited Band that is clearly separated by an energy gap to the lowest band only slowly decay to the first Brillouin zone (purple and red data points), this decay is significantly faster for the case of a closed Dirac point (blue and black data). Examples of the corresponding band-mapping images obtained after time-of-flight are shown in Fig. 6.10b for the final state $|2, -1\rangle$ at $\alpha = 0^\circ$. In Fig. 6.10c the difference of the decay timescales between the two scenarios is emphasized as time-of-flight images for the same initial state with opened and closed bands are shown. The different size in comparison to the $|2, -1\rangle$ state stems from the different Landé-factors of these hyperfine states: As mentioned above, the magnetic Stern-Gerlach field gradient is applied along the vertical direction such that the two states are observed for different total time-of-flights in order to simultaneously image both the initial as well as the final state of the microwave sweep on the CCD-camera. While in the case of a broken inversion symmetry, i.e., $\alpha = 0^\circ$ and $\tilde{m} = +1$ the first Brillouin zone is populated by a majority of atoms after waiting times larger than 10 ms, this intersection appears already at times of approximately 1.5 ms for the case of closed Dirac points.

As a closing of Dirac points corresponds to an energy gap of zero between the investigated bands, the condition for the adiabaticity of the band mapping procedure in Eq. (6.8) cannot be fulfilled for an effective magnetic quantum number of $\tilde{m} = 0$. Thus, in order to avoid an additionally induced transfer of atoms between the respective bands, we rotate the quantization axis back to its initial perpendicular orientation *prior* to the band mapping process instead of performing this step during the time-of-flight (compare Fig. 6.4). By this, the constraint $\hbar/T_{\text{BM}} \ll E_{\text{gap}}$ imposed on the lattice ramping time T_{BM} is fulfilled such that no additional inter-band transfers occur. The duration of the lattice rotation is reflected in the data as measurements start for a finite waiting time of 1 ms in this case (blue markers). For the same reason, the validity of observations corresponding to a final state of $|2, 0\rangle$ (gray markers) is limited: The band gap cannot be opened in this case.

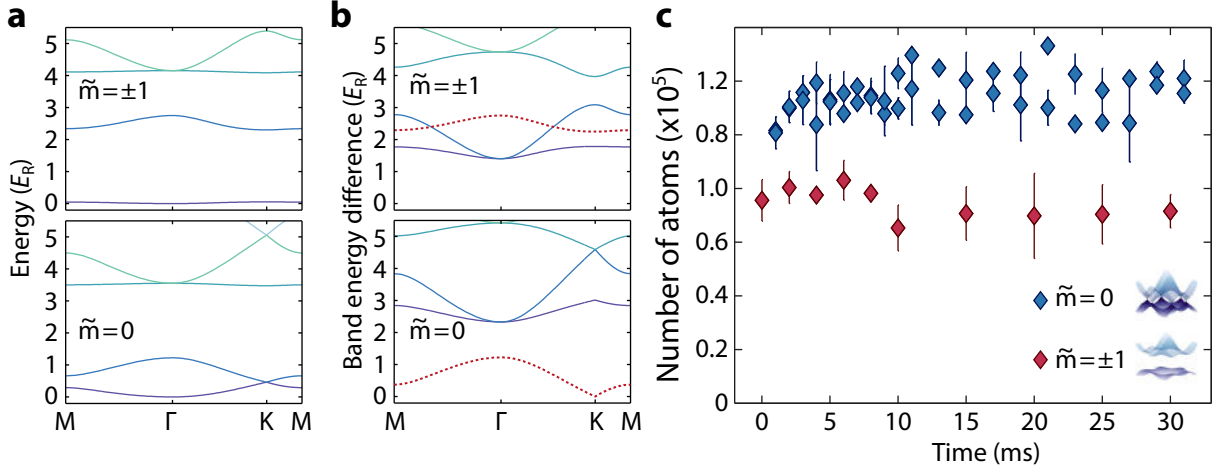


Figure 6.11: Possible inter-band decay mechanism and total atom number for the two lowest energy bands. **a** Band structures of the investigated system in Fig. 6.10 are plotted for the cases of effective quantum numbers $\tilde{m} = \pm 1$ and $\tilde{m} = 0$. In stark contrast to the symmetric honeycomb lattice with intersecting lowest energy bands, a large energy gap between the first Bloch bands is opened for $\tilde{m} = \pm 1$, i.e., $m_F = \pm 1$ and $\alpha = 90^\circ$. **b** Energy differences between the second band and all other bands are plotted. The difference from the second to the first band is shown as a dashed red line. An intersection of transitions for $\tilde{m} = \pm 1$ enables the decay channel of a simultaneous excitation to the fourth band. **c** Total atom number in the first two Brillouin zones for the measurements with a final state of $|1, -1\rangle$ reveal a constant behavior for both the opened and the closed band gap.

6.4.3 Decay mechanisms

In the preceding section the strong influence of the decay mechanism with respect to the presence of Dirac points in the honeycomb lattice has been demonstrated. The corresponding time-dependent populations of the first two Brillouin zones are well reproduced by double-exponential fits to the data that are depicted in Fig. 6.10a as solid lines. In the following, we discuss possible mechanisms for the observed decay processes.

As mentioned earlier, two distinct decay mechanisms have been identified for bosonic atoms in higher bands of optical lattices. A collision of atoms in the first excited Bloch band can either result in both atoms decaying into the lowest energy band or one atom being excited into a higher band while the other atom decays into the lowest band whereby both processes clearly are only allowed if energy and momentum can be conserved. In the former case the excess energy of the band gap is expected to be redistributed into an additional degree of freedom that can, e.g., be given by excitations along a weakly confining axis. However, experiments were performed in a true three-dimensional lattice with an additional perpendicular 1D-lattice confinement on the same order as the honeycomb lattice depth such that spatial excitations can be ruled out as the reservoir of excess energy. In the latter case, one expects the total number of atoms in the two lowest Bloch bands to decrease over time, while increasing population of the higher energy band

should be revealed by an increasing population of the corresponding Brillouin zone.

The scenario of exciting one atom into a higher Bloch band while another one decays into the lowest band is further investigated in Fig. 6.11. The band structure of the state-dependent honeycomb lattice is shown in Fig. 6.11a for the two distinct cases of an effective quantum number of $\tilde{m} = \pm 1$ and $\tilde{m} = 0$. The close-lying lowest bands for the symmetric lattice and the large opened band gap for a maximum energy offset between the sublattices are clearly visible. In part b of the figure, the corresponding energy differences between the second Bloch band and all other bands are plotted. Hereby, the difference between the second and the first band is emphasized as a dashed red line. Energy conservation of the discussed decay process requires the band difference to coincide with a transition to a higher band. While no such transitions exists for the case of $\tilde{m} = 0$ the band difference of the two lowest bands intersects with the excitation from the second to the fourth Bloch band such that the decay process is possible at these momenta. However, two observations contradict the presence of this decay mechanism: First, no increase of higher-band populations could be observed for any measurement series depicted in Fig. 6.10. Second, the combined atom number in the first and second Brillouin zone remains constant for the measurements of the $|1, -1\rangle$ as depicted in Fig. 6.11b. However, this is not the case for the seemingly similar $|2, -1\rangle$ measurement shown in Fig. 6.11c.

In principle, a third relaxation process is possible, that we have neglected so far: Under the influence of the external trapping potential, the momentum of atoms can oscillate in the excited band. For an oscillation through the minimal band gap atoms can, thus, undergo a Landau-Zener-Stückelberg transition into the lowest band. Yet, simulations of such transitions with the harmonic trapping frequencies present in the system yield timescales of such decay processes that are at least an order of magnitude larger as the observed lifetimes such that this transition process can safely be ruled out while the ambivalent results of the above considerations prohibit any further unambiguous statements regarding the relevant decay processes in the three-dimensional system.

6.5 Conclusion & outlook

In conclusion, we have successfully demonstrated a novel approach to continuously alter both the real-space lattice potential as well as the energy band structure of a state-dependent honeycomb lattice. Moreover, by breaking the inversion symmetry of the lattice, an energy gap can at the Dirac points can be opened and adjusted continuously. As this experimental technique solely relies on a change of the orientation of the systems quantization field it opens up new possibilities in both the static as well as the dynamic engineering of state-dependent optical potentials in a clean and easily controllable way.

In proof-of-principle experiments, the applicability of the implemented technique could be verified by an *in situ* probing of the state-dependent potential with band-selective microwave spectroscopy. The resulting spectra are in good agreement with numerical calculations of transition frequencies. Furthermore, interaction effects could be described

by means of an effective potential in the mean-field regime. Extensive *ab initio* simulations of a microwave spectrum over a large frequency range yield an excellent agreement with the obtained data by including the in-trap density distribution of atoms.

The study of decay mechanisms from the first excited Bloch band revealed a striking influence of the lifetime in the excited Band with respect to the presence of Dirac points. However, further systematic investigations are necessary in order to solve open questions regarding the identification of decay mechanisms.

Beyond the discussed experiments, the newly implemented technique offers many other possible applications. For example, the ability to quickly rotate the quantization axis could allow for excitation schemes similar to Ref.[66] and [67], where the sudden change of the anisotropy of sublattices enabled the coherent population of higher Bloch bands.

In a combination with time-reversal symmetry breaking induced by periodic lattice driving as presented in chapter 4 the inversion symmetry breaking due to the rotation of the quantization axis could be utilized to investigate topological phase transitions in the framework of the Haldane model [151] or to engineer non-Abelian gauge fields [2]. Moreover, the rotation itself can also be utilized for periodic driving schemes in analogy to the spatial translation discussed in the previous chapters. Here, a modulation of the sublattice energy offset may give rise to exotic dynamics in quantum spin-mixtures. In the following chapter we will investigate the rotation of the quantization field further with respect to the fully state-dependent polarization lattice.

7 Towards the realization of exotic quantum phases

This chapter provides an outlook on further possibilities for the engineering of quantum gas systems in the three-beam lattice. The previously introduced concepts of periodic lattice driving and the rotation of the quantization field are applied to state-dependent lattice systems. In addition, an expansion of the three-beam lattice setup is discussed that gives rise to peculiar lattice geometries.

In contrast to the triangular lattice, the honeycomb lattice described in the preceding chapter does not exhibit geometric frustration for antiferromagnetic interactions. Instead, the two sublattices will each feature a single spin alignment, resulting in a perfectly staggered Néel ordering of spins in the combined lattice. This situation changes drastically when processes beyond nearest neighbor tunneling become significantly large. A paradigm example is Haldane's model, where an intrinsic quantum Hall effect emerges in a two-dimensional honeycomb lattice for suitable complex *next-nearest-neighbor* tunneling [150, 274]. Recent studies conclude that the honeycomb lattice with next-nearest-neighbor tunneling may give rise to a variety of exotic states such as spin-liquids or *Bose metals* [275, 276] and topological phase transitions [277].

In this chapter we investigate possible applications of far off-resonant driving in the honeycomb lattice with respect to nearest- and next-nearest-neighbor tunneling renormalization. By adjusting the ratio of these tunneling amplitudes, a highly degenerate exotic band structure emerges within the framework of the tight-binding approximation. Furthermore, the presence of an energy-offset between the two sublattices as discussed in the preceding chapter with additional next-nearest-neighbor tunneling along the shallow sublattice could yield topological quantum spin Hall insulator phases for time-asymmetric driving schemes [2].

Beyond the next-nearest-neighbor tunneling effects, driving schemes relying on the rotation of the quantization axis in the purely state-dependent polarization lattice are briefly discussed with an emphasis on the generation of artificial gauge fields. In contrast to the previously implemented driving scheme for the realization of gauge fields, this approach relies on the staggered rotation of state-dependent lattice sites that emulates a Lorentz force acting on charged particles. Finally, an outlook concerning the expansion of the three-beam lattice setup is given that enables the creation of exotic lattices. In

this context, possible applications for the engineering of tunneling matrix elements are discussed.

7.1 Periodic inertial forcing in the honeycomb lattice

Due to the twofold atomic basis, the honeycomb lattice is comprised of two sublattices. Tunneling between nearest-neighboring lattice sites, thus, corresponds to a change of the occupied sublattices \mathbb{A} and \mathbb{B} . As depicted in Fig. 7.1a, the corresponding vectors describing the bonds of the honeycomb lattice are

$$\mathbf{h}_1 = \frac{a}{\sqrt{3}} (-1, 0, 0), \quad \mathbf{h}_2 = \frac{a}{2} (1/\sqrt{3}, -1, 0), \quad \mathbf{h}_3 = \frac{a}{2} (1/\sqrt{3}, 1, 0), \quad (7.1)$$

where a denotes the lattice constant of the triangular Bravais lattice. Tunneling to the next-nearest neighboring site preserves the occupied sublattice. Such tunneling processes take place along the bonds \mathbf{d}_i of the underlying triangular Bravais lattice as defined in Eq. (4.21). In the following, in accordance with the well-known $J_1 J_2$ quantum spin model including nearest- as well as next-nearest spin-spin interactions, we choose the notation J_1 and J_2 for the nearest- and next-nearest-neighboring tunneling matrix element respectively. Note that the notation t and t' is also common for these tunneling matrix elements.

7.1.1 Tight-binding description

Within the framework of the Bose-Hubbard model, a Hamiltonian including next-nearest-neighbor tunneling processes in the state-dependent honeycomb lattice is given by

$$\begin{aligned} \hat{\mathcal{H}} = & - \sum_{\langle i,j \rangle} \left(J_{1,ij} \hat{b}_i^\dagger \hat{b}_j + J_{1,ji} \hat{b}_j^\dagger \hat{b}_i \right) - \sum_{\langle\langle i,j \rangle\rangle} \left(J_{2,ij} \hat{b}_i^\dagger \hat{b}_j + J_{2,ji} \hat{b}_i^\dagger \hat{b}_j \right) \\ & + \frac{\Delta_{\mathbb{A}\mathbb{B}}}{2} \sum_{i \in \mathbb{A}} \hat{b}_i^\dagger \hat{b}_i - \frac{\Delta_{\mathbb{A}\mathbb{B}}}{2} \sum_{i \in \mathbb{B}} \hat{b}_i^\dagger \hat{b}_i, \end{aligned} \quad (7.2)$$

where the additional harmonic confinement as well as the on-site interaction energy have been omitted. The notation $\langle\langle i, j \rangle\rangle$ in the second term of the Hamiltonian indicates the summation over next-nearest-neighboring sites including both sublattices \mathbb{A} and \mathbb{B} . The last two terms take account for an energy offset of $\Delta_{\mathbb{A}\mathbb{B}}$ between the two sublattices. For complex tunneling matrix elements J_2 , Eq. (7.2) corresponds to the Haldane Hamiltonian. In the following, we will restrict our considerations to a homogeneous honeycomb lattice with degenerate sublattices ($\Delta_{\mathbb{A}\mathbb{B}} = 0$) and real-valued tunneling along all lattice directions, i.e., $J_{ij} = J_{ji}$. Nonetheless, an expansion of the discussed models to lattices with broken inversion symmetry and complex inhomogeneous tunneling is straightforward. A thorough treatment of such systems within the framework of the tight-binding approximation can be found, e.g., in [278] or, in the context of optical lattices, in the supplementary

material of [151]. With isotropic nearest-neighboring (NN) and next-nearest-neighboring (NNN) tunneling, the Hamiltonian (7.2) simplifies to

$$\hat{\mathcal{H}} = -J_1 \sum_{\langle i,j \rangle} (\hat{b}_i^\dagger \hat{b}_j + \hat{b}_j^\dagger \hat{b}_i) - J_2 \sum_{\langle\langle i,j \rangle\rangle} (\hat{b}_i^\dagger \hat{b}_j + \hat{b}_i^\dagger \hat{b}_j). \quad (7.3)$$

Indeed, the same inverse Holstein-Primakoff mapping applied in chapter 5 maps the Hamiltonian (7.3) onto the well known XY model discussed in the chapters 4 and 5 with an additional next-nearest-neighbor interaction [275].

With the set of three lattice bonds \mathbf{h}_i and sublattice bonds \mathbf{d}_i depicted in Fig. 7.1a, the Hamiltonian can be re-written as a sum over one of the two sublattices given by the set of triangular lattice vectors \mathbf{d} :

$$\begin{aligned} \hat{\mathcal{H}} = \sum_{\mathbf{d} \in \mathbb{A}} \sum_{i=1}^3 \left[J_1 (\hat{b}_{\mathbf{d}+\mathbf{h}_i}^\dagger \hat{b}_{\mathbf{d}} + \hat{b}_{\mathbf{d}}^\dagger \hat{b}_{\mathbf{d}+\mathbf{h}_i}) + J_2 (\hat{b}_{\mathbf{d}+\mathbf{d}_i}^\dagger \hat{b}_{\mathbf{d}} + \hat{b}_{\mathbf{d}}^\dagger \hat{b}_{\mathbf{d}+\mathbf{d}_i}) \right. \\ \left. + J_2 (\hat{b}_{\mathbf{d}+\mathbf{h}_1+\mathbf{d}_i}^\dagger \hat{b}_{\mathbf{d}+\mathbf{h}_1} + \hat{b}_{\mathbf{d}+\mathbf{h}_1}^\dagger \hat{b}_{\mathbf{d}+\mathbf{h}_1+\mathbf{d}_i}) \right]. \end{aligned} \quad (7.4)$$

In order to obtain the energy band structure in of the honeycomb lattice, it is convenient to express the creation and annihilation operators in quasimomentum space by applying a Fourier transformation:

$$\hat{b}_{\mathbb{A}/\mathbb{B},\mathbf{q}}^\dagger = \frac{1}{\sqrt{N}} \sum_{\mathbf{d} \in \mathbb{A}/\mathbb{B}} e^{i\mathbf{q} \cdot \mathbf{d}} \hat{b}_{\mathbf{d}}^\dagger, \quad \hat{b}_{\mathbb{A}/\mathbb{B},\mathbf{q}} = \frac{1}{\sqrt{N}} \sum_{\mathbf{d} \in \mathbb{A}/\mathbb{B}} e^{-i\mathbf{q} \cdot \mathbf{d}} \hat{b}_{\mathbf{d}}. \quad (7.5)$$

Now, the Hamiltonian in quasimomentum space can be written as a sum of 2×2 matrices

$$\hat{\mathcal{H}}_{\mathbf{q}} = \hat{\psi}_{\mathbf{q}}^\dagger \left[\hat{\mathcal{H}}_{\mathbf{q}}^{\text{NN}} + \hat{\mathcal{H}}_{\mathbf{q}}^{\text{NNN}} \right] \hat{\psi}_{\mathbf{q}}^T \quad \text{with} \quad \hat{\psi}_{\mathbf{q}}^\dagger = (\hat{b}_{\mathbb{A},\mathbf{q}}^\dagger, \hat{b}_{\mathbb{B},\mathbf{q}}^\dagger), \quad \hat{\psi}_{\mathbf{q}} = (\hat{b}_{\mathbb{A},\mathbf{q}}, \hat{b}_{\mathbb{B},\mathbf{q}}). \quad (7.6)$$

The corresponding matrix representations of the NN-tunneling and the NNN-tunneling are

$$\hat{\mathcal{H}}_{\mathbf{q}}^{\text{NN}} = -J_1 \begin{pmatrix} 0 & w_1(\mathbf{q}) \\ w_1^*(\mathbf{q}) & 0 \end{pmatrix}, \quad \hat{\mathcal{H}}_{\mathbf{q}}^{\text{NNN}} = -J_2 \begin{pmatrix} w_2(\mathbf{q}) & 0 \\ 0 & -w_2(\mathbf{q}) \end{pmatrix} \quad (7.7)$$

with the components

$$w_1(\mathbf{q}) = \sum_{i=1}^3 e^{i\mathbf{h}_i \cdot \mathbf{q}} \quad (7.8)$$

and

$$w_2(\mathbf{q}) = v_2(\mathbf{q}) + v_2^*(\mathbf{q}) \quad \text{with} \quad v_2(\mathbf{q}) = \sum_{i=1}^3 e^{i\mathbf{d}_i \cdot \mathbf{q}}. \quad (7.9)$$

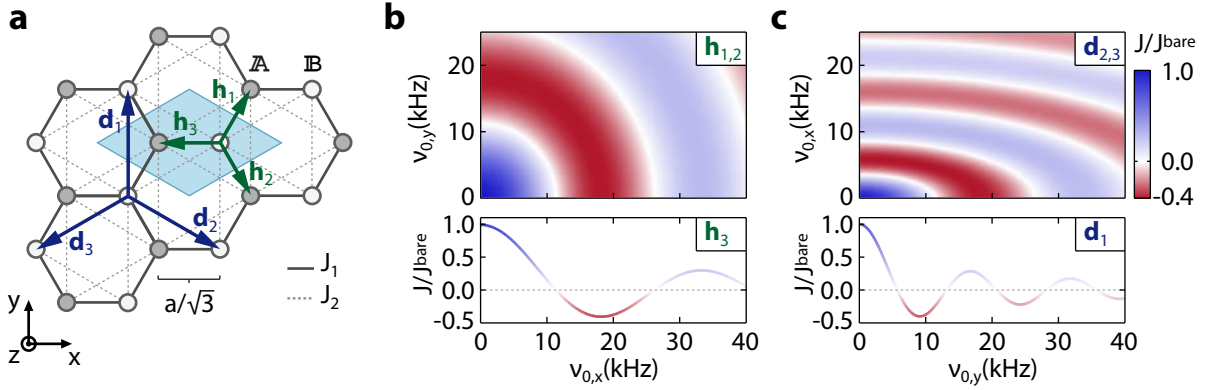


Figure 7.1: Next-nearest-neighbor tunneling in the honeycomb lattice. **a** The two sublattices \mathbb{A} and \mathbb{B} of the honeycomb lattice are connected by the nearest-neighbor bonds \mathbf{h}_i . While tunneling along these bonds (solid lines) changes the occupied sublattice, next-nearest-neighbor tunneling (dashed lines) along the triangular bonds \mathbf{d}_i takes place within the same sublattice. **b** Renormalization of the nearest-neighbor tunneling J_1 along the three bonds \mathbf{h}_i for elliptical lattice driving. Due to the shorter length of the bonds, the renormalization is weaker as compared to J_2 depicted in **c**. Note that the axes of the modulation frequencies have been exchanged due to the differing orientation of bonds. Part **c** of the figure is also shown for the similar case of the renormalization in the triangular lattice in Fig. 3.4.

It is straightforward to obtain the eigenvalues of the Hamiltonian in Eq. (7.6) analytically by calculating the determinant of the total 2×2 matrix. The result yields the dispersion of the two lowest energy bands

$$\begin{aligned}
 E^\mp(\mathbf{q}) &= J_2 w_2(\mathbf{q}) \mp |J_1 w_1(\mathbf{q})| \\
 &= 2J_2 \sum_{i=1}^3 \cos(\mathbf{d}_i \cdot \mathbf{q}) \mp \left| J_1 \sum_{i=1}^3 e^{i\mathbf{h}_i \cdot \mathbf{q}} \right|.
 \end{aligned} \tag{7.10}$$

The sign of the NN-tunneling J_1 is irrelevant to the outcome due to the particle-hole symmetry of the honeycomb lattice [275]. If the NNN-tunneling J_2 vanishes, the dispersion corresponds to the one discussed in chapter 6 for the homogeneous state-dependent honeycomb lattice. Here, the two bands touch at the K and K'-points of the band structure forming Dirac cones.

In general, the amplitude of the NNN-tunneling in the honeycomb lattice is comparatively small. A corresponding calculation of the Wannier functions in the Honeycomb lattice yields ratios of $J_2/J_1 < 0.05$ [5]. However, the periodic driving schemes introduced in chapter 3 allow for an adjustment of the ratio between nearest- and next-nearest neighbor tunneling to arbitrary values. In the following, we will explore the behavior of the band structure with respect to the ratio J_2/J_1 for the obtained tight-binding dispersion of Eq. (7.10).

7.1.2 Tuning of next-nearest-neighbor tunneling

The properties of the Bose-Hubbard Hamiltonian (7.3) are governed by the ratio between the nearest- and the next-nearest-neighbor tunneling $J_2/|J_1|$ as well as the sign of J_2 . If J_2 is chosen to be negative and real valued and the $|J_1|$ is small, the magnetic flux strength through a triangular plaquette spanned by any of the two sublattices is $\Phi = \pi$ and the system is maximally frustrated.

In Fig. 7.2 a series of tight-binding dispersions calculated from Eq. (7.10) are shown for different ratios of $J_2/|J_1|$ and negative NNN-tunneling J_2 as discussed, e.g., in Ref. [279]. A striking feature emerges if $J_2/|J_1| < -1/6$. Here, the lowest energy band $E^-(\mathbf{q})$ exhibits an *infinitely* degenerate minimum along a ring-shaped contour in momentum space. For decreasing ratios of $J_2/|J_1|$ the minimum contour grows towards larger quasimomenta. It finally crosses the boundaries of the first Brillouin zone and closes around the Dirac points which remain closed at all ratios of $J_2/|J_1|$. Accompanied by the formation of the degenerate contour ring, an energy maximum in the dispersion emerges at the Γ -point which continuously grows. The shape of the resulting lowest energy band resembles the isotropic Rashba spin orbit coupling [279–284].

Due to the diverging single-particle density of states at the minimum contour, a weakly interacting ultracold bosonic ensemble is not expected to condense at a certain point in quasimomentum space. Instead, the presence of a one-dimensional contour in quasimomentum space bears similarities to a Tonks-Girardeau gas [285–287]. For sufficiently large repulsive interactions, however, the degeneracy of the minimum contour may be lifted.

A variety of exotic physical phenomena are suggested for the presented dispersion relation. These include fermionization in the context of a Chern-Simmons gauge field [279], order-by-disorder effects [276, 288], Bose-metals [275] and other novel spin-liquid phases [276, 289]. In the following, we will investigate the experimental feasibility of engineering such dispersion relations by means of periodic lattice driving.

In analogy to the triangular lattice, far off-resonant lattice driving can be employed in the honeycomb lattice in order to adjust both the ratio $J_2/|J_1|$ as well as the sign of J_2 in order to generate the required condition for the creation of a dispersion relation with degenerate contour lines shown in Fig. 7.2.

The absolute necessity for a sufficiently large band gap for these driving schemes has been shown in chapter 3 as the driving frequency has to be chosen such that any multi-photon transitions to higher bands can be neglected. In contrast to the triangular lattice, no such band gap exists between the two lowest bands in the homogeneous honeycomb lattice. Nevertheless, a large gap is present between the second and the third band for suitable lattice depths (compare, e.g., Fig. 6.11a). At these frequencies, the coherent manipulation of tunneling matrix elements by periodic driving should be experimentally feasible without causing detrimental excitations.

In the following, we will focus on monochromatic driving as employed in experiments presented in the chapters 3 and 5. Here, the tunneling matrix elements renormalize with

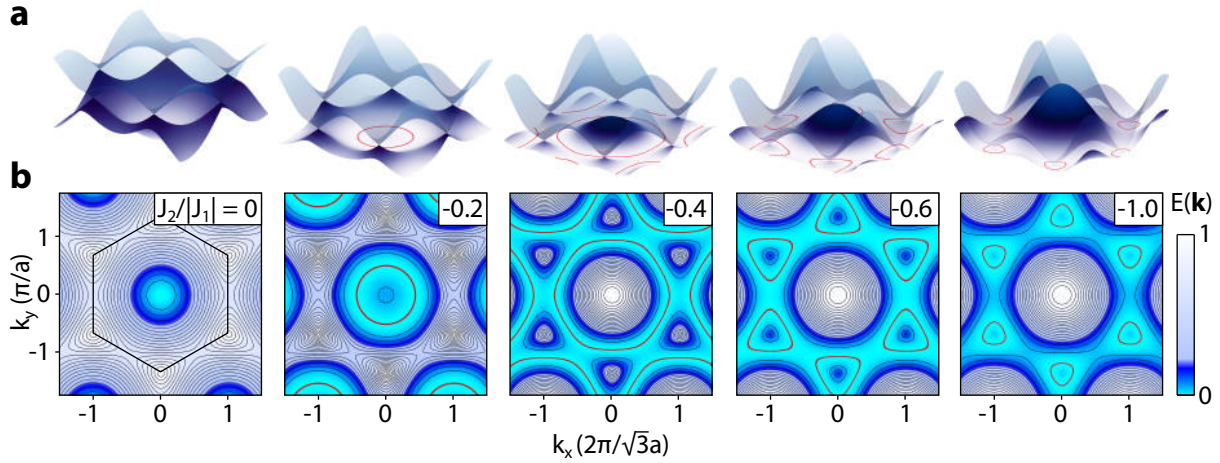


Figure 7.2: Energy bands in the honeycomb lattice with next-nearest-neighbor tunneling. **a** The two lowest energy bands obtained from Eq. (7.10) are plotted for different ratios of $J_2/|J_1|$. If the condition $J_2/|J_1| < -1/6$ is fulfilled, the lowest energy band exhibits an *infinitely* degenerate minimum along a contour in momentum space (red line) that grows towards the boundaries of the Brillouin zone with decreasing values of $J_2/|J_1|$. The contour closes around the Dirac points which remain present for all ratios. The lowest energy band is shown as a contour plot in **b**. The hexagon in the plot for $J_2/|J_1| = 0$ depicts the borders of the first Brillouin zone. For all calculations the nearest-neighboring tunneling amplitude was held fixed at a value of $J_1 = 1$.

a zeroth-order Bessel function of the first kind $J_{B0}(K)$ whereby the dimensionless forcing parameter K depends on the projection of the forcing onto the lattice bonds (see section 3.1). In Fig. 7.1b the tunneling renormalization is shown for the nearest-neighbor tunneling along the honeycomb bonds \mathbf{h}_i in dependence of the horizontal and vertical frequency modulation amplitudes $\nu_{0,x}$ and $\nu_{0,y}$. In comparison with the renormalization of the next-nearest-neighbor tunneling along the triangular Bravais lattice bonds \mathbf{d}_i (see Fig. 7.1c) the renormalization is weaker by a factor of $\sqrt{3}$ due to the projection of the forcing onto the respective lattice bonds with differing lengths.

Similar to the triangular lattice, the homogeneous forcing condition $\nu_{0,x} = \nu_{0,y}/\sqrt{3} \equiv \nu_0$ leads to an isotropic renormalization of the NN and NNN tunneling matrix elements along all lattice bonds. Due to the different total renormalization of J_1 and J_2 it is, thus, possible to adjust the ratio $J_2/|J_1|$. The corresponding Bessel functions for homogeneous forcing are shown in Fig. 7.3a. In the physically relevant region of $J_2 < 0$, the renormalization function of J_1 has a zero-crossing. Hence, arbitrary ratios of $J_2/|J_1|$ can be reached by tuning frequency modulation amplitude (see inset). As the ratio between the initial tunneling amplitudes $J_{1,2}^{\text{bare}}$ depends on the lattice depth, the obtained ratio $J_2/|J_1|$ is calculated in dependence of $J_2^{\text{bare}}/J_1^{\text{bare}}$ in Fig. 7.3b for values of up to $J_2^{\text{bare}} = 0.1J_1^{\text{bare}}$.

The tunability of $J_2/|J_1|$ comes at the cost of very small absolute tunneling amplitudes. In turn, this results in extremely long timescales that may not be accessible experimentally. Thus, the realization of sufficiently large next-nearest neighbor tunneling parameters with

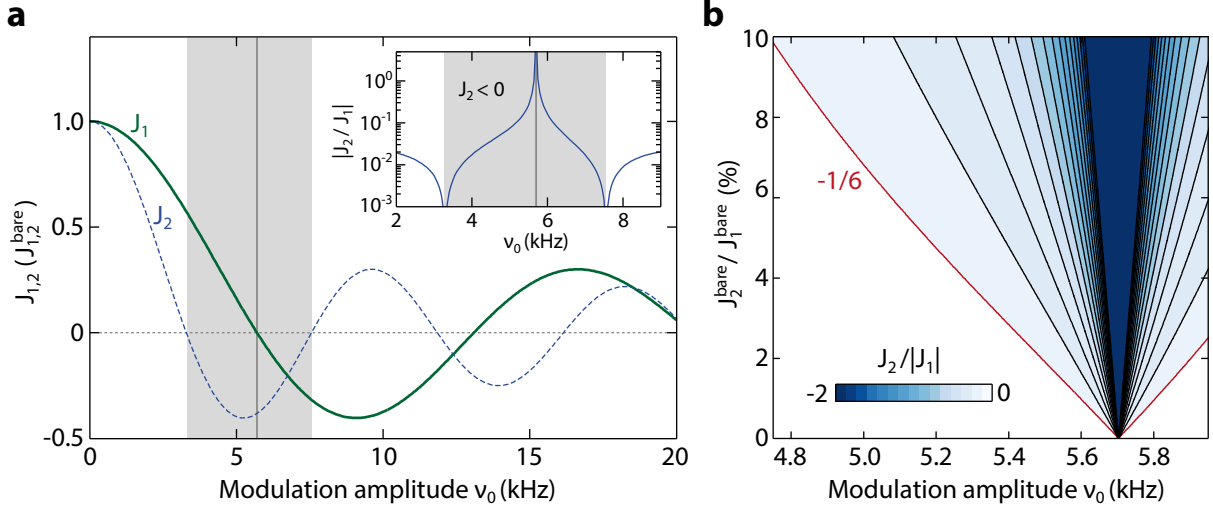


Figure 7.3: Engineering next-nearest-neighbor tunneling. **a** Renormalization of nearest-neighbor tunneling J_1 (green solid line) and next-nearest-neighbor tunneling J_2 (blue dashed line) for circular forcing. In the physically relevant region of $J_2 < 0$ the ratio $J_2/|J_1|$ can be tuned to arbitrary values due to the zero-crossing of the renormalizing Bessel function for J_1 (see inset). **b** The ratio $J_2/|J_1|$ is plotted in the vicinity of the first zero crossing of J_1 for different initial ratios of the two bare tunneling matrix elements $J_{1,2}^{\text{bare}}$. The critical boundary at $J_2/|J_1| = -1/6$ where a degenerate contour minimum in the lowest energy band appears is highlighted in red.

simple monochromatic far off-resonant driving appears to be difficult. However, recent studies suggest that an enhancement of tunneling by periodic driving is generally possible [290]. A different approach for increasing the amplitude of next-nearest-neighbor tunneling processes may be given by a coupling of energy bands with *near*-resonant driving as, e.g., in Ref. [213].

7.1.3 Topologically non-trivial bands

The engineering of nearest- and next-nearest-neighbor tunneling processes in the honeycomb lattice gives access to a manifold of physical systems. Beyond the previously discussed realization of a ring-shaped minimum contour in the energy dispersion it is, e.g., possible to create a topological insulator and a quantum spin Hall insulator in a state-dependent honeycomb lattice. The underlying experimental scheme, illustrated in Fig. 7.4a, is thoroughly described in Ref. [2]. Here, a hyperfine state with $m_F \neq 0$ is trapped at deeper \mathbb{B} -sites while next-nearest-neighbor tunneling takes place only with in the shallow \mathbb{A} sublattice. The value of the energy offset $\Delta_{\mathbb{A}\mathbb{B}}$ between the sublattices is chosen to energetically suppress tunneling along nearest-neighboring bonds. Thus, the sublattices \mathbb{A} and \mathbb{B} are decoupled.

Nearest-neighbor tunneling can be restored by resonant periodic forcing of the lattice potential at a driving frequency Ω corresponding to an integer multiple of the sublattice

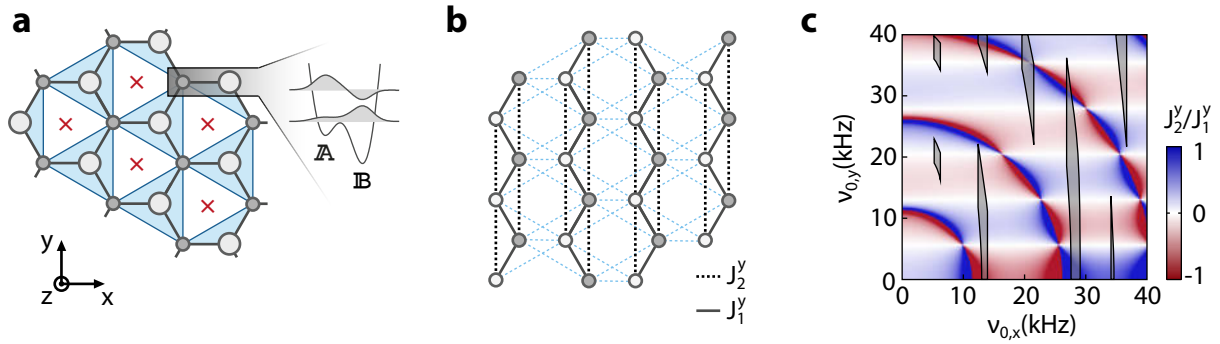


Figure 7.4: Engineering lattice geometries with next-nearest-neighbor interactions. **a** For a sufficiently large energy offset between \mathbb{A} and \mathbb{B} sites in the state-dependent honeycomb lattice, next-nearest-neighbor tunneling appears only along the shallow \mathbb{A} sublattice (blue solid lines). Restoring of nearest-neighbor tunneling with resonant driving together with the generation of staggered magnetic fluxes through the plaquettes of the \mathbb{A} sublattice (red crosses and blue areas) may give rise to topologically non-trivial bands. **b** An area of zig-zag lattices can be generated in the homogeneous honeycomb lattice by suppressing several tunneling processes (dashed blue lines) while the vertical tunneling elements J_1^y and J_2^y remain substantially large. **c** The ratio between vertical tunneling elements J_1^y and J_2^y is shown in dependence of the horizontal and vertical frequency modulation amplitudes $\nu_{0,x}$ and $\nu_{0,y}$ respectively. In addition, regions where the unwanted tunneling elements shown in **b** are suppressed by 90% are emphasized in gray.

energy offset $n\hbar\Omega = \Delta_{\mathbb{A}\mathbb{B}}$, $n = 1, 2, \dots$. Together with such *AC-induced* tunneling [188] the adjustment of artificial magnetic fluxes through the sublattice plaquettes of \mathbb{A} by time-asymmetric driving (see chapter 4) can give rise to energy bands with a nontrivial Chern number ± 1 and allows for the moving and merging of Dirac cones. In a similar context this behavior is also discussed in, e.g., in [291] and [76]. A filling of the lowest bands with fermions in a single spin state $|\uparrow\rangle$ gives rise to a topological insulator (see, e.g., [292–294]). Furthermore, for a mixture of two opposing spin state $|\uparrow\rangle$ and $|\downarrow\rangle$ that fills the lowest band, a quantum spin Hall-insulating state [274] emerges due to the interchanged roles of the \mathbb{A} and \mathbb{B} sublattices [2].

7.1.4 Zig-zag lattice arrays

An entirely different geometry can be engineered from the honeycomb lattice with NNN-hopping for a suitable suppression of tunneling along several lattice bonds. If tunneling along the horizontal NN-bonds and the diagonal NNN-bonds is suppressed (corresponding to the vectors \mathbf{h}_3 and $\mathbf{d}_{2,3}$ in Fig. 7.1a respectively) an array of *zig-zag* lattices remains. As depicted in Fig. 7.4b, is comprised of the nearest-neighbor bonds with vertical components $\mathbf{h}_{1,2}$ and the next-nearest neighbor bonds \mathbf{d}_1 . For antiferromagnetic interactions these chain of triangular plaquettes exhibit geometric frustration similar to the triangular lattice. However, owing to the reduced coordination number of $n_c = 4$ a variety of intrigu-

ing effects may arise in this geometry even for weakly interacting bosons [295] including a transition from a Haldane insulator to pair-superfluidity.

A static zig-zag lattice can also be realized by superimposing a triangular three-beam lattice and a repulsive one-dimensional lattice with a lattice constant of $a_{1D} = (3\sqrt{3}/2)a_{\triangle}$. Here, tunneling along each third triangular lattice row is suppressed due to the periodicity of the 1D-lattice. However, spatial periodic driving of such a superposition lattice in order to engineer negative valued tunneling matrix elements is inherently difficult as the relative position both lattices with respect to each other has to remain unchanged. In contrast, the suppression of lattice bonds described above does not require additional control mechanisms as the total lattice potential is rigid *per definitionem*.

The possibility of an experimental realization of the zig-zag lattice array with elliptic far-off resonant driving is explored in Fig. 7.4c. Here, the ratio of the remaining nearest- and next nearest-neighbor tunneling is plotted in dependence of the two frequency modulation amplitudes. In addition, regions where the tunneling along the horizontal NN- and diagonal NNN-bonds (blue dashed lines in Fig. 7.4b) is suppressed to a factor smaller than $0.1 J^{\text{bare}}$ are highlighted in gray. Regimes of geometric frustration and simultaneous suppression of additional tunneling are accessible. However, since the bare NNN-tunneling amplitude is much smaller than NN-tunneling, the horizontal bond along \mathbf{h}_3 has to be suppressed entirely in order to ensure a sufficiently large relative contribution of the remaining vertical NNN-tunneling J_2^y . This condition further narrows the accessible parameter regions shown in Fig. 7.4c. In addition, the tunneling suppression, yet again, comes at the cost of small total tunneling amplitudes such that the feasibility of the elliptical driving approach remains to be investigated experimentally.

7.2 Homogeneous gauge fields in a stirred polarization lattice

Within this thesis we have established versatile phase modulation schemes for the periodic driving of the three-beam lattice. An entirely different approach to periodic driving is provided by the state-dependency of the lattice potential: In chapter 6 we have investigated the striking influence of the orientation of the quantization axis onto the state-dependent honeycomb lattice which enabled a controlled breaking of inversion symmetry. Atoms are expected to follow the quantization field on timescales well below the respective Larmor frequency, which is already on the order of MHz for the employed field strength of 1 G. Hence, a periodic rotation of the quantization axis should allow for an application of driving schemes similar to the spatial translation induced by phase modulation.

In contrast to the effective engineering of dispersion relations by inertial forcing, this driving scheme directly alters the optical potential experienced by the atoms. It promises a high degree of stability, i.e., low technical noise levels, as no change of the light field itself is required. Furthermore, the application of the driving to spin-mixtures that respond

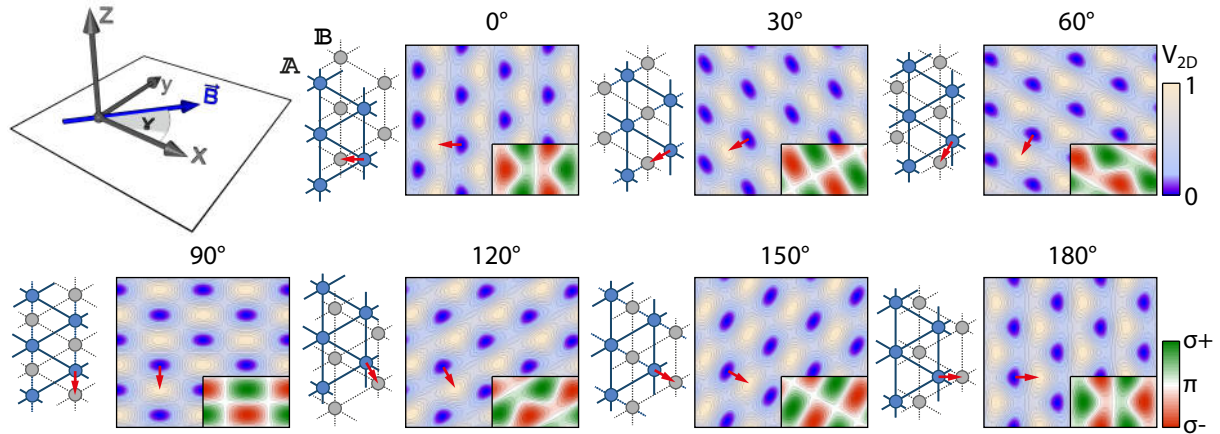


Figure 7.5: Generation of staggered vortices by rotating the quantization field. A rotation of the quantization field $\mathbf{B}(\mathbf{r})$ inside the lattice plane results in a vortex-like rotation of pairs of sublattice sites \mathbb{A} and \mathbb{B} with σ^- and σ^+ polarizations respectively. The rotation of the atomic basis vector connecting two sublattice sites is emphasized with a red arrow. For certain angles γ , in this case 30° , 90° and 150° , the coordination number of both triangular sublattices changes from initially $n_c = 6$ to 4 as tunneling along one of the three plaquette bonds is restricted by the other sublattice.

differently to the AC-Stark shift opens new possibilities for the study of interspecies dynamics. For example, a spin mixture of $|1, \pm 1\rangle$ atoms in the state-dependent honeycomb lattice interchanges the occupied sites twice for every revolution of the quantization field in the xz -plane perpendicular to the lattice. A thorough investigation of the dynamics induced by the offset energy modulation in dependence of the driving frequency and the involved spin-mixtures could provide valuable insights into spin transport phenomena. For a state-independent case, the scenario of a harmonic modulation of the energy offset between the sublattices of a checkerboard lattice is explored in Ref. [189], yielding a similar behavior of tunneling renormalization between \mathbb{A} and \mathbb{B} sites as for the periodic forcing approach.

A particularly suitable optical lattice potential for the application of quantization field induced periodic driving is given by the purely state-dependent polarization lattice. As discussed in section 2.4, it emerges if the linear polarization of the three running-wave lattice beams are aligned at angles of $\theta = \arccos(1/3)/2 \approx 35.26^\circ$ with respect to the lattice plane. In this case, the resulting light field intensity modulation of Eq.(2.32) vanishes completely. However, while the light field exhibits a constant intensity it still possesses an alternating pattern of circular polarization which will act as a lattice potential onto atoms with nonzero magnetic quantum number due to the AC-Stark shift. For the case of a quantization field pointing along the z -axis this kind of potential is illustrated in Fig. 2.7. The qualitative properties of the polarization lattice are thoroughly described in the PhD thesis of P. Soltan-Panahi [154], parts of which are published in Ref. [5].

So far, ultracold quantum gases in purely state-dependent polarization lattices have

been experimentally investigated in order to explore thermometry [180] and study interaction effects [296, 297]. However, a dynamic rotation of the quantization field offers novel intriguing possibilities for the *in situ* manipulation of the potential. In the following, we will briefly discuss the experimental realization of the three-beam polarization lattice and elaborate a particular driving scheme.

Owing to the large detuning of the lattice light with respect to atomic transitions and, thus, a small proportionality factor $\eta \approx 0.13$ in Eq. (2.33), the resulting potential shown in Fig. 2.7 is extremely shallow. Experimentally, a sufficiently deep polarization lattice can, however, be created at *magical* wavelengths located between two atomic transitions. Here, the attractive and repulsive contributions to the lattice potential arising from the simultaneous blue- and red detuning of the lattice laser light exactly cancel each other, leaving only a polarization-dependent component. For the case of the D_1 and D_2 lines in ^{87}Rb the magic wavelength is readily calculated with the condition $\mathcal{D}_1 = -2\mathcal{D}_2$ from Eq. (2.2) and (2.3). The obtained value of $\lambda_M = 790.7 \text{ nm}$ has, e.g., been verified for the creation of a polarization lattice in Ref. [180]. Beyond the larger accessible total potential depths, a lattice detuning to the magic wavelength has the advantage of an additional suppression of residual intensity-dependent potentials due to a slight misalignment of the laser polarization. While the small total detuning with respect to atomic transitions comes at the cost of larger spontaneous scattering lengths, the generation of suitable polarization lattices is experimentally feasible.

Due to the purely state-dependent nature of the three-beam polarization lattice, the rotation of the quantization field alters the entire potential rather than only a comparatively small percentage as in the state-dependent honeycomb lattice. A change in the direction of the quantization field can have a striking influence on the potential landscape. A scenario where the field is rotated inside the lattice plane yields a peculiar behavior of the lattice sites. The respective Euler angles in this case are $\alpha = 90^\circ$, while the in-plane angle γ is variable and the third angle β is irrelevant. In this case, the resulting polarization potential can be written as

$$V_{\text{pol}}(\mathbf{r}) = V_0 \sqrt{\frac{2}{3}} (-1)^F m_F \eta \sum_{i=1}^3 C_i \sin(\mathbf{b}_i \mathbf{r}) \quad (7.11)$$

with the truncated coefficients of Eq. (2.34) given by

$$C_1 = -2 \cos \gamma \quad \text{and} \quad C_{2,3} = \cos \gamma \pm \sqrt{3} \sin \gamma. \quad (7.12)$$

In Fig. 7.5 the potential (7.11) is depicted for different values of the Euler angle γ . Strikingly, the rotation of the quantization axis gives rise to a rotation of the twofold atomic basis as pairs of σ^+ and σ^- sites revolve around each other. The two triangular sublattices, however, retain their rigid shape and are only shifted with respect to each other. For certain angles γ , both sublattices are aligned along lattice bond such that the coordination number of both triangular sublattices changes from $n_c = 6$ to 4 as one tunneling direction is blocked by the other (repulsive) sublattice.

This peculiar behavior results in an array of microscopic vortices with the size of a single lattice plaquette. The rotation mimics the behavior of charged particles subjected to a Lorentz force (recall the similarity with the Coriolis force). Hence, the rotation of the magnetic quantization field gives rise to an artificial magnetic field. In contrast to the artificial gauge fields that were emulated in the triangular lattice (see chapter 4), this field is not staggered but homogeneous, as the rotation of both sublattices \mathbb{A} and \mathbb{B} is oriented in the same way. For sufficiently deep lattices and large rotation frequencies, the emulated magnetic flux through a lattice plaquette can as well reach values of a fundamental flux quantum [189, 298, 299], a regime that appears impossible to access for stirred bulk systems as, e.g., in Refs. [39, 107, 108] due to the increasing centrifugal forces that drag atoms out of the trap. In a similar context, arrays of locally rotating potentials have been realized in an optical lattice in order to reach the fractional quantum Hall limit [112].

In conclusion, the purely state-dependent polarization lattice derived from the three-beam setup is a promising candidate for the emulation of strong gauge fields that could allow for the investigation of physical regimes that are hard to access with solid state systems due to the comparatively small plaquette sizes. Only recently, large magnetic fluxes through two-dimensional Moiré superlattices have enabled a first glimpse into such strong field physics and the recursive Hofstadter energy spectrum [300–302]. Whether such regimes can be realized experimentally in the polarization lattice remains to be investigated.

7.3 From three- to six-beam lattices

Throughout this thesis we have explored a variety of lattice geometries that can be realized with the running-wave three beam lattice as introduced in section 2.4. Hereby, all considerations were restricted to linear polarized lattice beams. This description of the running-wave three beam lattice is far from being complete. By considering arbitrarily polarized light beams it is possible to realize a large variety of more complex lattice configurations that are not limited to two dimensions as, e.g., a truly three-dimensional hexagonal close-packed (hcp) lattice.

In the following, however, we will briefly explore an expansion of the running-wave three-beam lattice setup that allows for the generation of peculiar two-dimensional lattice geometries while being comparatively easy to implement: Retro-reflection of all three lattice beams as depicted in Fig. 7.6c according to Refs. [182, 303, 304].

While we have argued in chapter 2 that a configuration of more than $d+1$ laser beams in d -dimensions does not yield a stable interference pattern [30], the experimental realization of such a six-beam setup in two dimensions may very well be feasible for sufficiently stable retro-reflecting mirrors which unambiguously define the phases of the laser beams. In contrast the same reasoning does not necessarily hold for more than $d+1$ *running-wave* laser beams. This circumstance renders the realization of optical quasicrystals as, e.g., in Ref. [305] highly difficult as no defining points for the relative phases exist.

An intriguing state-independent potential landscapes arises for a configuration with all six individual laser beams being linearly polarized within the lattice plane, i.e., for polarization vectors $\epsilon_i = R_z(\pi/2) \mathbf{k}_i/|\mathbf{k}_i|$ or $\theta = 0$ similar to the state-dependent honeycomb lattice. In Fig. 7.6a and d the resulting potential is plotted for red- and blue-detuned lattice beams respectively that will be described in the following.

7.3.1 Kagome lattice

A red-detuned light field of the retro-reflected six-beam setup yields a kagome lattice that is distinguished by corner-sharing triangular plaquettes as illustrated in Fig. 7.6b. This type of two-dimensional lattice is of central interest in many condensed matter systems as it exhibits the highest known degree of geometric frustration in two dimensions (compare section 5.1.2) and quantum spin liquids or valence bond solids have been proposed as possible ground states [130, 306]. The underlying triangular Bravais lattice of the kagome lattice exhibits a three-fold atomic basis \mathbb{A} , \mathbb{B} and \mathbb{C} . All three individual lattice sites possess a coordination number of $n_c = 4$ as each site is shared by two triangular plaquettes. As a striking feature, the energy band structure of the kagome lattice exhibits a flat band in between the two (other) lowest bands which touch at Dirac cones similar to the honeycomb lattice. Demand for the realization of geometrically frustrated kagome lattices in model systems has been growing steadily due to the difficult spectroscopic probing of such systems in solid state materials [138, 307].

While an optical kagome lattice has recently been realized for ultracold atoms by a superposition of two commensurate triangular lattices [77], geometrical frustration, requiring the engineering of negative tunneling matrix elements, has not been realized so far. The presented setup, together with the application of periodic forcing could provide a pathway towards the study of frustration effects in this highly peculiar lattice and may enable the population of the flat band for a suitable engineering of the tunneling matrix elements.

7.3.2 Dice lattice

If the lattice setup described above is blue-detuned with respect to the relevant atomic transition lines, the kagome potential is inverted and its dual lattice emerges as shown in Fig. 7.6d. Due to its specific shape, this \mathcal{T}_3 -lattice is mostly referred to as the *dice* lattice which was first studied in Ref. [181].

Similar to the kagome lattice, the dice lattice has a three-fold atomic basis and an underlying triangular Bravais lattice (see Fig. 7.6e). Moreover, the lattice structure is comprised by two honeycomb sublattices that are occupied by the \mathbb{A} and \mathbb{B} sites with a coordination number of $n_c = 3$. The hub-sites \mathbb{C} , the larger potential minima in Fig. 7.6d, with a coordination number of $n_c = 6$ connect these two sublattices.

An exceptional effect arises for the dice lattice due to its geometry: If charged particles

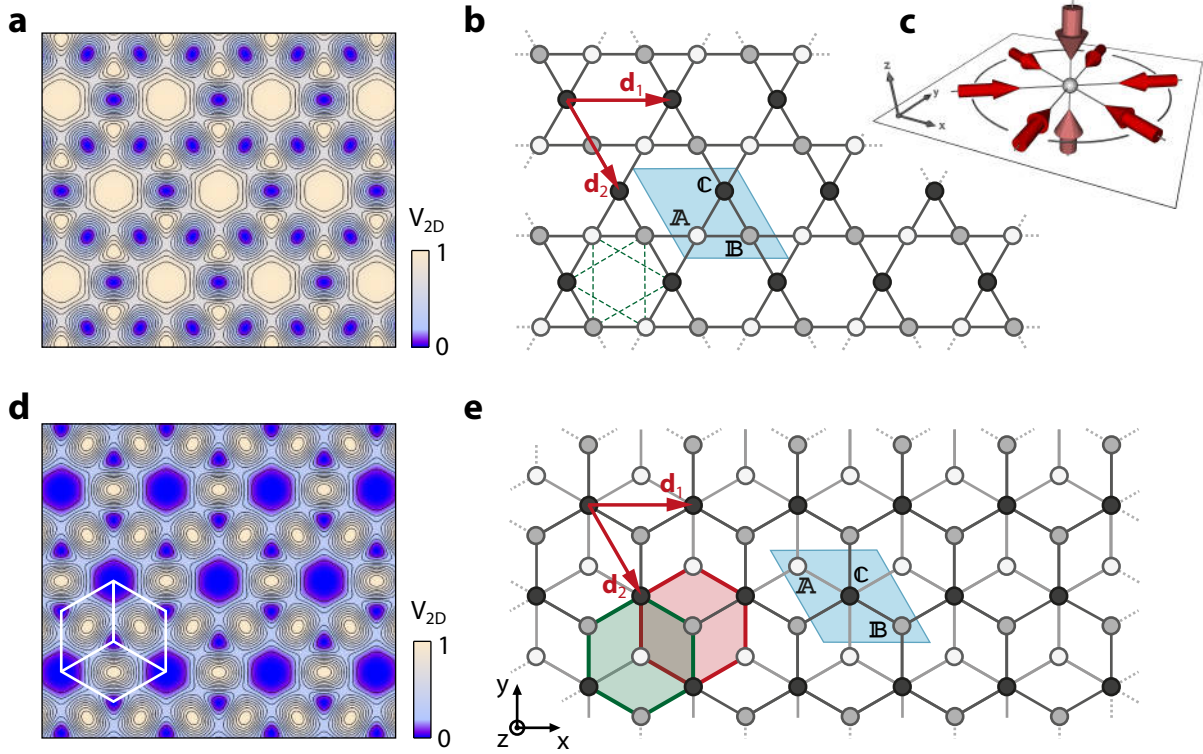


Figure 7.6: Kagome and dice lattice in the six-beam setup. **a** For a red detuned light field in the six-beam configuration (as shown in **c**), the resulting optical potential gives rise to a kagome lattice. It exhibits a three-fold atomic basis \mathbb{A} , \mathbb{B} and \mathbb{C} depicted in **b**. The translation vectors $\mathbf{d}_{1,2}$ form a triangular Bravais lattice with a unit cell highlighted as a blue rhombus. NNN-tunneling directions are exemplarily illustrated as dashed green lines. **d** For blue detuned laser light, the potential landscape gives rise to a Dice lattice emphasized by solid white lines in the lower left corner. **e** The dice lattice is comprised of two honeycomb sublattices highlighted in green and red with the same triangular Bravais lattice as in **a**.

in this lattice are subjected to a magnetic field with a strength of one-half flux quantum per plaquette, the emergence of so-called “Aharonov-Bohm cages” bounds particles to single lattice sites and restricts any motion [308]. This extreme localization mechanism results in the formation of three completely flat bands. Such a dispersionless spectrum corresponds to a macroscopic degeneracy that remains intact for finite interactions and may be lifted by the formation of a unique vortex lattice due to an order-by-disorder effect [309, 310]. Further proposed phenomena connected to the intriguing band structure of the dice lattice include the formation of Dirac-Weyl fermions [182] and exotic fractional quantum Hall effects [311].

An emulation of the required flux strength of $\Phi = \pi/2$ with ultracold atoms in the optical dice lattice could enable access to such intriguing phenomena. However, all lattice plaquette bonds of the dice lattice are pairwise parallel. Hence, the periodic driving

technique employed for the generation of artificial magnetic fluxes in chapter 4 cannot directly be applied to the dice lattice.

7.4 Conclusion & outlook

Periodically driven lattice model systems provide an ideal playground for the emulation of exotic quantum phenomena that are yet to be explored. Both the engineering of tunneling matrix elements in the state-dependent honeycomb lattice as well as the realization of plaquette vortices by a rotation of the quantization field in the purely state-dependent polarization lattice promise valuable insights into fundamental unresolved problems. Beyond that, the engineering of peculiar geometries as the geometrically frustrated kagome lattice and the dispersionless dice lattice with a retro-reflected setup represents a promising prospect for future experiments with ultracold atoms in unconventional driven lattices.

The presented considerations on possible future applications of periodic driving schemes are far from being complete and the mentioned proposals for the realization of novel exotic quantum many-body phenomena merely scratch the surface of the vast possibilities provided by the fast-paced theoretical and experimental progress in the field of ultracold quantum gases in optical lattices.

A Data analysis and representation

In this chapter we discuss central aspects concerning data evaluation and presentation. The behavior of crucial observables such as the maximum-pixel contrast is investigated in comparison with the peak-contrast and its robustness is verified. Furthermore, de-fringing algorithms that were utilized for data evaluation of time-of flight images are described and issues arising for the visualization of data are discussed.

The analysis and representation of data is a crucial aspect to almost every part of natural sciences. In the following, we discuss specific issues concerning evaluation and representation of data that are relevant to this thesis.

A.1 Comparison of contrast methods

In chapter 2 we have made use of two very different methods of extracting a measure for the level of coherence from obtained absorption images. The first one being the *momentum distribution contrast* and the latter being the so-called *maximum-pixel contrast*. As shown on Fig. 3.2, the momentum contrast relies on the knowledge of the positions of superfluid momentum peaks. Atoms in these regions are summed and subtracted by a sum over regions in between the peaks, where no atoms should reside for an ideal superfluid. On the one hand this method has two decisive advantages: To begin with, it yields *per definitionem* a normalized signal due to the summation and normalization over equal surfaces of the absorption image. Furthermore, the obtained contrast value does not only reveal the level of coherence in the system but also gives rise to a sign change of the signal if the dispersion is inverted as it is, e.g., the case for the monochromatic driving schemes discussed in chapter 3 and 5. However, it can become impractical to evaluate large contrast masks if the Wannier envelope of the momentum distribution oscillates over a large area due to periodic driving. The quality of the signal is also prone to fluctuations of the image position as the location of the superfluid momentum peaks has to be exactly defined. On the other hand, the maximum pixel contrast is insensitive to such disturbances as simply a number of pixels with the largest values are averaged in order to obtain a measure for the degree of coherence in the system. Although this method does not yield any information concerning the dispersion itself it is, thus, an excellent tool for measuring excitation processes for systems that result in an overall loss of coherence. To verify the applicability of the maximum-pixel contrast in comparison with the momentum contrast,

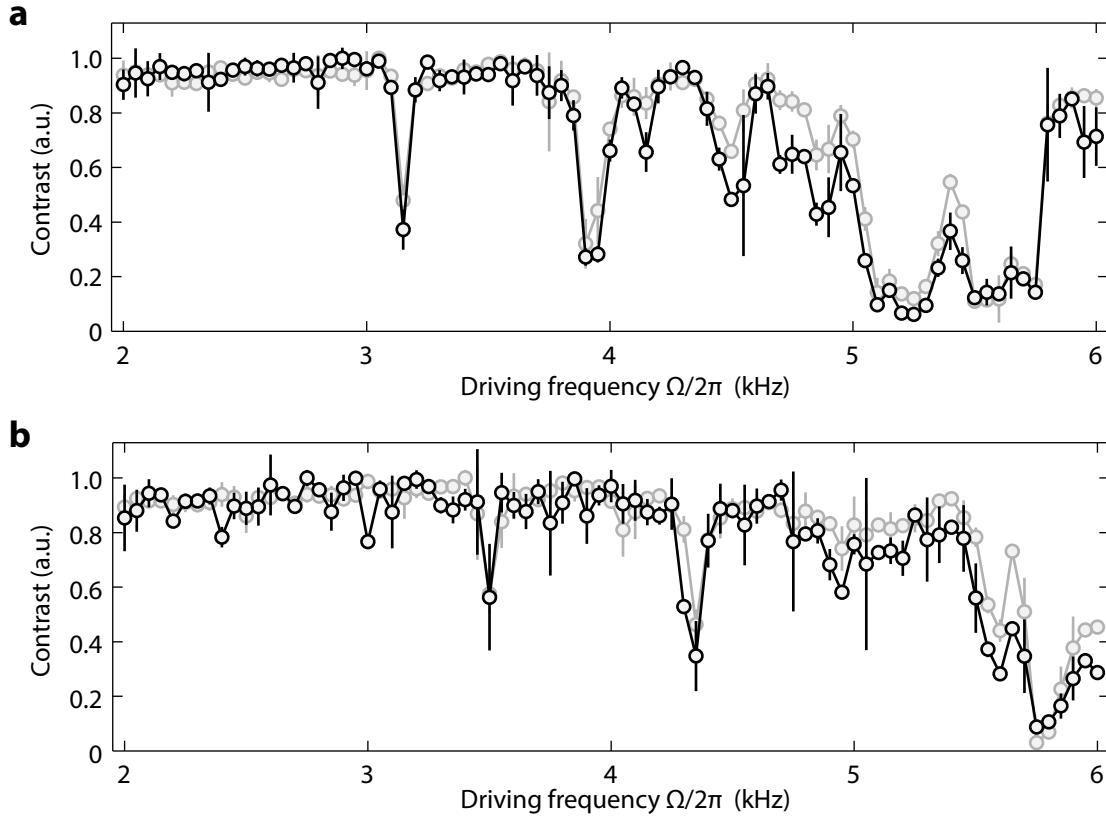


Figure A.1: Comparison of contrast methods. Spectra shown in **a** and **b** depict multi-photon resonances in the driven running-wave 1D-lattice similar to Fig. 3.6c and d. Data for the maximum-pixel contrast (black) and the momentum peak contrast (gray) match very well. The standard deviation for the maximum-pixel contrast depicted by error bars is slightly larger compared to the momentum peak contrast.

data obtained with the two methods is depicted in Fig. A.1. These spectra depict multi-photon resonances in a driven running-wave 1D-lattice and have already been shown in Fig. 3.6c and d. For both cases, the maximum-pixel contrast depicted by black data points is extracted for a number of included pixels of $n_{\text{pix}} = 3$. Gray data points depict the corresponding momentum peak contrast. In order to compare the signals qualitatively, all data sets have been normalized to a maximum contrast value of 1. Additionally, data points are connected with lines to emphasise the behavior at the resonances. Clearly, data sets for both measurements are in good agreement with each other, thus validating the applicability of the maximum pixel contrast for the extraction of excitation spectra.

The number $n_{\text{pix}} = 3$ of included pixels that are averaged to obtain the maximum-pixel contrast is arbitrary. A small number of pixels may result in a signal that is very sensitive to even small excitations in the investigated system but may also give rise to a larger sensitivity to detrimental fluctuations such as faulty CCD-pixels. In chapter 3 we have mainly employed a very small n_{pix} as the analyzed images were not prone to large

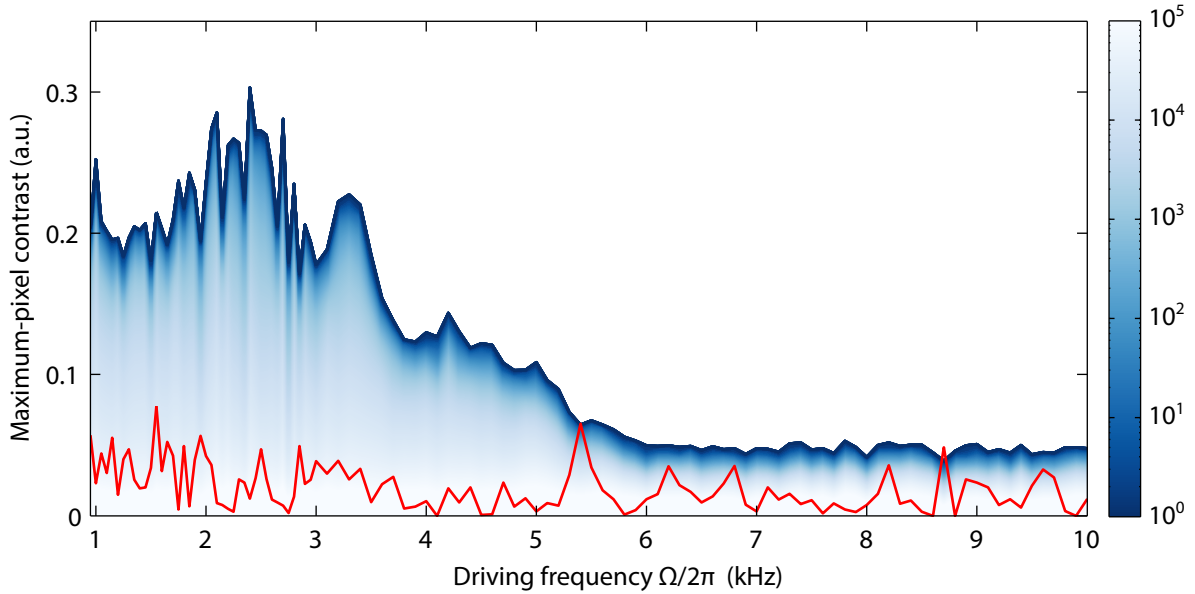


Figure A.2: Maximum-pixel contrast behavior of an excitation spectrum in dependence of the number of included pixels. Spectra for each value of included pixels are shown as colored lines with a color-coding corresponding to the color bar on the right hand side. The red line indicates the normalized standard deviation of the contrast data for a value of $n_{\text{pix}} = 1$.

fluctuations. However, it was necessary to include a large number of $n_{\text{pix}} = 10^3$ pixels in order to obtain comparable spectra of individual measurements in Fig. 3.8. In Fig. A.2 we investigate an excitation spectrum with respect to the number of included pixels in order to justify this large varying of the data analysis method. The excitation spectrum at hand is obtained for an isotropically driven triangular lattice over a comparatively large range of driving frequencies. The maximum-pixel contrast is plotted for n_{pix} ranging from 1 to 10^5 according to the depicted color coding. Although the total value of the contrast necessarily declines for larger numbers of included pixels, the relevant features indicated by cusps in the spectrum are clearly retained even for very large n_{pix} . Accordingly, it is legitimate to include even very large numbers of pixels in the contrast evaluation for the extraction of excitation spectra.

A.2 Color-coded data visualization

Data presented in this thesis is frequently color-coded by mapping scalar values to color, e.g., for the case of time-of-flight absorption images, potential landscapes and any other two-dimensional scalar arrays. The sole purpose of such color-coded data visualization is the unambiguous, easily recognizable depiction of proportions. Nonetheless, the excessive use of color-codings which explicitly contradict this purpose is still considered a persistent and wide spread problem in many fields of natural science [312–314]. A paradigm example

of falsely applied color-coding in data visualization is the use of the so-called *rainbow* colormap. Due to its lack of perceptual ordering and its luminance gradients, data is obscured and additional artifacts may arise from Mach bands. Within this thesis, two such perceptually unadjusted colormaps have been used, namely for the depiction of the three-beam lattice potential (see Fig. 2.5, 2.6, 2.7, 6.1, 6.2, 7.2, 7.5, 7.6) and the two-dimensional dispersion relation (see 3.5, 4.7, 4.10). Here, the application of distorted colormaps was chosen in order to emphasize the often rather shallow, but physically relevant minima of the depicted data. Nonetheless, in most cases the color map is accompanied by equidistant contour lines which allow for a realistic estimation of the actual data.

All other divergent and sequential color schemes employed within this thesis are adjusted with respect to gradients in perception and luminescence. However, they are still *not* adjusted to color vision deficiency.

A.3 Defringing algorithms

Time-of-flight absorption images may exhibit a significant amount of interference fringes that arise from the coherence properties of the detection light. In order to minimize the detrimental effects of such unwanted fringes onto the signal-to-noise ratio of the obtained data, two different defringing algorithms have been applied to sets of time-of-flight images within the scope of this thesis. The basic principle of both approaches is the construction of a suitable basis from a given set of absorption images that yields optimal pseudo-reference images which minimize fringes with respect to the corresponding absorption images. Hereby, the algorithm should be able to extrapolate the fringes appropriately into the region of interest, i.e., the area of the images where atoms are present.

The first method is based on an iterative construction of the basis set according to a Gram-Schmidt process [156, 158]. While the algorithm yields good results it is computationally costly for large image sets and, hence, comparatively slow such that additional selection processes have to be applied for the basis construction. The second method is closely related to the independent component analysis discussed in chapter 6 and follows a suggestion of Ockeloen *et al.* [315]. Here, the employed calculation of a set of linear equations is reasonably fast even for large data sets on the order of ~ 500 images.

A.4 Automated notch-filtering of correlation data

In chapter 5 second-order density density correlations were extracted from sets of time-of-flight images. In order to ensure reproducibility of the extracted data, all processing routines have been applied automatically to all sets of data without any selection of images by the experimenter. Post-processing of data included selection concerning particle number and width. Furthermore, a normalization and centering procedure of the single-shot time-of-flight images has been applied as well as filtering with a suitable Hamming fre-

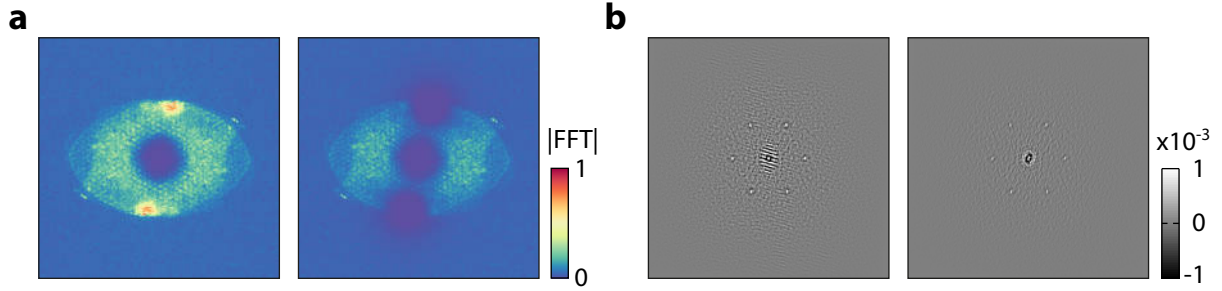


Figure A.3: Notch-filtering of correlation data. **a** In the first image, the unfiltered power spectrum of a correlation signal in the Mott-insulating regime of a staggered 2D-system in the triangular lattice is shown. Hereby, correlation peaks in the signal correspond to the shallow triangular pattern that is visible throughout the spectrum. Frequency components with larger amplitudes, e.g., the two predominant features in the spectrum, correspond to unwanted noise. In the second image, these regions of the spectrum are filtered out by applying a series of Gaussian notch filters with a width of three pixels to each pixel above a certain threshold. **b** Corresponding correlation images of the two power spectra in **a**. The filtered image exhibits substantially fewer noise while the noise correlation peaks remain visible.

quency window function. However, the obtained correlation data still exhibit a significant amount of periodic noise.

In order to filter such noise from the final correlation matrix, an automated notch filtering procedure is applied to the power spectrum. Here, Gaussian notch filters with a width of three pixels are applied for each pixel above a certain threshold value. This process is exemplified in Fig. A.3a where the predominant sources of noise can be easily identified as localized features in the spectrum in contrast to the extended shallow triangular pattern corresponding to the correlation signal. With the smooth Gaussian notch filtering of selected pixels rather than pre-defined regions, the resulting correlation image exhibits reasonably fewer noise while the correlation peaks remain visible as depicted in Fig. A.3b. Due to the considerable computational expense for the calculation of large numbers of individual Gaussian filters the method is applied only to the final correlation data rather than to each individual component of the data set.

B Correlation analysis of symmetry breaking

In this chapter we apply the correlation analysis method that was introduced in section 5.4 for the detection of quantum noise correlations to the data sets obtained for the coupled Ising-XY model presented in chapter 4. The appearance and behavior of anti-correlation peaks can be attributed to symmetry breaking in accordance with the interpretation of a thermally driven phase transition.

In chapter 4 we have employed several statistical data analysis tools for the verification of a (spontaneous) symmetry breaking in the coupled Ising-XY model, namely the Gaussian probability mixture clustering for the magnetization data of Fig. 4.11 and the model-free principal- and independent component image analysis. While the independent component analysis turned out to be impractical for the distinction of different physical processes, the principal component analysis revealed strong evidence for the entropy-dependent degree of symmetry breaking at staggered flux strengths close to π .

Here, we present additional evidence of entropy- and flux-dependent symmetry breaking in the Ising-XY model that relies on the correlation analysis. In section 5.4 this statistical analysis technique was used in order to detect quantum noise correlations in the deep Mott-insulating regime of the static and the driven three-dimensional lattice. We can, however, also employ the correlation analysis for the chiral Néel-superfluid of the weakly-interacting staggered flux system. In contrast to the deep Mott insulator, the first-order correlations do not vanish in this regime. Accordingly, the source of correlations in the Ising-XY data sets are fluctuations in the occupations of the superfluid quasimomentum peaks (see single-shot images presented in Fig. C.2 to C.4) rather than the second-order noise correlation signal: The local wave functions of the superfluid can be described as a superfluid state according to Eq. (5.7) which does not yield any second-order correlations [316]. With the appearance of first order coherence at the transition from a thermal ensemble to a Bose-Einstein condensate, second order correlations are completely suppressed [317–319].

In Fig. B.1 correlation signals of the data sets for all three initial entropies at a maximum staggered flux strength of $\Phi = \pi$. Similar to the noise correlation analysis, the single shot images have been subjected to a Hamming filter before being processed. However, no additional notch filtering has been applied to the obtained Fourier spectrum of the correlation signal as the total correlation magnitude resulting from the occupation

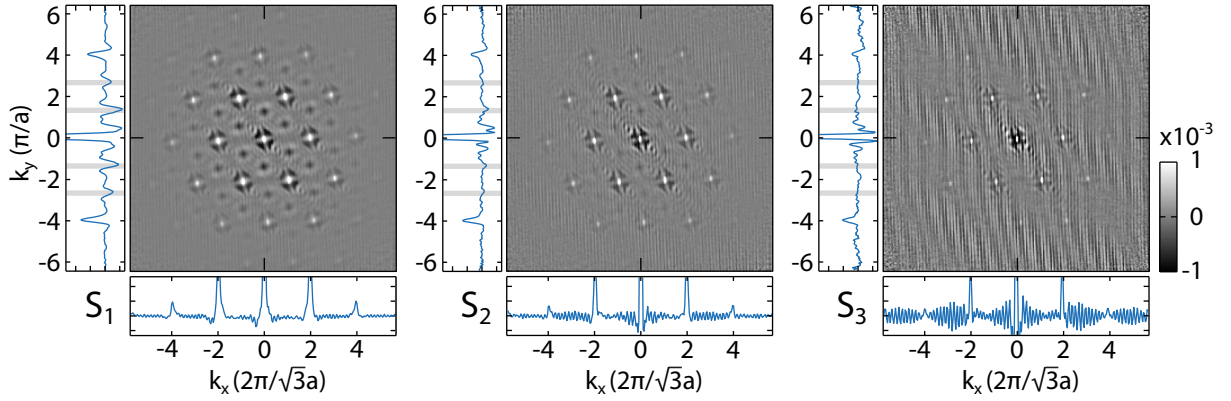


Figure B.1: Correlation analysis of symmetry breaking for the data sets at maximum staggered flux strength $\Phi = \pi$ and the three initial entropies $S_1 < S_2 < S_3$. In addition to the strong positive correlation signals of the superfluid momentum peaks, negative anti-correlation peaks can be observed for the two lowest entropies S_1 and S_2 , while no such anti-correlation is present for the largest initial entropy value S_3 . Plots of blue solid lines at the sides of the correlation images depict the signal along the hair cross. Gray lines in the vertical signal indicate the expected positions of anti-correlation peaks at $k_y = \pm 4\pi/(3a)$ and $k_y = \pm 8\pi/(3a)$.

of the superfluid momentum peaks is large compared to the remaining sources of noise. For all three initial entropies strong correlation signals are evident at the positions of the superfluid momentum peaks. Cross-shaped fringes with a negative correlation amplitude around the correlation peaks can be attributed to residual movements of the single-shot images.

Additionally, a striking feature is evident in the correlation signals: Negative anti-correlation peaks appear in between the expected positive correlation peaks for the two lowest initial entropies S_1 and S_2 . Since experiments were performed with a bosonic superfluid, the presence of these signals can only be attributed to the observed symmetry breaking process as anti-correlations resulting from Hanbury-Brown-Twiss interference of quantum particles can only arise for fermionic atoms as in Ref. [58]. If one of the two possible degenerate ground states is occupied, the superfluid atomic ensemble is present in a single quasimomentum mode corresponding to one of the minima in the dispersion relation. As the other minimum is not occupied, this results in an anti-correlation between nearest neighboring superfluid momentum peaks which is clearly visible. Plots at the sides of the correlation images in Fig. B.1 depict the respective correlation signal along the centered hair cross in the images. The expected positions of anti-correlations for the vertical signal at $k_y = \pm 4\pi/(3a)$ and $k_y = \pm 8\pi/(3a)$ are indicated by gray lines.

Anti-correlations are strongly pronounced for the lowest initial entropy S_1 , indicating a strong symmetry breaking process in accordance with the observed fluctuations of the magnetization signal (see Fig. 4.12) and the strength of the corresponding principal component (Fig. 4.14). Similarly, for the intermediate initial entropy S_2 , anti-correlation

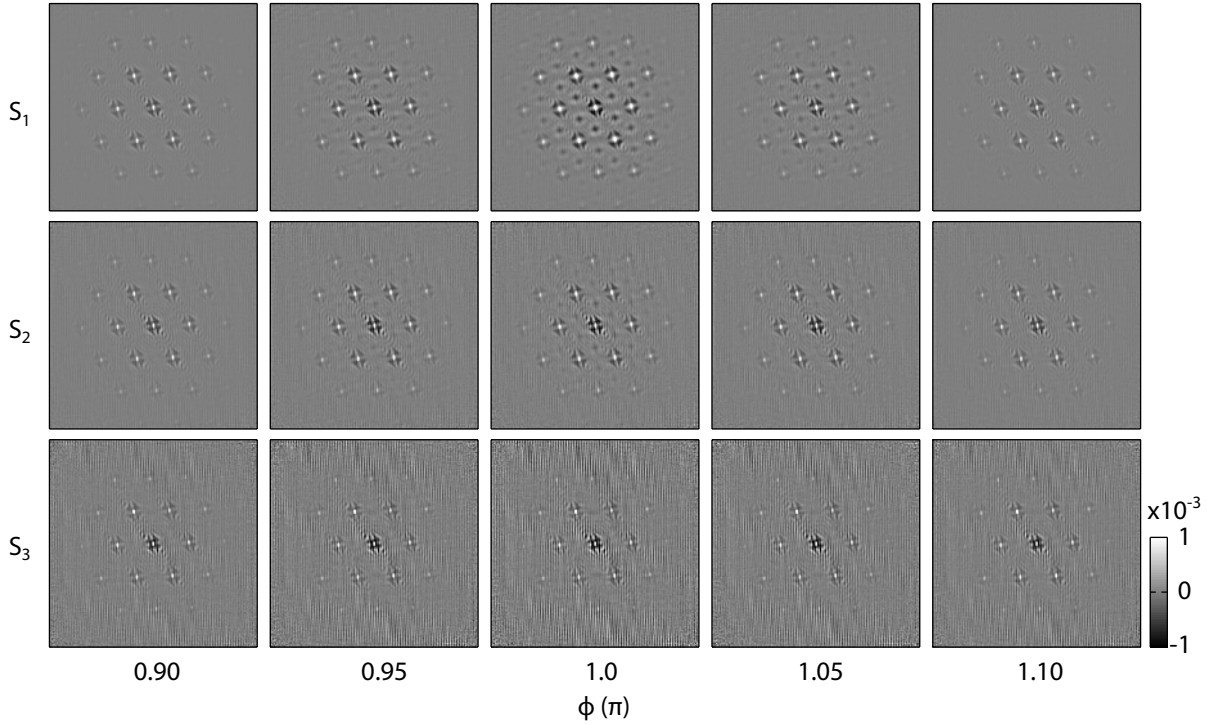


Figure B.2: Anti-correlation behavior for different flux strengths at all three initial entropies. For the two lowest entropies S_1 and S_2 , anti-correlation peaks resulting from a bimodal occupation of the two minima in the engineered dispersion relation are visible for staggered flux strengths close to the maximum value of π while they vanish for stronger detunings of the magnetic flux. No anti-correlations can be observed for the largest initial entropy S_3 at any value of the flux strength.

peaks are still clearly visible but also less pronounced. In the case of the largest entropy S_3 the anti-correlation signal vanishes completely while the magnitude of the positive correlation signals decreases only by roughly a factor of two as compared to the lowest entropy data. However, positive correlation peaks at the positions of the previously negative anti-correlations cannot be observed as it would be expected by a simultaneous coherent occupation of both superfluid momentum states. This circumstance can be interpreted in two ways: Either, the obtained signal stems exclusively from quantum noise correlations of incoherent atoms. The positions of the noise correlations will remain unchanged due to the lattice driving as they originate from interferences between particles from the real-space lattice sites as illustrated in Fig. 5.9. Or, the suppression of positive correlations between nearest neighboring momentum peaks due to the absence of long-range phase ordering between the two simultaneously occupied modes. In this case, residual fluctuations of the occupations of nearest neighboring peaks still remain uncorrelated. Nonetheless, the observations of the vanishing of anti-correlations confirms the interpretation of the thermally driven phase transition from an ordered ferromagnetic to an unordered paramagnetic phase, which results in the Ising- \mathbb{Z}_2 symmetry being fully

restored for the maximum staggered flux strength.

In Fig. B.2 correlation images are depicted for additional data sets of flux strengths differing from $\Phi = \pi$. In Accordance with the symmetry breaking behavior, anti-correlation peaks remain visible for the two lowest entropies even for flux strengths close, but different to π . For flux strengths far enough detuned from π the system is completely magnetized in one mode and anti-correlation signal vanishes. Again, anti-correlations are absent for the largest initial entropy at all flux values.

To conclude, the second-order correlation analysis that was originally employed for the detection of noise correlations in the Mott-insulating regime also serves as a reliable model-free statistical analysis tool for the verification of symmetry breaking of the staggered-flux superfluid in the Ising-XY model. Findings concerning the behavior of anti-correlation signals substantiate the interpretation of symmetry breaking and the thermally driven phase transition from an ordered ferromagnetic to an unordered paramagnetic phase.

C Single-shot symmetry breaking images

Here we show examples of the single-shot images resulting from the Ising-XY model system at maximum flux strength that were used in the respective data sets shown in chapter 4.

The (spontaneous) breaking of the \mathbb{Z}_2 symmetry in the coupled Ising-XY model discussed in chapter 3 was evidenced by single-shot fluctuations of quasimomentum mode occupations in the time-of-flight images. Both the magnetization data extracted from the absorption images as well as a statistical model-free data analysis revealed the increase of fluctuations corresponding to a breaking of the \mathbb{Z}_2 symmetry close to the maximum flux strength of $\Phi = \pi$ for sufficiently low initial entropies. As an example of the analyzed experimental signal, the first 99 single-shot optical density images, obtained at a maximum flux strength of π , that contribute to the data shown in Fig. 4.10 to Fig. 4.17 are presented in the following for all three values of the initial entropy.

For the first two data sets with initial entropies S_1 and S_2 , symmetry breaking was evidenced by various data processing methods while the largest initial entropy S_3 did not show such a behavior. Fig. C.1 depicts nine single-shot images for the three initial entropies for comparison.

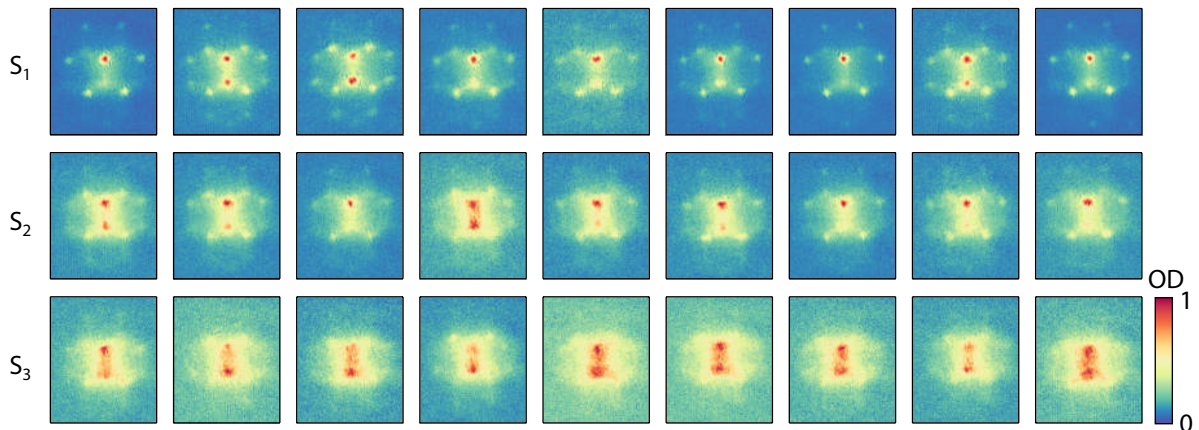


Figure C.1: Single-shot images for the three initial entropies at a staggered flux strength of $\Phi = \pi$.

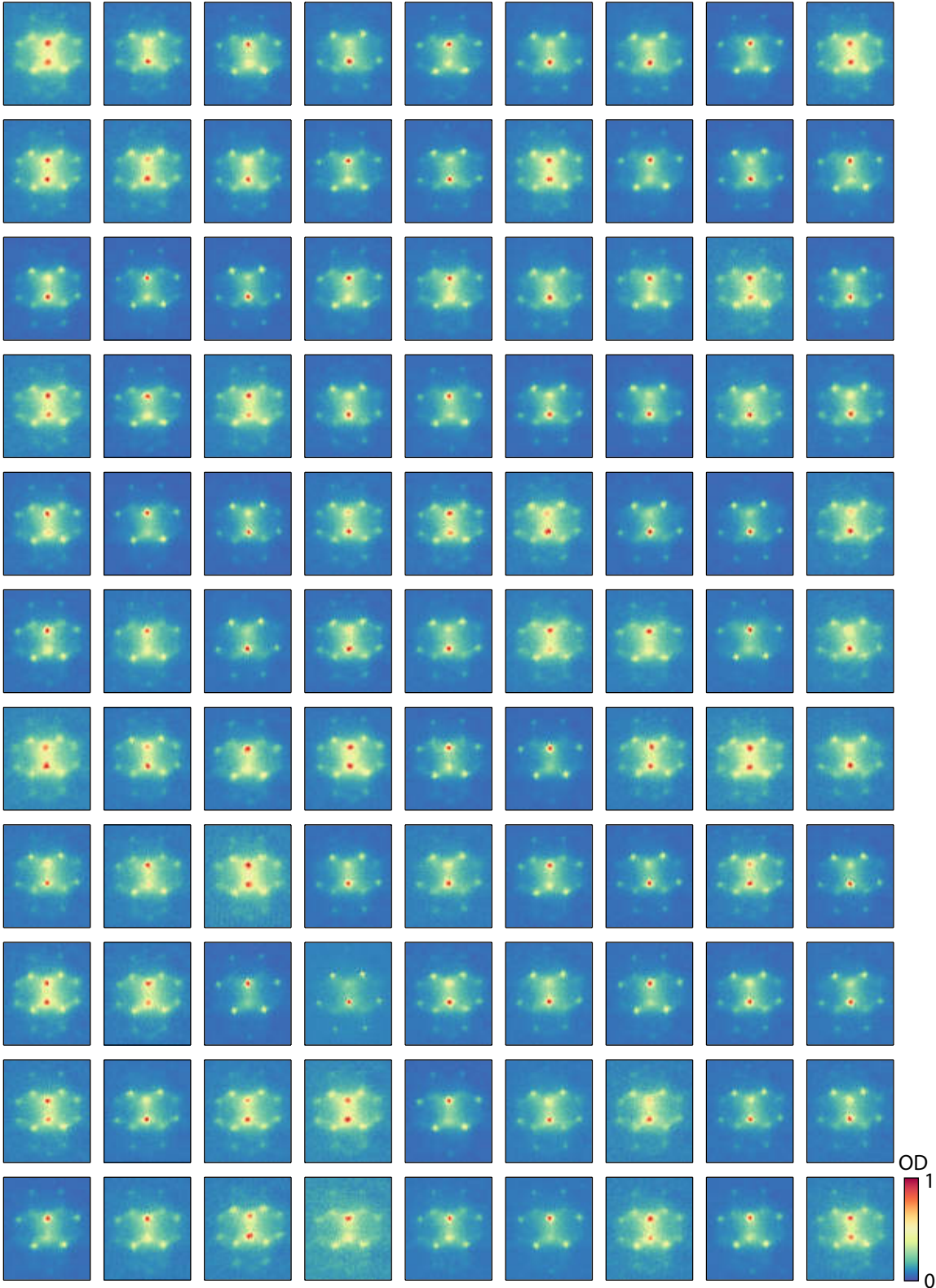


Figure C.2: Single-shot images at a staggered flux strength of $\Phi = \pi$ and an initial entropy S_1 .

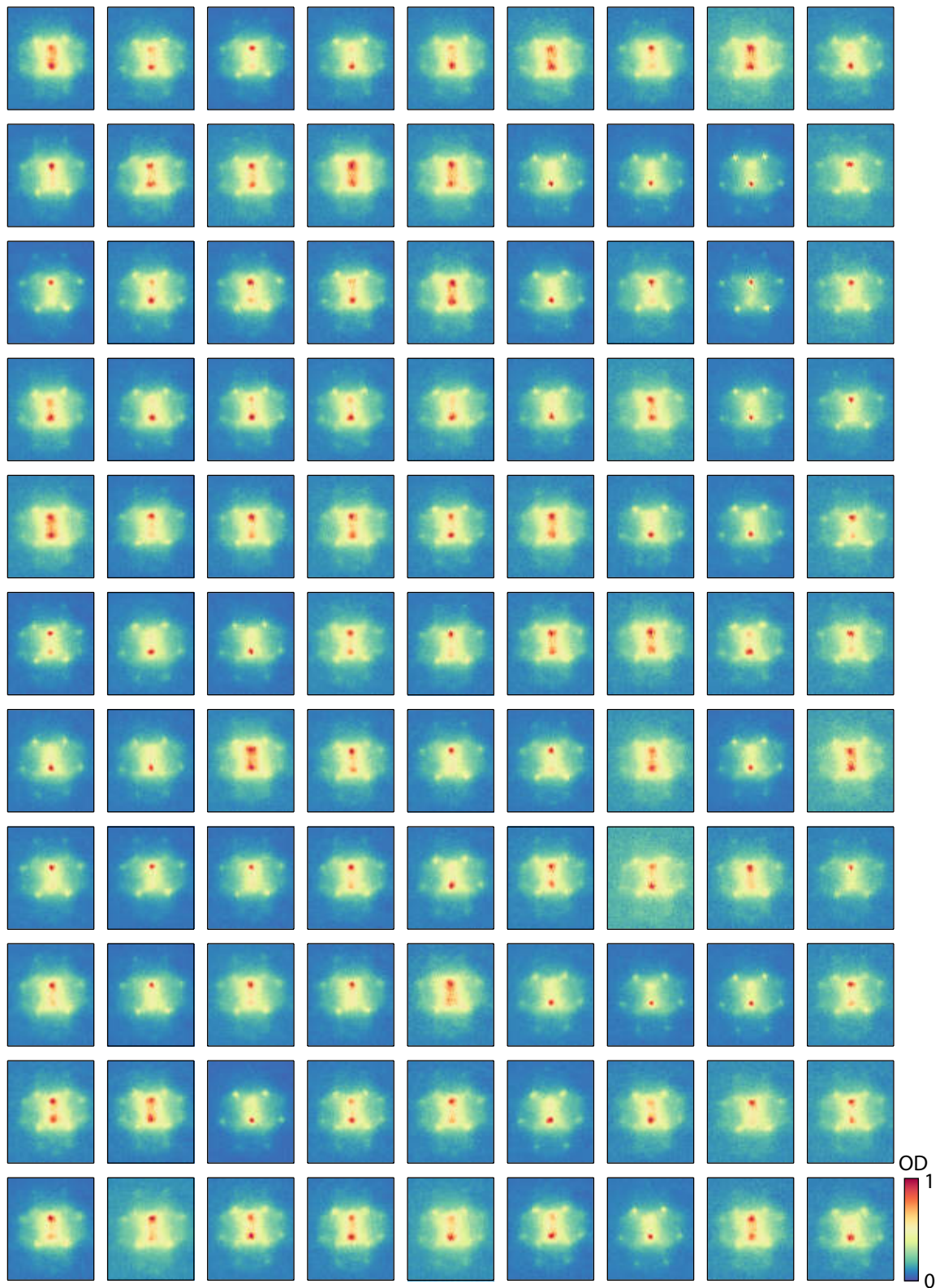


Figure C.3: Single-shot images at a staggered flux strength of $\Phi = \pi$ and an initial entropy S_2 .

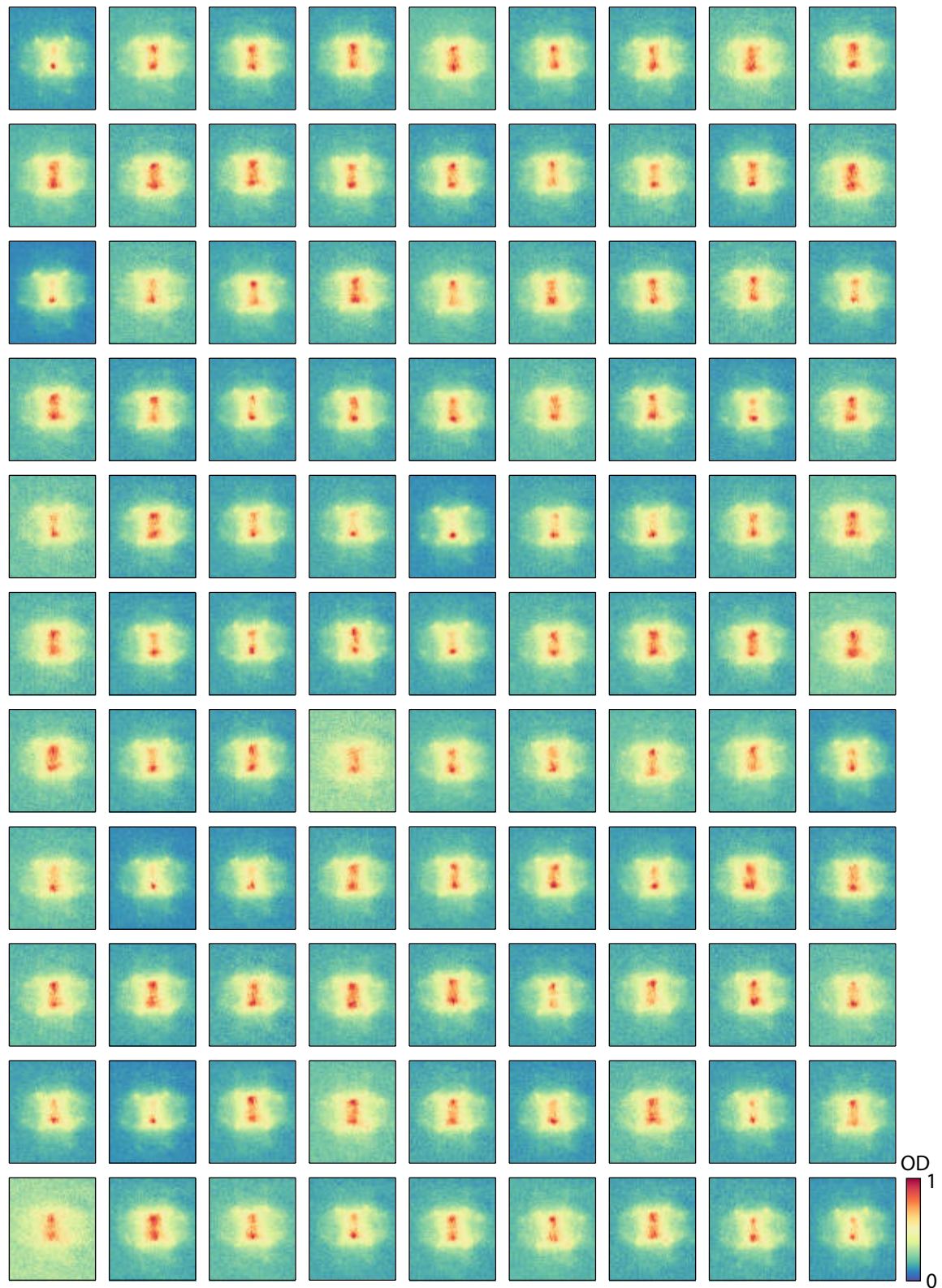


Figure C.4: Single-shot images at a staggered flux strength of $\Phi = \pi$ and an initial entropy S_3 .

D Experimental imperfections

In this chapter we describe several experimental imperfections of the BEC-apparatus that may lead to detrimental influences on the experiments presented throughout this thesis.

Experimental setups are always subject to a certain amount of imperfections. Due to their fragile nature, ultracold quantum gases are extremely prone to any kind of detrimental imperfections. In particular, destructive detection techniques such as time-of-flight absorption imaging require a high degree of stability: All such experiments rely on the reproducibility of conditions for the initially generated quantum gas for each experimental cycle.

In the following, we will briefly discuss two major imperfections of the experimental setup used throughout this thesis and evaluate their respective influences on the performed studies.

D.1 Measured three-beam lattice geometry

The running-wave three-beam lattice setup exhibits slight deviations from the ideal 120° configuration. It should be noted, however, that the main reason for such deviations is not an imperfect alignment of the lattice laser beams but rather limitations of the accessible geometries due to the shape of the vacuum setup and the magnetic compensation- and quantization field Helmholtz coils.

Wave vectors	Angles	Lattice constants
$\angle(\mathbf{k}_1, \mathbf{k}_2)$	$120.4^\circ \pm 0.4^\circ$	$ \mathbf{a}_1 = 560.6 \pm 1.0 \text{ nm}$
$\angle(\mathbf{k}_2, \mathbf{k}_3)$	$117.1^\circ \pm 0.2^\circ$	$ \mathbf{a}_2 = 545.9 \pm 0.8 \text{ nm}$
$\angle(\mathbf{k}_1, \mathbf{k}_3)$	$122.4^\circ \pm 0.4^\circ$	$ \mathbf{a}_1 - \mathbf{a}_2 = 554.3 \pm 1.0 \text{ nm}$

Table D.1: Measured angles and lattice constants of the three-beam lattice. Values were determined by evaluating a set of linear equations arising from the positions of quasimomentum peaks of Fig. D.1. Deviations from the ideal case of all $\angle(\mathbf{k}_i, \mathbf{k}_{j \neq i}) = 120^\circ$ and $|\mathbf{a}_i| = 553.3 \text{ nm}$ are evident.

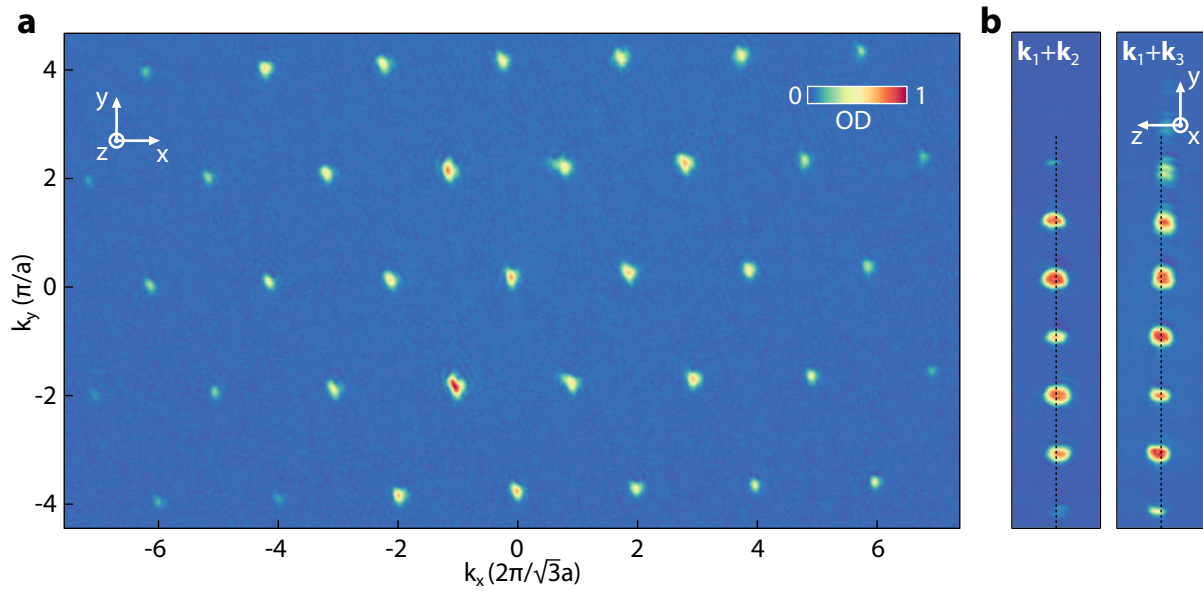


Figure D.1: Kapitza-Dirac diffraction patterns of the optical lattice. **a** The diffraction pattern of the triangular lattice can be used to determine the relative angles between the three lattice beams. **c** Similar diffraction patterns for pairs of lattice beams imaged along the lattice plane. The dashed line indicates ideal lattice plane orientation. Slight misalignments with respect to the ideal plane are evident.

The actual experimental alignment of laser beams can be derived from a Kapitza-Dirac diffraction of the ultracold atomic ensemble [320–322]. For this purpose, a Bose-Einstein condensate in a crossed dipole trap is subjected to a short pulse duration τ_{KD} of the lattice potential on the order of $\tau_{\text{KD}} \approx 10 \mu\text{s}$. The diffraction of atoms on the interference pattern populates many higher momentum components as shown in Fig. D.1a. The large number of momentum peaks allow for a reliable calculation of the three-beam lattice angles that are listed in Tab. D.1. In Addition, the resulting lattice constants of the running-wave 1D-lattice are shown. Note that all experiments that were performed in such a lattice within this thesis (see chapter 3) have employed the lattice comprised of the \mathbf{k}_2 and \mathbf{k}_3 laser beams. The determination of the three-beam lattice angles has initially been performed by C. Ölschläger [179].

An central assumption that is applied for the calculation of the values in Tab. D.1 is that all lattice beams are perfectly aligned in the xy -plane of the lattice. However, this condition is not exactly fulfilled as evident from the corresponding Kapitza-Dirac diffraction patterns of running-wave 1D-lattices imaged along the x -axis that are shown in Fig. D.1b. Hereby, the ideal lattice plane orientation is determined by the time-of-flight trajectory of atoms. The 1D-lattice comprised of the \mathbf{k}_2 and \mathbf{k}_3 beams cannot be imaged in this direction (as it solely extends along the x -direction). Nonetheless, the deviations from the ideal lattice plane are small and the assumption of a perfectly aligned plane can be justified *a posteriori*: The use of the experimentally determined three-beam lattice

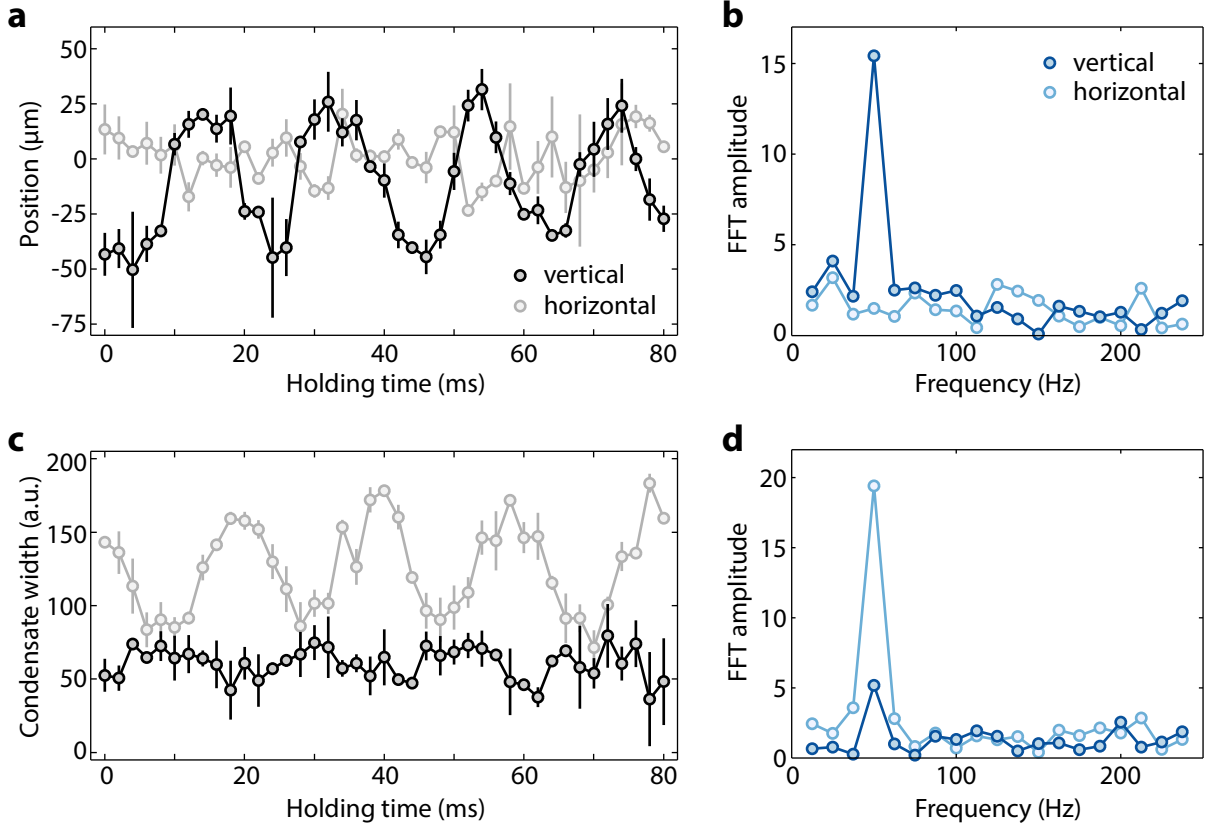


Figure D.2: Oscillations of the crossed dipole trap. **a** Time resolved measurement of vertical (black) and horizontal (gray) positions of a BEC in the elliptical crossed dipole trap. Oscillations in the vertical direction are clearly visible. **b** The Fourier spectrum of the data in **a** reveals a clear peak for the vertical oscillation at a frequency of 50 Hz. **c** Quadrupole-like oscillations of the condensate width in both directions with a phase-shift of π . **d** The corresponding Fourier spectrum for data in **c** exhibits distinct peaks at 50 Hz for both components.

alignment for calculations concerning the band structure and the Bessel-renormalization for the driving experiments in chapter 3 lead to an excellent agreement with the obtained data.

D.2 Residual oscillations in the crossed dipole trap

The harmonic confinement of the elliptical crossed dipole trap that has been used in most experiments throughout this thesis is chosen as small as possible in order to minimize the inhomogeneity of the atomic ensemble. Due to the small final laser power of the dipole trap, the Bose-Einstein condensate is extremely sensitive to variations of the laser power. Occasionally, we observe residual oscillations of the condensate along the vertical direction in the dipole trap while the horizontal position remains constant (see Fig. D.2a).

With a pronounced frequency of 50 Hz in the Fourier spectrum (Fig. D.2b) these oscillations likely stem from detrimental induction effects of the line voltage at the same frequency. Accompanied by the vertical oscillation of the BEC position are quadrupole oscillations of the condensate width with opposing phases as shown in Fig D.2c. Similar to the vertical oscillations they exhibit a distinct peak at 50 Hz in the Fourier spectrum of Fig. D.2d.

The appearance of these dynamics may result in unwanted excitations in the optical lattice and special care has to be taken in order to avoid such oscillations caused by the line voltage.

E Physical constants and rubidium line data

In the following we summarize physical constants relevant to this thesis. In addition, transition data of the utilized D-lines in ^{87}Rb is presented.

In the following, physical constants used for calculations throughout this thesis are summarized. Values are taken from the 2010 list of the *Committee on Data for Science and Technology* (CODATA) [323]. Furthermore, properties and relevant transition line data of ^{87}Rb are presented stem from Ref. [167] and references therein.

List of physical constants:

Quantity	Symbol	Value
Speed of light in vacuum	c	$2.9979245 \times 10^8 \text{ m/s}$
Permeability of vacuum	μ_0	$4\pi \times 10^{-7} \text{ N/A}$
Permittivity of vacuum	ϵ_0	$8.8541878 \times 10^{-12} \text{ F/m}$
Planck's constant	h	$6.6260696 \times 10^{-34} \text{ Js}$
	\hbar	$1.0545717 \times 10^{-34} \text{ Js}$
Elementary charge	e	$1.6021765 \times 10^{-10} \text{ C}$
Electron mass	m_e	$9.109382 \times 10^{-31} \text{ kg}$
Bohr radius	a_B	$0.5291772 \times 10^{-10} \text{ m}$
Bohr-Procopiu magneton	μ_B	$9.27400866 \times 10^{-24} \text{ J/T}$
		$h \cdot 1.3996246 \text{ MHz/G}$
Atomic mass unit	u	$1.6605388 \times 10^{-27} \text{ kg}$
Boltzmann's constant	k_B	$1.3806504 \times 10^{-23} \text{ J/K}$
Gravitational acceleration	g	9.80665 m/s^2

Physical properties of rubidium 87:

Atomic number	Z	37
Relative natural abundance	$\eta(^{87}\text{Rb})$	27.83 %
Atomic mass	m	86.9091805 u $1.4431606 \times 10^6 \text{ kg}$
Nuclear spin	I	3/2
s-wave scattering length a_0, \dots, a_{2F} for $F = 1$	a_0	$110.0 \pm 4.0 a_B$
	a_2	$107.0 \pm 4.0 a_B$
s-wave scattering length a_0, \dots, a_{2F} for $F = 2$	a_0	$89.4 \pm 3.0 a_B$
	a_2	$94.5 \pm 3.0 a_B$
	a_4	$106.0 \pm 4.0 a_B$

Rubidium 87 D_2 ($5^2S_{1/2} \rightarrow 5^2P_{3/2}$) transition properties:

Frequency	ω_0	$2\pi \cdot 384.2304844685 \text{ THz}$
Transition energy	$\hbar\omega_0$	1.589049439 eV
Wavelength (vacuum)	λ_0	780.241209686 nm
Wave number (vacuum)	$k_L/2\pi$	$12816.54938993 \text{ cm}^{-1}$
Lifetime	τ	26.24 ns
Decay rate/	Γ	$38.11e6 \times 10^6 \text{ s}^{-1}$
Natural line width (FWHM)		$2\pi \cdot 6.065 \text{ MHz}$

Rubidium 87 D_1 ($5^2S_{1/2} \rightarrow 5^2P_{1/2}$) transition properties:

Frequency	ω_0	$2\pi \cdot 377.1074635 \text{ THz}$
Transition energy	$\hbar\omega_0$	1.55959099 eV
Wavelength (vacuum)	λ_0	794.9788509 nm
Wave number (vacuum)	$k_L/2\pi$	$12578.950985 \text{ cm}^{-1}$
Lifetime	τ	27.70 ns
Decay rate/	Γ	$36.10 \times 10^6 \text{ s}^{-1}$
Natural line width (FWHM)		$2\pi \cdot 5.746 \text{ MHz}$

List of Figures

1.1	Multi-photon transitions due to periodic driving	3
1.2	Frustrated quantum antiferromagnetism	5
1.3	Tuning of Dirac points	6
2.1	Bose-Hubbard model	15
2.2	Lattice energy spectrum	17
2.3	Three-beam lattice setup	21
2.4	Bravais- and reciprocal lattice of the hexagonal lattice	23
2.5	Triangular lattice	26
2.6	Honeycomb lattice	27
2.7	Polarization lattice	28
2.8	Time-of-flight imaging of the momentum distribution	30
2.9	Time-of-flight patterns	31
2.10	Characteristic time-of-flight expansion.	32
3.1	Lattice driving in one dimension	36
3.2	Momentum distribution of driven lattices	42
3.3	Sinusoidal lattice driving with increasing amplitude	43
3.4	Driving of the triangular lattice	46
3.5	Effective dispersion relation of the driven triangular lattice.	47
3.6	Multi-photon transitions in the one-dimensional lattice	50
3.7	Excitation spectra of the driven 1D-lattice	52
3.8	Excitation resonances in dependence of the forcing amplitude	54
3.9	Driving resonances in the triangular lattice	56
3.10	Comparison of driving in the 2D- and 3D lattice	58
3.11	Excitation spectrum of the three-dimensional lattice	59
4.1	Peierls phases and gauge invariant fluxes	63
4.2	Engineering of Peierls phases by asymmetric driving	65
4.3	Realization of a fully tunable Peierls phase in the one-dimensional lattice	66
4.4	Time-resolved measurement of the momentum distribution	67
4.5	Peierls phases and fluxes on the triangular lattice	70
4.6	Time-resolved evolution during the ramping procedure of asymmetric forcing	71
4.7	Tunability of staggered fluxes	72
4.8	Staggered fluxes and order parameters of the coupled Ising-XY model	75

LIST OF FIGURES

4.9	Gauge-dependent weighting mask	77
4.10	Measurement series for increasing entropy	78
4.11	Statistical distribution of the magnetization for maximum flux strength	79
4.12	Magnetization behavior for the thermally driven phase transition	82
4.13	Momentum peak widths and free energy of the Ising-XY system	84
4.14	Principal component analysis of symmetry breaking	86
4.15	Symmetry breaking components and variance of the magnetization	88
4.16	Principal components and eigenvalues	89
4.17	Independent component basis	91
5.1	Mapping of the quantum XY model	95
5.2	Phase diagram for positive and negative tunneling matrix elements	96
5.3	Superfluid to Mott insulator transition	100
5.4	Mott insulator lifetime measurement	102
5.5	Detection of the on-site interaction energy.	103
5.6	Ramping timescales in the strongly confined 3D-lattice	105
5.7	Lattice driving parameters in the strongly interacting regime	107
5.8	Superfluid to Mott insulator transition in the driven lattice	108
5.9	Hanbury Brown-Twiss correlations for atoms released from an optical lattice	111
5.10	Quantum noise correlations in the static Mott insulator	114
5.11	Quantum noise correlations in the driven antiferromagnetic Mott-insulating regime	116
5.12	Order-by-disorder behavior of the strongly interacting driven 3D-system	118
6.1	State-dependency of the honeycomb lattice	124
6.2	Effective magnetic quantum number	127
6.3	Opening of the band gap for increasing lattice depths	128
6.4	Microwave spectroscopy	131
6.5	Microwave spectroscopy and spin dynamics	132
6.6	Microwave spectra of the tunable honeycomb lattice	135
6.7	Bloch functions of the two lowest bands	136
6.8	Quantitative investigation of microwave spectra	138
6.9	Microwave transition to excited bands	141
6.10	Band decay dynamics in the presence of Dirac cones	143
6.11	Possible inter-band decay mechanism and total atom number	145
7.1	Next-nearest-neighbor tunneling in the honeycomb lattice	152
7.2	Energy bands in the honeycomb lattice with next-nearest-neighbor tunneling.	154
7.3	Engineering next-nearest-neighbor tunneling	155
7.4	Engineering lattice geometries with next-nearest-neighbor interactions.	156
7.5	Generation of staggered vortices by rotating the quantization field	158
7.6	Kagome and dice lattice in the six-beam setup	162

A.1	Comparison of contrast methods	166
A.2	Maximum-pixel contrast	167
A.3	Notch-filtering of correlation data	169
B.1	Correlation analysis of symmetry breaking	172
B.2	Anti-correlation behavior for different flux strengths	173
C.1	Single-shot images for three initial entropies	175
C.2	Single-shot images for lowest initial entropy	176
C.3	Single-shot images for medium initial entropy	177
C.4	Single-shot images for the highest initial entropy	178
D.1	Kaptiza-Dirac diffraction patterns	180
D.2	Oscillations of the crossed dipole trap	181

Bibliography

- [1] J. Struck, C. Ölschläger, M. Weinberg, P. Hauke, J. Simonet, A. Eckardt, M. Lewenstein, K. Sengstock and P. Windpassinger: “[Tunable Gauge Potential for Neutral and Spinless Particles in Driven Optical Lattices](#)”, Phys. Rev. Lett. **108**, 225304 (2012).
- [2] P. Hauke, O. Tieleman, A. Celi, C. Ölschläger, J. Simonet, J. Struck, M. Weinberg, P. Windpassinger, K. Sengstock, M. Lewenstein and A. Eckardt: “[Non-Abelian Gauge Fields and Topological Insulators in Shaken Optical Lattices](#)”, Phys. Rev. Lett. **109**, 145301 (2012).
- [3] J. Struck, M. Weinberg, C. Ölschläger, P. Windpassinger, J. Simonet, K. Sengstock, R. Höppner, P. Hauke, A. Eckardt, M. Lewenstein and L. Mathey: “[Engineering Ising-XY spin-models in a triangular lattice using tunable artificial gauge fields](#)”, Nature Physics **9**, 738–743 (2013).
- [4] J. Simonet, J. Struck, M. Weinberg, C. Ölschläger, P. Hauke, A. Eckardt, M. Lewenstein, K. Sengstock and P. Windpassinger: “[Tunable gauge potential for spinless particles in driven lattices](#)”, EPJ Web of Conferences **57**, 01004 (2013).
- [5] D.-S. Lühmann, O. Jürgensen, M. Weinberg, J. Simonet, P. Soltan-Panahi and K. Sengstock: “[Quantum phases in tunable state-dependent hexagonal optical lattices](#)”, Phys. Rev. A **90**, 013614 (2014).
- [6] R. Feynman: “[Simulating physics with computers](#)”, Int. Jour. Theor. Phys. **21**, 467–488 (1982).
- [7] D. Deutsch: “[Quantum theory, the Church-Turing principle and the universal quantum computer](#)”, Proc. R. Soc. A **400**, 97–117 (1985).
- [8] S. Lloyd: “[Universal Quantum Simulators](#)”, Science **273**, 1073–1078 (1996).
- [9] I. M. Georgescu, S. Ashhab and F. Nori: “[Quantum simulation](#)”, Rev. Mod. Phys. **86**, 153–185 (2014).
- [10] E. Manousakis: “[A Quantum-Dot Array as Model for Copper-Oxide Superconductors: A Dedicated Quantum Simulator for the Many-Fermion Problem](#)”, J. Low Temp. Phys. **126**, 1501–1513 (2002).

- [11] A. Y. Smirnov, S. Savel'ev, L. G. Mouroukh and F. Nori: “Modelling chemical reactions using semiconductor quantum dots”, *EPL* **80**, 67008 (2007).
- [12] T. Byrnes, P. Recher, N. Y. Kim, S. Utsunomiya and Y. Yamamoto: “Quantum Simulator for the Hubbard Model with Long-Range Coulomb Interactions Using Surface Acoustic Waves”, *Phys. Rev. Lett.* **99**, 016405 (2007).
- [13] T. Byrnes, N. Y. Kim, K. Kusudo and Y. Yamamoto: “Quantum simulation of Fermi-Hubbard models in semiconductor quantum-dot arrays”, *Phys. Rev. B* **78**, 075320 (2008).
- [14] D. Leibfried, B. DeMarco, V. Meyer, M. Rowe, A. Ben-Kish, J. Britton, W. M. Itano, B. Jelenković, C. Langer, T. Rosenband and D. J. Wineland: “Trapped-Ion Quantum Simulator: Experimental Application to Nonlinear Interferometers”, *Phys. Rev. Lett.* **89**, 247901 (2002).
- [15] A. Friedenauer, H. Schmitz, J. T. Glueckert, D. Porras and T. Schaetz: “Simulating a quantum magnet with trapped ions”, *Nature Physics* **4**, 757–761 (2008).
- [16] K. Kim, M. S. Chang, S. Korenblit, R. Islam, E. Edwards, J. Freericks, G. D. Lin, L. M. Duan and C. Monroe: “Quantum simulation of frustrated Ising spins with trapped ions”, *Nature* **465**, 590–593 (2010).
- [17] R. Gerritsma, G. Kirchmair, F. Zähringer, E. Solano, R. Blatt and C. F. Roos: “Quantum simulation of the Dirac equation”, *Nature* **463**, 68–71 (2010).
- [18] B. P. Lanyon, C. Hempel, D. Nigg, M. Müller, R. Gerritsma, F. Zähringer, P. Schindler, J. T. Barreiro, M. Rambach, G. Kirchmair, M. Hennrich, P. Zoller, R. Blatt and C. F. Roos: “Universal Digital Quantum Simulation with Trapped Ions”, *Science* **334**, 57–61 (2011).
- [19] J. W. Britton, B. C. Sawyer, A. C. Keith, C. C. J. Wang, J. K. Freericks, H. Uys, M. J. Biercuk and J. J. Bollinger: “Engineered two-dimensional Ising interactions in a trapped-ion quantum simulator with hundreds of spins”, *Nature* **484**, 489–492 (2012).
- [20] M. J. Hartmann, F. G. S. L. Brandao and M. Plenio: “Strongly interacting polaritons in coupled arrays of cavities”, *Nature Physics* **2**, 849–855 (2006).
- [21] A. D. Greentree, C. Tahan, J. H. Cole and L. C. L. Hollenberg: “Quantum phase transitions of light”, *Nature Physics* **2**, 856–861 (2006).
- [22] D. G. Angelakis, M. F. Santos and S. Bose: “Photon-blockade-induced Mott transitions and XY spin models in coupled cavity arrays”, *Phys. Rev. A* **76**, 031805 (2007).

-
- [23] B. P. Lanyon, J. D. Whitfield, G. G. Gillett, M. E. Goggin, M. P. Almeida, I. Kassal, J. D. Biamonte, B. J. Powell, M. Barbieri, A. Aspuru-Guzik and A. G. White: “Towards quantum chemistry on a quantum computer”, *Nature Chem.* **2**, 106 – 111 (2010).
- [24] A. A. Houck, H. E. Tureci and J. Koch: “On-chip quantum simulation with superconducting circuits”, *Nature Physics* **8**, 292–299 (2012).
- [25] G. Paraoanu: “Recent Progress in Quantum Simulation Using Superconducting Circuits”, *J. Low Temp. Phys.* **175**, 633–654 (2014).
- [26] W. S. Warren: “The Usefulness of NMR Quantum Computing”, *Science* **277**, 1688–1690 (1997).
- [27] J. Du, N. Xu, X. Peng, P. Wang, S. Wu and D. Lu: “NMR Implementation of a Molecular Hydrogen Quantum Simulation with Adiabatic State Preparation”, *Phys. Rev. Lett.* **104**, 030502 (2010).
- [28] M. Lewenstein, A. Sanpera, V. Ahufinger, B. Damski, A. Sen De and U. Sen: “Ultracold atomic gases in optical lattices: mimicking condensed matter physics and beyond”, *Advances in Physics* **56**, 243–379 (2007).
- [29] I. Bloch, J. Dalibard and W. Zwerger: “Many-body physics with ultracold gases”, *Rev. Mod. Phys.* **80**, 885–964 (2008).
- [30] G. Grynberg, B. Lounis, P. Verkerk, J. Y. Courtois and C. Salomon: “Quantized motion of cold cesium atoms in two- and three-dimensional optical potentials”, *Phys. Rev. Lett.* **70**, 2249–2252 (1993).
- [31] A. Hemmerich and T. Hänsch: “Two-dimensional atomic crystal bound by light”, *Phys. Rev. Lett.* **70**, 410–413 (1993).
- [32] M. H. Anderson, J. R. Ensher, M. R. Matthews, C. E. Wieman and E. A. Cornell: “Observation of Bose-Einstein Condensation in a Dilute Atomic Vapor”, *Science* **269**, 198–201 (1995).
- [33] K. Davis, M. Mewes, M. Andrews, N. van Druten, D. Durfee, D. Kurn and W. Ketterle: “Bose-Einstein Condensation in a Gas of Sodium Atoms”, *Phys. Rev. Lett.* **75**, 3969–3973 (1995).
- [34] C. Bradley, C. Sackett, J. Tollett and R. Hulet: “Evidence of Bose-Einstein Condensation in an Atomic Gas with Attractive Interactions”, *Phys. Rev. Lett.* **75**, 1687–1690 (1995).
- [35] D. Jin, J. Ensher, M. Matthews, C. Wieman and E. Cornell: “Collective Excitations of a Bose-Einstein Condensate in a Dilute Gas”, *Phys. Rev. Lett.* **77**, 420–423 (1996).

- [36] M. O. Mewes, M. Andrews, N. van Druten, D. Kurn, D. Durfee, C. Townsend and W. Ketterle: “**Collective Excitations of a Bose-Einstein Condensate in a Magnetic Trap**”, Phys. Rev. Lett. **77**, 988–991 (1996).
- [37] M. R. Andrews, C. G. Townsend, H. J. Miesner, D. S. Durfee, D. M. Kurn and W. Ketterle: “**Observation of Interference Between Two Bose Condensates**”, Science **275**, 637–641 (1997).
- [38] M. O. Mewes, M. R. Andrews, D. M. Kurn, D. S. Durfee, C. G. Townsend and W. Ketterle: “**Output Coupler for Bose-Einstein Condensed Atoms**”, Phys. Rev. Lett. **78**, 582–585 (1997).
- [39] M. Matthews, B. Anderson, P. Haljan, D. Hall, C. Wieman and E. Cornell: “**Vortices in a Bose-Einstein Condensate**”, Phys. Rev. Lett. **83**, 2498–2501 (1999).
- [40] H. Feshbach: “**Unified theory of nuclear reactions**”, Annals of Physics **5**, 357–390 (1958).
- [41] S. Inouye, M. Andrews, J. Stenger, H. Miesner, D. Stamper-Kurn, W. Ketterle and D. Miesner: “**Observation of Feshbach resonances in a Bose-Einstein condensate**”, Nature **392**, 151–154 (1998).
- [42] B. DeMarco and D. S. Jin: “**Onset of Fermi Degeneracy in a Trapped Atomic Gas**”, Science **285**, 1703–1706 (1999).
- [43] F. Schreck, L. Khaykovich, K. L. Corwin, G. Ferrari, T. Bourdel, J. Cubizolles and C. Salomon: “**Quasipure Bose-Einstein Condensate Immersed in a Fermi Sea**”, Phys. Rev. Lett. **87**, 080403 (2001).
- [44] A. G. Truscott, K. E. Strecker, W. I. McAlexander, G. B. Partridge and R. G. Hulet: “**Observation of Fermi Pressure in a Gas of Trapped Atoms**”, Science **291**, 2570–2572 (2001).
- [45] J. Bardeen, L. N. Cooper and J. R. Schrieffer: “**Theory of Superconductivity**”, Phys. Rev. **108**, 1175–1204 (1957).
- [46] M. Zwierlein, C. Stan, C. Schunck, S. Raupach, S. Gupta, Z. Hadzibabic and W. Ketterle: “**Observation of Bose-Einstein Condensation of Molecules**”, Phys. Rev. Lett. **91**, 250401 (2003).
- [47] T. Bourdel, L. Khaykovich, J. Cubizolles, J. Zhang, F. Chevy, M. Teichmann, L. Tarruell, S. Kockelmans and C. Salomon: “**Experimental Study of the BEC-BCS Crossover Region in Lithium 6**”, Phys. Rev. Lett. **93**, 050401 (2004).
- [48] C. Regal, M. Greiner and D. Jin: “**Observation of Resonance Condensation of Fermionic Atom Pairs**”, Phys. Rev. Lett. **92**, 040403 (2004).

-
- [49] J. Kinast, S. Hemmer, M. Gehm, A. Turlapov and J. Thomas: “Evidence for Superfluidity in a Resonantly Interacting Fermi Gas”, *Phys. Rev. Lett.* **92**, 150402 (2004).
- [50] C. Chin, M. Bartenstein, A. Altmeyer, S. Riedl, S. Jochim, J. H. Denschlag and R. Grimm: “Observation of the Pairing Gap in a Strongly Interacting Fermi Gas”, *Science* **305**, 1128–1130 (2004).
- [51] M. Zwierlein, J. Abo-Shaeer, A. Schirotzek, C. Schunck and W. Ketterle: “Vortices and superfluidity in a strongly interacting Fermi gas”, *Nature* **435**, 1047–1051 (2005).
- [52] C. Westbrook, R. Watts, C. Tanner, S. Rolston, W. Phillips, P. Lett and P. Gould: “Localization of atoms in a three-dimensional standing wave”, *Phys. Rev. Lett.* **65**, 33–36 (1990).
- [53] A. Kastberg, W. Phillips, S. Rolston, R. Spreew and P. Jessen: “Adiabatic Cooling of Cesium to 700 nK in an Optical Lattice”, *Phys. Rev. Lett.* **74**, 1542–1545 (1995).
- [54] M. P. Fisher, G. Grinstein and D. S. Fisher: “Boson localization and the superfluid-insulator transition”, *Physical Review B* **40**, 546–570 (1989).
- [55] D. Jaksch, C. Bruder, J. Cirac, C. Gardiner and P. Zoller: “Cold Bosonic Atoms in Optical Lattices”, *Phys. Rev. Lett.* **81**, 3108–3111 (1998).
- [56] M. Greiner, O. Mandel, T. Esslinger, T. Hänsch and I. Bloch: “Quantum phase transition from a superfluid to a Mott insulator in a gas of ultracold atoms”, *Nature* **415**, 39–44 (2002).
- [57] S. Fölling, F. Gerbier, A. Widera, O. Mandel, T. Gericke and I. Bloch: “Spatial quantum noise interferometry in expanding ultracold atom clouds”, *Nature* **434**, 481–484 (2005).
- [58] T. Rom, T. Best, D. van Oosten, U. Schneider, S. Fölling, B. Paredes and I. Bloch: “Free fermion antibunching in a degenerate atomic Fermi gas released from an optical lattice”, *Nature* **444**, 733–736 (2006).
- [59] M. Köhl, H. Moritz, T. Stöferle, K. Günter and T. Esslinger: “Fermionic Atoms in a Three Dimensional Optical Lattice: Observing Fermi Surfaces, Dynamics, and Interactions”, *Phys. Rev. Lett.* **94**, 080403 (2005).
- [60] R. Jördens, N. Strohmaier, K. Günter, H. Moritz and T. Esslinger: “A Mott insulator of fermionic atoms in an optical lattice”, *Nature* **455**, 204–207 (2008).

- [61] U. Schneider, L. Hackermüller, S. Will, T. Best, I. Bloch, T. Costi, R. Helmes, D. Rasch and A. Rosch: “Metallic and Insulating Phases of Repulsively Interacting Fermions in a 3D Optical Lattice”, *Science* **322**, 1520–1525 (2008).
- [62] W. Bakr, J. Gillen, A. Peng, S. Fölling and M. Greiner: “A quantum gas microscope for detecting single atoms in a Hubbard-regime optical lattice”, *Nature* **462**, 74–77 (2009).
- [63] J. Sherson, C. Weitenberg, M. Endres, M. Cheneau, I. Bloch and S. Kuhr: “Single-atom-resolved fluorescence imaging of an atomic Mott insulator”, *Nature* **467**, 68–72 (2010).
- [64] W. S. Bakr, A. Peng, M. E. Tai, R. Ma, J. Simon, J. I. Gillen, S. Fölling, L. Pollet and M. Greiner: “Probing the Superfluid-to-Mott Insulator Transition at the Single-Atom Level”, *Science* **329**, 547–550 (2010).
- [65] C. Weitenberg, M. Endres, J. Sherson, M. Cheneau, P. Schauß, T. Fukuhara, I. Bloch and S. Kuhr: “Single-spin addressing in an atomic Mott insulator”, *Nature* **471**, 319–324 (2011).
- [66] G. Wirth, M. Ölschläger and A. Hemmerich: “Evidence for orbital superfluidity in the P-band of a bipartite optical square lattice”, *Nature Physics* **7**, 147–153 (2011).
- [67] M. Ölschläger, G. Wirth and A. Hemmerich: “Unconventional Superfluid Order in the F Band of a Bipartite Optical Square Lattice”, *Phys. Rev. Lett.* **106**, 15302 (2011).
- [68] P. Soltan-Panahi, D.-S. Lühmann, J. Struck, P. Windpassinger and K. Sengstock: “Quantum phase transition to unconventional multi-orbital superfluidity in optical lattices”, *Nature Physics* **8**, 71–75 (2011).
- [69] T. Kock, M. Ölschläger, A. Ewerbeck, W.-M. Huang, L. Mathey and A. Hemmerich: “Observation of chiral superfluid order by matter wave heterodyning”, preprint arXiv: 1411.3483 (2014).
- [70] U. Bissbort, S. Götze, Y. Li, J. Heinze, J. Krauser, M. Weinberg, C. Becker, K. Sengstock and W. Hofstetter: “Detecting the Amplitude Mode of Strongly Interacting Lattice Bosons by Bragg Scattering”, *Phys. Rev. Lett.* **106**, 205303 (2011).
- [71] M. Endres, T. Fukuhara, D. Pekker, M. Cheneau, P. Schauß, C. Gross, E. Demler, S. Kuhr and I. Bloch: “The ‘Higgs’ amplitude mode at the two-dimensional superfluid/Mott insulator transition”, *Nature* **487**, 454–458 (2012).
- [72] S. Braun, J. P. Ronzheimer, M. Schreiber, S. S. Hodgman, T. Rom, I. Bloch and U. Schneider: “Negative Absolute Temperature for Motional Degrees of Freedom”, *Science* **339**, 52–55 (2013).

-
- [73] M. Greiner, I. Bloch, O. Mandel, T. Hänsch and T. Esslinger: “Exploring Phase Coherence in a 2D Lattice of Bose-Einstein Condensates”, *Phys. Rev. Lett.* **87**, 160405 (2001).
- [74] C. Becker, P. Soltan-Panahi, J. Kronjäger, S. Dörscher, K. Bongs and K. Sengstock: “Ultracold quantum gases in triangular optical lattices”, *New J. Phys.* **12**, 065025 (2010).
- [75] P. Soltan-Panahi, J. Struck, P. Hauke, A. Bick, W. Plenkers, G. Meineke, C. Becker, P. Windpassinger, M. Lewenstein and K. Sengstock: “Multi-component quantum gases in spin-dependent hexagonal lattices”, *Nature Physics* **7**, 434–440 (2011).
- [76] L. Tarruell, D. Greif, T. Uehlinger, G. Jotzu and T. Esslinger: “Creating, moving and merging Dirac points with a Fermi gas in a tunable honeycomb lattice”, *Nature* **483**, 302–305 (2012).
- [77] G.-B. Jo, J. Guzman, C. K. Thomas, P. Hosur, A. Vishwanath and D. M. Stamper-Kurn: “Ultracold Atoms in a Tunable Optical Kagome Lattice”, *Phys. Rev. Lett.* **108**, 045305 (2012).
- [78] C. Schori, T. Stöferle, H. Moritz, M. Köhl and T. Esslinger: “Excitations of a Superfluid in a Three-Dimensional Optical Lattice”, *Phys. Rev. Lett.* **93**, 240402 (2004).
- [79] T. Stöferle, H. Moritz, C. Schori, M. Köhl and T. Esslinger: “Transition from a Strongly Interacting 1D Superfluid to a Mott Insulator”, *Phys. Rev. Lett.* **92**, 130403 (2004).
- [80] J. Heinze, S. Götze, J. S. Krauser, B. Hundt, N. Fläschner, D. S. Lühmann, C. Becker and K. Sengstock: “Multiband Spectroscopy of Ultracold Fermions: Observation of Reduced Tunneling in Attractive Bose-Fermi Mixtures”, *Phys. Rev. Lett.* **107**, 135303 (2011).
- [81] J. F. Sherson, S. J. Park, P. L. Pedersen, N. Winter, M. Gajdacz, S. Mai and J. Arlt: “The pump–probe coupling of matter wave packets to remote lattice states”, *New J. Phys.* **14**, 083013 (2012).
- [82] J. Heinze, J. S. Krauser, N. Fläschner, B. Hundt, S. Götze, A. P. Itin, L. Mathey, K. Sengstock and C. Becker: “Intrinsic Photoconductivity of Ultracold Fermions in Optical Lattices”, *Phys. Rev. Lett.* **110**, 085302 (2013).
- [83] W. Bakr, P. Preiss, M. Tai, R. Ma, J. Simon and M. Greiner: “Orbital excitation blockade and algorithmic cooling in quantum gases”, *Nature* **480**, 500–503 (2011).
- [84] R. Ma, M. Tai, P. Preiss, W. Bakr, J. Simon and M. Greiner: “Photon-Assisted Tunneling in a Biased Strongly Correlated Bose Gas”, *Phys. Rev. Lett.* **107**, 095301 (2011).

- [85] D. Greif, L. Tarruell, T. Uehlinger, R. Jördens and T. Esslinger: “**Probing Nearest-Neighbor Correlations of Ultracold Fermions in an Optical Lattice**”, Phys. Rev. Lett. **106**, 145302 (2011).
- [86] D. Dunlap and V. Kenkre: “**Dynamic localization of a charged particle moving under the influence of an electric field**”, Physical Review B **34**, 3625–3633 (1986).
- [87] F. Grossmann, T. Dittrich, P. Jung and P. Hänggi: “**Coherent destruction of tunneling**”, Phys. Rev. Lett. **67**, 516–519 (1991).
- [88] F. Großmann, P. Jung, T. Dittrich and P. Hänggi: “**Tunneling in a periodically driven bistable system**”, Zeitschrift für Physik B **84**, 315–325 (1991).
- [89] F. Großmann and P. Hänggi: “**Localization in a Driven Two-Level Dynamics**”, EPL **18**, 571–576 (1992).
- [90] M. Holthaus: “**Collapse of minibands in far-infrared irradiated superlattices**”, Phys. Rev. Lett. **69**, 351–354 (1992).
- [91] X.-G. Zhao: “**The suppression of a Bloch band in a driving laser field**”, J. Phys.: Condens. Matter **6**, 2751–2756 (1994).
- [92] A. Eckardt, C. Weiss and M. Holthaus: “**Superfluid-Insulator Transition in a Periodically Driven Optical Lattice**”, Phys. Rev. Lett. **95**, 260404 (2005).
- [93] K. Madison, M. Fischer, R. Diener, Q. Niu and M. Raizen: “**Dynamical Bloch Band Suppression in an Optical Lattice**”, Phys. Rev. Lett. **81**, 5093–5096 (1998).
- [94] H. Lignier, C. Sias, D. Ciampini, Y. Singh, A. Zenesini, O. Morsch and E. Arimondo: “**Dynamical Control of Matter-Wave Tunneling in Periodic Potentials**”, Phys. Rev. Lett. **99**, 220403 (2007).
- [95] A. Zenesini, H. Lignier, D. Ciampini, O. Morsch and E. Arimondo: “**Coherent Control of Dressed Matter Waves**”, Phys. Rev. Lett. **102**, 100403 (2009).
- [96] J. Struck, C. Ölschläger, R. L. L. Targat, P. Soltan-Panahi, A. Eckardt, M. Lewenstein, P. Windpassinger, K. Sengstock and R. L. L. Targat: “**Quantum Simulation of Frustrated Classical Magnetism in Triangular Optical Lattices**”, Science **333**, 996–999 (2011).
- [97] S. Arlinghaus and M. Holthaus: “**Driven optical lattices as strong-field simulators**”, Physical Review A **81**, 063612 (2010).
- [98] W. Ehrenberg and R. E. Siday: “**The Refractive Index in Electron Optics and the Principles of Dynamics**”, Proc. R. Soc. B **62**, 8 (1949).

-
- [99] Y. Aharonov and D. Bohm: “Significance of Electromagnetic Potentials in the Quantum Theory”, Phys. Rev. **115**, 485–491 (1959).
- [100] Y. Aharonov and D. Bohm: “Further Considerations on Electromagnetic Potentials in the Quantum Theory”, Phys. Rev. **123**, 1511–1524 (1961).
- [101] K. Klitzing, G. Dorda and M. Pepper: “New Method for High-Accuracy Determination of the Fine-Structure Constant Based on Quantized Hall Resistance”, Phys. Rev. Lett. **45**, 494–497 (1980).
- [102] R. Laughlin: “Quantized Hall conductivity in two dimensions”, Physical Review B **23**, 5632–5633 (1981).
- [103] D. C. Tsui, H. L. Stormer and A. C. Gossard: “Two-Dimensional Magnetotransport in the Extreme Quantum Limit”, Phys. Rev. Lett. **48**, 1559–1562 (1982).
- [104] R. B. Laughlin: “Anomalous Quantum Hall Effect: An Incompressible Quantum Fluid with Fractionally Charged Excitations”, Phys. Rev. Lett. **50**, 1395–1398 (1983).
- [105] P. G. Harper: “Single Band Motion of Conduction Electrons in a Uniform Magnetic Field”, Proc. R. Soc. A **68**, 874–878 (1955).
- [106] D. Hofstadter: “Energy levels and wave functions of Bloch electrons in rational and irrational magnetic fields”, Physical Review B **14**, 2239–2249 (1976).
- [107] K. Madison, F. Chevy, W. Wohlleben and J. Dalibard: “Vortex Formation in a Stirred Bose-Einstein Condensate”, Phys. Rev. Lett. **84**, 806–809 (2000).
- [108] J. R. Abo-Shaeer, C. Raman, J. M. Vogels and W. Ketterle: “Observation of Vortex Lattices in Bose-Einstein Condensates”, Science **292**, 476–479 (2001).
- [109] V. Schweikhard, I. Coddington, P. Engels, V. Mogendorff and E. Cornell: “Rapidly Rotating Bose-Einstein Condensates in and near the Lowest Landau Level”, Phys. Rev. Lett. **92**, 040404 (2004).
- [110] V. Bretin, S. Stock, Y. Seurin and J. Dalibard: “Fast Rotation of a Bose-Einstein Condensate”, Phys. Rev. Lett. **92**, 050403 (2004).
- [111] N. R. Cooper: “Rapidly rotating atomic gases”, Advances in Physics **57**, 539–616 (2008).
- [112] N. Gemelke, E. Sarajlic and S. Chu: “Rotating Few-body Atomic Systems in the Fractional Quantum Hall Regime”, preprint arXiv: 1007.2677 (2010).

- [113] A. Fetter: “Rotating trapped Bose-Einstein condensates”, *Rev. Mod. Phys.* **81** (2), 647–691 (2009).
- [114] Y. J. Lin, R. Compton, K. Jiménez-García, J. von Porto and I. Spielman: “Synthetic magnetic fields for ultracold neutral atoms”, *Nature* **462**, 628–632 (2009).
- [115] Y. J. Lin, R. Compton, A. Perry, W. Phillips, J. von Porto and I. Spielman: “Bose-Einstein Condensate in a Uniform Light-Induced Vector Potential”, *Phys. Rev. Lett.* **102**, 130401 (2009).
- [116] Y. J. Lin, R. Compton, K. Jiménez-García, W. Phillips, J. von Porto and I. Spielman: “A synthetic electric force acting on neutral atoms”, *Nature Physics* **7**, 531–534 (2011).
- [117] M. Aidelsburger, M. Atala, S. Nascimbène, S. Trotzky, Y. A. Chen and I. Bloch: “Experimental Realization of Strong Effective Magnetic Fields in an Optical Lattice”, *Phys. Rev. Lett.* **107**, 255301 (2011).
- [118] K. Jiménez-García, L. LeBlanc, R. Williams, M. Beeler, A. Perry and I. Spielman: “Peierls Substitution in an Engineered Lattice Potential”, *Phys. Rev. Lett.* **108**, 225303 (2012).
- [119] M. Aidelsburger, M. Atala, S. Nascimbène, S. Trotzky, Y. A. Chen and I. Bloch: “Experimental realization of strong effective magnetic fields in optical superlattice potentials”, *Applied Physics B* **113**, 1–11 (2013).
- [120] M. Aidelsburger, M. Atala, M. Lohse, J. T. Barreiro, B. Paredes and I. Bloch: “Realization of the Hofstadter Hamiltonian with Ultracold Atoms in Optical Lattices”, *Phys. Rev. Lett.* **111**, 185301 (2013).
- [121] M. Atala, M. Aidelsburger, M. Lohse, J. T. Barreiro, B. Paredes and I. Bloch: “Observation of chiral currents with ultracold atoms in bosonic ladders”, *Nature Physics* **10**, 588–593 (2014).
- [122] M. Aidelsburger, M. Lohse, C. Schweizer, M. Atala, J. T. Barreiro, S. Nascimbène, N. R. Cooper, I. Bloch and N. Goldman: “Measuring the Chern number of Hofstadter bands with ultracold bosonic atoms”, preprint arXiv: 1407.4205 (2014).
- [123] J. Vannimenus and G. Toulouse: “Theory of the frustration effect. II. Ising spins on a square lattice”, *J. Phys. C: Solid State Phys.* **10**, L537 (1977).
- [124] G. Wannier: “Antiferromagnetism. The Triangular Ising Net”, *Physical Review* **79**, 357–364 (1950).
- [125] A. Auerbach: *Interacting Electrons and Quantum Magnetism*, Springer New York (1994).

-
- [126] S. Sachdev: “Quantum magnetism and criticality”, *Nature Physics* **4**, 173–185 (2008).
- [127] P. Anderson: “Resonating valence bonds: A new kind of insulator?”, *Materials Research Bulletin* **8**, 153 – 160 (1973).
- [128] P. W. Anderson: “The Resonating Valence Bond State in La_2CuO_4 and Superconductivity”, *Science* **235**, 1196–1198 (1987).
- [129] S. A. Kivelson, D. S. Rokhsar and J. P. Sethna: “Topology of the resonating valence-bond state: Solitons and high- T_c superconductivity”, *Phys. Rev. B* **35**, 8865–8868 (1987).
- [130] L. Balents: “Spin liquids in frustrated magnets”, *Nature* **464**, 199–208 (2010).
- [131] C. Nayak, S. H. Simon, A. Stern, M. Freedman and S. Das Sarma: “Non-Abelian anyons and topological quantum computation”, *Rev. Mod. Phys.* **80**, 1083–1159 (2008).
- [132] Y. Shimizu, K. Miyagawa, K. Kanoda, M. Maesato and G. Saito: “Spin Liquid State in an Organic Mott Insulator with a Triangular Lattice”, *Phys. Rev. Lett.* **91**, 107001 (2003).
- [133] R. S. Manna, M. de Souza, A. Brühl, J. A. Schlueter and M. Lang: “Lattice Effects and Entropy Release at the Low-Temperature Phase Transition in the Spin-Liquid Candidate $\kappa\text{-(BEDT-TTF)}_2\text{Cu}_2(\text{CN})_3$ ”, *Phys. Rev. Lett.* **104**, 016403 (2010).
- [134] Y. Shimizu, K. Miyagawa, K. Kanoda, M. Maesato and G. Saito: “Emergence of inhomogeneous moments from spin liquid in the triangular-lattice Mott insulator $\kappa\text{-(ET)}_2\text{Cu}_2(\text{CN})_3$ ”, *Phys. Rev. B* **73**, 140407 (2006).
- [135] S. Yamashita, Y. Nakazawa, M. Oguni, Y. Oshima, H. Nojiri, Y. Shimizu, K. Miyagawa and K. Kanoda: “Thermodynamic properties of a spin-1/2 spin-liquid state in a κ -type organic salt”, *Nature Physics* **4**, 459 – 462 (2008).
- [136] F. L. Pratt, P. J. Baker, S. J. Blundell, T. Lancaster, S. Ohira-Kawamura, C. Baines, Y. Shimizu, K. Kanoda, I. Watanabe and G. Saito: “Magnetic and non-magnetic phases of a quantum spin liquid”, *Nature* **471**, 612 – 616 (2011).
- [137] K. Matan, T. Ono, Y. Fukumoto, T. J. Sato, J. Yamaura, M. Yano, K. Morita and H. Tanaka: “Pinwheel valence-bond solid and triplet excitations in the two-dimensional deformed kagome lattice”, *Nature Physics* **6**, 865–869 (2010).
- [138] T.-H. Han, J. S. Helton, S. Chu, D. G. Nocera, J. A. Rodriguez-Rivera, C. Broholm and Y. S. Lee: “Fractionalized excitations in the spin-liquid state of a kagome-lattice antiferromagnet”, *Nature* **492**, 406 – 410 (2012).

- [139] D. Greif, T. Uehlinger, G. Jotzu, L. Tarruell and T. Esslinger: “Short-Range Quantum Magnetism of Ultracold Fermions in an Optical Lattice”, *Science* **340**, 1307–1310 (2013).
- [140] A. Eckardt, P. Hauke, P. Soltan-Panahi, C. Becker, K. Sengstock and M. Lewenstein: “Frustrated quantum antiferromagnetism with ultracold bosons in a triangular lattice”, *EPL* **89**, 10010 (2010).
- [141] J. Simon, W. Bakr, R. Ma, M. Tai, P. Preiss and M. Greiner: “Quantum simulation of antiferromagnetic spin chains in an optical lattice”, *Nature* **472**, 307–312 (2011).
- [142] K. S. Novoselov, A. K. Geim, S. V. Morozov, D. Jiang, Y. Zhang, S. V. Dubonos, I. V. Grigorieva and A. A. Firsov: “Electric Field Effect in Atomically Thin Carbon Films”, *Science* **306**, 666–669 (2004).
- [143] A. K. Geim and K. S. Novoselov: “The rise of graphene”, *Nature Materials* **6**, 183–191 (2007).
- [144] A. H. Castro Neto, F. Guinea, N. M. R. Peres, K. S. Novoselov and A. K. Geim: “The electronic properties of graphene”, *Rev. Mod. Phys.* **81**, 109–162 (2009).
- [145] K. S. Novoselov, V. I. Fal’ko, L. Colombo, P. R. Gellert, M. G. Schwab and K. Kim: “A roadmap for graphene”, *Nature* **490**, 192 – 200 (2012).
- [146] K. S. Novoselov, A. K. Geim, S. V. Morozov, D. Jiang, M. I. Katsnelson, I. V. Grigorieva, S. V. Dubonos and A. A. Firsov: “Two-Dimensional Gas of Massless Dirac Fermions in Graphene”, *Nature* **438**, 197–200 (2005).
- [147] T. Salger, C. Grossert, S. Kling and M. Weitz: “Klein Tunneling of a Quasirelativistic Bose-Einstein Condensate in an Optical Lattice”, *Phys. Rev. Lett.* **107**, 240401 (2011).
- [148] L. J. LeBlanc, M. C. Beeler, K. Jiménez-García, A. R. Perry, S. Sugawa, R. A. Williams and I. B. Spielman: “Direct observation of zitterbewegung in a Bose-Einstein condensate”, *New Journal of Physics* **15**, 073011 (2013).
- [149] L. Duca, T. Li, M. Reitter, I. Bloch, M. Schleier-Smith and U. Schneider: “An Aharonov-Bohm interferometer for determining Bloch band topology”, preprint arXiv: 1407.5635 (2014).
- [150] F. D. Haldane: “Model for a Quantum Hall Effect without Landau Levels: Condensed-Matter Realization of the "Parity Anomaly"”, *Phys. Rev. Lett.* **61**, 2015–2018 (1988).

-
- [151] G. Jotzu, M. Messer, R. Desbuquois, M. Lebrat, T. Uehlinger, D. Greif and T. Esslinger: “[Experimental realisation of the topological Haldane model with ultracold fermions](#)”, *Nature* **515**, 237–240 (2014).
- [152] I. Bloch: “[Exploring quantum matter with ultracold atoms in optical lattices](#)”, *J. Phys. B: At. Mol. Opt. Phys.* **38**, 629–643 (2005).
- [153] C. Becker: “[Multi component Bose-Einstein Condensates](#)”, Ph.D. thesis, Universität Hamburg (2009).
- [154] P. Soltan-Panahi: “[Multi-Component Quantum Gases in Hexagonal Lattices](#)”, Ph.D. thesis, Universität Hamburg (2010).
- [155] J. Struck: “[Artificial Gauge Fields in Driven Optical Lattices](#)”, Ph.D. thesis, Universität Hamburg (2013).
- [156] M. Erhard: “[Experimente mit mehrkomponentigen Bose-Einstein-Kondensaten](#)”, Ph.D. thesis, Universität Hamburg (2004).
- [157] H. Schmaljohann: “[Spindynamik in Bose-Einstein Kondensaten](#)”, Ph.D. thesis, Universität Hamburg (2004).
- [158] J. Kronjäger: “[Coherent Dynamics of Spinor Bose-Einstein Condensates](#)”, Ph.D. thesis, Universität Hamburg (2007).
- [159] P. Lett, R. Watts, C. Westbrook, W. Phillips, P. Gould and H. Metcalf: “[Observation of Atoms Laser Cooled below the Doppler Limit](#)”, *Phys. Rev. Lett.* **61**, 169–172 (1988).
- [160] J. Dalibard and C. Cohen-Tannoudji: “[Laser cooling below the Doppler limit by polarization gradients: simple theoretical models](#)”, *J. Opt. Soc. Am. B* **6**, 2023–2045 (1989).
- [161] H. J. Metcalf and P. van der Straten: *Laser Cooling and Trapping*, Springer New York (1999).
- [162] M. Kottke: “[Magnetfallen und Signaturen der Eindimensionalität für Bose-Einstein-Kondensate](#)”, Ph.D. thesis, Universität Hannover (2004).
- [163] J. Dalibard and C. Cohen-Tannoudji: “[Dressed-atom approach to atomic motion in laser light: the dipole force revisited](#)”, *J. Opt. Soc. Am. B* **2**, 1707–1720 (1985).
- [164] C. Cohen-Tannoudji, J. Dupont-Roc and G. Grynberg: *Atom-Photon Interactions*, Wiley-VCH (2004).

BIBLIOGRAPHY

- [165] G. G. C. Cohen-Tannoudji, J. Dupont-Roc: *Photons and Atoms: Introduction to Quantum Electrodynamics*, Wiley-VHC (1997).
- [166] R. Grimm, M. Weidemüller and Y. B. Ovchinnikov: “Optical Dipole Traps for Neutral Atoms”, *Adv. At. Mol. Opt. Phys.* **42**, 95–170 (2000).
- [167] D. A. Steck: “Rubidium 87 D Line Data”, (2014).
- [168] R. C. Jones: “A New Calculus for the Treatment of Optical Systems”, *J. Opt. Soc. Am.* **31**, 488–493 (1941).
- [169] F. Bloch: “Über die Quantenmechanik der Elektronen in Kristallgittern”, *Zeitschrift für Physik* **52**, 555–600 (1929).
- [170] N. W. Ashcroft and N. D. Mermin: *Solid state physics*, Brooks Cole (1976).
- [171] G. Wannier: “The Structure of Electronic Excitation Levels in Insulating Crystals”, *Physical Review* **52**, 191–197 (1937).
- [172] W. Kohn: “Analytic Properties of Bloch Waves and Wannier Functions”, *Physical Review* **115**, 809–821 (1959).
- [173] L. P. Pitaevskii: “Vortex Lines in an Imperfect Bose Gas”, *Sov. Phys. JETP* **13**, 451–454 (1961).
- [174] E. Gross: “Structure of a quantized vortex in boson systems”, *Il Nuovo Cimento Series 10* **20**, 454–477 (1961).
- [175] L. P. Pitaevskii and S. Stringari: *Bose-Einstein Condensation*, Clarendon Press (2003).
- [176] H. Gersch and G. Knollman: “Quantum Cell Model for Bosons”, *Physical Review* **129**, 959–967 (1963).
- [177] M. Greiner: “Ultracold quantum gases in three-dimensional lattice potentials”, Ph.D. thesis, Ludwig-Maximilians Universität München (2003).
- [178] K. I. Petsas, A. B. Coates and G. Grynberg: “Crystallography of optical lattices”, *Phys. Rev. A* **50**, 5173–5189 (1994).
- [179] C. Ölschläger: “Quantensimulation von frustriertem Magnetismus in einem optischen Dreiecksgitter”, Master’s thesis, Universität Hamburg (2011).
- [180] D. McKay and B. DeMarco: “Thermometry with spin-dependent lattices”, *New J. Phys.* **12**, 055013 (2010).

-
- [181] T. Horiguchi and C. C. Chen: “Lattice Green’s function for the diced lattice”, *J. Math. Phys.* **15**, 659–660 (1974).
- [182] D. Bercioux, D. F. Urban, H. Grabert and W. Häusler: “Massless Dirac-Weyl fermions in a \mathcal{T}_3 optical lattice”, *Phys. Rev. A* **80**, 063603 (2009).
- [183] V. Kashurnikov, N. Prokof’ev and B. Svistunov: “Revealing the superfluid–Mott-insulator transition in an optical lattice”, *Physical Review A* **66**, 031601 (2002).
- [184] W. Zwerger: “Mott-Hubbard transition of cold atoms in optical lattices”, *J. Opt. B: Quantum Semiclass. Opt.* **5**, 9–16 (2003).
- [185] F. Gerbier, S. Trotzky, S. Fölling, U. Schnorrberger, J. Thompson, A. Widera, I. Bloch, L. Pollet, M. Troyer, B. Capogrosso-Sansone, N. von Prokof’ev and B. von Svistunov: “Expansion of a Quantum Gas Released from an Optical Lattice”, *Phys. Rev. Lett.* **101**, 155303 (2008).
- [186] T. Kraemer, J. Herbig, M. Mark, T. Weber, C. Chin, H.-C. Nägerl and R. Grimm: “Optimized production of a cesium Bose-Einstein condensate”, *Applied Physics B* **79**, 1013–1019 (2004).
- [187] T. van Zoest, N. Gaaloul, Y. Singh, H. Ahlers, W. Herr, S. T. Seidel, W. Ertmer, E. Rasel, M. Eckart, E. Kajari, S. Arnold, G. Nandi, W. P. Schleich, R. Walser, A. Vogel, K. Sengstock, K. Bongs, W. Lewoczko-Adamczyk, M. Schiemangk, T. Schuldt, A. Peters, T. Könnemann, H. Müntinga, C. Lämmerzahl, H. Dittus, T. Steinmetz, T. W. Hänsch and J. Reichel: “Bose-Einstein Condensation in Microgravity”, *Science* **328**, 1540–1543 (2010).
- [188] A. Eckardt and M. Holthaus: “AC-induced superfluidity”, *EPL* **80**, 50004 (2007).
- [189] A. Hemmerich: “Effective time-independent description of optical lattices with periodic driving”, *Physical Review A* **81**, 063626 (2010).
- [190] W. Houston: “Acceleration of Electrons in a Crystal Lattice”, *Physical Review* **57**, 184–186 (1940).
- [191] A. Eckardt, M. Holthaus, H. Lignier, A. Zenesini, D. Ciampini, O. Morsch and E. Arimondo: “Exploring dynamic localization with a Bose-Einstein condensate”, *Physical Review A* **79**, 013611 (2009).
- [192] C. J. Pethick and H. Smith: *Bose-Einstein Condensation in Dilute Gases*, Cambridge University Press (2008).
- [193] J. Shirley: “Solution of the Schrödinger Equation with a Hamiltonian Periodic in Time”, *Physical Review* **138**, 979–987 (1965).

- [194] G. Floquet: “[Sur les équations différentielles linéaires à coefficients périodiques](#)”, *Annales scientifiques de l'École Normale Supérieure, Sér. 2* **12**, 47–88 (1883).
- [195] E. Arimondo, D. Ciampini, A. Eckardt, M. Holthaus and O. Morsch: “[Kilohertz-Driven Bose-Einstein Condensates in Optical Lattices](#)”, *Advances in Atomic, Molecular, and Optical Physics* **61**, 515–547 (2012).
- [196] M. Grifoni and P. Hänggi: “[Driven quantum tunneling](#)”, *Physics Reports* **304**, 229–354 (1998).
- [197] A. Eckardt and M. Holthaus: “[Avoided-Level-Crossing Spectroscopy with Dressed Matter Waves](#)”, *Phys. Rev. Lett.* **101**, 245302 (2008).
- [198] D. Poletti and C. Kollath: “[Slow quench dynamics of periodically driven quantum gases](#)”, *Physical Review A* **84**, 013615 (2011).
- [199] E. Kierig, U. Schnorrberger, A. Schietinger, J. Tomkovic and M. Oberthaler: “[Single-Particle Tunneling in Strongly Driven Double-Well Potentials](#)”, *Phys. Rev. Lett.* **100**, 190405 (2008).
- [200] R. Peierls: “[Zur Theorie des Diamagnetismus von Leitungselektronen](#)”, *Zeitschrift für Physik* **80**, 763–791 (1933).
- [201] H. Miyake, G. A. Siviloglou, C. J. Kennedy, W. C. Burton and W. Ketterle: “[Realizing the Harper Hamiltonian with Laser-Assisted Tunneling in Optical Lattices](#)”, *Phys. Rev. Lett.* **111**, 185302 (2013).
- [202] S. Teitel and C. Jayaprakash: “[Phase transitions in frustrated two-dimensional XY models](#)”, *Physical Review B* **27**, 598–601 (1983).
- [203] S. Miyashita and H. Shiba: “[Nature of the Phase Transition of the Two-Dimensional Antiferromagnetic Plane Rotator Model on the Triangular Lattice](#)”, *J. Phys. Soc. Jpn.* **53**, 1145–1154 (1984).
- [204] M. Yosefin and E. Domany: “[Phase transitions in fully frustrated spin systems](#)”, *Physical Review B* **32**, 1778–1795 (1985).
- [205] M. Choi and S. Doniach: “[Phase transitions in uniformly frustrated XY models](#)”, *Physical Review B* **31**, 4516–4526 (1985).
- [206] E. Granato and J. Kosterlitz: “[Critical behavior of coupled XY models](#)”, *Physical Review B* **33** (7), 4767–4776 (1986).
- [207] S. Korshunov and G. Uimin: “[Phase transitions in two-dimensional uniformly frustrated XY models. I. Antiferromagnetic model on a triangular lattice](#)”, *Journal of Statistical Physics* **43**, 1–16 (1986).

-
- [208] P. Olsson: “Two Phase Transitions in the Fully Frustrated XY Model”, *Phys. Rev. Lett.* **75**, 2758–2761 (1995).
- [209] G. S. Jeon, S. Y. Park and M. Y. Choi: “Double transitions in the fully frustrated XY model”, *Physical Review B* **55**, 14088–14091 (1997).
- [210] E. Boubcheur and H. Diep: “Critical behavior of the two-dimensional fully frustrated XY model”, *Physical Review B* **58**, 5163–5165 (1998).
- [211] S. Okumura, H. Yoshino and H. Kawamura: “Spin-chirality decoupling and critical properties of a two-dimensional fully frustrated XY model”, *Physical Review B* **83**, 094429 (2011).
- [212] T. Obuchi and H. Kawamura: “Spin and Chiral Orderings of the Antiferromagnetic XY Model on the Triangular Lattice and Their Critical Properties”, *J. Phys. Soc. Jpn.* **81**, 054003 (2012).
- [213] C. V. Parker, L.-C. Ha and C. Chin: “Direct observation of effective ferromagnetic domains of cold atoms in a shaken optical lattice”, *Nature Physics* **9**, 769–774 (2013).
- [214] H. Steinhaus: “Sur la division des corps matériels en parties.”, *Bull. Acad. Pol. Sci., Cl. III* **4**, 801–804 (1957).
- [215] J. MacQueen: “Some methods for classification and analysis of multivariate observations”, *Proc. Fifth Berkeley Symp. on Math. Statist. and Prob.* **1**, 281–297 (1967).
- [216] S. Lloyd: “Least squares quantization in PCM”, *Information Theory, IEEE Transactions on* **28**, 129–137 (1982).
- [217] G. Lejeune Dirichlet: “Über die Reduction der positiven quadratischen Formen mit drei unbestimmten ganzen Zahlen.”, *Journal für die reine und angewandte Mathematik* **40**, 209–227 (1850).
- [218] A. Okabe, B. Boots, K. Sugihara and S. N. Chiu: *Spatial Tessellations: Concepts and Applications of Voronoi Diagrams, 2nd Edition*, John Wiley (2000).
- [219] J. C. Bezdek: *Pattern Recognition with Fuzzy Objective Function Algorithms*, Kluwer Academic Publishers (1981).
- [220] G. Schwarz: “Estimating the Dimension of a Model”, *The Annals of Statistics* **6**, 461–464 (1978).
- [221] H. Akaike: “A new look at the statistical model identification”, *Automatic Control, IEEE Transactions on* **19**, 716–723 (1974).

- [222] S. R. Segal, Q. Diot, E. A. Cornell, A. A. Zozulya and D. Z. Anderson: “Revealing buried information: Statistical processing techniques for ultracold-gas image analysis”, *Phys. Rev. A* **81**, 053601 (2010).
- [223] G. D. Brown, S. Yamada and T. J. Sejnowski: “Independent component analysis at the neural cocktail party”, *Trends in Neurosciences* **24**, 54 – 63 (2001).
- [224] O. Lahav, A. Naim, L. Sodre and M. Storrie-Lombardi: “Neural computation as a tool for galaxy classification: methods and examples”, *Mon. Not. R. Astron. Soc* **208**, 207 (1996).
- [225] M. Ungureanu, C. Bigan, R. Strungaru and V. Lazarescu: “Independent Component Analysis Applied in Biomedical Signal Processing”, *Measurement Science Review* **4** (2004).
- [226] J. Kim, J. Choi and J. Yi: “ICA Based Face Recognition Robust to Partial Occlusions and Local Distortions”, pages 147–154, Springer Berlin Heidelberg (2004).
- [227] C. Serviere and P. Fabry: “Principal component analysis and blind source separation of modulated sources for electro-mechanical systems diagnostic”, *Mechanical Systems and Signal Processing* **19**, 1293 – 1311 (2005).
- [228] C. Ding and X. He: “K-means Clustering via Principal Component Analysis”, *Proc. of Int’l Conf. Machine Learning* **1**, 225–232 (2004).
- [229] H. Zha, X. He, C. Ding, H. Simon and M. Gu: “Spectral Relaxation for K-means Clustering”, *Neural Information Processing Systems* **14**, 1057–1064 (2001).
- [230] K. Pearson: “On lines and planes of closest fit to systems of points in space”, *Phil. Mag. Ser.* **2**, 559–572 (1901).
- [231] R. Dubessy, C. D. Rossi, T. Badr, L. Longchambon and H. Perrin: “Imaging the collective excitations of an ultracold gas using statistical correlations”, *New Journal of Physics* **16**, 122001 (2014).
- [232] A. Hyvärinen. and E. Oja: “Independent component analysis: algorithms and applications”, *Neural Net* **13**, 411–430 (2000).
- [233] A. Dhar, M. Maji, T. Mishra, R. V. Pai, S. Mukerjee and A. Paramekanti: “Bose-Hubbard model in a strong effective magnetic field: Emergence of a chiral Mott insulator ground state”, *Physical Review A* **85**, 041602 (2012).
- [234] A. Dhar, T. Mishra, M. Maji, R. Pai, S. Mukerjee and A. Paramekanti: “Chiral Mott insulator with staggered loop currents in the fully frustrated Bose-Hubbard model”, *Physical Review B* **87**, 174501 (2013).

-
- [235] M. P. Zaletel, S. A. Parameswaran, A. Rüegg and E. Altman: “Chiral bosonic Mott insulator on the frustrated triangular lattice”, *Phys. Rev. B* **89**, 155142 (2014).
- [236] R. Schmied, T. Roscilde, V. Murg, D. Porras and J. I. Cirac: “Quantum phases of trapped ions in an optical lattice”, *New J. Phys.* **10**, 045017 (2008).
- [237] T. Holstein and H. Primakoff: “Field Dependence of the Intrinsic Domain Magnetization of a Ferromagnet”, *Physical Review* **58**, 1098–1113 (1940).
- [238] R. Liebmann: *Statistical Mechanics of Periodic Frustrated Ising Systems*, Springer Berlin Heidelberg (1986).
- [239] B. S. Shastry and B. Sutherland: “Exact ground state of a quantum mechanical antiferromagnet”, *Physica B* **108**, 1069 – 1070 (1981).
- [240] C. Mora and Y. Castin: “Extension of Bogoliubov theory to quasicondensates”, *Phys. Rev. A* **67**, 053615 (2003).
- [241] D. van Oosten, P. van der Straten and H. Stoof: “Quantum phases in an optical lattice”, *Physical Review A* **63**, 053601 (2001).
- [242] B. DeMarco, C. Lannert, S. Vishveshwara and T. C. Wei: “Structure and stability of Mott-insulator shells of bosons trapped in an optical lattice”, *Physical Review A* **71**, 063601 (2005).
- [243] S. Fölling, A. Widera, T. Müller, F. Gerbier and I. Bloch: “Formation of Spatial Shell Structure in the Superfluid to Mott Insulator Transition”, *Phys. Rev. Lett.* **97**, 060403 (2006).
- [244] K. Mitra, C. J. Williams and C. A. R. Sá de Melo: “Superfluid and Mott-insulating shells of bosons in harmonically confined optical lattices”, *Phys. Rev. A* **77**, 033607 (2008).
- [245] J. K. Freericks and H. Monien: “Phase diagram of the Bose-Hubbard Model”, *EPL* **26**, 545 (1994).
- [246] M. Greiner, O. Mandel, T. Hänsch and I. Bloch: “Collapse and revival of the matter wave field of a Bose-Einstein condensate”, *Nature* **419**, 51–54 (2002).
- [247] E. M. Wright, D. F. Walls and J. C. Garrison: “Collapses and Revivals of Bose-Einstein Condensates Formed in Small Atomic Samples”, *Phys. Rev. Lett.* **77**, 2158–2161 (1996).
- [248] E. M. Wright, T. Wong, M. J. Collett, S. M. Tan and D. F. Walls: “Collapses and revivals in the interference between two Bose-Einstein condensates formed in small atomic samples”, *Phys. Rev. A* **56**, 591–602 (1997).

- [249] N. Mermin and H. Wagner: “Absence of Ferromagnetism or Antiferromagnetism in One- or Two-Dimensional Isotropic Heisenberg Models”, *Phys. Rev. Lett.* **17**, 1133–1136 (1966).
- [250] P. C. Hohenberg: “Existence of Long-Range Order in One and Two Dimensions”, *Physical Review* **158**, 383–386 (1967).
- [251] E. Altman, E. Demler and M. Lukin: “Probing many-body states of ultracold atoms via noise correlations”, *Physical Review A* **70**, 013603 (2004).
- [252] S. Fölling: “Probing Strongly Correlated States of Ultracold Atoms in Optical Lattices”, Ph.D. thesis, Johannes Gutenberg Universität Mainz (2008).
- [253] S. Fölling: “Quantum Noise Correlation Experiments with Ultracold Atoms”, preprint arXiv: 1403.6842 (2014).
- [254] R. Hanbury Brown and R. Q. Twiss: “Correlation between Photons in two Coherent Beams of Light”, *Nature* **177**, 27 – 29 (1956).
- [255] R. Hanbury Brown and R. Q. Twiss: “A Test of a New Type of Stellar Interferometer on Sirius”, *Nature* **178**, 1046 – 1048 (1956).
- [256] E. M. Purcell: “The Question of Correlation between Photons in Coherent Light Rays”, *Nature* **178**, 1449 – 1450 (1956).
- [257] I. Spielman, W. Phillips and J. von Porto: “Mott-Insulator Transition in a Two-Dimensional Atomic Bose Gas”, *Phys. Rev. Lett.* **98**, 080404 (2007).
- [258] K. Xu, Y. Liu, D. E. Miller, J. K. Chin, W. Setiawan and W. Ketterle: “Observation of Strong Quantum Depletion in a Gaseous Bose-Einstein Condensate”, *Phys. Rev. Lett.* **96**, 180405 (2006).
- [259] A. K. Geim: “Nobel Lecture: Random walk to graphene”, *Rev. Mod. Phys.* **83**, 851–862 (2011).
- [260] K. S. Novoselov: “Nobel Lecture: Graphene: Materials in the Flatland”, *Rev. Mod. Phys.* **83**, 837–849 (2011).
- [261] A. K. Geim: “Graphene: Status and Prospects”, *Science* **324**, 1530–1534 (2009).
- [262] J. Kronjäger, C. Becker, P. Navez, K. Bongs and K. Sengstock: “Magnetically Tuned Spin Dynamics Resonance”, *Phys. Rev. Lett.* **97**, 110404 (2006).
- [263] D. McKay, M. White and B. DeMarco: “Lattice thermodynamics for ultracold atoms”, *Physical Review A* **79**, 063605 (2009).

-
- [264] V. W. Scarola and S. Das Sarma: “Quantum Phases of the Extended Bose-Hubbard Hamiltonian: Possibility of a Supersolid State of Cold Atoms in Optical Lattices”, Phys. Rev. Lett. **95**, 033003 (2005).
- [265] V. W. Scarola, E. Demler and S. Das Sarma: “Searching for a supersolid in cold-atom optical lattices”, Phys. Rev. A **73**, 051601 (2006).
- [266] C. Wu, W. V. Liu, J. Moore and S. Das Sarma: “Quantum Stripe Ordering in Optical Lattices”, Phys. Rev. Lett. **97**, 190406 (2006).
- [267] V. M. Stojanovic, C. Wu, W. V. Liu and S. Das Sarma: “Incommensurate Superfluidity of Bosons in a Double-Well Optical Lattice”, Phys. Rev. Lett. **101**, 125301 (2008).
- [268] C. Wu, D. Bergman, L. Balents and S. Das Sarma: “Flat Bands and Wigner Crystallization in the Honeycomb Optical Lattice”, Phys. Rev. Lett. **99**, 070401 (2007).
- [269] T. Müller, S. Fölling, A. Widera and I. Bloch: “State Preparation and Dynamics of Ultracold Atoms in Higher Lattice Orbitals”, Phys. Rev. Lett. **99**, 200405 (2007).
- [270] M. Ölschläger, T. Kock, G. Wirth, A. Ewerbeck, C. M. Smith and A. Hemmerich: “Interaction-induced chiral $p_x \pm ip_y$ superfluid order of bosons in an optical lattice”, New Journal of Physics **15**, 083041 (2013).
- [271] M. Ölschläger, G. Wirth, T. Kock and A. Hemmerich: “Topologically Induced Avoided Band Crossing in an Optical Checkerboard Lattice”, Phys. Rev. Lett. **108** (7), 75302 (2012).
- [272] J.-P. Martikainen: “Dynamical instability and loss of p -band bosons in optical lattices”, Phys. Rev. A **83**, 013610 (2011).
- [273] S. Paul and E. Tiesinga: “Formation and decay of Bose-Einstein condensates in an excited band of a double-well optical lattice”, Phys. Rev. A **88**, 033615 (2013).
- [274] C. L. Kane and E. J. Mele: “Quantum Spin Hall Effect in Graphene”, Phys. Rev. Lett. **95**, 226801 (2005).
- [275] C. N. Varney, K. Sun, V. Galitski and M. Rigol: “Kaleidoscope of Exotic Quantum Phases in a Frustrated XY Model”, Phys. Rev. Lett. **107**, 077201 (2011).
- [276] S. Okumura, H. Kawamura, T. Okubo and Y. Motome: “Novel Spin-Liquid States in the Frustrated Heisenberg Antiferromagnet on the Honeycomb Lattice”, Journal of the Physical Society of Japan **79**, 114705 (2010).

- [277] W. Beugeling, J. C. Everts and C. Morais Smith: “Topological phase transitions driven by next-nearest-neighbor hopping in two-dimensional lattices”, *Phys. Rev. B* **86**, 195129 (2012).
- [278] K. Kishigi, H. Hanada and Y. Hasegawa: “Energy Gap and Averaged Inversion Symmetry of Tight-Binding Electrons on Generalized Honeycomb Lattice”, *J. Phys. Soc. Jpn.* **77**, 074707 (2008).
- [279] T. A. Sedrakyan, L. I. Glazman and A. Kamenev: “Absence of Bose condensation on lattices with moat bands”, *Phys. Rev. B* **89**, 201112 (2014).
- [280] Y. A. Bychkov and E. I. Rashba: “Oscillatory effects and the magnetic susceptibility of carriers in inversion layers”, *Journal of Physics C: Solid State Physics* **17**, 6039–6045 (1984).
- [281] E. G. Mishchenko, A. V. Shytov and B. I. Halperin: “Spin Current and Polarization in Impure Two-Dimensional Electron Systems with Spin-Orbit Coupling”, *Phys. Rev. Lett.* **93**, 226602 (2004).
- [282] D. Campbell, G. Juzeliūnas and I. Spielman: “Realistic Rashba and Dresselhaus spin-orbit coupling for neutral atoms”, *Physical Review A* **84**, 025602 (2011).
- [283] T. A. Sedrakyan, A. Kamenev and L. I. Glazman: “Composite fermion state of spin-orbit-coupled bosons”, *Phys. Rev. A* **86**, 063639 (2012).
- [284] V. Galitski and I. B. Spielman: “Spin-orbit coupling in quantum gases”, *Nature* **494**, 49–54 (2013).
- [285] L. Tonks: “The Complete Equation of State of One, Two and Three-Dimensional Gases of Hard Elastic Spheres”, *Phys. Rev.* **50**, 955–963 (1936).
- [286] M. Girardeau: “Relationship between Systems of Impenetrable Bosons and Fermions in One Dimension”, *Journal of Mathematical Physics* **1**, 516–523 (1960).
- [287] B. Paredes, A. Widera, V. Murg, O. Mandel, S. Fölling, I. Cirac, G. von Shlyapnikov, T. Hänsch and I. Bloch: “Tonks-Girardeau gas of ultracold atoms in an optical lattice”, *Nature* **429**, 277–281 (2004).
- [288] A. Mulder, R. Ganesh, L. Capriotti and A. Paramekanti: “Spiral order by disorder and lattice nematic order in a frustrated Heisenberg antiferromagnet on the honeycomb lattice”, *Phys. Rev. B* **81**, 214419 (2010).
- [289] J. Carrasquilla, A. D. Ciolo, F. Becca, V. Galitski and M. Rigol: “Nature of the phases in the frustrated XY model on the honeycomb lattice”, *Phys. Rev. B* **88**, 241109 (2013).

-
- [290] A. Verdeny, A. Mielke and F. Mintert: “**Accurate Effective Hamiltonians via Unitary Flow in Floquet Space**”, Phys. Rev. Lett. **111**, 175301 (2013).
- [291] S. Koghee, L.-K. Lim, M. O. Goerbig and C. M. Smith: “**Merging and alignment of Dirac points in a shaken honeycomb optical lattice**”, Phys. Rev. A **85**, 023637 (2012).
- [292] E. Alba, X. Fernandez-Gonzalvo, J. Mur-Petit, J. Pachos and J. Garcia-Ripoll: “**Seeing Topological Order in Time-of-Flight Measurements**”, Phys. Rev. Lett. **107**, 235301 (2011).
- [293] T. Kitagawa, T. Oka, A. Brataas, L. Fu and E. Demler: “**Transport properties of nonequilibrium systems under the application of light: Photoinduced quantum Hall insulators without Landau levels**”, Phys. Rev. B **84**, 235108 (2011).
- [294] N. Goldman, I. Satija, P. Nikolic, A. Bermudez, M. A. Martin-Delgado, M. Lewenstein and I. B. Spielman: “**Realistic Time-Reversal Invariant Topological Insulators with Neutral Atoms**”, Phys. Rev. Lett. **105**, 255302 (2010).
- [295] S. Greschner, L. Santos and T. Vekua: “**Ultracold bosons in zig-zag optical lattices**”, Physical Review A **87**, 033609 (2013).
- [296] B. Gadway, D. Pertot, R. Reimann and D. Schneble: “**Superfluidity of Interacting Bosonic Mixtures in Optical Lattices**”, Phys. Rev. Lett. **105**, 045303 (2010).
- [297] D. C. McKay, C. Meldgin, D. Chen and B. DeMarco: “**Slow Thermalization between a Lattice and Free Bose Gas**”, Phys. Rev. Lett. **111**, 063002 (2013).
- [298] L.-K. Lim, C. Smith and A. Hemmerich: “**Staggered-Vortex Superfluid of Ultracold Bosons in an Optical Lattice**”, Phys. Rev. Lett. **100**, 130402 (2008).
- [299] L.-K. Lim, A. Lazarides, A. Hemmerich and C. M. Smith: “**Competing pairing states for ultracold fermions in optical lattices with an artificial staggered magnetic field**”, Physical Review A **82**, 013616 (2010).
- [300] C. R. Dean, L. Wang, P. Maher, C. Forsythe, F. Ghahari, Y. Gao, J. Katoch, M. Ishigami, P. Moon, M. Koshino, T. Taniguchi, K. Watanabe, K. L. Shepard, J. Hone and P. Kim: “**Hofstadter’s butterfly and the fractal quantum Hall effect in moiré superlattices**”, Nature **497**, 598–602 (2013).
- [301] B. Hunt, J. D. Sanchez-Yamagishi, A. F. Young, M. Yankowitz, B. J. LeRoy, K. Watanabe, T. Taniguchi, P. Moon, M. Koshino, P. Jarillo-Herrero and R. C. Ashoori: “**Massive Dirac Fermions and Hofstadter Butterfly in a van der Waals Heterostructure**”, Science **340**, 1427–1430 (2013).

- [302] L. A. Ponomarenko, R. V. Gorbachev, G. L. Yu, D. C. Elias, R. Jalil, A. A. Patel, A. Mishchenko, A. S. Mayorov, C. R. Woods, J. R. Wallbank, M. Mucha-Kruczynski, B. A. Piot, M. Potemski, I. V. Grigorieva, K. S. Novoselov, F. Guinea, I. V. Fal'ko and A. K. Geim: “Cloning of Dirac fermions in graphene superlattices”, *Nature* **497**, 594–597 (2013).
- [303] M. Rizzi, V. Cataudella and R. Fazio: “Phase diagram of the Bose-Hubbard model with \mathcal{T}_3 symmetry”, *Phys. Rev. B* **73**, 144511 (2006).
- [304] A. A. Burkov and E. Demler: “Vortex-Peierls States in Optical Lattices”, *Phys. Rev. Lett.* **96**, 180406 (2006).
- [305] L. Sanchez-Palencia and L. Santos: “Bose-Einstein condensates in optical quasicrystal lattices”, *Phys. Rev. A* **72**, 053607 (2005).
- [306] S. Yan, D. A. Huse and S. R. White: “Spin Liquid Ground State of the $S = 1/2$ Kagome Heisenberg Model”, *Science* **332**, 1173 (2011).
- [307] M. P. Shores, E. A. Nytko, B. M. Bartlett and D. G. Nocera: “A Structurally Perfect $S = 1/2$ Kagome Antiferromagnet”, *Journal of the American Chemical Society* **127** (39), 13462–13463 (2005).
- [308] J. Vidal, R. Mosseri and B. Douçot: “Aharonov-Bohm Cages in Two-Dimensional Structures”, *Phys. Rev. Lett.* **81**, 5888–5891 (1998).
- [309] G. Möller and N. R. Cooper: “Correlated Phases of Bosons in the Flat Lowest Band of the Dice Lattice”, *Phys. Rev. Lett.* **108**, 045306 (2012).
- [310] M. Payrits and R. Barnett: “Order-by-disorder degeneracy lifting of interacting bosons on the dice lattice”, *Phys. Rev. A* **90**, 013608 (2014).
- [311] F. Wang and Y. Ran: “Nearly flat band with Chern number $C = 2$ on the dice lattice”, *Phys. Rev. B* **84**, 241103 (2011).
- [312] B. E. Rogowitz, L. A. Treinish and S. Bryson: “How Not to Lie with Visualization”, *Comput. Phys.* **10**, 268–273 (1996).
- [313] A. Light and P. J. Bartlein: “The end of the rainbow? Color schemes for improved data graphics”, *Eos, Transactions American Geophysical Union* **85**, 385–391 (2004).
- [314] D. Borland and R. M. T. II: “Rainbow Color Map (Still) Considered Harmful”, *IEEE Comp. Graph. App.* **27**, 14–17 (2007).
- [315] C. F. Ockeloen, A. F. Tauschinsky, R. J. C. Spreeuw and S. Whitlock: “Detection of small atom numbers through image processing”, *Phys. Rev. A* **82**, 061606 (2010).

- [316] R. J. Glauber: “[Photon Correlations](#)”, *Phys. Rev. Lett.* **10**, 84–86 (1963).
- [317] E. A. Burt, R. W. Ghrist, C. J. Myatt, M. J. Holland, E. A. Cornell and C. E. Wieman: “[Coherence, Correlations, and Collisions: What One Learns about Bose-Einstein Condensates from Their Decay](#)”, *Phys. Rev. Lett.* **79**, 337–340 (1997).
- [318] M. Schellekens, R. Hoppeler, A. Perrin, J. V. Gomes, D. Boiron, A. Aspect and C. I. Westbrook: “[Hanbury Brown Twiss Effect for Ultracold Quantum Gases](#)”, *Science* **310**, 648–651 (2005).
- [319] J. V. Gomes, A. Perrin, M. Schellekens, D. Boiron, C. I. Westbrook and M. Belsley: “[Theory for a Hanbury Brown Twiss experiment with a ballistically expanding cloud of cold atoms](#)”, *Phys. Rev. A* **74**, 053607 (2006).
- [320] P. L. Kapitza and P. A. M. Dirac: “[The reflection of electrons from standing light waves](#)”, *Mat. Proc. Cam. Phil. Soc.* **29**, 297–300 (1933).
- [321] P. L. Gould, G. A. Ruff and D. E. Pritchard: “[Diffraction of atoms by light: The near-resonant Kapitza-Dirac effect](#)”, *Phys. Rev. Lett.* **56**, 827–830 (1986).
- [322] Y. B. Ovchinnikov, J. H. Müller, M. R. Doery, E. J. D. Vredenburg, K. Helmerson, S. L. Rolston and W. D. Phillips: “[Diffraction of a Released Bose-Einstein Condensate by a Pulsed Standing Light Wave](#)”, *Phys. Rev. Lett.* **83**, 284–287 (1999).
- [323] P. J. Mohr, B. N. Taylor and D. B. Newell: “[CODATA recommended values of the fundamental physical constants: 2010](#)”, *Rev. Mod. Phys.* **84**, 1527–1605 (2012).

Acknowledgements

A large number of people have contributed to the completion of this thesis, some of whom I would like to thank in the following.

Foremost, I thank my advisor Klaus Sengstock for the possibility of performing my PhD thesis in his research group and for his continuous support and motivation throughout my studies at the *Institut für Laserphysik*. From providing such a thriving working environment to the countless vivid discussions his guidance has helped me in all aspects of my research for which I am immensely thankful. My sincere thanks also goes to Andreas Hemmerich for the kind evaluation of this thesis on an extremely short-term basis.

I owe the results presented in this thesis to the small number of experimental researchers in the driven-lattices team. The scope of this acknowledgement is not sufficient to express my gratitude towards my principal investigator Juliette Simonet for all the support in so many crucial aspects. Her matchless positive attitude, drive and expertise have been a delight throughout my studies. Together with Juliette, my fellow PhD students Julian Struck and Christoph Ölschläger have comprised an outstanding core team at the driven lattice experiment whom I would like to thank dearly for all the four years spent doing research in such high spirits. You guys are great.

I would like to thank Patrick Windpassinger for all of his helpful advice during the years in this group who has enriched this team with his unique Bavarian character. I also wish to thank Parvis Soltan-Panahi. Even though our time working together has been short, so much of the work concerning the honeycomb lattice is based on his findings. Special thanks also goes to “my” two skilled diploma and master students Christina Staarmann and Simon Prella respectively. Everybody in the driven lattice team and the whole research group on quantum gases belongs to the smartest and, which I find at least equally important, funniest and most interesting persons I happen to know. I am deeply grateful to have had the chance of working with such a bunch of amazing people.

Many successfully collaborations have been established throughout this thesis. For this, I want to thank André Eckardt, Philipp Hauke, Robert Höppner, Ole Jürgensen, Maciej Lewenstein, Dirk-Sören Lühmann and Ludwig Mathey.

I am sincerely thankful for the excellent administrative support by Janina Dahms, Ellen Gloy and Nadja Wardenburg and also for the dedicated help with all our countless technical issues by Reinhard Mielck.

In addition, I thank Christiane Schmidt for all the fruitful discussions of multivariate statistical data analysis and Karolin Hahn for the presumably quite tough proofreading of the introduction chapter.

Finally, I would like to thank my closest friends and my family for their unconditional support which can hardly be expressed in writing.